


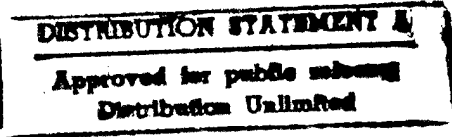
REPORT DOCUMENTATION PAGE

Public reporting burden for this collection of information is estimated to average 1 hour per response, including the reviewing the data needed, and completing and reviewing the collection of information. Send comments regarding this burden estimate or any other aspect of this collection of information, including suggestions for reducing this burden to Washington Headquarters Services, Directorate for Information Operations and Reports, 1215 Jefferson Davis Highway, Suite 1204, Arlington, VA 22202-4302, and to the Office of Management and Budget, Paperwork Reduction Project (0704-0188), Washington, D.C. 20503.

11

Form and
Instructions,
GPO, VA

0634

1. AGENCY USE ONLY (Leave Blank)		2. REPORT DATE August 25, 1995		3. REPORT TYPE AND DATES COVERED Final January '92 to July '95	
4. TITLE AND SUBTITLE New Reagents for CVD and CVI of Carbon Containing Boron and Other Oxidation Inhibitors				5. FUNDING NUMBERS C:F49620-92-J-0148	
6. AUTHOR(S) W.J. Lackey, J.A. Hanigofsky, G.B. Freeman, B.N. Beckloff, J.S. Lewis, H.C. King, M.A. Miller, E.M. Pickering, M.D. Langman, T.S. Moss, III, S. Vaidyaraman, P.K. Agrawal, E.K. Barefield, et al.					
7. PERFORMING ORGANIZATION NAME(S) AND ADDRESS(ES) Georgia Institute of Technology Atlanta, GA 30332				8. PERFORMING ORGANIZATION REPORT NUMBER A-9148	
9. SPONSORING/MONITORING AGENCY NAME(S) AND ADDRESS(ES) Dr. Alexander Pechenik AFOSR/MD Bldg. 410 Bolling Air Force Base Washington, DC 20332-6448				10. SPONSORING/MONITORING AGENCY REPORT NUMBER F49620-92-J-0148	
11. SUPPLEMENTARY NOTES COR:					
12a. DISTRIBUTION/AVAILABILITY STATEMENT Unlimited				12b. DISTRIBUTION CODE	
					
13. ABSTRACT (Maximum 200 words) The objectives of this three-year project were to: (1) identify and evaluate new multielement reagents to be used for the deposition of carbon containing one or more of the oxidation inhibitors boron and silicon, (2) determine the feasibility of the forced flow-thermal gradient CVI process for the rapid fabrication of carbon-carbon composites, and (3) understand the CVD of SiC and boron carbide and codeposition of these two phases since these materials have potential as oxidation protective coatings and matrices for carbon-carbon and other composites. Only satisfactory progress was made on objective No. 1, but excellent progress was made in regard to the other two objectives. Carbon-carbon was prepared in 3 h using the FCVI process and a thorough kinetics and deposit microstructure knowledge base was established for the CVD of SiC, boron carbide, and codeposition of these materials. A novel technique for monitoring the progression of densification during CVI was conceived and demonstrated. Importantly, a new class of materials, laminated matrix composites, was produced.					
14. SUBJECT TERMS Coatings, Chemical Vapor Deposition, Chemical Vapor Infiltration, Composites, Carbon, Oxidation Protection				15. NUMBER OF PAGES 302	
				16. PRICE CODE	
17. SECURITY CLASSIFICATION OF REPORT Unclassified		18. SECURITY CLASSIFICATION OF THIS PAGE Unclassified		19. SECURITY CLASSIFICATION OF ABSTRACT Unclassified	
				20. LIMITATION OF ABSTRACT UL	

Final Report
A-9148

NEW REAGENTS FOR CVD AND CVI OF CARBON CONTAINING
BORON AND OTHER OXIDATION INHIBITORS

W. J. Lackey, J. A. Hanigofsky, G. B. Freeman,
B. N. Beckloff, J. S. Lewis, H. C. King, M. A. Miller,
E. M. Pickering, and M. D. Langman
Georgia Tech Research Institute

T. S. Moss, III
School of Materials Science and Engineering

S. Vaidyaraman and P. K. Agrawal
School of Chemical Engineering

and

E. K. Barefield and D. S. Bruno
School of Chemistry and Biochemistry

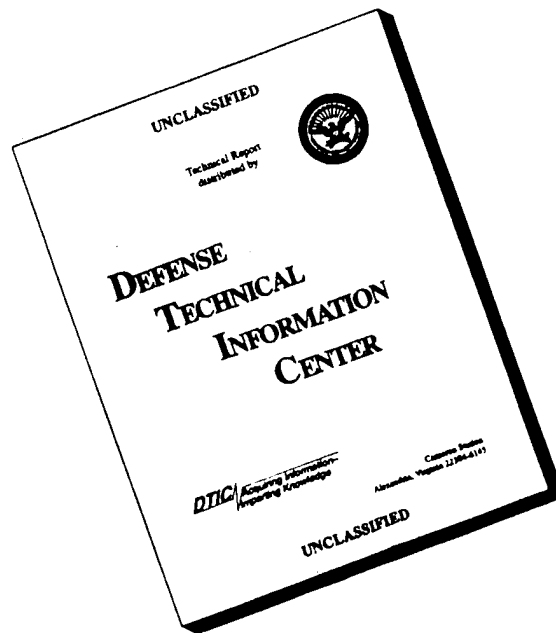
Prepared for
Dr. Alexander Pechenik
Air Force Office of Scientific Research
Washington, D.C.

Under Contract Number F49620-92-J-0148

Final Report for the period January 1992 - July 1995

19951011 023

DISCLAIMER NOTICE



**THIS DOCUMENT IS BEST
QUALITY AVAILABLE. THE
COPY FURNISHED TO DTIC
CONTAINED A SIGNIFICANT
NUMBER OF PAGES WHICH DO
NOT REPRODUCE LEGIBLY.**

New Reagents for CVD and CVI of Carbon Containing Boron and Other Oxidation Inhibitors

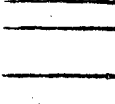
EXECUTIVE SUMMARY

Introduction

The objectives of this three-year project were to: (1) identify and evaluate new multielement reagents to be used for the deposition of carbon containing one or more of the oxidation inhibitors boron and silicon, (2) determine the feasibility of the forced flow-thermal gradient CVI process for the rapid fabrication of carbon-carbon composites, and (3) understand the CVD of SiC and boron carbide and codeposition of these two phases since these materials have potential as oxidation protective coatings and matrices for carbon-carbon and other composites. Only satisfactory progress was made on objective No. 1, but excellent progress was made in regard to the other two objectives. Carbon-carbon was prepared in 3 h using the forced flow-thermal gradient chemical vapor infiltration process (FCVI) and a thorough kinetics and deposit microstructure knowledge base was established for the CVD of SiC, boron carbide, and codeposition of these materials. A novel technique for monitoring the progression of densification during CVI was conceived and demonstrated. Importantly, a new class of materials, laminated matrix composites, was produced.

Carbon-Boron Films via New Reagents

The feasibility of using organoboranes as precursors for the deposition of carbon-boron films in a hot-wall CVD furnace was investigated. The reagents studied include trimethylborane, triethylborane, tributylborane, and triphenylborane. The films deposited from trimethylborane were rich in carbon and did not contain boron. Films deposited from triethyl and tributylborane

n of carbon-boron e trimethylborane, m trimethylborane and tributylborane	<input checked="checked" type="checkbox"/> <input type="checkbox"/> <input type="checkbox"/>	Codes
Dist A-1	Avail and/or Special	

were rich in boron at low temperatures and pressures and rich in carbon at high temperatures and pressures. We believe conventional reagents, rather than organoboranes, are better suited for CVD within the B-C-Si system.

Rapid Fabrication of Carbon-Carbon

It was shown that the FCVI process was well suited to the rapid fabrication of carbon-carbon composites. Composites were successfully prepared using propylene, propane, and methane as the source of carbon. When using propylene, dense, uniform composites were prepared in 3 h; about 7 h were required when using propane. Extensive microstructural characterization was performed and a model was developed that accurately describes the FCVI of carbon.

Technique for Monitoring CVI

During the study of the FCVI of carbon-carbon, a "marker technique" that readily permits monitoring of the progression of densification was conceived and demonstrated. The preparation of a carbon-matrix composite was investigated by momentarily interrupting, at various times, the carbon infiltration process to permit deposition of thin layers of SiC. Microscopic examination of these layers on a polished cross-section permitted determination of the extent of infiltration at various locations within the composite as a function of infiltration time.

Laminated Matrix Composites

A new type of composite, which consists of a reinforcement phase plus a matrix composed of alternate thin layers of two different materials, was conceived. Layered structures are known to enhance mechanical toughness and thus, their use as the matrix, along with the

reinforcement phase, should enhance the toughness of the overall composite. CVI appears to be an appropriate process for the fabrication of this class of materials. The reinforcement could be either fibers, whiskers, platelets or particulates, used individually or as a mixture. The matrix layers could be either ceramic, metallic, or polymeric. We successfully fabricated such a composite using the forced flow-thermal gradient CVI process. A carbon fibrous preform was infiltrated with alternate layers of C and SiC having thicknesses of 0.01 to 0.5 μm .

CVD in the B-C-Si System

The influence of processing conditions, when using conventional reagents, on the CVD of boron carbide, SiC, and the codeposition of these two materials was thoroughly studied. Statistically designed and analyzed experiments were used. Processing variables of interest were temperature, pressure, and flow rate of the reagents. Extensive SEM and TEM characterization permitted correlation of microstructure and kinetics/mass transport with the process variables.

Codeposition of B_{13}C_2 and SiC was successfully demonstrated using the mixtures of $\text{BCl}_3 + \text{MTS} + \text{CH}_4 + \text{H}_2 + \text{Ar}$ in a vertical, hot wall reactor using a modified impinging jet geometry. A comparison of the observed and predicted deposition rate, where the prediction was based on the prior studies of deposition of single phase B_{13}C_2 and SiC, showed that the two deposition reactions did not occur independently. A methodology was developed for comparing actual codeposition rates with rates predicted from single phase deposition. This work showed that during codeposition crystal nucleation and growth phenomena were important in influencing the kinetics of the deposition process.

Publications

This program resulted in the Ph.D. dissertations of Drs. Thomas S. Moss, III, and S. Vaidyaraman. Further, two patent applications and ten refereed publications were also prepared. A copy of each of the refereed publications is attached. The titles of the ten refereed papers are listed below in the order in which they appear in the attachment.

1. Fabrication of Carbon-Carbon Composites by Forced Flow-Thermal Gradient Chemical Vapor Infiltration
2. Forced Flow-Thermal Gradient Chemical Vapor Infiltration (FCVI) for Fabrication of Carbon/Carbon
3. Carbon/Carbon Processing by Forced Flow-Thermal Gradient Chemical Vapor Infiltration (FCVI) Process Using Propylene
4. Carbon/Carbon Processing by Forced Flow-Thermal Gradient Chemical Vapor Infiltration (FCVI) Using Propane
5. Technique for Monitoring Densification During Chemical Vapor Infiltration
6. Laminated Matrix Composites - A New Class of Materials
7. The Chemical Vapor Deposition of $B_{13}C_2$ from Mixtures of BCl_3 - CH_4 - H_2 -Ar
8. Kinetics of the CVD of SiC in a Hot Wall Reactor Using a Modified Impinging Jet Geometry
9. Factors Affecting the CVD of $B_{13}C_2$ +SiC Dispersed Phase Composites
10. Chemical Vapor Deposition of Boron-Carbon Films Using Organometallic Reagents

Fabrication of carbon-carbon composites by forced flow-thermal gradient chemical vapor infiltration

Sundar Vaidyaraman

School of Chemical Engineering, Georgia Institute of Technology, Atlanta, Georgia 30332

W. Jack Lackey and Garth B. Freeman

Georgia Tech Research Institute, Georgia Institute of Technology, Atlanta, Georgia 30332

Pradeep K. Agrawal

School of Chemical Engineering, Georgia Institute of Technology, Atlanta, Georgia 30332

Matthew D. Langman

Georgia Tech Research Institute, Georgia Institute of Technology, Atlanta, Georgia 30332

(Received 21 November 1994; accepted 13 February 1995)

Carbon fiber-carbon matrix composites were fabricated using the forced flow-thermal gradient chemical vapor infiltration (FCVI) process. The preforms for the infiltration were prepared by stacking 40 layers of carbon cloth in a graphite holder. The preforms were infiltrated with carbon using propylene or methane as a reactant, with hydrogen as a diluent. Composites with porosities as low as 7% have been processed within 8–12 h. The highest deposition rate obtained in the present study was $\sim 3 \mu\text{m/h}$, which is more than an order of magnitude faster than the typical value of $0.1\text{--}0.25 \mu\text{m/h}$ for the isothermal infiltration process.

I. INTRODUCTION

Carbon fiber-carbon matrix composites offer unique capabilities for mechanical systems in high temperature ($\sim 1000\text{--}2000^\circ\text{C}$) applications where high strength, stiffness, toughness, and thermal shock resistance are desired, as well as light weight. These composites are considered for use as jet engine components, nose cones, aircraft disk brakes, and leading edges on the space shuttle and high speed aircraft.¹ Recently, the range of applications has been broadened to include thermal management in electronic components and aerospace structures where the high thermal conductivity of carbon-carbon composites is advantageous. Lackey and Starr² have reviewed recent developments in the CVI of carbon-carbon. Kotlensky³ has prepared an excellent review of early carbon-carbon CVI work.

Carbon-carbon composites are at present fabricated using many cycles of resin or pitch infiltration followed by carbonization and graphitization, or by the use of the isothermal chemical vapor infiltration process (CVI).^{2–5} In the CVI process, large isothermal furnaces (hot zone of 1.8 m diameter and length of 2.0 m) containing multiple parts predominate. A hydrocarbon gas is flowed through the furnace at reduced pressure. The gas diffuses into the fibrous preforms and reacts to deposit the carbon matrix on the carbon fibers. In this case, the deposition occurs preferentially near the outer surface of the preform (Fig. 1) because the concentration of the reagent is at its maximum value near the

outer surface and reduces drastically on progressing inside the preform. Also, this preferential deposition tends to cause blockage of pores due to deposition of an impermeable coating at the outer surface. Consequently, the infiltration process must be interrupted to machine the impermeable skin to facilitate the reagent flow into the preform.³ The isothermal CVI process has to be carried out at low temperatures and pressures in order to enhance infiltration; i.e., chemical reaction rather than diffusion should be the rate-limiting step in the deposition process. Diffusion is a slow process, and the low temperature and pressure of the operation lead to very low deposition rates ($\sim 0.1\text{--}0.25 \mu\text{m/h}$);² hence, this method requires infiltration times on the order of several weeks and is restricted to thin components. These limitations add considerably to the cost of components and limit the application of this material.

Some of the shortcomings of the above process were overcome by the rapid infiltration process conceived by Lackey and Caputo⁶ and Caputo *et al.*^{7,8} That process uses forced flow of the reagent gas stream rather than relying on diffusion to transport the reagent through the preform. The forced flow-thermal gradient process is referred to as FCVI. It offers the advantages of much reduced processing times due to forced flow of the reagent and, as a result, potential for improved economics. In addition, it offers product uniformity and the ability to tailor physical, chemical, and mechanical properties. In principle, the FCVI process should be

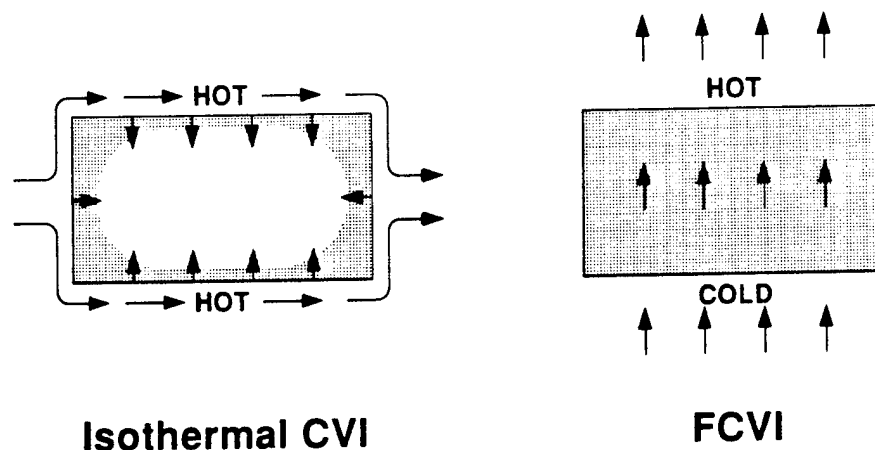


FIG. 1. Flow patterns for the isothermal CVI and FCVI processes. The different shades indicate different densities, with the lighter shade indicating less dense material.

applicable to the manufacture of a vast number of composite materials where the matrix could be selected from carbon, oxide, nitride, carbide, boride, silicide, or metal families of materials.

In the FCVI process a temperature gradient on the order of 200–500 °C is applied across the preform, and the reagent gases are forced to flow through the preform from the cold to the hot surface (Fig. 1). Ideally, it is desirable to obtain uniform deposition throughout the preform. This can be accomplished by choosing the reagent concentration and the temperature as well as the flow rate such that the high reagent concentration at the cold side offsets the lower temperature, and the lower concentration at the hot side offsets the high temperature, resulting in a uniform deposition rate. Also, the temperature gradient helps in prevention of the formation of an impermeable skin at the surface of the preform that is first exposed to the reagent. This methodology allows the process to be operated at much higher temperatures than the isothermal process, thereby further reducing the processing time significantly. The forced flow-thermal gradient technique also offers greater flexibility in the selection of the processing conditions. It is not essential to use the low temperatures, pressures, and reagent concentrations as in the isothermal process. Consequently, there is a wider latitude in selection of the conditions to obtain deposits possessing the required microstructure and properties.²

FCVI has been developed extensively for the fabrication of SiC–SiC composites. Over the past ten years, development at the Oak Ridge National Laboratory^{6–9} and Georgia Tech^{10,11} has brought this improved process for the manufacture of SiC composites near to commercialization. In contrast, application of the rapid CVI method to carbon-carbon composites has been sparse. Gebhart *et al.*^{12,13} conducted a few infiltration runs for the manufacture of carbon-carbon composites by

applying both a thermal gradient and forced flow of the reagent. However, no detailed study of this process was carried out. In the past, most researchers who did not use the isothermal process have focused on using a thermal gradient^{14,15} or forced flow¹⁶ separately for the manufacture of carbon-carbon composites. Hence, the focus of the present work was to investigate the FCVI process for the fabrication of carbon-carbon composites.

II. EXPERIMENTAL PROCEDURE

A. Preform fabrication

A circular carbon cloth 4.8 cm in diameter was used to prepare the preform. The carbon cloth, obtained from Fabric Development Inc. (Quaker Town, PA), consisted of a plain weave of T-300 fibers containing 3000 filaments per tow; each filament had a diameter of 7 μm . Typically, forty layers of cloth were stacked in a graphite preform holder (Fig. 2). The layers were stacked in such a way that each layer was oriented at 30° to the adjacent layer. Hence, the fiber tows of layers 1, 4, 7, etc. were in the same orientation. The lay-up was then compressed with a graphite punch (Fig. 2) with a force of ~900 N (200 lbf). The resulting preform holder assembly was then dried in an oven overnight to remove any moisture. This assembly was then placed in a resistively heated hot wall furnace (Fig. 3) to carry out the infiltration process.

B. Apparatus

The FCVI equipment is shown in Fig. 3. The details of the water-cooled gas injector are shown in Fig. 4. The water-cooled injector is responsible for the establishment of the thermal gradient across the preform. The bottom of the preform holder assembly is cooled by the injector and the top is heated by the furnace. This leads to the development of the temperature gradient. The temperature inside the preform and the temperature

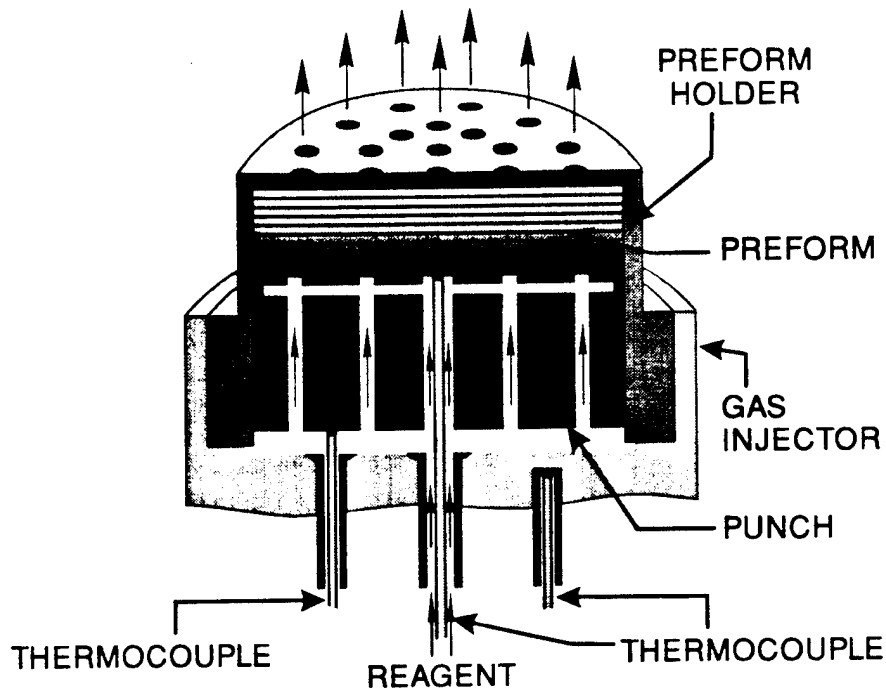


FIG. 2. Cross section of the preform holder assembly.

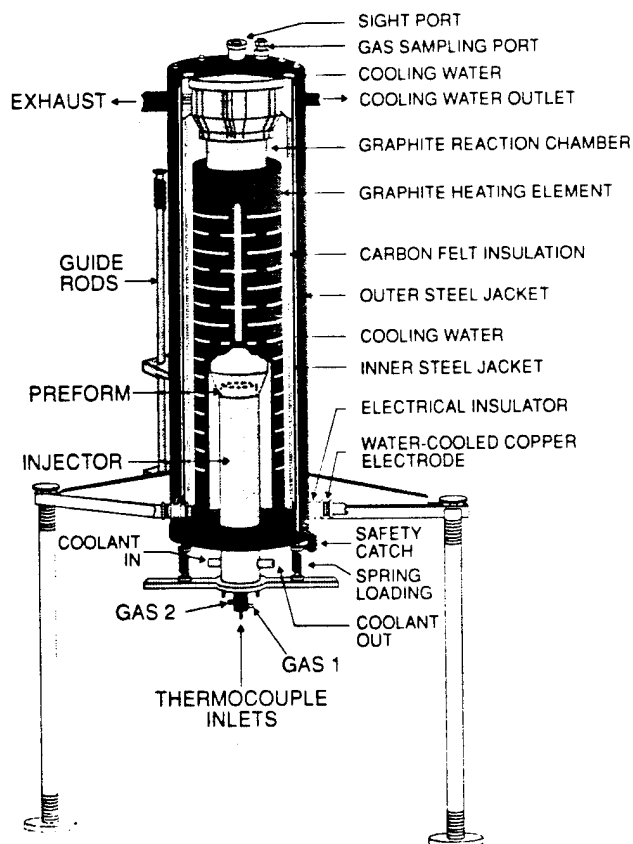


FIG. 3. FCVI reactor for fabrication of carbon-carbon composites.

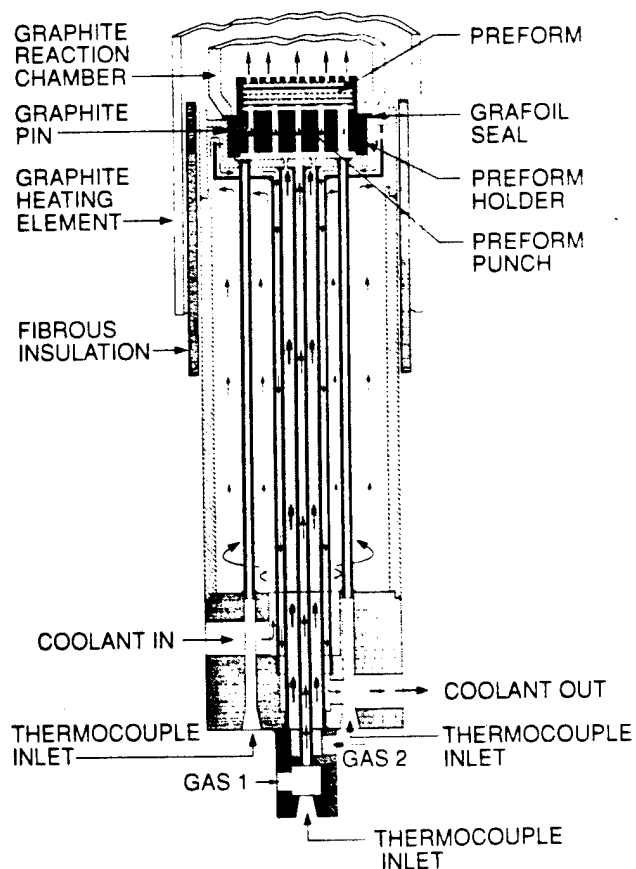


FIG. 4. Schematic of water-cooled gas injector.

gradient can be varied by either varying the height of the preform holder or the preform thickness. A taller holder or a thicker preform reduces the cooling effects due to the injector and vice versa. Three types of preform holders, categorized by the distance they extended above the injector, were employed (Fig. 2). This distance was 2.54, 5.08, and 7.62 cm for preform holders referred to as types 1, 2, and 3, respectively. A Grafoil (UCAR Carbon Company Inc., Cleveland, OH) seal (Fig. 4) was used to ensure that the process gas stream was constrained to flow through the fibrous preform.

C. Reagents

Table I describes the reagents used in the infiltration runs. The process gas stream typically consisted of a carbon source gas and a diluent. The carbon source gas employed for the infiltration runs included propylene and methane, and the diluent was hydrogen. The propylene was 99.5% pure, polymer purity (Matheson, East Rutherford, NJ). The methane was 99.97% pure, ultrahigh purity, and hydrogen was 99.999% pure, ultrahigh purity (HoloX, Atlanta, GA).

D. FCVI procedure

The first step before starting each run was to evacuate the furnace and check for leaks. Upon verification that the leak rate was below 0.5 Torr/min, the furnace was filled with argon to atmospheric pressure. Following this step, the furnace was heated to the required temperature with argon flowing in the region outside the reaction chamber (Fig. 3); this protects the heating element. The furnace was operated at constant power throughout the infiltration run. Once the temperature was stabilized (~ 15 min), the reagent gas plus diluent

was forced through the preform. The flow rates were controlled using mass flow controllers (Model 1259, MKS Instruments Inc., Andover, MA). The pressure above the preform was atmospheric and the pressure in the reagent supply line was ~ 3.4 KPa (0.5 psi) above atmospheric pressure at the beginning of the run. This pressure gradient forced the reagent through the preform. The reagent gas first came in contact with the cooler side of the preform and flowed up through the preform to the hot side. As the infiltration progressed, the back pressure increased as the pores in the preform were filled by the deposited matrix. The infiltration process was typically terminated once the back pressure increased to about 170 KPa (10 psig). The temperatures at the bottom of the preform and that of the graphite punch were measured throughout the run using type K thermocouples. The initial temperature at the top of the preform was obtained from a temperature calibration, the details of which are explained in the next section. After cooling to room temperature, the infiltrated composite was removed intact from the graphite preform holder.

E. Temperature profiling

Since light reflection from the heated chamber was found to interfere with use of an optical pyrometer that sighted vertically downward from the top of the furnace, a temperature calibration experiment was conducted in order to relate the temperature at the top of the preform with the gas flow rate and power supplied to the furnace. Typically, a thermocouple for measuring the temperature at the top of the preform would be inserted through the top sight port. However, in these initial runs it was judged important to physically observe the sample through the sight port in order to follow the

TABLE I. Operating conditions for FCVI.

						Preform temperature (°C)	
Run no.	Preform holder type	Cloth layers	Reagent flow rate (sccm)	Diluent flow rate (sccm)	Time (h)	Top	Bottom
<u>Propylene</u>							
PCVI-4	3	40	200	200	1.25	1300	1050
PCVI-5	1	40	125	375	10	...	160
PCVI-6	2	40	50	150	24.25	1180	830
PCVI-8	2	40	100	100	8	1200	850
PCVI-9	2	40	200	200	12	1180	830
PCVI-10	2	80	100	100	23	...	650
PCVI-12	2	10	100	100	2	...	850
PCVI-13	2	10	100	100	2	...	960
<u>Methane</u>							
MCVI-1	1	40	250	250	31.5	...	115
MCVI-3	2	40	250	250	6.5	...	560
MCVI-7	3	40	50	150	43	1320	1108
MCVI-11	3	40	50	50	38.5	1320	1050

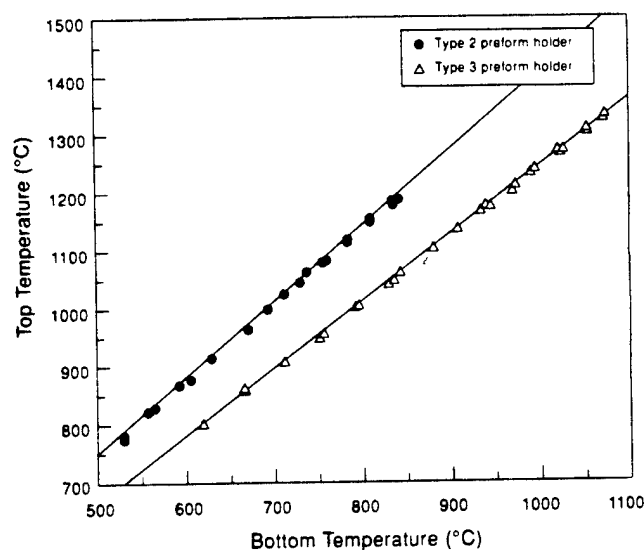


FIG. 5. Relationship between the bottom and top temperatures of the preform for two types of preform holders.

progress of deposition and detect any changes in gas flow rates. Consequently, it was not possible to measure the temperature at the top of the preform during the run.

For the temperature profiling experiment, type C and K thermocouples were used to measure the temperature at the top and bottom of the preform, respectively. From these measurements, it was found that the temperature at the top of an uninfiltrated, 0.85 cm thick preform was related to the bottom temperature, as shown in Fig. 5. The temperature differences between the top and the bottom of the preform were $\sim 250^\circ\text{C}$ with the type 3 holder and $\sim 350^\circ\text{C}$ with the type 2 holder at the operating conditions. In the actual runs the bottom

temperature was used to estimate the top temperature using the calibration graph shown in Fig. 5.

F. Characterization

The fiber content and the initial porosity of the preform were obtained from the fiber mass and known fiber density of 1.77 g/cm^3 . The apparent volume of the composite was measured using Archimedes' principle with methanol. The sample was also weighed after saturating with methanol to permit calculation of the open pore volume. These two values were added to obtain the bulk volume of the composite. As a check on the bulk volume, the above procedure was repeated using distilled water. The density of the deposited matrix was assumed to be 1.9 g/cm^3 in order to permit the calculation of the total porosity. It was seen that changing the assumed matrix density from 1.8 to 2.1 g/cm^3 changed the value of the total porosity at most by only 3%. Densities in the range of 1.9 to 2.0 g/cm^3 are typically observed for CVI carbon.¹⁴

The composites were mounted in epoxy, sectioned, and polished. The polished sections were observed via optical and scanning electron microscopy to permit evaluation of the uniformity of the infiltration.

G. Mechanical properties

The flexural strength of 2.54 cm (1 in.) long beams from the composites was measured at room temperature using four-point bending. The inner and the outer spans were 10 and 20 mm, respectively. The crosshead speed used was 0.01 in./min.

TABLE II. Properties of the infiltrated composites.

Run no.	Fiber content (vol %)	Rate of weight gain (g/h)	Bulk density (g/cm^3)	Total porosity (%)	Open porosity (%)	Deposition efficiency (%)
Propylene						
PCVI-4	40.8	1.73	0.861	51.9	...	9.0
PCVI-5	37.5	~ 0	~ 0
PCVI-6	52.2	0.36	1.480	18.5	...	7.4
PCVI-8	58.3	1.10	1.686	7.3	4.2	11.4
PCVI-9	59.9	0.69	1.689	7.0	4.1	3.6
PCVI-10	51.4	0.77	1.513	16.9	10.2	8.0
PCVI-12 ^a	53.0	0.19	1.028	42.3	37.0	1.9
PCVI-13 ^a	43.3	0.82	1.128	37.7	31.0	7.6
Methane						
MCVI-1	37.5	~ 0	~ 0
MCVI-3	52.2	~ 0	~ 0
MCVI-7	46.3	0.16	1.226	32.3	...	10.0
MCVI-11	50.5	0.25	1.514	16.9	5.0	15.4

^aOne cloth layer came off while removing the composite. Density, total, and open porosity were found for the nine-layer composite.

III. RESULTS AND DISCUSSION

Table II summarizes the fiber volume, weight gain, density, and calculated open and total porosities of the composites prepared by the FCVI process.

Initially, the type 1 preform holder was used for both propylene (PCVI-5) and methane (MCVI-1). The preform temperature with this holder was about 150–400 °C, which is too low for carbon deposition. In order to obtain higher preform temperatures, the type 3 preform holder was employed. However, in the case of propylene (PCVI-4), the temperature in the punch portion of the preform holder was high enough to pyrolyze the reagent. This resulted in carbon deposition in the holes of the punch, thereby blocking the gas flow to the preform.

This problem was avoided in the subsequent propylene runs by using the type 2 preform holder. These runs resulted in well-infiltrated composites, with no significant carbon deposition in the punch. In the case of methane, the type 3 preform holder was used, as the typical pyrolysis temperature of methane (~1100–1400 °C) is much higher than that of propylene.

The following sections describe in more detail the effect of operating conditions and reagent types and flow rates on porosity, microstructure, and deposition rate and efficiency.

A. Total porosity

Composites with total porosities as low as 7% were densified in 8–12 h using a propylene concentration of 50% (PCVI-8, 9). When the concentration was reduced to 25% (PCVI-6), the final porosity increased to ~18%. In the case of PCVI-10, a thicker preform was employed which led to a cooler bottom preform temperature (650 °C), resulting in higher total porosity. The two runs conducted with 10 cloth layers (PCVI-12, 13) also resulted in high total porosity because the runs were terminated after 2 h of infiltration. The composites prepared using methane had much higher porosity when compared to propylene. For example, the porosity was 17% when a 50% concentration of methane was used, compared to 7% when using the same concentration of propylene. From the above observations it can be seen that composites can be densified in a very short time using the FCVI method, provided the proper operating conditions are used.

B. Open and closed porosity

The open porosity of fully infiltrated composites was typically ~4%. The closed porosity for propylene runs was ~3–6%. In the case of methane the closed porosity was about 10%. The high value of closed porosity may be due to either of the following two reasons: (i) the actual matrix density may be lower than the assumed

value of 1.9 g/cm³ used to calculate the total porosity, or (ii) the kinetics of carbon deposition from methane for the specific operating conditions used to prepare sample MCVI-11 result in larger amounts of closed porosity. The first reason can be discounted since, as previously mentioned, the calculated total porosity is not very sensitive to the value assumed for the matrix density. Hence, the second reason is a more plausible explanation of high closed porosity in methane runs. When the composite contained only 10 cloth layers, the open porosity was ~31–37%.

C. Microstructure

It is important to examine if the infiltration is uniform throughout the thickness of the component. Figure 6 shows scanning electron micrographs of the hot, middle, and cold side of the composite from run PCVI-8. Very little difference in densification is evident for the three locations. Even when the concentration of

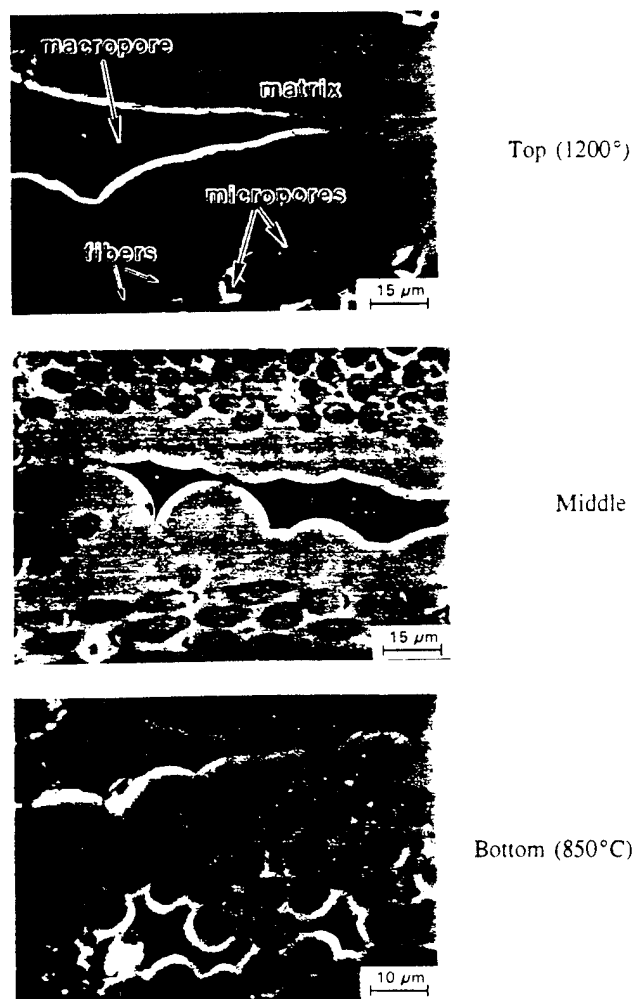


FIG. 6. Micrographs of a polished section of the composite densified using 50% propylene (PCVI-8).



FIG. 7. Micrograph from the center of the composite densified using 25% propylene (PCVI-6).

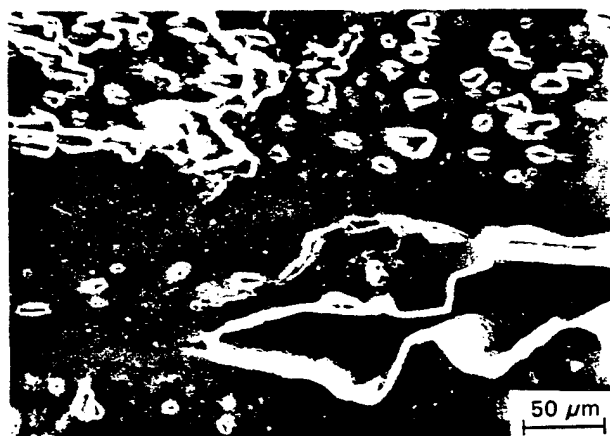


FIG. 8. Micrograph of the composite densified using 25% methane (MCVI-7).

propylene was reduced to 25%, extensive and apparently uniform densification was obtained (Fig. 7). However, the pores remaining between the cloth layers were larger in this case compared to PCVI-8, since less carbon was deposited. The densification was found to be uniform and appreciable when methane, instead of propylene, was used as the reagent (Fig. 8). This particular micrograph is interesting in that it shows how, during the infiltration process, coating of individual fibers creates the matrix. The present work showed that the FCVI process is well suited for fabricating carbon-carbon composites. That is, uniform and thorough densification was achieved over a wide range of operating conditions without any detailed optimization of the process.

D. Deposition rate

From the micrographs just presented, and similar ones, it was also possible to measure the coating thickness in macro- and micropores. Deposition rates for the two types of regions were obtained by dividing by

the infiltration time. The deposition rates, expressed as coating thickness per unit time, associated with macro- and micropores are different. The deposition rate in the micropores was much higher than in the micropores. In a cloth lay-up, macropores are found between some layers of cloth, and the micropores are typically within the fiber tow of a cloth.

The highest deposition rate obtained from macropores in this study was 2.9–3.0 $\mu\text{m/h}$ in the run conducted with 50% propylene (PCVI-8). This deposition rate is comparable to that obtained for the FCVI processing of SiC–SiC composites¹⁷ and is more than an order of magnitude larger than the deposition rates (0.1–0.25 $\mu\text{m/h}$) for isothermal CVI of carbon or SiC.² The deposition rate with 25% propylene (PCVI-6) was 0.6–0.7 $\mu\text{m/h}$. The deposition rate in macropores with 25% methane (MCVI-7) was $\sim 0.5 \mu\text{m/h}$.

The deposition rate in micropores was 0.14–0.4 $\mu\text{m/h}$ at 50% propylene concentration (PCVI-8) and 0.05–0.12 $\mu\text{m/h}$ for 25% propylene concentration (PCVI-6). In the case of methane, the deposition rate was found to be about 0.04–0.08 $\mu\text{m/h}$ (MCVI-7).

E. Rate of weight gain

The rate of weight gain when propylene was used as the reagent was much higher than for methane under similar flow conditions. This can be attributed to the higher reactivity of propylene. The rate of weight gain was about 0.7–1.1 g/h for runs with 50% propylene concentration (PCVI-8, -9, and -10). The low rate of weight gain for run PCVI-9 was due to leakage of the reagent during the run. In the case of PCVI-10, the use of 80 instead of 40 layers of cloth caused overcooling of the bottom of the preform, resulting in a smaller value for the rate of weight gain. This preform was appreciably infiltrated in 23 h, although additional time or higher flow rate would be necessary to achieve optimum infiltration. When the concentration of the propylene was reduced to 25%, the rate of weight gain reduced to 0.36 g/h.

For methane runs the rate of weight gain was 0.25 g/h for 50% concentration (MCVI-11) and 0.16 g/h for 25% concentration (MCVI-7). The rate of weight gain was much lower for methane than for propylene, even though the methane runs were carried out at much higher temperatures. This can be explained by the higher stability of the radicals produced by methane pyrolysis compared to propylene.

F. Deposition efficiency

Deposition efficiency, or the ratio of the moles of carbon deposited to the total moles of carbon entering in the reagent gas stream, is an important process parameter. The observed deposition efficiency with propylene

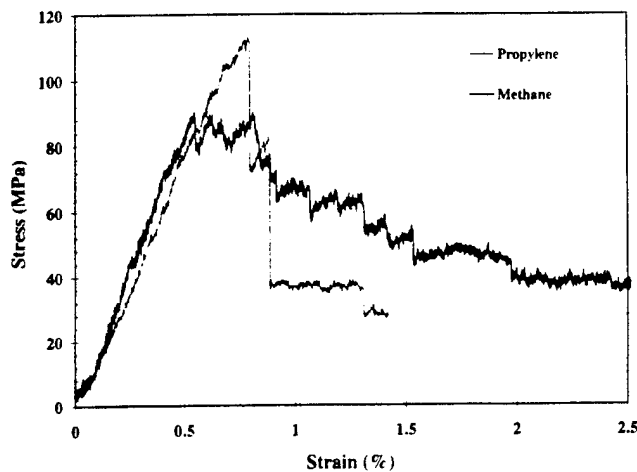


FIG. 9. Stress-strain curves for four-point flexural testing of carbon-carbon composites.

was between 7 and 12%. The deposition efficiency with methane was 10–15%. The only reported value for the deposition efficiency for an isothermal process was only 0.8–1.5% at 700 °C.¹⁸ The low value for deposition efficiency for PCVI-9 can be attributed to reagent leakage. Even this value is much higher than for the isothermal process.

G. Mechanical properties

Figure 9 gives the typical stress-strain curves of composites made with propylene and methane. The composites made from propylene exhibited slightly higher strength and similar strain at failure compared to those made using methane, as shown in Table III. The moduli of the samples prepared using propylene and methane were similar. The mechanical properties reported here are comparable to the results reported by Oh and Lee¹⁹ for carbon-carbon composites prepared using the thermal gradient method with propane.

The strength of the composites can be further increased by modifying the lay-up used to make the preform. In the configuration used in the present work, the nominal fiber volume is 50% and a fiber fraction of ~8% is aligned with each fiber direction for a 0°, 30°, 60° lay-up. This value can be increased to ~20–25% by

employing a 0-90° lay-up which would lead to increased strength.

H. Preform thickness

The versatility of the process was tested using preforms with thicknesses of 0.2, 0.85, and 1.66 cm (10, 40, and 80 layers of cloth). In the case of the thickest preform (PCVI-10), the temperature of the bottom cloth was about 650 °C, resulting in a more porous structure in the bottom portion of the preform. However, we speculate that this limitation could be eliminated by either employing the taller type 3 preform holder or by extending the run time. The rate of weight gain for this run was comparable to the runs carried out with 40 cloth layers at similar conditions.

For the initial run (PCVI-12) with 10 layers of cloth, the preform was not sufficiently hot to achieve full densification. The preform cloth acts as insulation between the cool injector and the hot heating element resulting in the temperature gradient. The reduction in the number of cloth layers caused excess cooling. Consequently, in the following run 15 layers of 0.025 cm thick Grafoil were added between the preform and the gas injector; holes were punched in the Grafoil to permit gas flow. The presence of the Grafoil resulted in higher preform temperatures and higher weight gain. The rate of weight gain was about 0.8 g/h, which is comparable to the rate of weight gain obtained with 0.85 cm thick preforms. These results show that the FCVI process for carbon-carbon composites is applicable to both thin and thick components.

IV. CONCLUSIONS

The following conclusions were drawn from the present work:

- (1) Dense carbon-carbon composites can be fabricated in a relatively short time using the FCVI process.
- (2) The deposition was uniform throughout the preform.
- (3) Composites with total porosities as low as 7% were obtained in 8–12 h.
- (4) Propylene required shorter processing times compared to methane.

ACKNOWLEDGMENTS

This work was supported by the Air Force Office of Scientific Research. The guidance of Dr. Alexander Pechenik throughout the course of this work is appreciated. We thank Ms. Sheree Collins for her expertise and diligence in graphics preparation. Typing of the original manuscript by Ms. Virginia Myers is gratefully acknowledged.

TABLE III. Mechanical properties of carbon-carbon composites.

Properties	Propylene CPCVI-8		Methane MCVI-11	
	Sample 1	Sample 2	Sample 1	Sample 2
Flexural strength	113	98.5	90.3	94.4
MPa (Ksi)	(16.4)	(14.3)	(13.1)	(13.7)
Flexural modulus	14.95	16.26	16.95	13.37
GPa (Msi)	(2.17)	(2.36)	(2.46)	(1.94)
Strain at failure (%)	0.77	0.78	0.8	1.0

REFERENCES

1. J.D. Buckley, *Am. Ceram. Soc. Bull.* **67**, 364-368 (1988).
2. W.J. Lackey and T.L. Starr, in *Fiber Reinforced Ceramic Composites*, edited by K.S. Mazdizasni (Noyes Publications, Park Ridge, NJ, 1991), pp. 397-449.
3. W.V. Kotlensky, in *Chemistry and Physics of Carbon*, edited by P.L. Walker, Jr. and P.A. Thrower (Marcel Dekker Inc., New York, 1973), Vol. 9, pp. 173-262.
4. R.L. Bickerdike, A.R.G. Brown, G. Hughes, and H. Ranson, in *Proc. Fifth Conf. on Carbon*, edited by S. Mrozowski, M.C. Studebaker, and P.L. Walker (Pergamon Press, New York, 1962), Vol. 1, pp. 575-582.
5. W.C. Jenkins, US Patent 3 160 517 (1964).
6. W.J. Lackey and A.J. Caputo, US Patent 4 580 523 (1986).
7. A.J. Caputo and W.J. Lackey, *Ceram. Eng. Sci. Proc.* **5** (7-8), 654-667 (1984).
8. A.J. Caputo, W.J. Lackey, and D.P. Stinton, *Ceram. Eng. Sci. Proc.* **6** (7-8), 694-706 (1985).
9. D.P. Stinton, A.J. Caputo, and R.A. Lowden, *Am. Ceram. Soc. Bull.* **65**, 347-350 (1986).
10. T.L. Starr, *Ceram. Eng. Sci. Proc.* **8**, 951-957 (1987).
11. T.L. Starr, in *Chemical Vapor Deposition of Refractory Metals and Ceramics II*, edited by T.M. Besmann, B.M. Gallois, and J. Warren (Mater. Res. Soc. Symp. Proc. **250**, Pittsburgh, PA, 1992), pp. 207-214.
12. J.J. Gebhart, AFML-TR-78-115, Air Force Materials Laboratory, Wright-Patterson Air Force Base, OH 45433.
13. J.J. Gebhardt, E.R. Stover, W. Mueller, and J. Yodsnuks, in *Petroleum Derived Carbons*, edited by M.L. Deviney and T.M. O'Grady (ACS Symposium Series), Vol. 21, pp. 213-227.
14. S-H. Oh and J-Y. Lee, *Carbon* **26**, 763-768 (1988).
15. J.D. Theis, Jr., in *Proc. Third Int. Conf. on Chemical Vapor Deposition*, edited by F.A. Glaski (Electrochemical Society, Princeton, NJ, 1972), pp. 561-573.
16. S. Kimura, E. Yasuda, N. Takase, and S. Kayusa, *High Temp. High Press.* **13**, 193-199 (1980).
17. A.J. Caputo, R.A. Lowden, and D.P. Stinton, ORNL/TM-9651, Oak Ridge National Laboratory, Oak Ridge, TN (June 1985).
18. S. Marinkovic and S. Dimitrijevic, *Carbon* **23**, 691-699 (1985).
19. S-H. Oh and J-Y. Lee, *Carbon* **27**, 423-430 (1989).

Forced Flow-Thermal Gradient Chemical Vapor Infiltration (FCVI) for Fabrication of Carbon/Carbon

S. Vaidyaraman, W. J. Lackey, P. K. Agrawal and G. B. Freeman

Georgia Institute of Technology, Atlanta, GA 30332

Carbon/carbon composites are at present fabricated using many cycles of resin or pitch impregnation followed by carbonization and frequently high temperature graphitization [1-2]. Since the resin and pitch shrink during the carbonization and graphitization steps, numerous cycles of impregnation have to be carried out to obtain sufficiently dense components. Isothermal chemical vapor infiltration (CVI) is also well established for the manufacture of carbon/carbon composites [3-6]. In this process the reactors have to be operated at low pressures and temperatures in an attempt to obtain uniformly dense composites. The low temperatures coupled with low pressures lead to very low deposition rates, hence, this method requires infiltration times on the order of several weeks and is restricted to thin components. The limitations enumerated above for the various processes add considerably to the cost of the components and limit the application of this material. Some of these limitations can be overcome by using the forced flow-thermal gradient chemical vapor infiltration process which is often referred to as FCVI [7-9]. The main advantages of this process include reduced processing times due to forced flow of the reagent and uniform densification throughout the preform.

In the FCVI process, a temperature gradient of the order of 200-500°C is applied across the preform and the reagent gases are forced to flow through the cold to the hot surface of the

preform. Ideally, the goal is to obtain uniform deposition throughout the preform. This can be accomplished by choosing reagent concentration, temperature, and the flow rate such that the high reagent concentration at the cold side offsets the lower temperature, and the lower concentration at the hot side offsets the high temperature resulting in a uniform deposition rate. The goal of the present work was to rapidly fabricate carbon/carbon composites with uniform density using the FCVI process.

2. Experimental Details

2.1 Preform Fabrication

Preforms were prepared by stacking 40 layers of carbon cloth in 0-30-60-90° orientation inside a graphite holder. The carbon cloth consisted of a plain weave of T-300 fibers containing 3000 filaments per tow; each filament had a diameter of 7 μm . The lay-up was then compressed with a graphite punch (Figure 1) with a force of ~ 900 N (200 lbf). The resulting preform holder assembly was dried overnight before the infiltration.

2.2 Apparatus

The schematic of the FCVI process is shown in Figure 1. The water cooled injector is responsible for the establishment of the thermal gradient across the preform. The bottom of the preform holder assembly is cooled by the injector and the top is heated by the furnace. This leads to the development of the temperature gradient. The temperature inside the preform and the temperature gradient can be varied by either varying the height of the preform holder or the preform thickness. Three types of preform holders, categorized by the distance extended above the injector were employed (Figure 1). The distance was 1, 2 and 3 inches for preform holders referred to as types 1, 2, and 3, respectively.

2.3 Reagents

The feed gas typically consisted of a carbon source gas and hydrogen as a diluent. The carbon source gases employed for the infiltration runs include propylene, propane, and methane. The propylene was 99.5 % pure, propane was 99.5% pure, and methane was 99.97 % pure.

2.4 Procedure

The resistively heated furnace was heated to the required temperature with argon flowing in the region outside the reaction chamber; this protects the heating element. The furnace was operated at constant power throughout the infiltration run. Once the temperature was stabilized (~ 15 min), the reagent gas plus diluent was forced through the preform. All the infiltration runs were carried out at atmospheric pressure. As the infiltration progressed, the back pressure increased as the pores in the preform were filled with deposited matrix. The infiltration process was terminated once the back pressure reached about 69 kPa (10 psig). The temperatures at the bottom of the preform were measured using a K-type thermocouple. The initial temperature at the top of the preform was obtained from a calibration chart, which relates the furnace power to the preform top temperature. Table 1 summarizes the operating conditions for different infiltration runs.

2.5 Characterization

The fiber content and the initial porosity of the preform were obtained from the fiber mass and known fiber density of 1.77 g/cm³. The total volume (bulk) of the composite was measured using Archimedes' principle with methanol. The sample was also weighed after saturating with methanol to permit calculation of the open porosity. As a check on the bulk volume, the above procedure was repeated using water. The density of the deposited matrix was

assumed to be 1.9 g/cm^3 in order to permit the calculation of the total porosity. It was seen that changing the assumed matrix density from 1.8 to 2.1 g/cm^3 changed the value of the total porosity at most by only 3%. Densities in the range 1.9 to 2.0 g/cm^3 are typically observed for CVI carbon.[10]

3. Results

Table 2 summarizes the fiber volume, rate of weight gain, infiltration time, density, and calculated open and total porosity for the composites prepared by FCVI. Preliminary infiltration runs showed that the temperature of the preform, when using the type 1 holder ($\sim 140\text{--}400^\circ\text{C}$), was too low for carbon deposition. The type 2 preform holder, with temperatures for the bottom of the preform of $\sim 840^\circ\text{C}$, was employed to fabricate carbon composites when propylene was used as the reagent. In the case of methane, the longer type 3 preform holder was used, as the typical pyrolysis temperature of methane ($\sim 1100\text{--}1400^\circ\text{C}$) is much higher than that of propylene. In the case of propane, which requires intermediate deposition temperatures, the type 3 preform holder with a bottom temperature of $\sim 940^\circ\text{C}$ was found to be suitable for carbon deposition.

The following sections describe in more detail the effect of operating conditions and the reagent types on porosity, microstructure, deposition rate, and rate of weight gain.

3.1 Porosity

3.1.1 Total Porosity

Composites with total porosities as low as 7% were densified in 8-12 h using propylene concentrations of 50% (PCVI-8,9). When the concentration of propylene was reduced to 25% (PCVI-6), the final porosity increased to 16-18%. The porosity of the composite prepared using

propane was similar to that of propylene. For example, the total porosity was 8% with 50% propane (PACVI-16) as compared to 7% with 50% propylene (PCVI-8). The composites prepared using methane had higher porosities. For example, the total porosity of a composite prepared using 50% concentration of methane was 17% compared to 7% in the case of propylene. From the above observations it can be seen that the FCVI process has the potential to infiltrate composites in a short time.

3.1.2 Open Porosity

The open porosity of infiltrated composites was typically ~4%. This value of open porosity can be subtracted from the total porosity to obtain the closed porosity. The closed porosity for propylene and propane runs was ~3-4%. In the case of methane the closed porosity was about 10%. This high value of closed porosity may be due to either of the following two reasons: (1) The actual matrix density may be lower than the assumed value of 1.9 g/cm³ used to calculate the total porosity, or (2) the kinetics of carbon deposition from methane for the specific operating conditions used to prepare sample MCVI-11 result in larger amounts of closed porosity. The first reason can be discounted since, as previously mentioned, the calculated total porosity is not very sensitive to the value assumed for matrix density. Hence, the second reason is a more plausible explanation for the high closed porosity in methane runs.

3.2 Microstructure

Scanning electron microscopy was used to determine if the infiltration was uniform throughout the thickness of the component. Micrographs of the hot, middle, and cold side of the different composites prepared using propylene as the reagent showed very little difference in

densification for the three locations. An example of the uniformity is shown in Figure 2. The densification was found to be uniform and appreciable even in the cases where methane, instead of propylene, was used as the reagent. The present work showed that the FCVI process is well suited for fabricating carbon/carbon composites. That is, uniform and thorough densification was achieved over a wide range of operating conditions without any detailed optimization.

3.3 Coating Thickness

Using scanning electron microscopy it was possible to measure the coating thickness in macro and micropores. In a cloth lay-up, such as that used in the present work, macropores are found between the cloth layers and the tows in a cloth, whereas, micropores are found within a tow in a cloth layer. Figure 3 shows the coating thickness in micropores as a function of the distance from the cold side of the preform for sample PCVI-8. It can be clearly seen that coating thickness is independent of position within the composite. The scatter of the data is due to different fiber spacings in the tows resulting in different coating thicknesses. Figure 4 shows the coating thickness for macropores as a function of distance from the cold side of the preform. In this case the coating thickness increases with increase in distance from the cold side. The coating thickness is about 8 μm at the cold side compared to 22-24 μm at the hot side. This trend implies that the depletion of the reagent while flowing through the preform did not fully neutralize the effect due to the temperature gradient in the preform for the specific processing conditions used to prepare this sample. It should be noted that the highest coating thickness was only 3 times more than the minimum value. This is considerably less variation than that observed for the isothermal CVI process. This suggests that there may be potential to tailor the

concentration to get uniform macropore coating thickness across the preform with the FCVI process.

3.4 Deposition Rate

Deposition rate was calculated by dividing the coating thickness by the infiltration time. The deposition rate for macropores was different from that for micropores. In the present work the highest deposition rates obtained for macropores were 3.0-3.5 $\mu\text{m/h}$ in the runs with 50% propylene (PCVI-8) and with 50% propane (PACVI-16). This deposition rate is comparable to that obtained for FCVI processing of SiC-SiC composites [11] and is more than an order of magnitude larger than the deposition rates of 0.1-0.25 $\mu\text{m/h}$ for isothermal CVI of carbon or SiC [6]. The deposition rate with 25% propylene (PCVI-6) was 0.6-0.7 $\mu\text{m/h}$. The deposition rate in macropores with 25% methane (MCVI-7) was $\sim 0.5 \mu\text{m/h}$.

The deposition rate in micropores was 0.14-0.4 $\mu\text{m/h}$ at 50% propylene concentration (PCVI-8) and 0.05-0.12 $\mu\text{m/h}$ for 25% propylene concentration (PCVI-6). In the case of propane and methane, the deposition rates were found to be 0.07-0.2 $\mu\text{m/h}$ and 0.04-0.08 $\mu\text{m/h}$ (MCVI-7) respectively. The large variation in the value of the deposition rate in micropores for a given processing condition can be attributed to the variations in the fiber spacing.

3.5 Rate of Weight Gain

The rate of weight gain was much higher when propylene or propane was used as the reagent compared to methane at similar flow conditions. The rate of weight gain was 0.7-1.1 g/h for runs with 50% propylene (PCVI-8,9). When the concentration of the propylene was reduced to 25% (PCVI-6) the rate of weight gain reduced to 0.36 g/h. The rate of weight gain was 0.88 g/h for the case of 50% propane (PACVI-16). For methane runs the rate of weight

gain was 0.25 g/h for 50% concentration (MCVI-11) and 0.16 g/h for 25% concentration (MCVI-7). The rate of weight gain was much lower for methane than for propylene or propane, even though the methane runs were carried out at much higher temperatures. This can be explained by the higher stability of the radicals produced by methane pyrolysis compared to propylene or propane.

4. Conclusions

The following conclusions were drawn from the present work:

- (1) Dense carbon/carbon composites can be fabricated in a relatively short time using the FCVI process.
- (2) Composites with total porosities as low as 7% were obtained in 8-12 h.
- (3) Propylene and propane required shorter processing times compared to methane to achieve comparable, or better, densities and porosities.

References:

1. J. D. Buckley, American Ceramic Society Bulletin, **67**, 364 (1988).
2. Carbon/carbon Materials and Composites, ed. by J. D. Buckley and Dan D. Edie, Noyes Publications, Park Ridge, NJ, pages 111-118 and 211-215 (1993).
3. R. L. Bickerdike, A. R. G. Brown, G. Hughes, and H. Ranson, in S. Mrozowski, M. C. Studebaker, and P. L. Walker, eds. Proc. Fifth Conf. on Carbon, Vol. 1, Pergamon Press, New York, 575-582 (1962).
4. W. C. Jenkin, U.S. Patent 3,160,517 (December 8, 1964) to Union Carbide Corporation.
5. W. V. Kotlensky, in P. L. Walker, Jr. and P. A. Thrower, eds., Chemistry and Physics of Carbon, Vol. 9, Marcel Dekker, Inc., New York, 173-262 (1973).
6. W. J. Lackey, and T. L. Starr, Fiber Reinforced Ceramic Composites, (ed. K. S. Mazdiyansi), pp. 397-449, Noyes Publication, NJ (1991).
7. W. J. Lackey and A. J. Caputo, U.S. Patent 4,580,523 (April 8, 1986).
8. A. J. Caputo and W. J. Lackey, Ceramic Engineering and Science proceedings, **5**, 654(1984).
9. A. J. Caputo and W. J. Lackey, Ceramic Engineering and Science proceedings, **6**, 694(1985).
10. S-M Oh and J-Y Lee, Carbon, **26** (6), 763-768(1988).
11. A. J. Caputo, R. A. Lowden, and D. P. Stinton, "Improvements in the Fabrication of Ceramic-fiber-ceramic-matrix Composites by Chemical Vapor Infiltration," ORNL/TM-9651, Oak Ridge National Laboratory, Oak Ridge, TN (June 1985).

Acknowledgements:

This work was supported by Dr. Alexander Pechenik of the Air Force Office of Scientific Research. We appreciate the typing of the original manuscript by Virginia Myers.

Table 1. Operating Conditions for the FCVI Process

Table 2. Properties of the Infiltrated Composites

Figure 1. Schematic of the FCVI process.

Figure 2. SEM micrographs from Run PCVI-8 showing uniform densification throughout the composite.

Figure 3. Coating thickness in micropores, located inside the tow, as a function of distance from the bottom of the composite.

Figure 4. Coating thickness in macropores increases with distance from the bottom of the composite.

Table 1. Operating Conditions for the FCVI Process

Run Number	Preform Holder Type	Reagent Flow Rate (sccm)	Diluent Flow Rate (sccm)	Preform Temperature (°C)	
				Top	Bottom
Propylene					
PCVI-6	2	50	150	1180	830
PCVI-8	2	100	100	1200	850
PCVI-9	2	200	200	1180	830
Propane					
PACVI-16	3	100	100	1190	940
Methane					
MCVI-7	3	50	150	1320	1108
MCVI-11	3	50	50	1320	1050

Table 2. Properties of the Infiltrated Composites

Run Number	Fiber Content (v/o)	Rate of Weight Gain (g/h)	Infiltration Time (h)	Bulk Density (g/cm³)	Total Porosity (%)	Open Porosity (%)
Propylene						
PCVI-6	52.2	0.36	24.25	1.48	18.5	--
PCVI-8	58.3	1.1	8	1.69	7.3	4.2
PCVI-9	59.9	0.69	12	1.69	7.0	4.1
Propane						
PACVI-16	50.3	0.88	14	1.68	8.0	3.6
Methane						
MCVI-7	46.3	0.16	43	1.23	32.3	--
MCVI-11	50.5	0.25	38.5	1.51	16.9	5.0

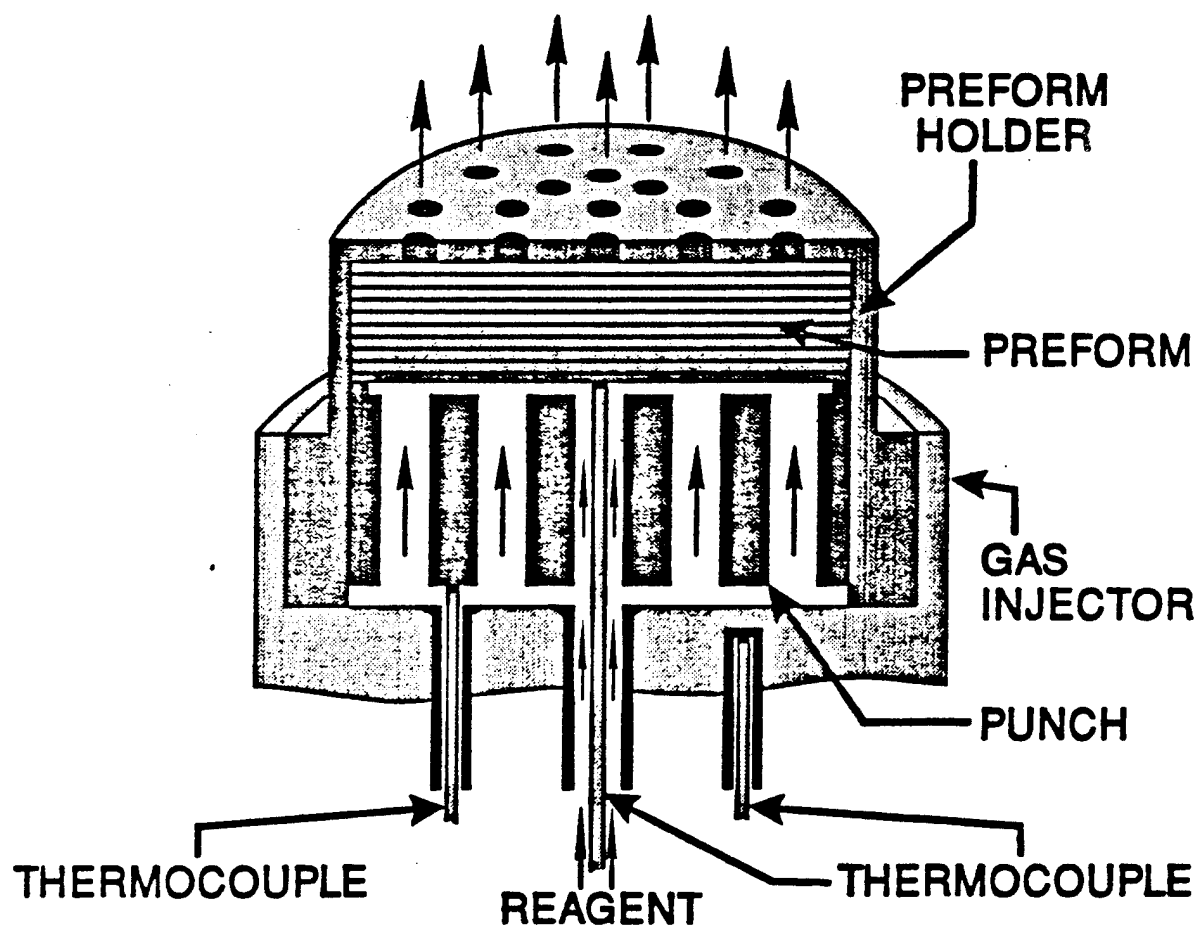
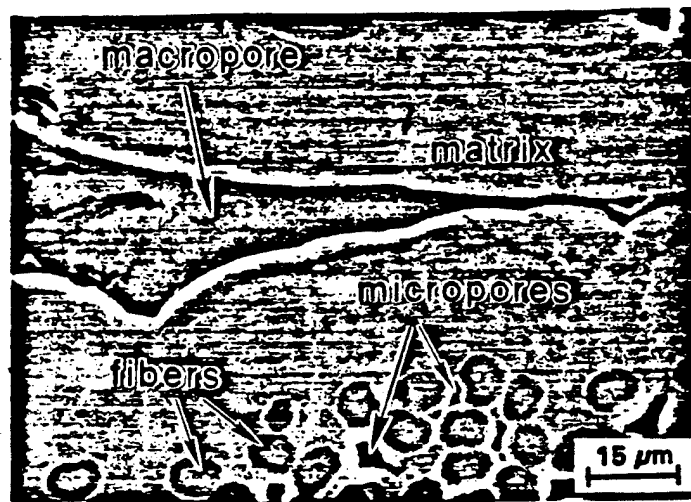


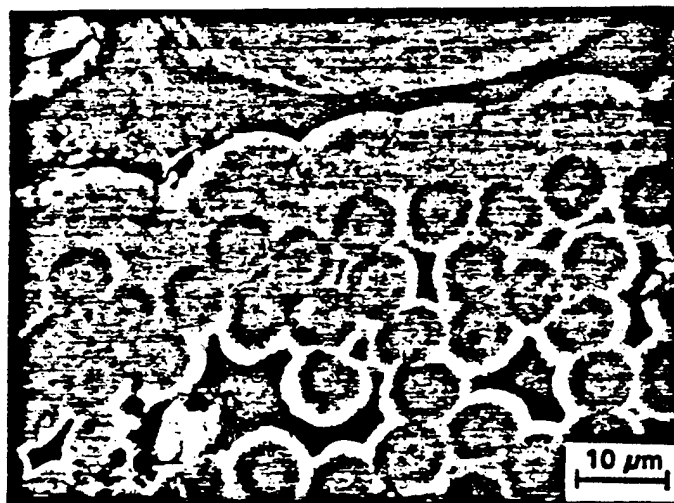
Figure 1. Schematic of the FCVI process.



Top (1200°C)



Middle



Bottom (850°C)

Figure 2. SEM micrographs from Run PCVI-8 showing uniform densification throughout the composite.

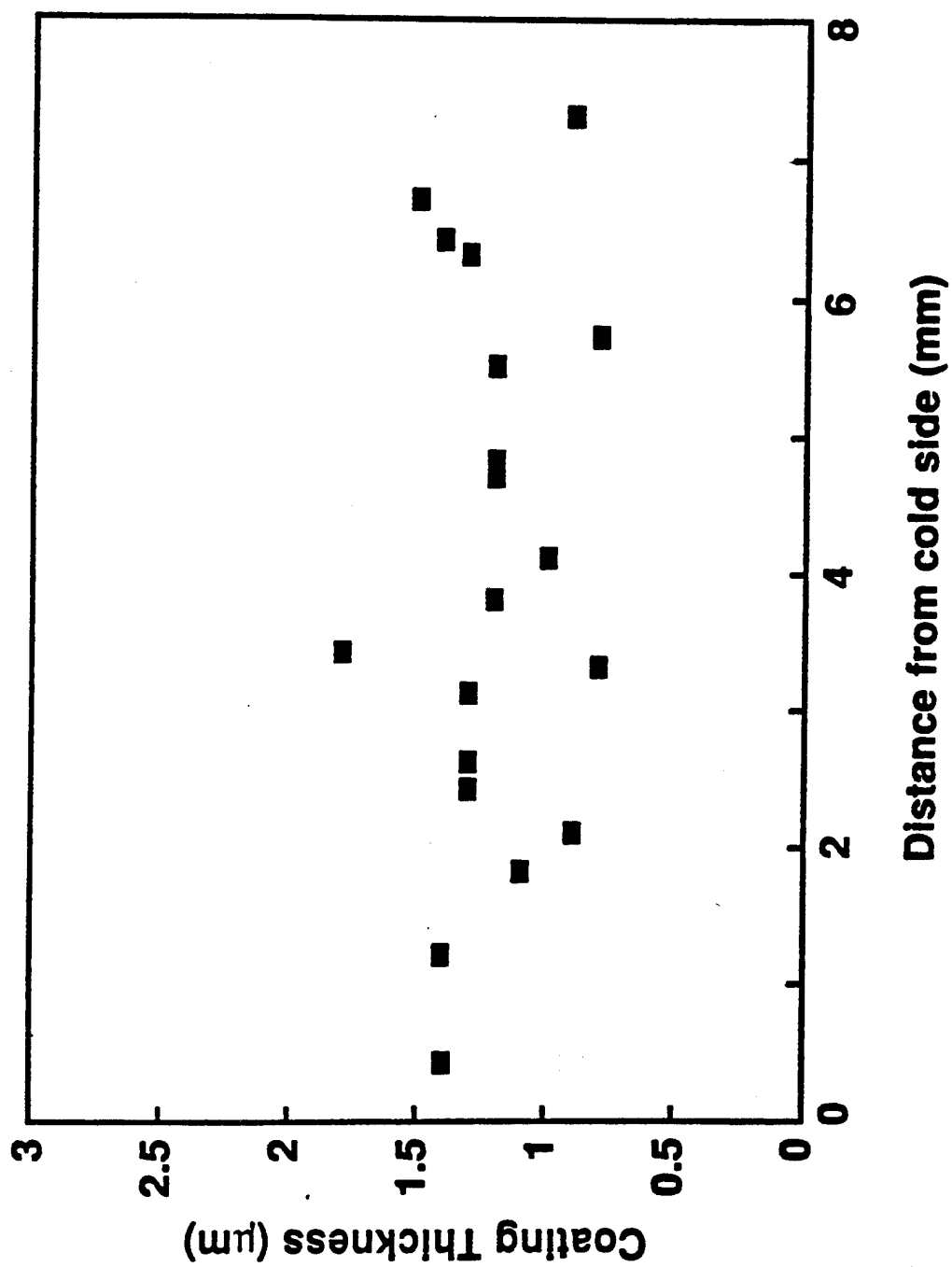


Figure 3. Coating thickness in micropores, located inside the tow, as a function of distance from the bottom of the composite.

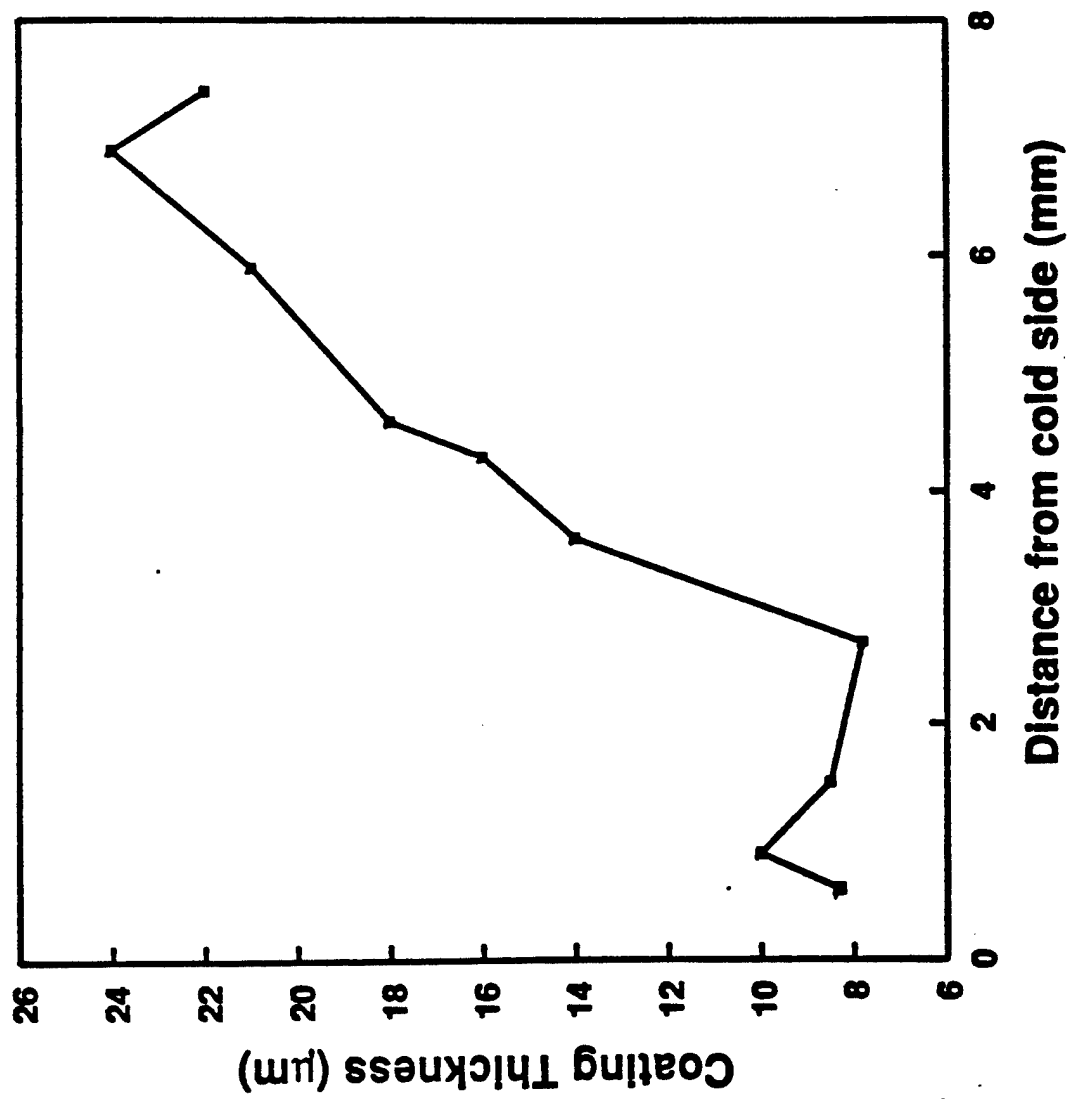


Figure 4. Coating thickness in macropores increases with distance from the bottom of the composite.

Carbon/Carbon Processing by Forced Flow-Thermal Gradient Chemical Vapor Infiltration (FCVI) Process Using Propylene

Sundar Vaidyaraman†, W. Jack Lackey*, Pradeep K. Agrawal†

and Michael A. Miller*

†School of Chemical Engineering

*Georgia Tech Research Institute

Georgia Institute of Technology

Atlanta, GA 30332

Abstract

The fabrication of carbon/carbon disks using the forced flow-thermal gradient chemical vapor infiltration process was studied using a 2^3 factorial statistical design. Propylene, diluted with hydrogen, was used as the reagent. The independent variables were the temperature of the bottom of the fibrous preform, concentration of the reagent, and total flow rate. The response variables were infiltration time, final porosity, rate of weight gain, and uniformity of densification. It was found that the infiltration time and rate of weight gain were affected by each of the three independent variables. It was also observed that the densification of the composites could be monitored by the in-situ measurement of the back pressure. The composites were cut into twelve slices 1 cm long, 4 mm wide and 2 mm deep to measure the uniformity of densification. It was found that the density of the slices varied very little with position within an individual composite disk. Also, coating thickness as a function of position was measured for different composites. In most of the runs the coating thickness increased exponentially from

the cold side to the hot side of the disk. The coating thicknesses near the cold and hot sides were used to calculate the rate constant for the pyrolysis of propylene in the preform. The activation energy was found to be ~ 18.6 Kcal/mol and the rate constant is given by $\ln k = 8.2 - 9375.1/T$.

Keywords: Carbon composites, FCVI, propylene, uniformity, rate constant.

1. Introduction

Carbon/carbon composites are unique materials in that they exhibit high specific strength, stiffness and toughness, and more importantly, the ability to retain these properties at elevated temperatures (1000-2000 °C). The applications of these materials include rocket nose cones, aircraft disc brakes, heat shields for re-entry vehicles, and heat sinks and radiators. The different aspects of carbon composites have been reviewed extensively in journals [1-3] and books [4-7].

Carbon composites are at present fabricated using either an impregnation method or the isothermal chemical vapor infiltration (CVI) process [3,4]. In the former, the carbon preforms are impregnated with resin or pitch followed by carbonization and graphitization. Both the resin and pitch shrink during the carbonization and graphitization steps, necessitating numerous cycles of impregnation and carbonization to obtain dense carbon composites. Also, the carbon matrix produced by pyrolysis of resin does not graphitize easily below 3000°C [5]. Further, there are quality control problems associated with use of pitch for manufacture of carbon composites [5]. The isothermal chemical vapor infiltration process [1,8,9] has been one of the most prevalent

processes to fabricate carbon composites for high temperature applications. The main disadvantages of this process are long processing times (500-600 h), density gradients, and the need to remove, via machining, the outer impermeable skin from the composite to facilitate infiltration. Prior researchers have used novel methods to overcome some of the above shortcomings with limited success. For example, a temperature gradient [10-13,15] was applied across the thickness of the preform during the infiltration process so that a higher temperature at the surface away from the reagent source counteracts the effect of reduced reagent concentration due to diffusion resulting in uniform densification. This results in progressive densification from the hot surface toward the cooler surface. The processing time required by this temperature gradient process was found to be much shorter than for isothermal CVI, however, the effect of diffusion becomes significant near the end of the infiltration causing significant reductions in the rate of densification. Kimura et al. [14] and Kotlensky [15] employed forced flow of the reagent through the thickness of the preform and were able to reduce the processing time. But the depletion of reagent while flowing through the preform resulted in non-uniform densification and plugging of the flow path at the surface where the reagent first contacted the preform. Pulse CVD has also been used to infiltrate composites [16,17]. The main disadvantages of this method are the high number of pulses required and the vacuum equipment. Hence, there is still a need for developing an infiltration process which will produce dense, uniform composites in a short time.

The forced flow-thermal gradient chemical vapor infiltration process (FCVI) which incorporates the advantages of both forced flow and thermal gradient processes has been found to be very effective in rapidly fabricating uniformly dense SiC/SiC composites [18-21]. We

have shown, in feasibility studies, that the FCVI process is also applicable to the fabrication of carbon/carbon composites using propylene, propane, or methane [22,23]. The present work was undertaken to provide an in-depth quantitative understanding of the FCVI processing variables, i.e., temperature, propylene concentration, and total flow rate on the infiltration time, final porosity and uniformity of carbon/carbon composites. To this end, a statistically designed factorial experiment was employed.

2. Experimental Details

The details of the equipment and experimental procedure has been explained elsewhere [21]. Briefly, the preforms consisted of 40 layers of T-300 plain weave carbon cloth oriented at 0-30-60°. These layers were stacked in a graphite preform holder (Figure 1). The type 2 preform holder, described in the prior publication [22], which extends 6.98 cm above the gas injector was employed for the present work. The height of the preform holder affected the temperature and the temperature gradient across the preform. The temperature difference between the hot and cold side with type 2 preform holder was $\sim 350^{\circ}\text{C}$.

The bottom of the preform holder (Figure 1) was cooled by the water cooled gas injector and the top of the preform was heated by the furnace resulting in the establishment of the temperature gradient. The pressure gradient forces the gas through the preform. The feed gas typically consisted of propylene (99.5% pure) with hydrogen as a diluent. As the infiltration progressed, reduction in porosity resulted in an increase in the back pressure. The runs were typically terminated once the back pressure reached ~ 142 kPa (6 psig) for a standardized gas flow consisting of 100 cm³/min each of propylene and hydrogen. The temperatures of the

preform top and bottom were monitored using K-type thermocouples during the infiltration. The infiltrated composites were removed intact from the holder after cooling the furnace.

The apparent volume of the composite was determined using Archimides' principle with methanol ($\rho = 0.79 \text{ g/cm}^3$). The open pore volume was calculated by weighing the composite saturated with methanol. These two values were added to obtain the bulk volume. As a check on bulk volumes, the above procedure was repeated with distilled water.

Slices 1 cm long, 4 mm wide and 2 mm deep were cut out of the composite to determine the uniformity of the infiltration. Four slices were cut in the radial direction and three slices in the axial direction (Figure 2). Hence, there were twelve slices for each composite sample. The slices were identified as hot, middle or cold side depending on the axial position of the slice and inside or outside depending on their radial position. The slices near the center of the composite were termed inside and those which included the circumference of the composite as one side were termed outside. The density of each slice was measured from its weight and volume. The volume was calculated from the dimensions of the slice.

An entire cross-section of each composite disk was mounted in epoxy and polished. The polished sections were observed via scanning electron microscopy in order to measure coating thicknesses as a function of position and also to permit observation of the composite microstructure.

2.1 Experimental Design

The main objective of the experimental design was to obtain quantitative data about effects of the three major process variables with a minimum number of experiments. A 2^3

factorial experiment [24] was judged to be the most efficient method for this purpose. For each of the three independent variables there was a low and high set point. For a full factorial experimental design, experiments are conducted with all possible combinations of the levels of the factors to be investigated. In many such designs, experiments are also conducted with all the variables set at their midpoint value. The latter type of design was employed.

The first step in designing the experiments was to identify the independent variables. In the present work three independent variables, which affect the infiltration process significantly, were chosen. The variables included the temperature of the bottom of the preform, propylene concentration, and total gas flow rate. A 2^3 factorial experiment with replication of the center point, was conducted. Table 1 gives the high, low, and midpoint values for each of the independent variables. These values were chosen based on previous feasibility studies [22,23]. Table 2 lists the details of the processing conditions for each run. The final number of data points were more than initially planned due to replication of several experiments. The replications were undertaken to ascertain the reproducibility of the results. Experiments are typically identified (second column in Table 2) by the level of a factor in that experiment. For example, "TC" refers to the experiment conducted with variable T (temperature) and C (propylene concentration) at the high value and the variable Q (total flow rate) at its low value. The notation "(1)" refers to all variables at their low value.

The temperature of the bottom of the preform was found to vary as much as $\sim 80^\circ\text{C}$ from the desired value for many of the experiments (Figure 3). Initially, the temperature rose rapidly because of reduction in the thermal conductivity of the gas between the punch and the injector (Figure 1), thereby reducing the cooling effects of the injector. The distance between

the punch and the injector was ~ 3 cm for the type 2 preform holder. The thermal conductivity of the gas reduced as a result of changing the feed from pure hydrogen to a mixture containing propylene and hydrogen at the start of the infiltration. From the heat of reaction calculations it was determined that the exothermic nature of the propylene pyrolysis did not contribute significantly to the initial temperature increase. In the case of PCVI-22 (Figure 3), after the initial temperature increase, the temperature essentially stabilized at 0.5 h. After about 1.25 h, the temperature at the bottom of the preform began to decrease rapidly. This was attributed to the reduction in the radiative contribution to the heating of the bottom of the preform, due to partial filling of pores especially near the hot side. After about 2 h, the temperature increased as a result of increased thermal conductivity of the composite caused by densification. In many other runs the furnace power had to be increased to increase the temperature of the bottom of the preform. The decrease in temperature was more pronounced when high hydrocarbon concentrations were used. Because of these temperature variations, a time averaged temperature was employed for the analysis of the data. Table 2 summarizes this averaged temperature for each infiltration run. Process variables, other than the three being studied, were held constant. Total pressure above the preform was kept constant at 1 atm for all experiments. The initial porosity of the preforms was $\sim 45\%$. Actual values for each sample are given in Table 3. As previously mentioned, each run was terminated once the back pressure reached 142 kPa for the standardized flow.

The response variables for the infiltration process were chosen based on the process and product requirements. These included infiltration time, final porosity, rate of weight gain, and the uniformity of densification. The uniformity of densification was ascertained from density

of slices cut from a composite sample. Ideally, one would like to minimize the infiltration time and final porosity. At the same time the infiltrated composite should be uniformly dense independent of the position within the composite.

2.2 Data Analysis

One method prevalently used to analyze unbalanced designs, such as that used here, is regression [25]. The main concern when using regression is choosing the appropriate variables. In over-zealousness to better fit the response surface, one might add independent variables which do not have any physical relationship to the response variable. One way of overcoming this limitation is to use "all possible-regression selection procedure." In this approach the response is regressed against all possible independent variables and their interactions. From this set, a few "good" models are chosen based on some criterion. These models are in turn examined in detail leading to the selection of the final regression model to be employed. In the following paragraphs some of the most common criteria employed in the present study for comparing different regression models are briefly described.

R_p^2 criterion: This value is defined by the following:

$$R_p^2 = \frac{SSR_p}{SSTO} = 1 - \frac{SSE_p}{SSTO} \quad (1)$$

Where, SSTO is the total sum of squares of the response, SSR_p is the sum of squares due to regression and SSE_p is the error sum of squares. Thus, R_p^2 gives an estimate of the amount of

variation observed for the response that can be explained by the regression. For example, a value of 75% indicates that 75% of the variation of the experimental data is explained by that particular regression. The error sum of squares will always reduce as more variables are added to the equation. Hence, the value of R_p^2 will always increase with the addition of new variables. This value can be used to ascertain the point where addition of new variables does not lead to an appreciable improvement of the model.

R_a^2 criterion: This is the adjusted coefficient of multiple regression which takes the number of independent variables into account. The value of R_a^2 can be found using Equation (2).

$$R_a^2 = 1 - \left(\frac{n-1}{n-p} \right) (1 - R_p^2) \quad (2)$$

Where 'n' is the number of data points and 'p-1' gives the number of independent variables in the regression equation. The value of R_a^2 does not always increase with the addition of new independent variables. Thus, one can find the "best" regression by finding the equation that yields the maximum R_a^2 value.

C_p Criterion: This is concerned with the "total mean squared error" of the 'n' fitted values for each regression model. The C_p values for different regression models are plotted against the value of 'p' for the model. Models whose C_p value fall near the line $C_p = p$ are preferable since they have minimum bias. Where bias is defined as the difference between the predicted value with the regression and the mean of the response variable.

t-ratio: It is defined as the ratio of the value of the coefficient in the regression equation to the standard deviation of the same. If the value of the t-ratio is greater than 2.0 then the effect of the variable is considered significant.

The above criteria were applied to the regression model. It is also important to find the influence of a given data point on the regression especially for cases with a limited number of data points. In the following paragraph the parameter used to find the influence of a given data point is explained.

Influence of fitted values (DFFITS): This gives a measure of the influence of a particular point on the fitted regression. It is defined as

$$(DFFITS)_i = \frac{\hat{Y}_i - \hat{Y}_{i(i)}}{\sqrt{MSE_{(i)} h_{ii}}} \quad (3)$$

Where \hat{Y}_i is the fitted value of the i th case when all n cases are used to fit the regression, $\hat{Y}_{i(i)}$ is the fitted value for the i th case when the i th case is omitted in fitting the regression, and h_{ii} is the leverage value. The influence of a data point on the regression was considered very high if the DFFITS value was much greater than 1.

The above criteria were applied to the data collected in the present work for developing a model relating the response to the independent variables. Even though these criterion were employed, the final choice of the model was based on the physical laws of the process. In a few instances models which represented the physical phenomena of the process better were chosen even though the statistical criteria pointed to other models.

3. Results and Discussion

Table 3 lists the infiltration time, rate of weight gain, porosity, density and deposition efficiency for the 15 FCVI runs. The following sections explain in detail the relationships found between the response variables and the independent variables. The regressions were performed against the coded variables (Table 2) to help in ascertaining the relative effect of changing the independent variables on the response.

3.1 Infiltration Time

The infiltration time is defined as the time taken for the back pressure to reach 142 kPa (6 psig). In the present work the longest time (28.5 h) occurred when all the variables were kept at their low level and the minimum infiltration time of less than 3 h occurred when all the variables were at their high values. The infiltration time was regressed against different sets of independent variables and second order interactions. The resulting regression is given below:

$$\begin{aligned} \text{Infiltration Time} &= 10.3 - 3.66T_{cod} - 5.43C_{cod} + 2.26T_{cod} * C_{cod} \\ S_{regression} &= 3.455 \quad R_p^2 = 80.3\% \quad R_a^2 = 74.9\% \end{aligned} \quad (4)$$

The above regression equation showed satisfactory fit to the experimental data. However, when the residuals were plotted against the predicted values the graph showed a trend. In an ideal case the residuals must be random with respect to the predicted values. The presence of a trend suggested curvilinear effects in the response and a simple linear regression was not adequate to explain the data. The response could be linearized by use of a simple transformation. Also, analysis of each data point indicated that the DFFITS values for

experiment "(1)" was 2.52. This implied that this data point was an outlier. However, there were no experimental reasons to delete this point from the regression equation.

There are many standard transformations, for example, logarithmic, square root, squares, etc. Hence, it was important to choose the appropriate transformation to analyze the data. In the present work, the Box-Cox criteria [26] was employed in choosing the transformation. This criteria is based on reducing the error sum of squares.

In the case of infiltration time, the natural logarithm transformation of the response variable was found to be the most appropriate. This transformed variable was regressed against the coded variables and the following regression equation was found to be the best fit of the experimental data. Transformation also reduced the influence of experiment "(1)" on the regression equation.

$$\begin{aligned} \ln (\text{InfiltrationTime}) &= 2.11 - 0.359 T_{cod} - 0.541 C_{cod} - 0.245 Q_{cod} \\ S_{regression} &= 0.216 \quad R_p^2 = 91.7\% \quad R_a^2 = 89.5\% \end{aligned} \quad (5)$$

Each of the three independent variables were found to have a significant effect on the infiltration time. As temperature, propylene concentration, and total flow rate were increased, the time required for densification decreased (Table 3). Concentration was found to have the most influence on the infiltration time followed by temperature and flow rate, respectively. The interactions between the independent variables were found to be negligible. The C_p value was found to be below 4 which indicated little bias.

3.2 Rate of Weight Gain

The overall weight gain was divided by the infiltration time to obtain the rate of weight gain. This parameter could be thought of as an average mass deposition rate for a particular experiment. The data were first regressed linearly and Equation (6) was obtained.

$$\begin{aligned} \text{Rate of Weight Gain} &= 1.55 + 0.569 T_{cod} + 0.699 C_{cod} + 0.421 Q_{cod} \\ S_{regression} &= 0.497 \text{ g/h} \quad R_p^2 = 81.6\% \quad R_a^2 = 76.6\% \end{aligned} \quad (6)$$

In this case, too, the plot of residual versus predicted values showed a trend. Also, a C_p value much greater than 4 indicated high bias in the regression equation. Consequently, the response variable was transformed based on the Box-Cox criteria. The natural logarithm was once again found to be the most appropriate transformation. The resulting regression equation is given in Equation (7).

$$\begin{aligned} \ln(\text{Rate of Weight Gain}) &= 0.234 + 0.381 T_{cod} + 0.503 C_{cod} + 0.235 Q_{cod} \\ S_{regression} &= 0.229 \quad R_p^2 = 90.5\% \quad R_a^2 = 87.8\% \end{aligned} \quad (7)$$

From the above equation it can be seen that the rate of densification was affected only by the main variables, namely, the preform bottom temperature, concentration of the reagent, and the total flow rate; there were no significant interaction terms. If kinetics controlled the reaction, the flow rate would not affect the rate of densification. If mass transfer controlled the reaction, the temperature would have minimal effect on the rate of densification. For the FCVI of carbon, for the conditions used here, there appeared to be an intermediate regime where both kinetics and mass transfer had an influence on the rate of densification.

3.3 Porosity and Density

The final total porosity of each composite disk was calculated assuming the density of the carbon deposit to be 1.9 g/cm^3 . It was found that changing the assumed value of the matrix density from $1.8\text{-}2.1 \text{ g/cm}^3$ affected the calculated porosity at most by only 3%. Also, the densities of carbon matrices produced by CVI have been observed to be in the range $1.9\text{-}2.1 \text{ g/cm}^3$ [12]. The final porosity was typically 5-10% with the exception of sample PCVI-31. The open porosity was typically 3-6%.

The density of the composite was found by dividing the mass of the composite by the bulk volume. The bulk density was typically $\sim 1.65 \text{ g/cm}^3$. The minimum and maximum values were 1.58 and 1.71 g/cm^3 . The bulk density values were analyzed against the independent variables and their interactions. It was found that the density was independent of preform bottom temperature and flow rate was only very weakly related to the concentration of the reagent. This weak correlation in the present work was anticipated since the infiltration was stopped once the back pressure reached a predetermined value. The back pressure is related to the permeability (porosity) across the composite. This back pressure was taken as a measure of the densification. From the present result it was seen that the back pressure is closely related to the final density and could be used to monitor and control the densification of the composite.

3.4 Density Gradient

The density of slices obtained from different parts of each composite was determined to evaluate the spatial uniformity of densification. The bulk density of the slices for different composites are given in Table 4. The variation of density with position is shown by the box-

and-whisker plot (Figure 4). Half of the values fall within the box, the remaining half are indicated by the whiskers, except for outliers. The horizontal line within the box indicates the median density. This figure shows that there is little difference in the bulk density between the hot side and middle of the composite. The bulk density of slices from the cold side exhibited lower values. It can be observed for all slices, except those from PCVI-22, 23, and 28, that the density was $\sim 1.7 \text{ g/cm}^3$ for the locations identified as hot side and middle. In PCVI-22, high temperatures and reagent concentrations near the hot side resulted in increased residual porosity within the tow region resulting in reduced density, probably as a result of canning. In the case of PCVI-28 the cold side of the composite densified more than the hot side as can be seen from the density of the slices and the deposition rate data (Figure 5). Hence, the reagent could not flow to the hot side of the preform resulting in a porous structure. At this point it is not clear why lower densities were observed at the hot side of composite PCVI-23. While excellent reproducibility for replicate runs was typically observed, this run was an exception. It was not similar to other midpoint runs.

The densities of the slices from the cold side of the composites were typically $1.4\text{-}1.6 \text{ g/cm}^3$ which is slightly lower than for the hot portion or middle of the composites. But even these values are only $\sim 10\%$ lower than the average bulk density. To further analyze density variation within a given sample, the density range was computed for each sample. The minimum and maximum values were 0.11 (PCVI-24) and 0.33 (PCVI-21) g/cm^3 . Hence, it can be seen that rather uniformly dense composites were obtained over a very wide range of processing conditions with a single cycle of infiltration using the FCVI process. For those samples having the largest within sample variation in density, the value was inflated by the low

density at the cold side. In these instances, low temperatures (~ 830 - 860°C) for the cold side resulted in low densities ($1.4 - 1.45 \text{ g/cm}^3$). The density of the cold side could be increased, to further improve the uniformity, by changing the operating conditions near the end of the infiltration, i.e. by raising the temperature.

3.5 Deposition rate

The coating thicknesses in macropores (large pores between cloth layers and between tows in a cloth layer) were measured using a scanning electron microscope. These values were divided by the infiltration time to obtain the average deposition rate. The measurements were made at three radial positions as a function of distance from the cold side of the composite. The resulting deposition rates for different composites are plotted in Figure 5-7. The radial position is denoted by the normalized variable " r/R ", where, " r " is the distance from the center of the composite, and " R " denotes the radius of the composite. In all but one run, the rate increased with increasing distance from the cold side. This implies that in most of the runs the depletion of reagent did not neutralize the effect of increased temperature. An exponential relationship (Table 5) was observed between deposition rate and the distance from the cold side. An exponential dependence is reasonable given the strong influence of temperature on the reaction rate. If a linear thermal gradient exists across the preform thickness, then, from the temperature effect alone, an exponential variation in coating thickness would be expected. Run PCVI-28 (TC) (Figure 5) was the exception to the above behavior. For this run, the coating thickness was much higher near the cold side than the hot side. This can be attributed to the high residence time (low flow rates) and high temperatures resulting in higher reagent conversion near

the cold surface. Consequently, the reagent concentration profile would be different in this run as compared to other runs. Hence, this run was not included in the following analysis.

3.5.1 Axial

The equation of the line fitting the deposition rate to distance from the cold side of the composite was used to calculate the ratio of deposition rate at the hot side to that at the cold side.

$$\phi = \frac{\text{Deposition rate at hotside}}{\text{Deposition rate at coldside}} = \text{Exp}(a \cdot z) \quad (8)$$

Where, "a" is the coefficient of the exponential factor in the regression equation (Table 3) and "z" is the distance from the cold side. The average thickness of the composites was ~7.5 mm. This value was used for calculating the axial deposition rate ratio, ϕ , for different experiments. These ratios were then regressed against the process variables. The resulting equations for different radial positions are summarized below:

at $r/R = 0.0$

$$\begin{aligned} \phi &= 4.61 - 1.58 T_{cod} \\ S_{\text{regression}} &= 1.402 \quad R_p^2 = 60.4\% \quad R_a^2 = 56.0\% \end{aligned} \quad (9)$$

at $r/R = 0.5$

$$\begin{aligned} \phi &= 5.62 - 1.37 T_{cod} - 1.73 C_{cod} \\ S_{regression} &= 1.572 \quad R_p^2 = 58.0\% \quad R_a^2 = 47.5\% \end{aligned} \quad (10)$$

at $r/R = 1.0$

$$\begin{aligned} \phi &= 2.48 - 1.03 T_{cod} - 0.986 C_{cod} \\ S_{regression} &= 1.572 \quad R_p^2 = 58.0\% \quad R_a^2 = 47.5\% \end{aligned} \quad (11)$$

One interesting feature to note is the value to the intercept at different positions. For r/R equal to 0 and 0.5, " ϕ " is about 5. However, near the circumference of the composite ($r/R = 1.0$) the deposition is much more uniform (Figure 5-7(c)) compared to other positions. This can be explained by the cooling effect of the graphite holder on the edges of the composites. Hence, the axial temperature gradient near the circumference of the composite would be much lower than at the center line leading to more uniform deposition near the circumference. It should be noted that even though the deposition rate varied exponentially with distance, the density variation within the composite was not very significant. This is because the majority of the initial porosity was within the tow (and therefore eventually the majority of the matrix) and not within the macropores. Starr [26] showed that for the case of a Nicalon cloth layup, 70% of the porosity was within the tow. Hence, the uniformity of density in a composite is primarily controlled by effective infiltration of the tow. In all the composite samples we observed, appreciable infiltration of the tow occurred independent of its position within the composite.

3.5.2 Radial

The radial variation of deposition rate was estimated at three axial positions. The three positions considered were near the hot side, the cold side, and at a distance of 4 mm from the cold side. These positions were chosen so as to ascertain the trend as one moves from the cold side to the hot side.

The ratio of the deposition rate at the center of the composite to the circumference at the same distance from the cold side was determined for the purpose of estimating radial variation. It was found on regression that this deposition rate ratio, ϕ_r , near the cold side and at a distance of 4 mm from the cold side were unaffected by the operating conditions. However, the ratio at the hot side was affected by concentration and a two way interaction as shown in Equation (12).

$$\begin{aligned} \phi_r &= 1.86 + 0.584 C_{cod} + 0.363 T_{cod} * Q_{cod} \\ S_{regression} &= 0.507 \quad R_p^2 = 61.8\% \quad R_a^2 = 52.2\% \end{aligned} \quad (12)$$

The above observation can be explained by the heat flow characteristics in the system. For any given axial location, the circumference of the composite was cooler than the center because of the cooling effects of the graphite holder. For the hot surface of the composite this temperature gradient was observable through a sight port located in the top of the reactor. From Figure 1 it can be seen that near the cold side, the preform is getting cooled significantly at the circumference by the graphite holder and the bottom is cooled by the graphite punch. This would result in reduction of the radial temperature gradient when moving from the hot side to the cold side of the composite. This in turn would lead to more uniform deposition rates radially

near the cold side. The radial and axial effects for a typical sample (PCVI-33) are depicted in Figure 8. The contour lines shown in the figure were obtained from a polynomial fit of the axial and radial positions to the coating thickness as shown in Equation (13).

$$\text{CoatingThickness}(t) = 3.00 + 0.2803z - 0.6252(r/R)*z \quad (13)$$

Where "t" is coating thickness in μm , and "r/R" and "z" are as previously defined.

3.6 Deposition Efficiency

Deposition efficiency is defined as the ratio of the amount of carbon deposited in the preform to the carbon in the reagent. It is a measure of the amount of carbon successfully used for deposition. In the present work, the deposition efficiency varied between 5-20% depending on the operating conditions. This is much higher than the only value in the literature, 0.5-1.5%, reported for the isothermal chemical vapor infiltration process of carbon [28]. The deposition efficiency was affected only by the temperature. The relationship is given by Equation (14).

$$\begin{aligned} \text{Deposition Efficiency} &= 14.2 + 4.76 T_{\text{cod}} \\ S &= 2.95 \quad R_p^2 = 74.5\% \quad R_a^2 = 72.6\% \end{aligned} \quad (14)$$

3.7 Microstructure

Composite microstructures were characterized using scanning electron microscopy. Interesting features were observed near the hot side of the composites. Some of the typical microstructures are shown in Figures 9 and 10. The matrix deposited adjacent to the fiber had

a different appearance from the remaining matrix as shown in Figure 9. On closer examination it was seen that the deposit adjacent to the fibers contained plate-like features, small pores (Figure 10), or columnar features (Figure 9(b)). This structure existed only within the first 1-2 μm of coating and there was a sharp interface beyond which the coating was rather uniform in appearance. At this juncture the reason for the drastic change in the microstructure of the deposits is not known, but this same feature has also been observed by Kimura et al. [14] when using the isothermal forced flow CVI process. One can speculate that there might have been a change in the local conditions with time. However, it still does not explain the sharp interface which was seen in several samples and only near the hot side of the composites.

3.8 Effect of Cloth Weave

Since eight harness satin weave is often used for the fabrication of carbon-carbon for structural applications, we investigated the applicability of the FCVI process to preforms made using this weave [29]. All the infiltration runs described previously were carried out with plain weave cloth which contained 12.5 by 12.5 yarns (tows) per square inch. The eight harness satin weave cloth used in the present work had 24 by 24 yarns (tows) per square inch. Hence, only 20-22 cloth layers were required to obtain a preform thickness similar to that of 40 layers of plain weave cloth. The main difference between these two weaves is the size of the pores. In the case of plain weave preforms, the pore sizes have a bimodal distribution with smaller pores found within the tows and larger pores between tows and layers of cloth. In the case of eight harness satin weave, because of the high number of tows per cloth and the type of weave, the pore size distribution is unimodal with a broad range of pore sizes. Consequently, it was

important to investigate the effect of the pore size distribution of the preform on the infiltration. Table 6 summarizes the infiltration conditions for the eight harness satin cloth preforms and Table 7 gives the results for the infiltrated composites.

In the infiltration runs with eight harness satin weave the temperature of the bottom of the preform dropped sharply during the course of the infiltration. The temperature drop was also observed in the case of plain weave preforms but the magnitude of the temperature drop was much lower (Figure 3). The larger temperature drop for the satin weave could be attributed to the pore size in the preform. It was speculated that because of smaller pores, as compared to plain weave preforms, the hot side got rapidly densified resulting in reduction of the radiative contribution to the heating of the bottom of the preform. Also, the thermal conductivity of the composite, which depends on densification, had not increased sufficiently to counteract the above effect. Consequently, the bottom of the eight harness satin preform was cooler during the latter stages of the infiltration process. The bottom of the satin weave preforms could not be heated to higher temperatures because of equipment limitations. In spite of this, the infiltration times and the density of the composites obtained using eight harness satin weave preform were comparable to those of plain weave preform. For example, the final density of HS-5 was 1.67 g/cm³ compared to 1.66 g/cm³ obtained with plain weave at similar conditions (PCVI-36) and the infiltration time was ~ 7.5 h for both runs. Hence it can be seen that the FCVI process is sufficiently versatile to infiltrate preforms containing cloth of different weaves.

3.9 Kinetic Analysis

The deposition rate data obtained by measuring coating thicknesses in the macropores of the plain weave samples were used to obtain a first order kinetic rate constant. The carbon deposition process is typically first order with respect to the concentration of the hydrocarbon reagent [30,31]. Hence, the following equation was used to calculate the reaction rate constant, k .

$$\text{DepositionRate } (\mu\text{m/h}) = kP_{\text{propylene}} \quad (15)$$

Where: k = reaction rate constant, $\mu\text{m}/(\text{h-atm})$

$P_{\text{propylene}}$ = Partial pressure of propylene = yP

y = Mole fraction of reagent in feed

P = Total pressure (atm)

The rate constant was calculated using the deposition rate data from the cold side of the composite, where the values of the temperature and concentration were known. The total pressure for the calculation near the cold side was found from the time averaged value of the inlet pressure. A second set of " k " values was also obtained for the hot side of the composite using the average outlet concentration for each run, which was estimated from the deposition efficiency. The average outlet concentration was obtained from the following equation:

$$y_{\text{out}} = y_{\text{in}}(1-X) \quad (16)$$

Where: y_{in} = Inlet concentration
 X = Deposition Efficiency

The natural logarithm of the "k" values were plotted against the reciprocal absolute temperature in Figure 11. The data points were linearly regressed to obtain the following equation.

$$\ln k = 8.2 - 9375.1/T \quad (17)$$

The activation energy calculated from Equation 17 was found to be ~ 18.6 Kcal/mol. This value is lower than the 35-60 Kcal/mol reported for carbon deposition from propylene [28]. The activation energy for a typical mass transfer controlled regime is very low, i.e., $\sim 3-4$ Kcal/mol [32]. Hence, the activation energy value obtained in the present work suggests a transition regime where kinetics and mass transfer are of similar magnitude and thus both have a role in controlling the densification process. The same conclusion was previously reached from regression of the rate of weight gain with the independent process variables.

4. Conclusions

The following conclusions were drawn from the present work on the FCVI processing of carbon/carbon.

- (1) All three variables studied, namely, temperature of the bottom of the preform, hydrocarbon concentration, and flow rate, affected the infiltration time and rate of weight gain.
- (2) Minimum infiltration time, 2.75 h, was achieved when the higher process set points were used for temperature, concentration, and flow rate. For applications where density uniformity is critical, use of somewhat lower concentration is recommended as a compromise.

- (3) The final bulk density of the composite was independent of the processing conditions. This can be attributed to the termination of the experiments at a specified back pressure. Hence, back pressure can be used to control the infiltration process.
- (4) Spatial density variations were not excessive. The bulk density of the slices cut from a composite sample varied only by $\pm 10\%$ of the average bulk density.
- (5) The average deposition rate in macropores increased exponentially on moving from the cold side to the hot side of the composite. This implies that the reagent depletion did not completely counteract the influence of the temperature gradient in the present study. Even though the deposition rates varied by as much as a factor of 8, density variation density was at most only $\pm 0.15 \text{ g/cm}^3$. This is due to the fact that most of the pore volume is within the tow rather than in macropores.
- (6) The FCVI process is sufficiently versatile to infiltrate preforms containing cloths of different weaves.
- (7) The deposition rate data were amenable to an Arrhenius plot and the equation $\ln k = 8.2 - 9375.1/T$ fit the data well and yielded an apparent activation energy of $\sim 18.6 \text{ kcal/mol}$ which implies that kinetic and mass transfer affects are similar in magnitude.

References

- [1] W. V. Kolensky, in *Chemistry and Physics of Carbon*, edited by P.L. Walker, Jr., and P. A. Thrower, **9**, 173 (1962).
- [2] E. Fitzer, *Carbon*, **25**, 163 (1987).
- [3] W. J. Lackey and T. L. Starr, in *Fiber Reinforced Ceramic Composites*, edited by K. S. Mazdiasni, Noyes Publication, NJ, 397 (1991).
- [4] G. Savage, *Carbon-Carbon Composites*, Chapman & Hall, NY 1993.
- [5] C. R. Thomas, ed., *Essentials of Carbon-Carbon Composites*, Royal Society of Chemistry, London, 1993.
- [6] J. D. Buckley and D. D. Edie, eds., *Carbon-Carbon Materials and Composites*, Noyes Publications, Park Ridge, NJ (1993).
- [7] M. A. Wright and K. R. Palmer, eds., *Research Into Structural Carbons*, Southern Illinois University at Carbondale, 1994.
- [8] R. L. Bickerdike, A. R. G. Brown, G. Hughes, and H. Ranson, in *Proc. Fifth Conf. on Carbon*, edited by S. Mrozowski, M. D. Studebaker, and P. L. Walker, Pergamon Press, **1**, 575 (1962).
- [9] W. C. Jenkins, U.S. Patent 3,160,517 (1964).
- [10] H. O. Pierson, Sandia Laboratories Development Report SC-DR-67-2969, December 1967.
- [11] J. D. Theis, Jr., in F. A. Glaski, ed., *Proc. Third Int. Conf. on Chemical Vapor Deposition*, Am. Nucl. Soc., Hinsdale, IL, 561 (1972).

- [12] S.-M. Oh and J.-Y. Lee, *Carbon*, **26**, 763 (1988); *Carbon*, **26**, 769 (1988); *Carbon* **27**, 423 (1989).
- [13] I. Golecki, R. C. Morris and D. Narasimhan, U.S. Patent 5,348,774 (1994).
- [14] S. Kimura, E. Yasuda, N. Takase and S. Kayusa, *High Temp. High Press.*, **13**, 193 (1980).
- [15] W. V. Kotlensky, SAMPE 16th National Symposium and Exhibit, **16**, 257 (1971).
- [16] R. L. Beatty and D. V. Kiplinger, *Nucl. Appl. Tech.*, **8**, 488 (1970).
- [17] K. Sugiyama and T. Nakamura, *J. Mat. Sci. Lett.*, **6**, 331 (1987).
- [18] W. J. Lackey and A. J. Caputo, U.S. Patent 4,580,523, 1986.
- [19] A. J. Caputo and W. J. Lackey, *Ceram. Eng. Sci. Proc.*, **5**(7-8), 654 (1984).
- [20] A. J. Caputo, W. J. Lackey, and D. P. Stinton, *Ceram. Eng. Sci. Proc.*, **6**(7-8), 694 (1985).
- [21] D. P. Stinton, A. J. Caputo, and R. A. Lowden, *Am. Ceram. Soc. Bull.*, **65** 347-350 (1986).
- [22] S. Vaidyaraman, W. J. Lackey, G. B. Freeman, P. K. Agrawal and M. D. Langman, *J. Mat. Res.*, **10**, 1469 (1995).
- [23] S. Vaidyaraman, W. J. Lackey, P. K. Agrawal and G. B. Freeman, *Carbon*, in press (1995).
- [24] D. D. Montgomery, *Design and Analysis of Experiments*, Wiley, NY 1991.
- [25] J. Neter, W. Wasserman, and M. H. Kutner, *Applied Linear Regression Models*, 2nd ed., Irwin, Boston, MA (1989).
- [26] G. E. P. Box and D. R. Cox, *J. Royal Stat. Soc B*, **26**, 211 (1964).

- [27] T. L. Starr, in *Chemical Vapor Deposition of Refractories and Metals*, T. M. Besmann, B. M. Gallois and J. Warren, eds., MRS Sym. Proc. **250**, 207 (1991).
- [28] S. Marinkovic and S. Dimitrijevic, *Carbon*, **23**, 691 (1985).
- [29] F. E. Heredia, S. M. Spearing, T. J. Mackin, M. Y. He, A. G. Evans, P. Mosher and P. Brondsted, *J. Am. Ceram. Soc.*, **77**, 2817 (1994).
- [30] P. A. Tesner, in *Chemistry and Physics of Carbon*, edited by P. A. Thrower, **19**, 65 1983.
- [31] P. McAllister, J. F. Hendricks, and E. E. Wolf, *Carbon*, **28**, 579 (1990).
- [32] K. Hedden and E. Wicke, in *Proceedings of the Third Conference on Carbon*, Pergamon Press, NY, 249 (1957).

Acknowledgements

This work was supported by the Air Force Office of Scientific Research. The guidance of Dr. Alexander Pechenik throughout the course of this work is appreciated. We thank Dr. John Sparrow for help with scanning electron microscopy and Ms. Sheree Collins for her expertise and diligence in graphics preparation. Typing of the original manuscript by Ms. Virginia Myers is gratefully acknowledged.

List of Tables

Table 1: Independent variables and range studied.

Table 2: Operating conditions for the FCVI processing of carbon/carbon.

Table 3: Properties of the infiltrated composites.

Table 4: Bulk density as a function of position within composite.

Table 5: Regression equations relating deposition rate (Y) in $\mu\text{m/h}$ to the distance Z in mm from the cold side of the composite.

Table 6: Operating conditions for infiltration of eight harness satin weave preforms.

Table 7: Properties of the infiltrated eight harness satin weave composites.

List of Figures

Figure 1: Schematic of the FCVI process.

Figure 2: Schematic showing location of density samples.

Figure 3: Variation of the temperature of the bottom of the preform with time.

Figure 4: Bulk density as a function of axial and radial position within the composite disk.

Figure 5: Deposition rates for experiments at high temperature (a) near the center of the composite disk, (b) between the center and circumference of the composite disk, (c) near the circumference of the composite disk.

Figure 6. Deposition rates for experiments at low temperature (a) near the center of the composite disk, (b) between the center and circumference of the composite disk, (c) near the circumference of the composite disk.

Figure 7. Deposition rates for midpoint experiments (a) near the center of the composite disk, (b) between the center and circumference of the composite disk, (c) near the circumference of the composite disk.

Figure 8. Coating thickness for Sample PCVI-33 as a function of radial position and axial distance. Contour lines were obtained by regressing the data (Eqn. 13).

Figure 9. Micrograph from hot side of composite PCVI-36 showing the layered structure.

Figure 10. Micrograph showing porosity in the layered matrix structure near the fiber (PCVI-24).

Figure 11. Arrhenius plot for deposition of carbon in the preforms.

Table 1. Independent variables and range studied

Variable I.D.	Variable	Low Value	Mid-point	High Value	Coded Variable
T	Preform Bottom Temperature (°C)	850	900	950	$(T-900) \div 50$
C	Concentration (%)	25	37.5	50	$(C-37.5) \div 12.5$
Q	Total Flow Rate (cm ³ /min)	200	300	400	$(Q-300) \div 100$

Table 2. Operating conditions for the FCVI processing of carbon/carbon

Run Number	Experiment	Actual Values			Coded Values		
		T (°C)	C (%)	Q (cm ³ /min)	T _{cod}	C _{cod}	Q _{cod}
PCVI-33	(1)	845	25	200	-1.0922	-1	-1
PCVI-24	T	942	25	200	0.8342	-1	-1
PCVI-32	C	852	50	200	-0.9581	1	-1
PCVI-37	C	836	50	200	-1.2883	1	-1
PCVI-28	TC	940	50	200	0.7975	1	-1
PCVI-27	Q	857	25	400	-0.8526	-1	1
PCVI-25	TQ	965	25	400	1.3081	-1	1
PCVI-36	CQ	833	50	400	-1.3407	1	1
PCVI-22	TCQ	924	50	400	0.4782	1	1
PCVI-31	TCQ	918	50	400	0.3533	1	1
PCVI-21	Midpoint	833	37.5	300	-1.3368	0	0
PCVI-23	Midpoint	803	37.5	300	-1.9350	0	0
PCVI-35	Midpoint	897	37.5	300	-0.0642	0	0
PCVI-38	Midpoint	878	37.5	300	-0.4465	0	0
PCVI-43	--	941	50	300	0.8286	1	0

Table 3. Properties of the infiltrated composites

Run Number	Initial Porosity (v/o)	Infiltration Time (h)	Rate of Weight Gain (g/h)	Final Porosity (%)	Open Porosity (%)	Density (g/cm ³)	Deposition Efficiency (%)
PCVI-33	45.64	28.50	0.3683	8.00	4.75	1.677	7.6
PCVI-24	45.65	11.50	0.9581	6.13	3.69	1.713	19.9
PCVI-32	45.86	10.50	0.9776	8.94	—	1.660	10.1
PCVI-37	44.59	9.00	1.0902	8.22	4.65	1.672	11.3
PCVI-28	44.76	6.00	1.5478	10.77	7.86	1.624	16.1
PCVI-27	44.42	21.50	0.4619	7.78	4.69	1.680	4.8
PCVI-25	48.62	7.00	1.6976	8.04	4.62	1.680	17.6
PCVI-36	46.48	7.75	1.3537	8.96	4.58	1.660	7.0
PCVI-22	44.96	2.75	3.5133	9.81	6.56	1.642	18.2
PCVI-31	44.25	2.75	3.0636	13.15	—	1.578	15.9
PCVI-21	45.67	11.50	0.8913	8.72	5.93	1.664	8.3
PCVI-23	45.95	12.25	0.8171	10.23	6.56	1.635	7.6
PCVI-35	45.63	8.75	1.2481	6.19	3.85	1.712	11.5
PCVI-38	43.90	8.50	1.1791	6.49	4.36	1.704	10.8
PCVI-43	49.41	3.50	3.5317	7.15	3.97	1.698	24.43

Table 4. Bulk density as a function of position within composite

Run #	Experiment	Bulk Density (g/cm ³)											
		Hot Side				Middle				Cold Side			
		Inside		Outside		Inside		Outside		Inside		Outside	
PCVI-33	(1)	1.703	1.726	1.676	1.715	1.735	1.708	1.717	1.727	1.56	1.52	1.57	1.566
PCVI-24	T	1.718	1.714	1.677	1.681	1.653	1.65	1.64	1.67	1.607	1.625	1.646	1.633
PCVI-37	C	1.73	1.721	1.712	1.637	1.68	1.663	1.669	1.623	1.54	1.567	1.544	1.516
PCVI-28	TC	1.61	1.61	1.53	1.461	1.721	1.735	1.681	1.669	1.572	1.613	1.592	1.551
PCVI-27	Q	1.74	1.73	1.71	1.746	1.72	1.712	1.698	1.72	1.467	1.443	1.49	1.469
PCVI-25	TQ	1.69	1.659	1.64	1.699	1.684	1.681	1.695	1.71	1.542	1.58	1.658	1.59
PCVI-36	CQ	1.746	1.713	1.676	1.672	1.705	1.681	1.61	1.674	1.556	1.556	1.504	--
PCVI-22	TCQ	1.571	1.584	1.58	1.558	1.691	1.73	1.709	1.705	1.578	1.58	1.563	1.705
PCVI-21	Midpoint	1.718	1.726	1.724	1.722	1.722	1.724	1.658	1.668	1.477	1.487	1.49	1.4
PCVI-23	Midpoint	1.593	1.644	1.591	1.494	1.664	1.714	1.689	1.694	1.603	1.599	1.581	1.506
PCVI-35	Midpoint	1.716	1.697	1.7	1.719	1.766	--	1.724	1.735	1.639	1.646	1.637	--
PCVI-38	Midpoint	1.705	1.703	1.711	1.709	1.708	1.695	1.661	1.715	1.477	1.389	1.545	1.45
PCVI-43	--	1.66	1.604	1.668	1.612	1.69	1.68	1.652	1.668	1.514	1.49	1.621	1.485

Table 5. Regression equations relating deposition rate (Y) in $\mu\text{m/h}$ to the distance (Z) in mm from the cold side of the composite

Radial Position	Run Number	Equation	R ²
r/R = 0.0	PCVI-33	$Y = 0.0814 \text{ Exp } (0.2803 Z)$	97.3
	PCVI-24	$Y = 0.5499 \text{ Exp } (0.1159 Z)$	74.5
	PCVI-37	$Y = 0.3831 \text{ Exp } (0.2697 Z)$	99.3
	PCVI-28	$Y = 2.8732 \text{ Exp } (-0.1997 Z)$	75.3
	PCVI-27	$Y = 0.1088 \text{ Exp } (0.2747 Z)$	99.8
	PCVI-25	$Y = 0.8203 \text{ Exp } (0.1838 Z)$	87.6
	PCVI-36	$Y = 0.4277 \text{ Exp } (0.2470 Z)$	96.6
	PCVI-22	$Y = 1.5426 \text{ Exp } (0.1473 Z)$	91.1
	PCVI-21	$Y = 0.2637 \text{ Exp } (0.2475 Z)$	98.0
	PCVI-23	$Y = 0.1894 \text{ Exp } (0.2422 Z)$	97.3
	PCVI-35	$Y = 0.8130 \text{ Exp } (0.1360 Z)$	97.8
	PCVI-38	$Y = 0.3846 \text{ Exp } (0.2192 Z)$	96.8
r/R = 0.5	PCVI-33	$Y = 0.0659 \text{ Exp } (0.2953 Z)$	97.7
	PCVI-24	$Y = 0.4208 \text{ Exp } (0.2238 Z)$	94.1
	PCVI-37	$Y = 0.2359 \text{ Exp } (0.2405 Z)$	57.1
	PCVI-28	$Y = 1.9128 \text{ Exp } (-0.1388 Z)$	71.8
	PCVI-27	$Y = 0.0953 \text{ Exp } (0.2999 Z)$	91.0
	PCVI-25	$Y = 0.5307 \text{ Exp } (0.2553 Z)$	91.6
	PCVI-36	$Y = 0.2969 \text{ Exp } (0.2482 Z)$	81.6
	PCVI-22	$Y = 1.2963 \text{ Exp } (0.1770 Z)$	84.5
	PCVI-21	$Y = 0.1611 \text{ Exp } (0.3014 Z)$	96.5
	PCVI-23	$Y = 0.1579 \text{ Exp } (0.2464 Z)$	99.4
	PCVI-35	$Y = 0.7785 \text{ Exp } (0.1543 Z)$	95.2
	PCVI-38	$Y = 0.5281 \text{ Exp } (0.2216 Z)$	98.8

Table 5. Regression equations relating deposition rate (Y) in $\mu\text{m/h}$ to the distance (Z) in mm from the cold side of the composite (continued)

Radial Position	Run Number	Equation	R ²
r/R = 1.0	PCVI-33	$Y = 0.0875 \text{ Exp } (0.2114 Z)$	95.8
	PCVI-24	$Y = 0.4978 \text{ Exp } (0.1130 Z)$	94.0
	PCVI-37	$Y = 0.4958 \text{ Exp } (0.0833 Z)$	72.2
	PCVI-28	$Y = 1.5693 \text{ Exp } (-0.3106 Z)$	77.2
	PCVI-27	$Y = 0.1466 \text{ Exp } (0.1855 Z)$	98.0
	PCVI-25	$Y = 1.0118 \text{ Exp } (0.1276 Z)$	91.4
	PCVI-36	$Y = 0.4125 \text{ Exp } (0.1851 Z)$	95.0
	PCVI-22	Data scattered	--
	PCVI-22	$Y = 0.2082 \text{ Exp } (0.1887 Z)$	98.6
	PCVI-23	$Y = 0.1500 \text{ Exp } (0.1950 Z)$	94.5
	PCVI-35	$Y = 0.7212 \text{ Exp } (0.0788 Z)$	75.4
	PCVI-38	$Y = 0.5657 \text{ Exp } (0.1585 Z)$	95.7

Table 6. Operating conditions for infiltration of eight harness satin weave preforms

Run Number	Temperature of Preform Bottom	Concentration (%)	Total Flow Rate (cm ³ /min)
HS-1	885	50	400
HS-3	885	50	400
HS-5	867	50	400

Table 7. Properties of the infiltrated eight harness satin weave composites

Run Number	Initial Porosity (v/o)	Infiltration Time (h)	Rate of Weight Gain (g/h)	Final Total Porosity (%)	Open Porosity (%)	Density (g/cm ³)	Deposition Efficiency (%)
HS-1	41.76	2.6	3.22	13.81	9.47	1.562	16.7
HS-3	46.34	3.5	2.76	12.45	7.32	1.594	14.3
HS-5	45.98	7.5	1.22	8.39	5.00	1.670	6.4

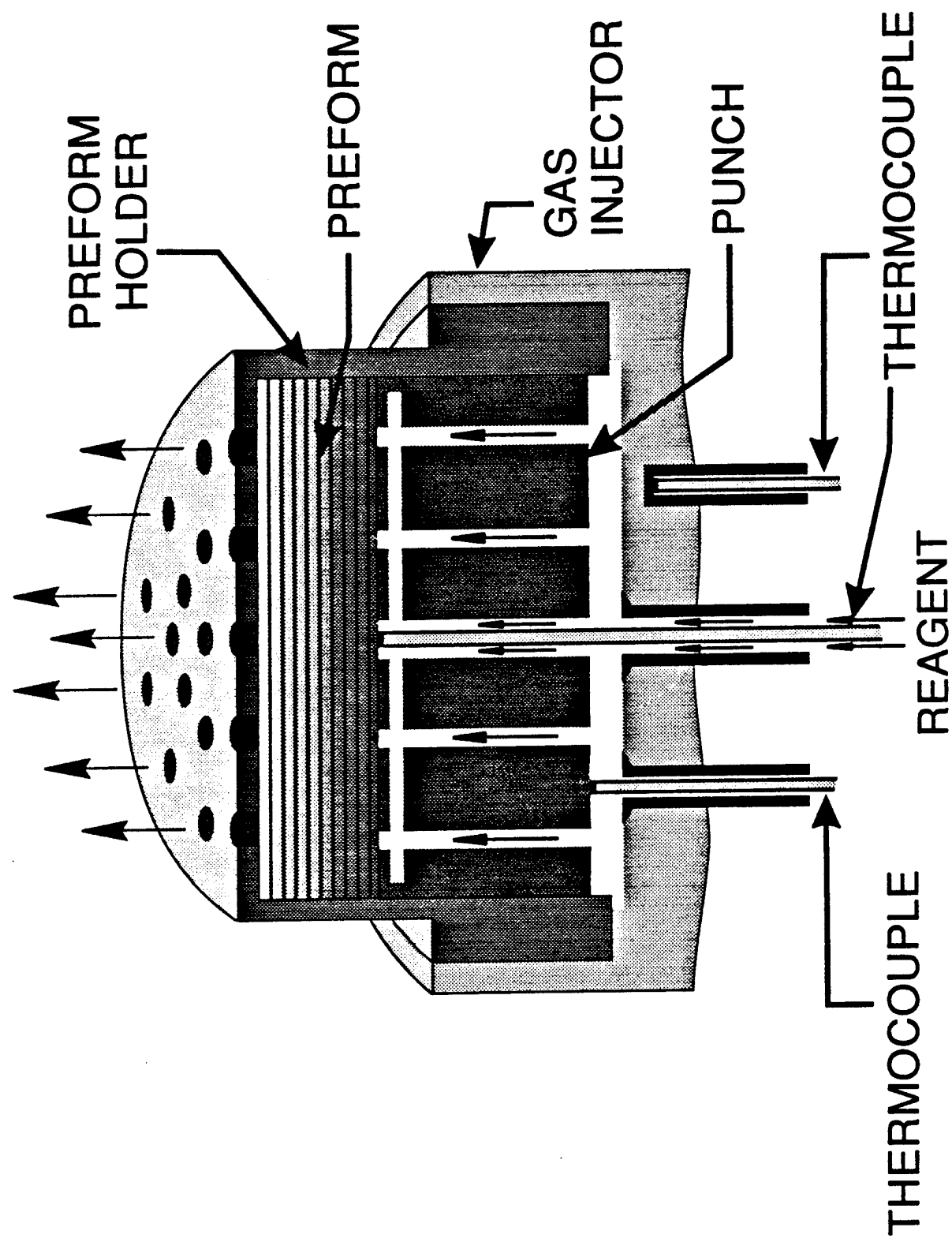
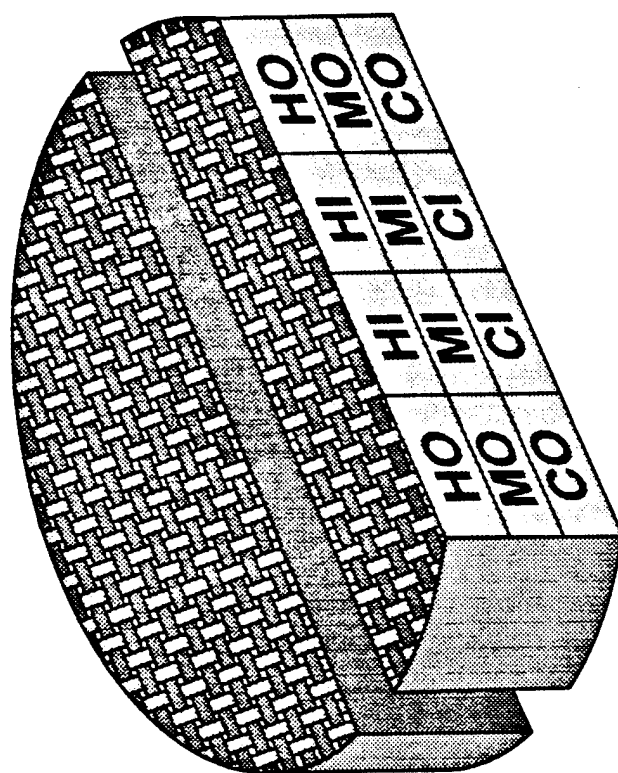


Figure 1. Schematic of the FCVI process.



H: HOT SIDE
M: MIDDLE
C: COLD SIDE
I: INSIDE
O: OUTSIDE

Figure 2. Schematic showing the location of density samples.

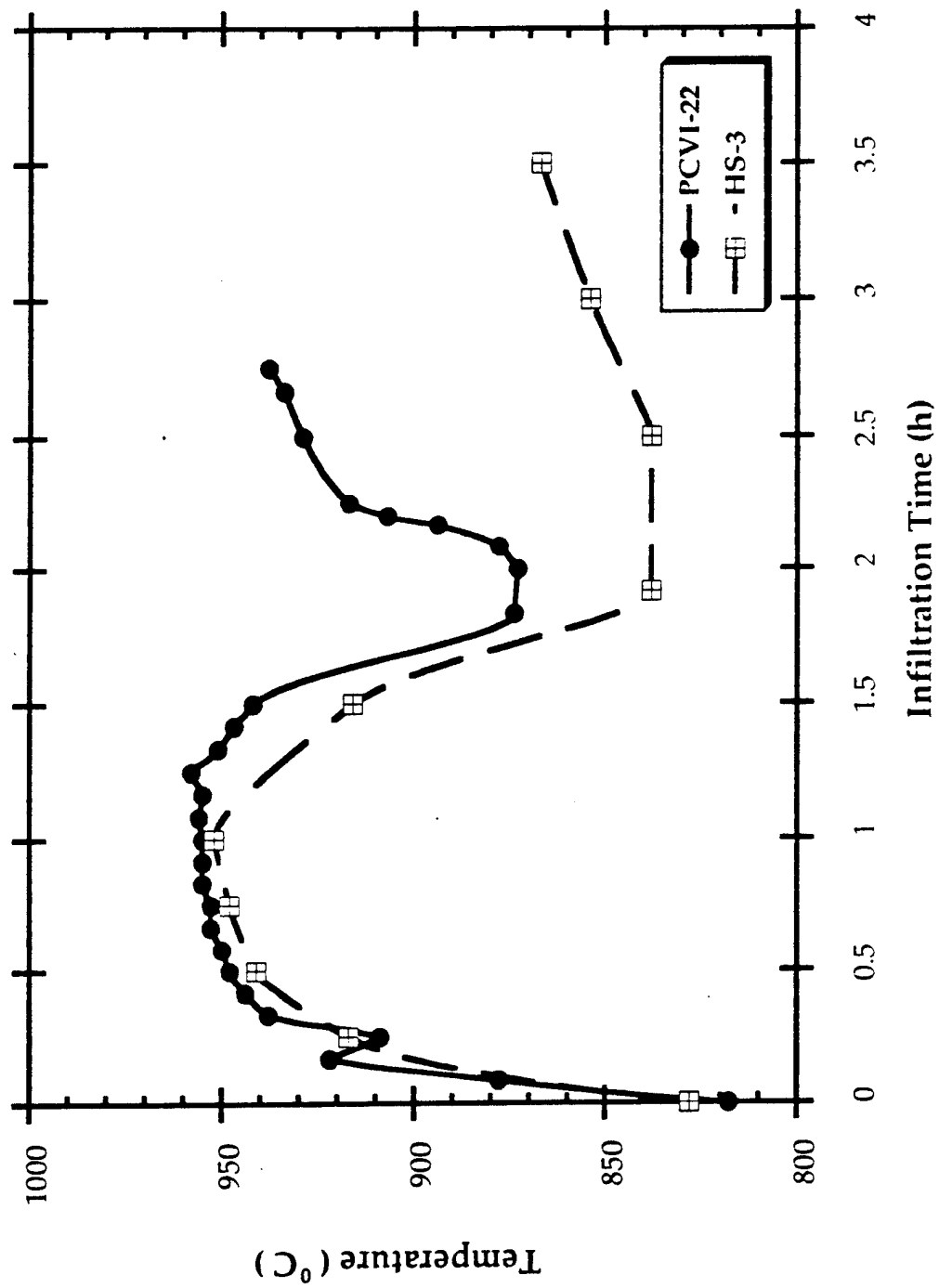


Figure 3. Variation of the temperature of the bottom of the preform with time.

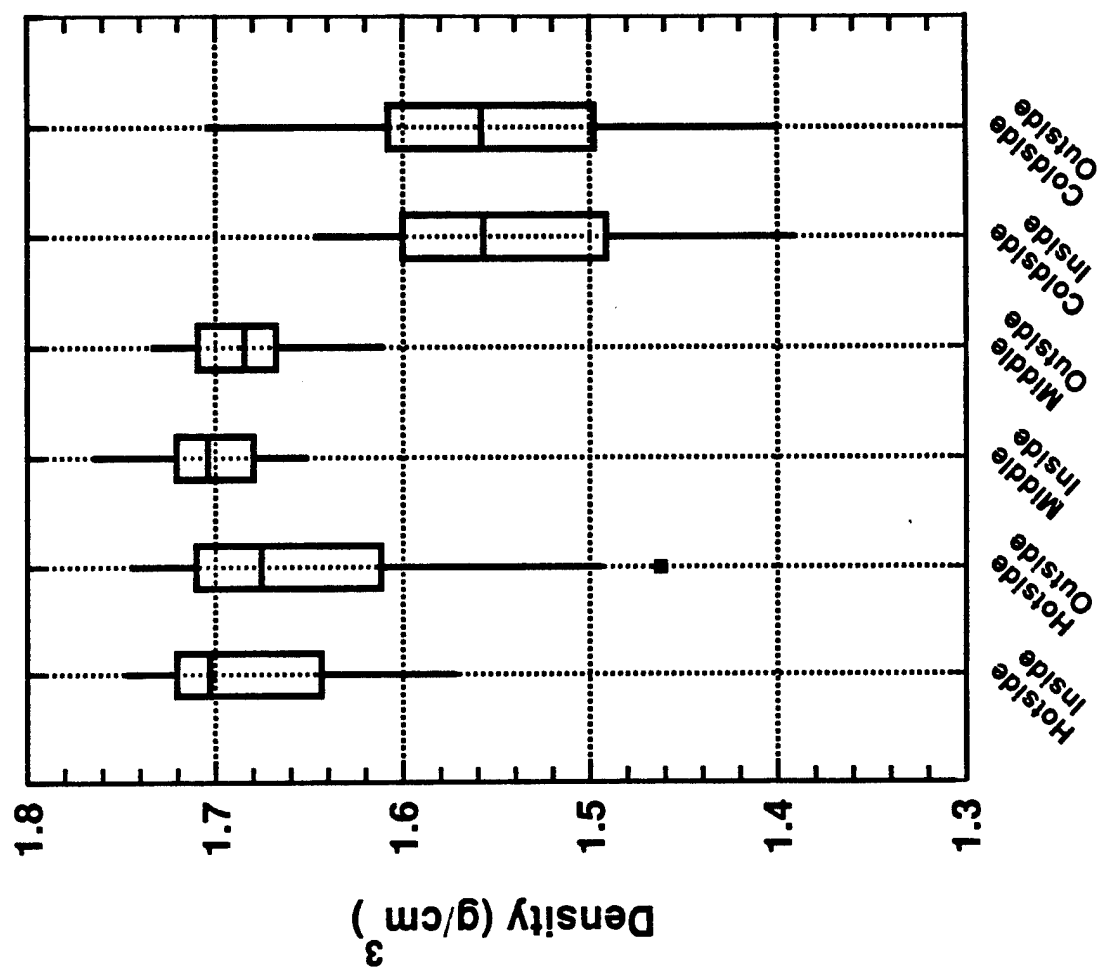


Figure 4. Bulk density as a function of radial and axial position within the composite disk.

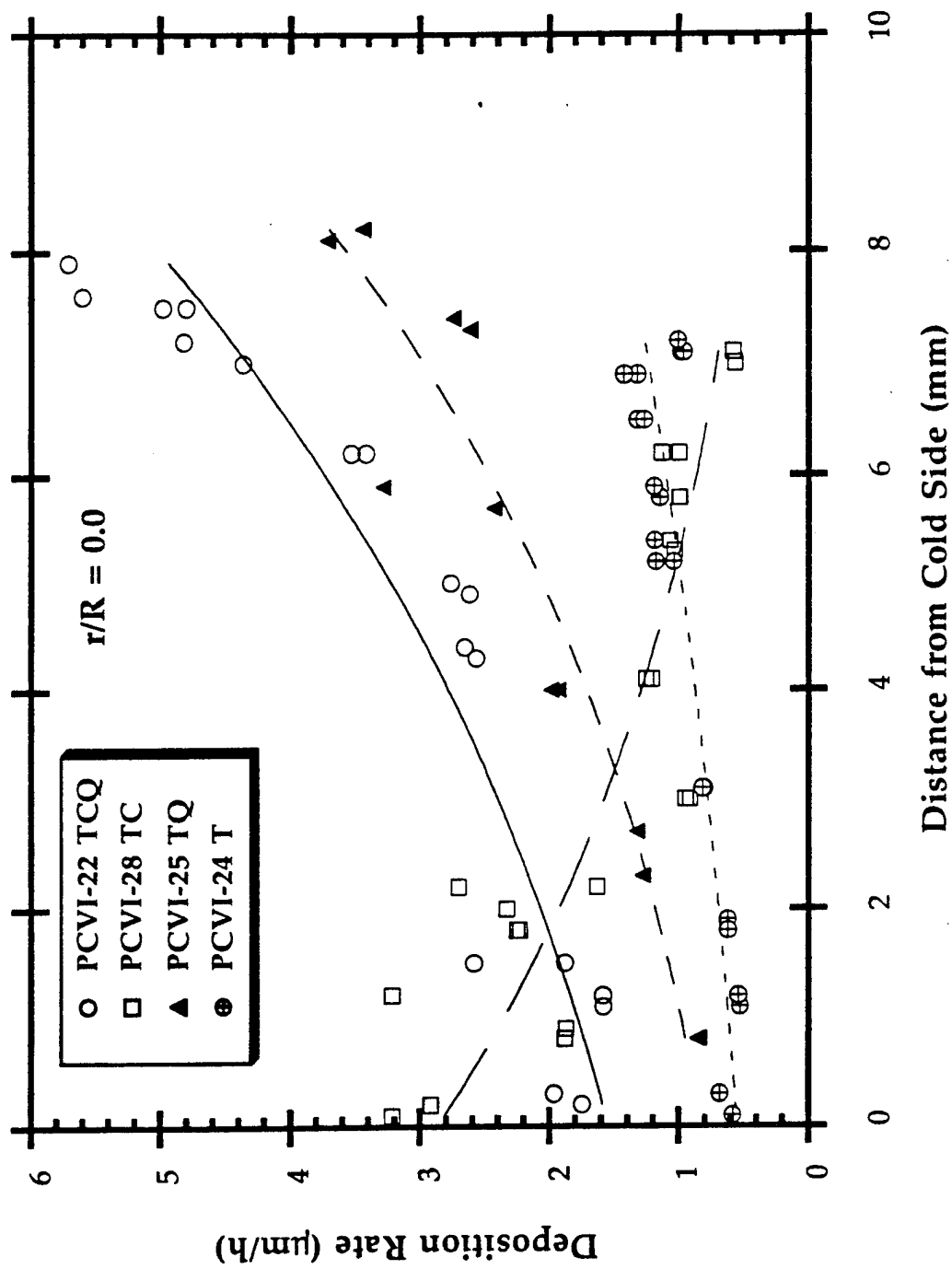


Figure 5. Deposition rates for experiments at high temperature (a) near the center of the composite disk.

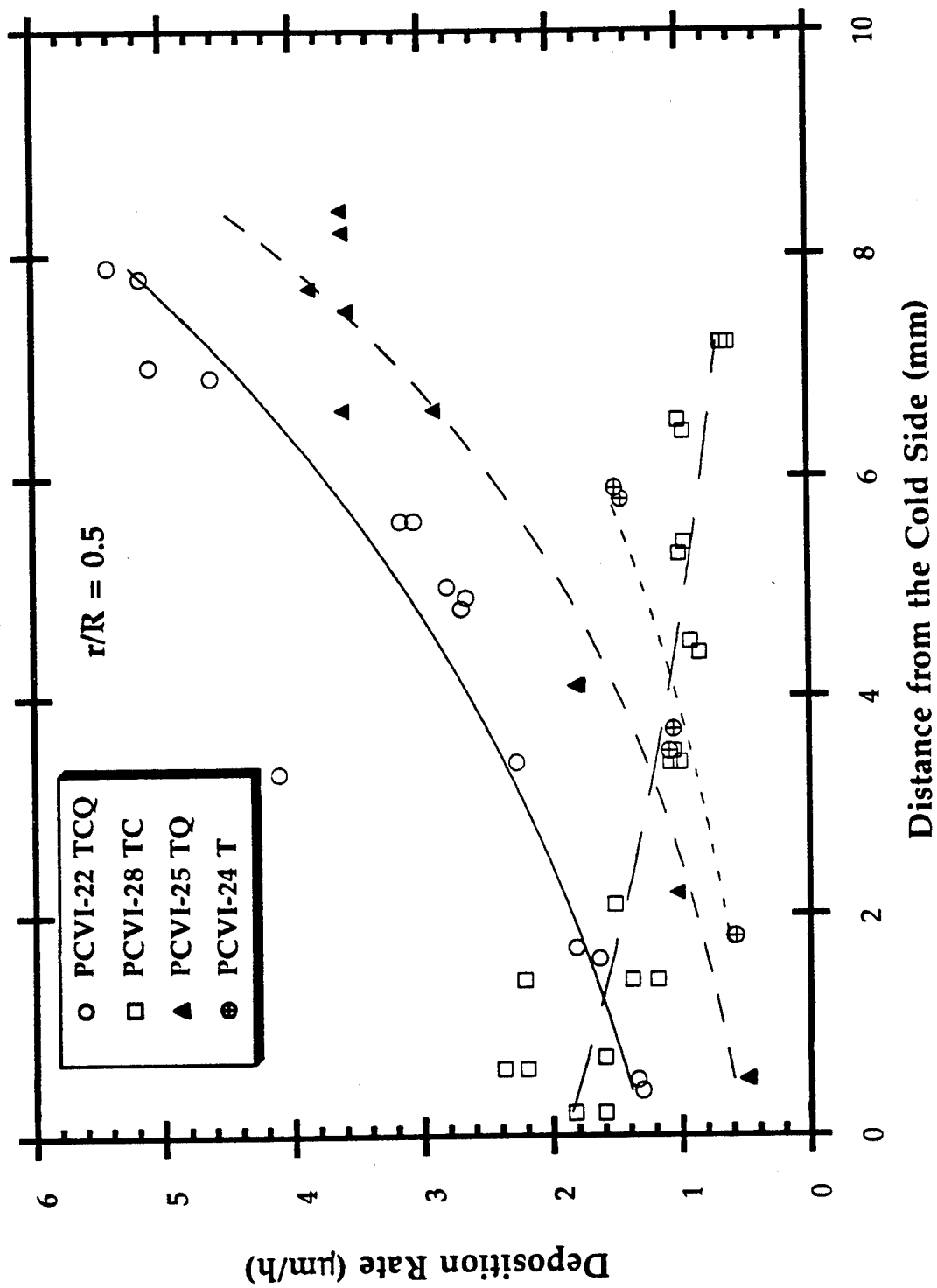


Figure 5. (b) between the center and circumference of the composite disk.

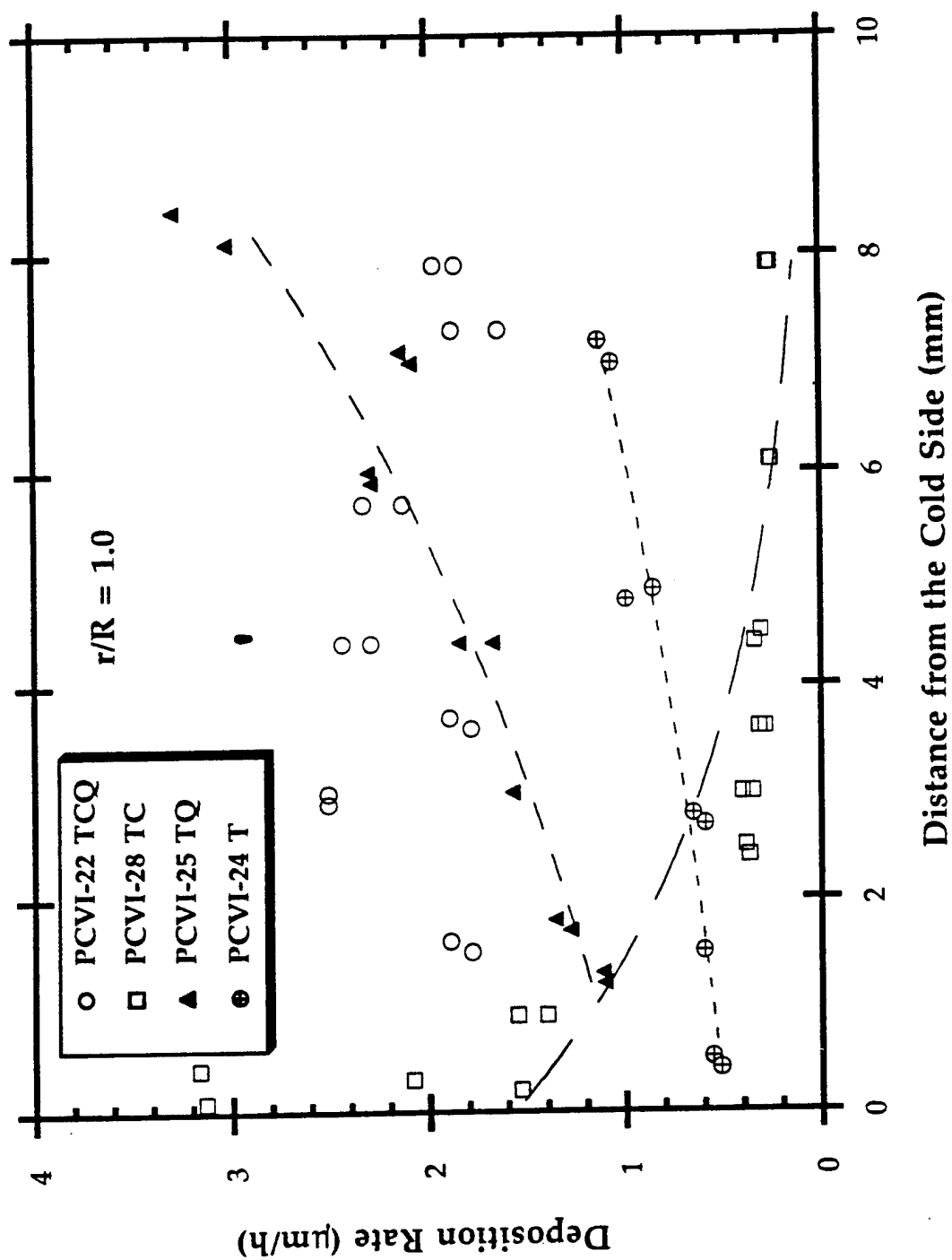


Figure 5. (c) near the circumference of the composite disk.

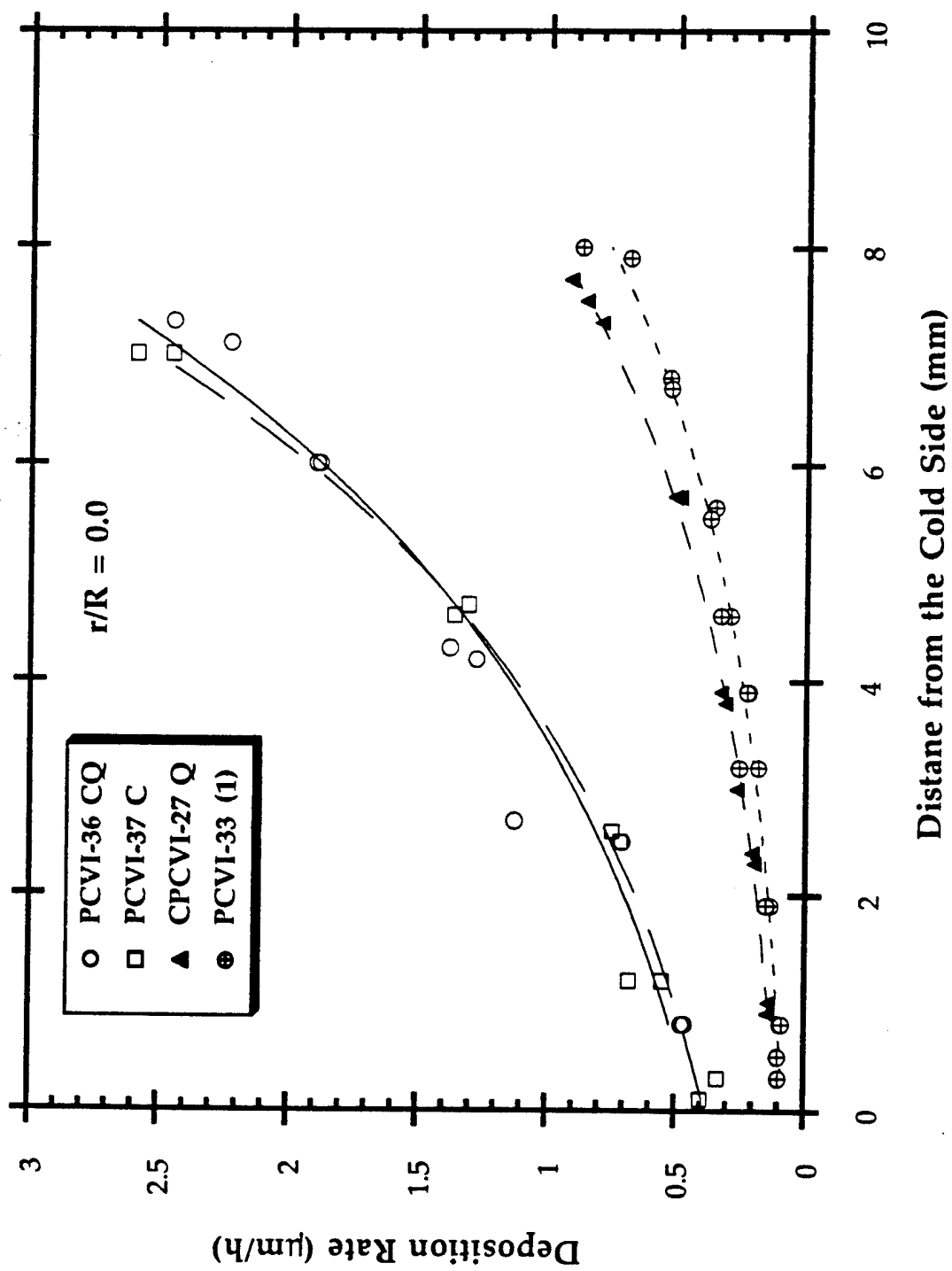


Figure 6. Deposition rates for experiments at low temperature (a) near the center of the composite disk.

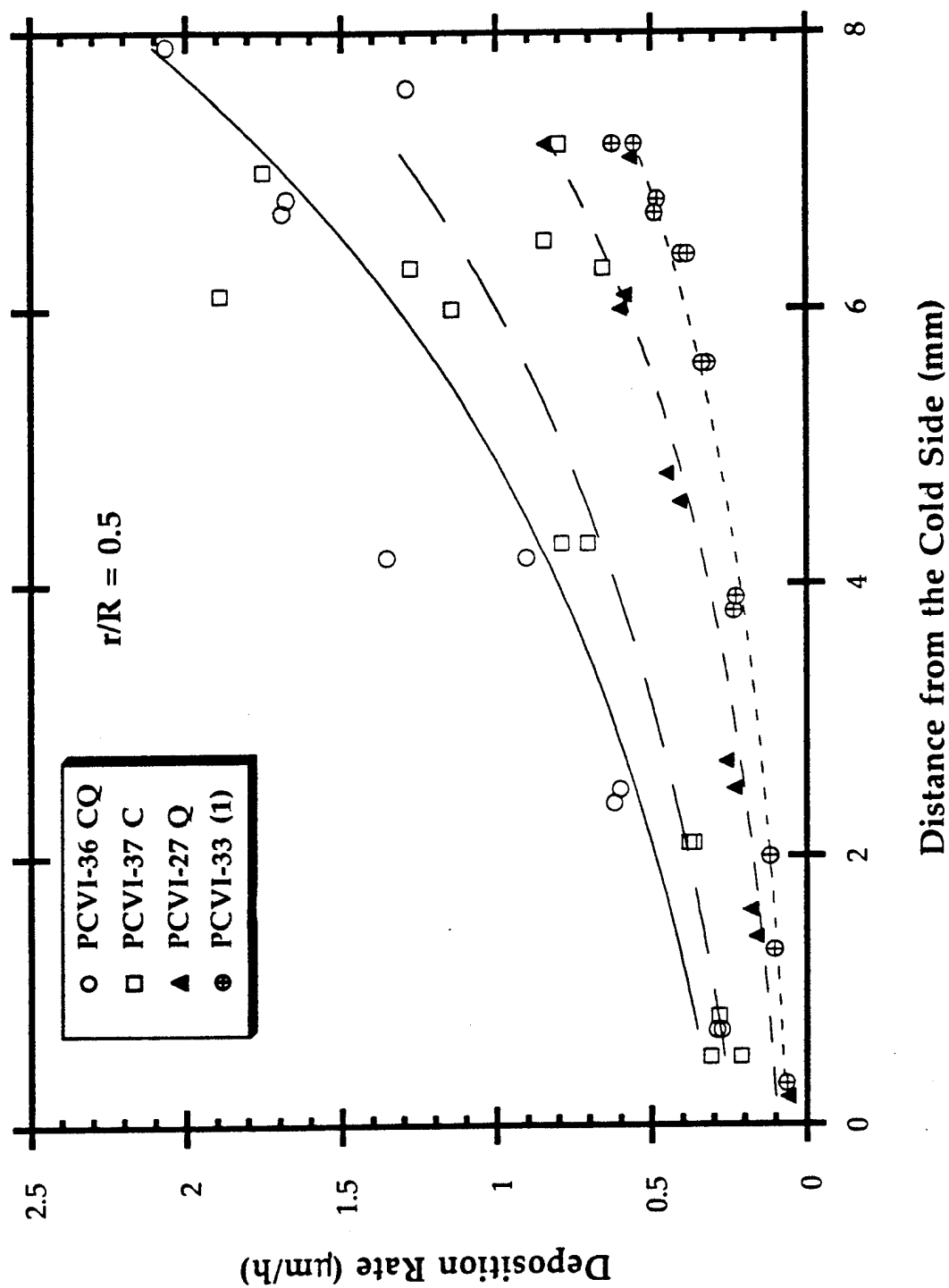


Figure 6. (b) between the center and circumference of the composite disk.

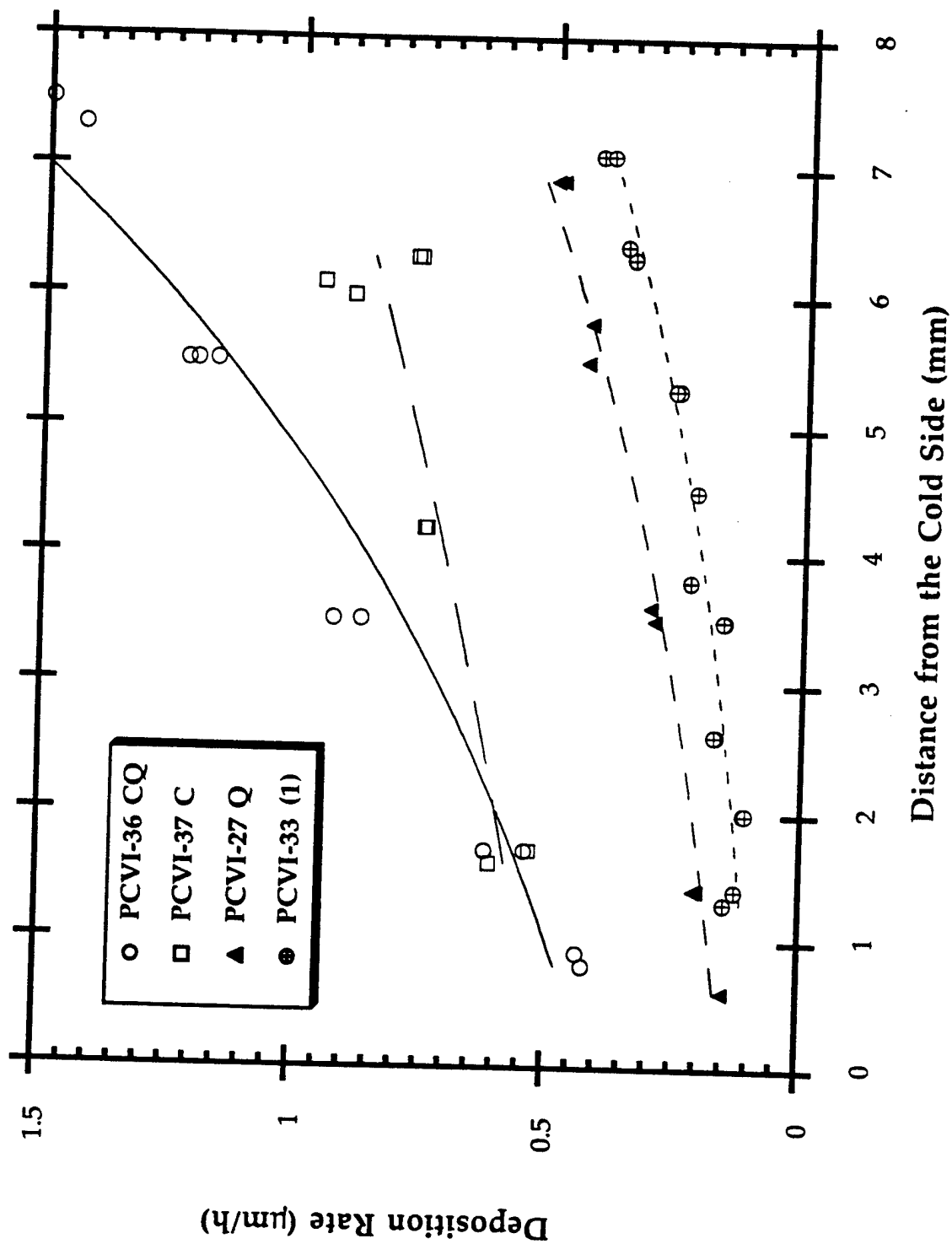


Figure 6. (c) near the circumference of the composite disk.

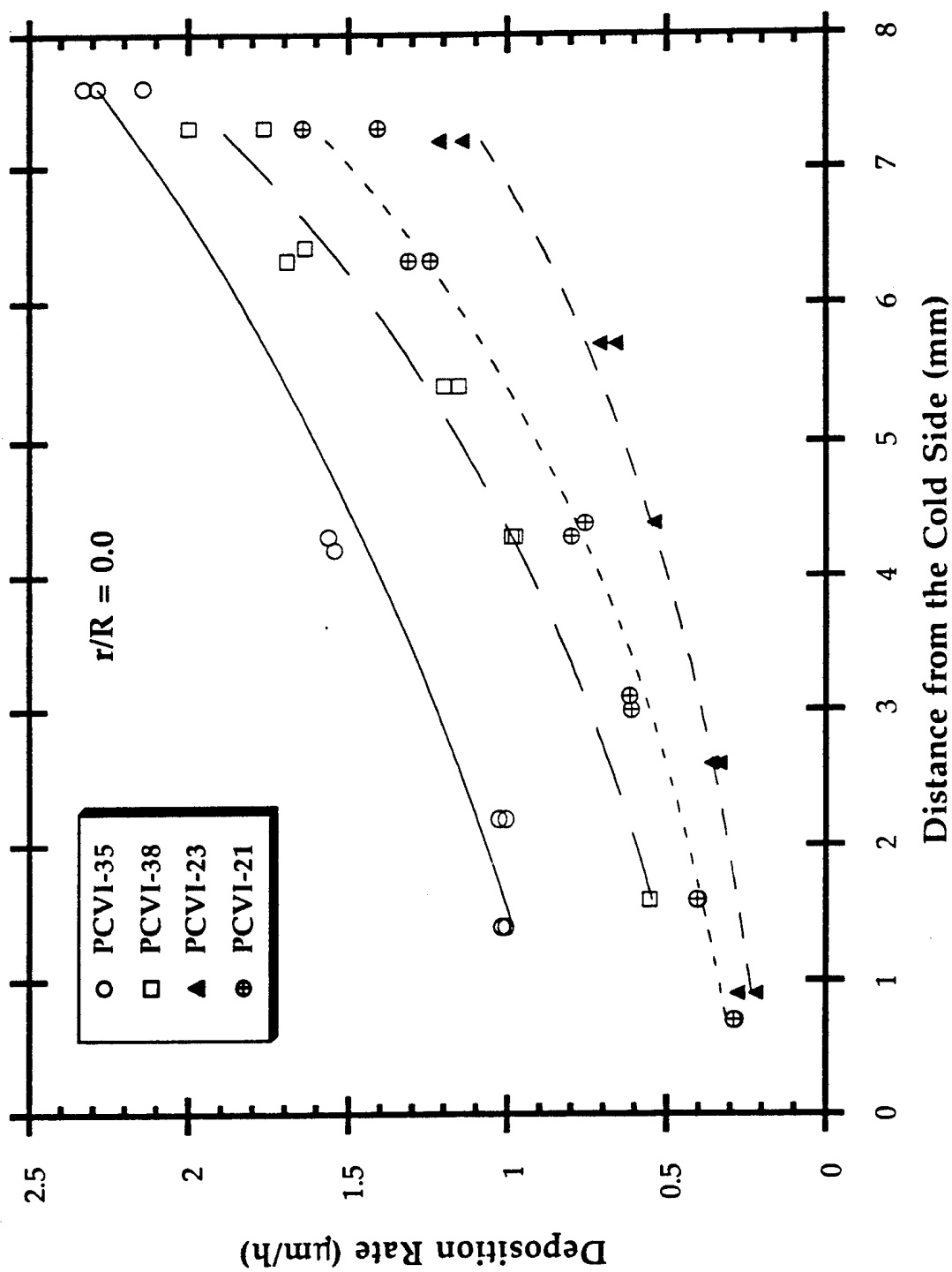


Figure 7. Deposition rates of midpoint temperature experiments (a) near the center of the composite disk.

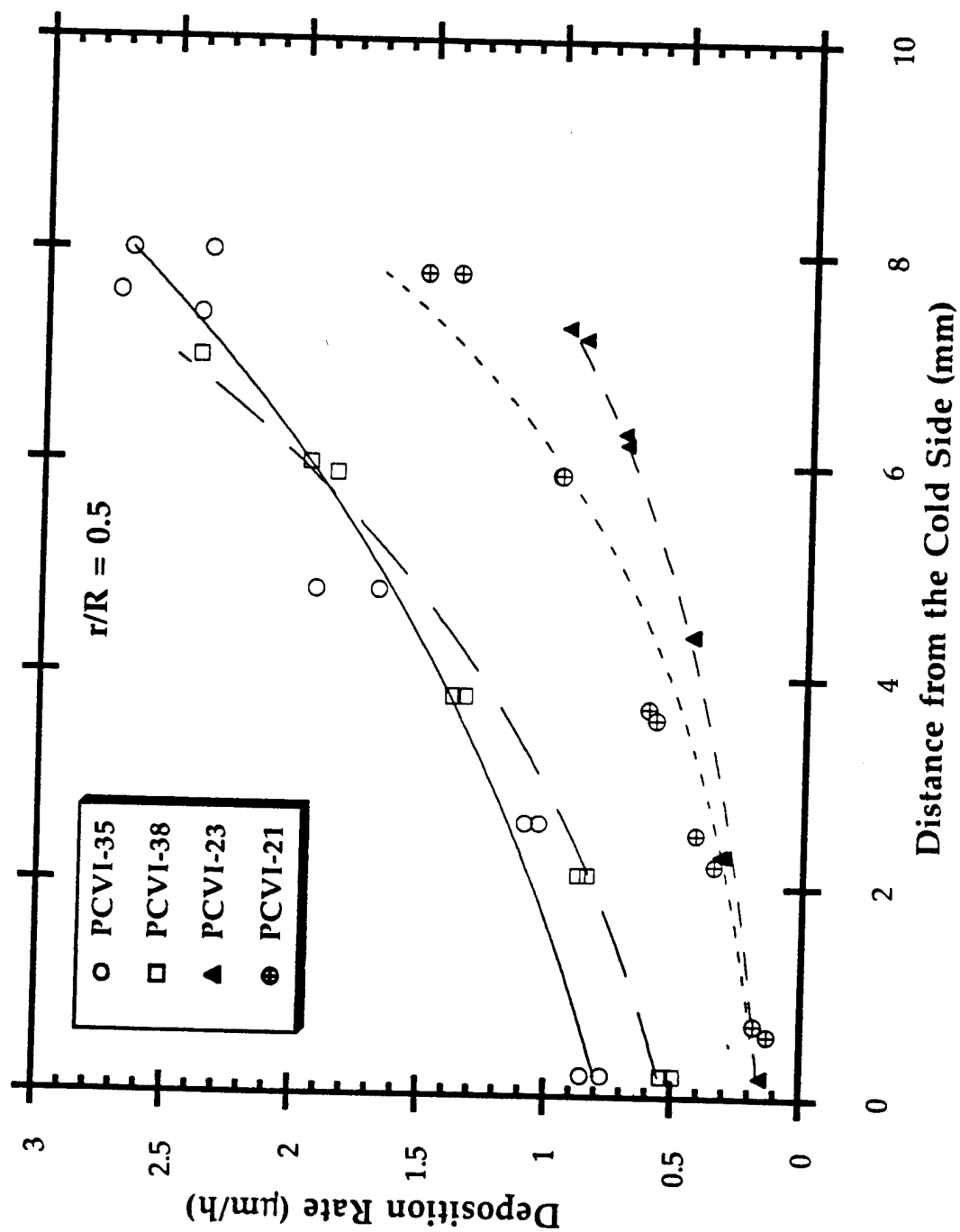


Figure 7. (b) between the center and circumference of the composite disk.

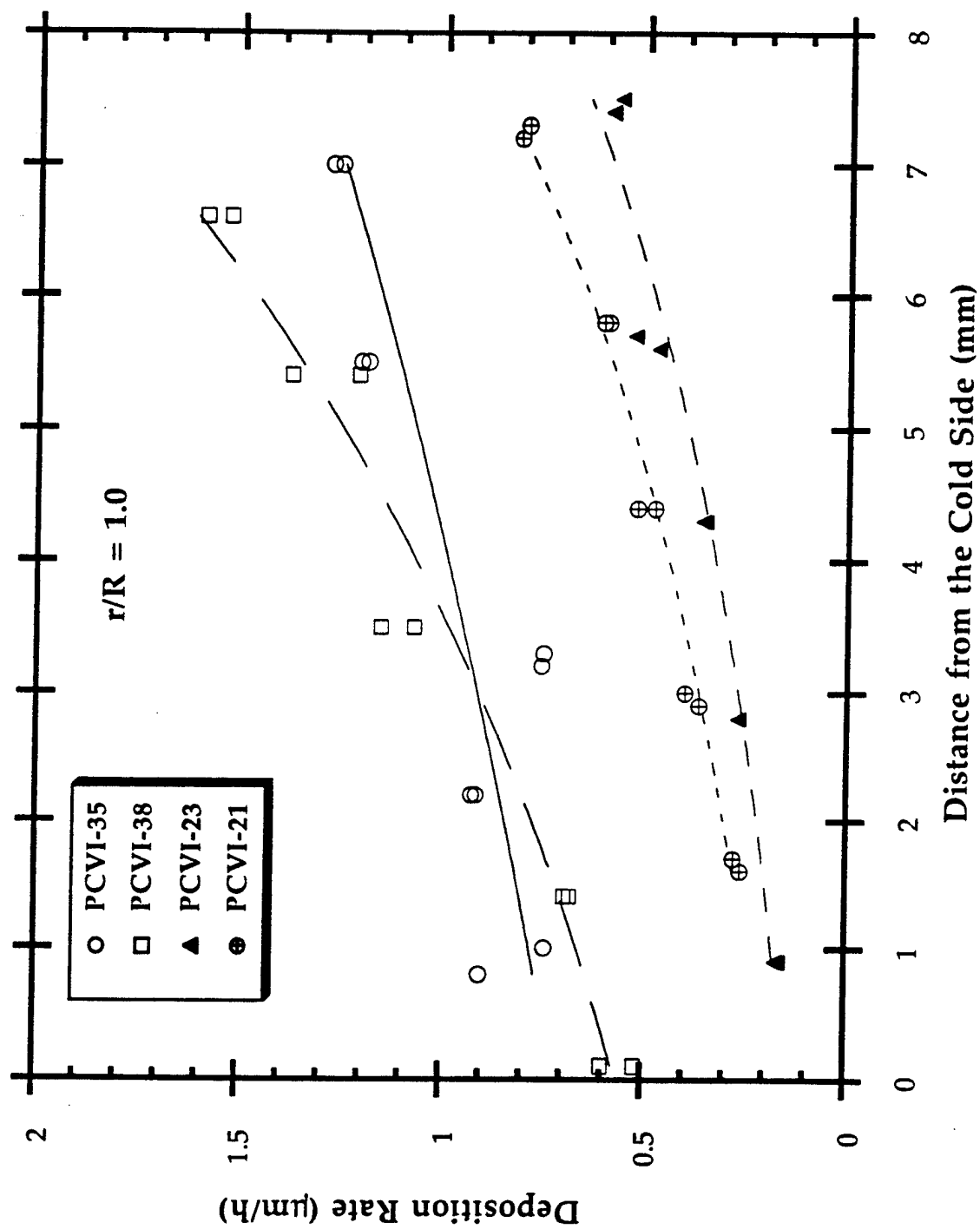


Figure 7. (c) near the circumference of the composite disk.

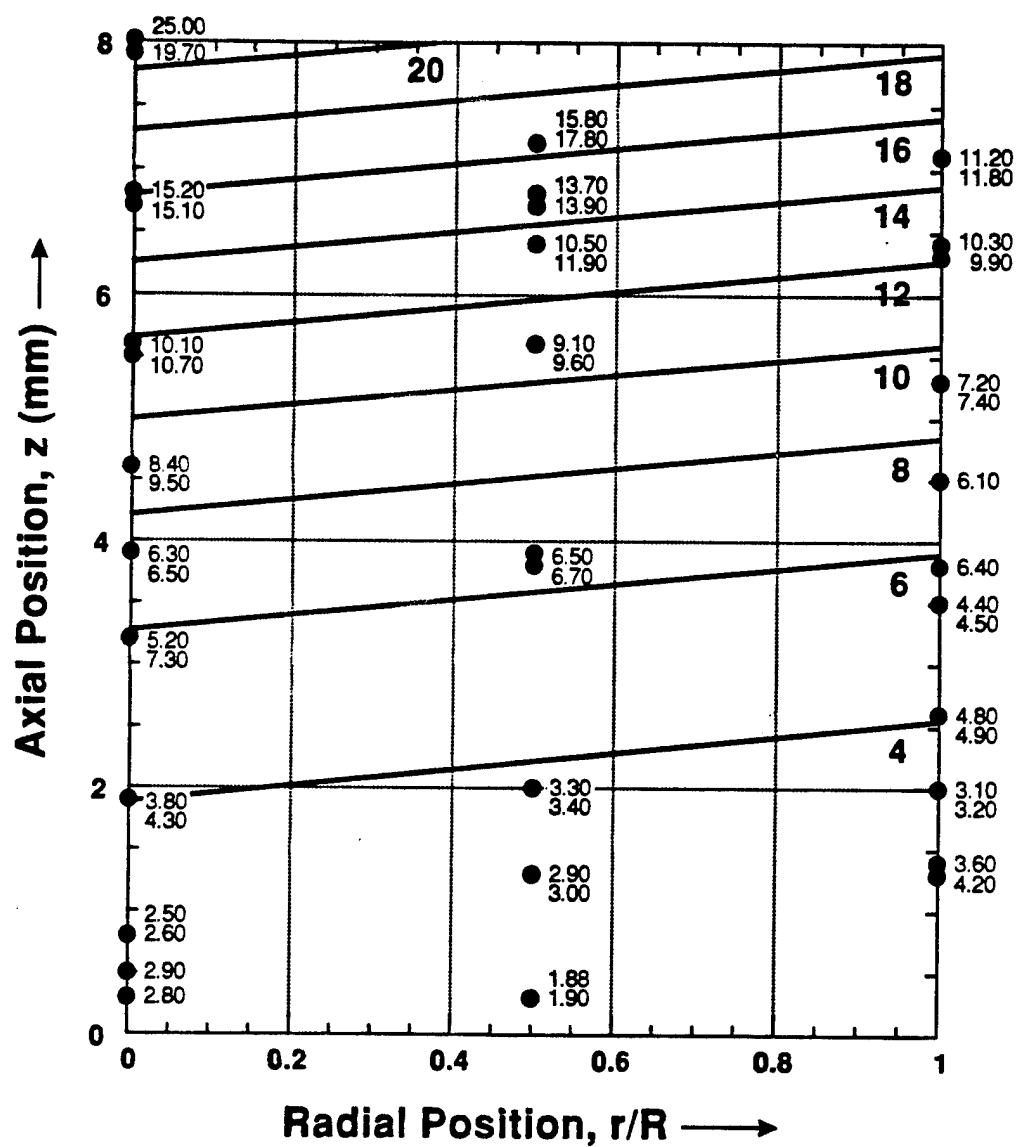


Figure 8. Coating thickness for Sample PCVI-33 as a function of radial position and axial distance. Contour lines were obtained by regressing the data (Eqn. 13).

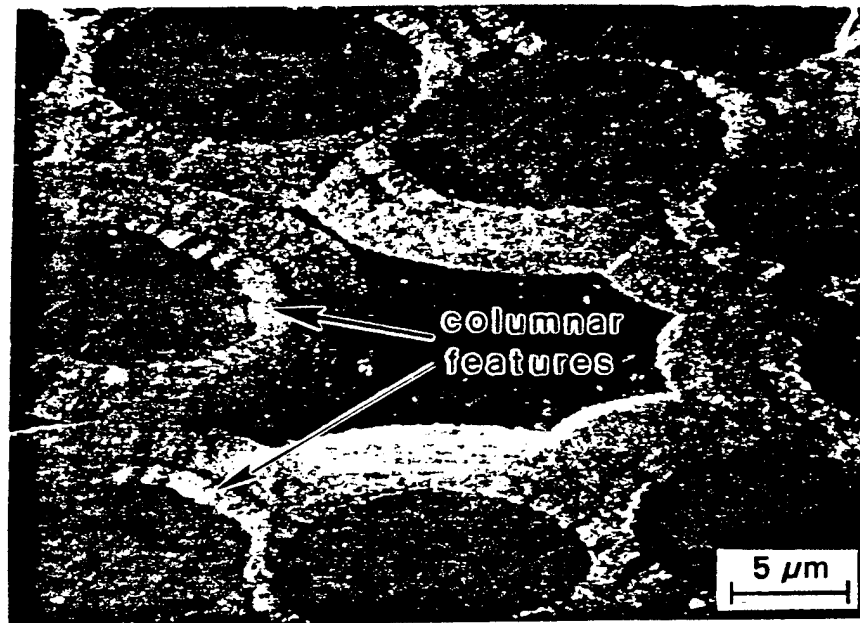
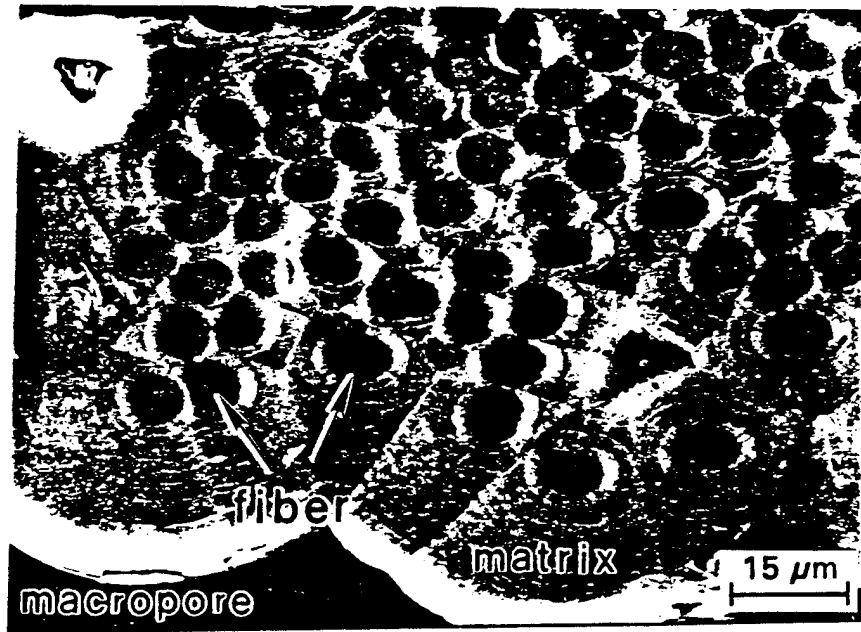


Figure 9. Micrographs from hot side of composite PCVI-36 showing the layered structure.

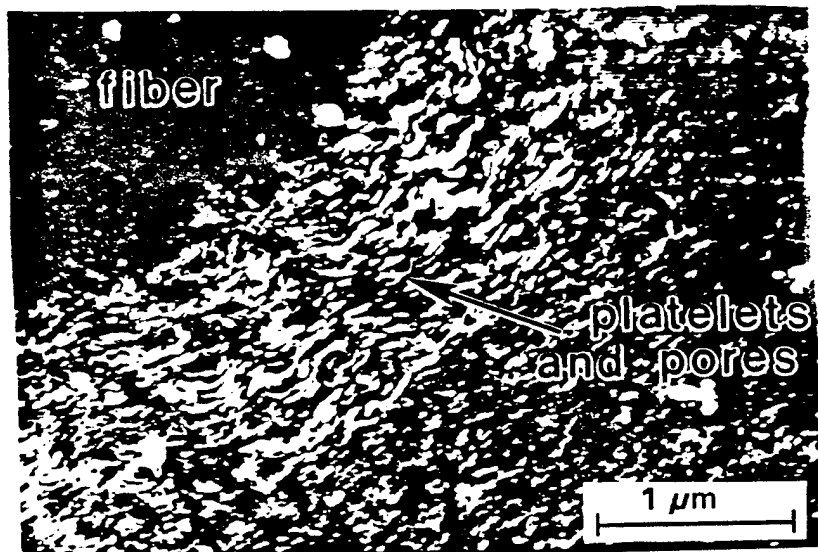


Figure 10. Micrograph showing porosity in the layered matrix structure near the fiber (PCVI-24).

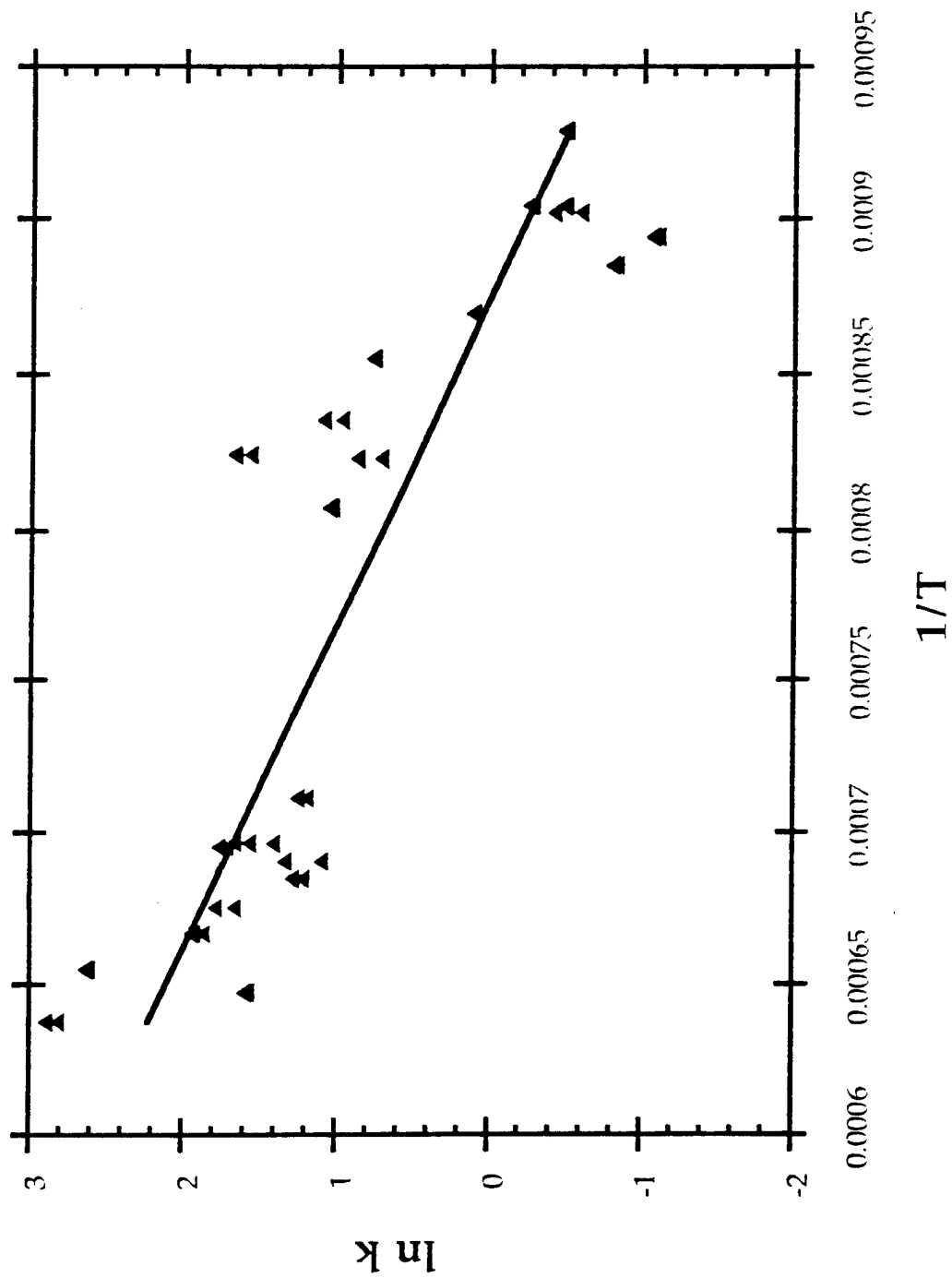


Figure 11. Arrhenius plot for deposition of carbon in the preforms.

Carbon/Carbon Processing by Forced Flow-Thermal Gradient Chemical Vapor Infiltration (FCVI) Using Propane

Sundar Vaidyaraman†, W. Jack Lackey*‡, and Pradeep K. Agrawal†

†School of Chemical Engineering
*Georgia Tech Research Institute
Georgia Institute of Technology
Atlanta, GA 30332

Abstract

A 2^3 factorial statistically designed experiment was used to study fabrication of carbon/carbon composites using the forced flow-thermal gradient chemical vapor infiltration process. Propane, diluted with hydrogen, was used as the feed. The independent variables were the temperature of the bottom of the preform holder, concentration of the reagent, and total flow rate. The response variables were infiltration time, final porosity, rate of weight gain, and uniformity of infiltration. It was found that the infiltration time was affected only by the temperature of the preform and the concentration of the reagent. Infiltration times as low as 7 h were achieved. The bulk density of the final composite was found to be independent of the operating conditions, provided the process was continued until a fixed pressure drop was achieved. Density variations with position within a given composite were no more than ± 0.08 g/cm³. Deposition efficiency ranged from 3 to 14% and increased with temperature while decreasing with flow rate. The values of the coating thickness near the hot and cold sides of the composite were used to calculate the rate constant for pyrolysis of propane. The activation

‡Author for correspondence.

energy was found to be ~ 23.6 Kcal/mol and the rate constant was given by $\ln k_s(\text{cm/s}) = 2.2 - 23610/RT$.

Keywords: Carbon Composites, FCVI, propane, uniformity, processing

1. INTRODUCTION

Carbon/carbon composites are unique materials in that they combine the desirable properties of fiber reinforced composites, such as high specific strength, stiffness, and toughness, with the refractory properties of carbon, namely, retention of strength at high temperatures in an inert atmosphere and resistance to creep and thermal shock. The applications of these materials include rocket nose cones, aircraft disc brakes, heat shields, etc. Processing, properties, and applications of carbon composites have been reviewed extensively in journals [1-3] and books [4-7].

The commercial processing methods used to fabricate carbon composites are very slow and highly inefficient. These limitations add considerably to the cost of the components and limit the application of this material. Hence, there is a need to develop a process to rapidly and economically fabricate carbon composites. We have shown [8-10] that the forced flow-thermal gradient chemical vapor infiltration (FCVI) process, conceived by Lackey and Caputo [11] and further developed by Caputo et al. [12,13] for SiC/SiC, can be used to fabricate dense carbon/carbon composites using propylene, propane, or methane as the reagent. The FCVI process has been optimized for fabrication of carbon composites using propylene [10]. Processing times were reduced to 3 h. The present work was undertaken to similarly optimize the FCVI process when propane was used as the reagent. To this end, we have pursued a

quantitative understanding of the influence of the FCVI process variables, i.e., temperature, propane concentration, and total flow rate, on the infiltration process and the properties of the infiltrated composites. This was accomplished by using a factorial experiment.

2. EXPERIMENTAL DETAILS

The details of the equipment and experimental procedure have been explained elsewhere [8,9]. Briefly, the preforms consisted of 40 layers of T-300 plain weave carbon cloth, 4.8 cm in diameter, oriented at 0-30-60°. These layers were stacked in a graphite preform holder. A type 3 preform holder, described in the prior publication [8], which extends 7.6 cm above the gas injector was employed for carbon infiltration using propane. The height of the preform holder affects the temperature and the temperature gradient across the preform. The temperature difference between the hot and the cold side of the preform for the type 3 holder was $\sim 150^{\circ}\text{C}$.

The bottom of the preform was cooled by the water cooled gas injector and the top of the preform was heated by the furnace, resulting in the establishment of the temperature gradient. The pressure gradient forces the gas through the preform. The feed gas typically consisted of propane (99.5% pure, Instrument Grade, Matheson, East Rutherford, NJ) with hydrogen as a diluent. As the infiltration progressed, reduction in porosity caused an increase in the back pressure. The runs were typically terminated once the back pressure reached ~ 136 kPa (5 psig) for a standardized gas flow consisting of 100 cm³/min of propane and 100 cm³/min of hydrogen. The temperatures of the preform top and bottom were monitored using K-type thermocouples during the infiltration. The infiltrated composites were then removed intact from the holder after cooling the furnace.

The apparent volume of each composite was determined using Archimedes' principle with methanol ($\rho = 0.79 \text{ g/cm}^3$). The open pore volume was calculated by weighing the composite saturated with methanol. These two values were added to obtain the bulk volume. As a check on the bulk volume, the above procedure was repeated with distilled water. Total porosities were calculated assuming a deposit density of 1.9 g/cm^3 . The composites were also cut into slices 10 mm long, 4 mm wide, and 2 mm deep to determine the uniformity of the infiltration. The details of the location of the slices are given elsewhere [10]. The density of each slice was calculated from its weight and volume. The volume was calculated from the dimensions of the slice.

An entire cross-section of each composite disk was mounted in epoxy and polished. The polished sections were observed via scanning electron microscopy in order to measure coating thickness as a function of axial and radial position.

2.1 Experimental Design and Data Analysis

The factorial experimental design has been explained previously [10]. To summarize, a 2^3 factorial experiment with two center points was chosen to study the FCVI process. The independent variables studied included the temperature of the bottom of the preform, the propane concentration, and the total flow rate. Table 1 gives the high, low, and mid values for each of the independent variables. These values were chosen based on a previous feasibility study with propane [9]. Table 2 lists the processing conditions for each run. The temperature of the bottom of the preform varied by $10\text{--}15^\circ\text{C}$ during the course of the infiltration. Hence, a time averaged temperature (Table 2) was employed for the data analysis. In this study the pressure above the preform was kept constant at 1 atm and the initial porosity of the preform was $\sim 50\%$.

The response variables for the infiltration process were chosen based on the process and product requirements. These included infiltration time, final porosity, rate of weight gain, uniformity of densification, and deposition efficiency. The uniformity of densification was ascertained from the density of slices cut from a composite sample. Ideally, one would like to reduce the infiltration time and final porosity. At the same time, the infiltrated composite should be uniformly dense, independent of the position within the composite.

The effects of the operating variables on the response variables were analyzed using a linear regression model. The model was chosen based on accepted statistical criteria, i.e., R_p^2 , R_s^2 , C_p , and DFFITS. The details of the application of these parameters to similar experimental data have been explained elsewhere [10]. Despite the use of these criteria, the final choice of the model was based on the physical laws of the process. In a few instances, models which better represented the physical phenomena of the process were chosen even though the statistical criteria might have pointed to other models.

3. RESULTS AND DISCUSSION

Table 3 lists the infiltration time, rate of weight gain, porosity, density, and deposition efficiency for the 11 FCVI runs conducted with propane as the reagent. The following sections explain in detail the relationships found between the response variables and the independent variables. The regressions were performed against the coded variables (Table 2) to help ascertain the relative effect that changing the independent variables had on the response.

All the infiltration experiments resulted in dense carbon composites, except the experiment "TC" (PA-9). The designation "TC" indicates that for this experiment the

temperature and concentration were at their high levels. In this experiment the back pressure increased from 1 to 4 psig within 5 minutes after 2 h of infiltration. The rapid increase in back pressure was due to preferential densification of the cold side of the composite. This was probably caused by a long residence time due to the low flow rate, thereby, preventing gas flow to the other parts of the preform. This resulted in a very non-uniform composite for which the top ~25 cloth layers were not appreciably densified and came off freely. This experiment was repeated two more times with the same result. Inclusion of the results from this experiment in the regression analysis would bias the model because of its extreme behavior. Consequently, it was decided to carry out the statistical analysis without the experiment "TC".

3.1 Infiltration Time

The infiltration time is defined as the time taken for the back pressure to reach 5 psig for a feed of 100 cm³/min of propane and 100 cm³/min of hydrogen. The infiltration time was shortest, ~7 h, when all the independent variables were at their high value. The longest infiltration time, 34 h, was obtained for experiments "(1)" and "Q". The infiltration time was regressed against the independent variables and their interactions. The best regression relating the infiltration time to the operating variables is given below:

$$\begin{aligned} \text{Infiltration Time} &= 17.6 - 6.48 T_{\text{cod}} - 6.88 C_{\text{cod}} \\ S_{\text{regression}} &= 3.98, \quad R_p^2 = 86.1\%, \quad R_a^2 = 82.6\% \end{aligned} \quad (1)$$

The above regression showed good fit to the experimental data. However, the variances were not the same at different levels of a given independent variable. This could be due to either the limited number of experimental data points or the presence of some quadratic effects in the response. Quadratic effects cannot be estimated with the present experimental design. But any

quadratic effect was not expected to be very high because the temperature and the concentration terms explained ~86% of the variation of the infiltration time.

The infiltration time was affected only by the temperature and the concentration of the feed; the magnitudes of the effects were very similar. Increases in concentration or temperature typically reduced the infiltration time. The total flow rate did not seem to affect the time of infiltration. The infiltration times for propane were about twice as long as those observed for propylene [10]. For example, experiment "T" took about 11 h with propylene as compared to 19 h with propane and TCQ required 7 h for propane versus 3 h for propylene.

3.2 Rate of Weight Gain

The rate of weight gain was computed by dividing the total weight gain by the infiltration time. This parameter can be thought of as a mass deposition rate for CVI experiments. The result of the regression is given in Equation 2.

$$\begin{aligned} \text{Rate of Weight Gain} &= 0.881 + 0.374 T_{cod} + 0.361 C_{cod} + 0.205 T_{cod} * C_{cod} \\ S_{\text{regression}} &= 0.08, R_p^2 = 98.3\%, R_a^2 = 97.5\% \end{aligned} \quad (2)$$

The rate of weight gain was affected by temperature, concentration, and the quadratic interaction between temperature and concentration. The quadratic interaction accounts for the larger effect that changing the concentration had on the rate of weight gain for the high temperature experiments as compared to the low temperature experiments. Once again, the total flow rate did not affect the rate of weight gain. The fact that flow rate did not affect the infiltration rate suggests that mass transfer had a negligible effect on the infiltration process. The average rate of weight gain was ~0.95 g/h for propane compared with ~1.5 g/h for propylene [10]. The lower rates of weight gain for the propane experiments were caused by: (1) slower carbon

deposition because of the absence of double bonds, and (2) the hot side temperature with the type 3 preform holder (propane) was only $\sim 1100^{\circ}\text{C}$ compared with $\sim 1300^{\circ}\text{C}$ using the type 2 preform holder (propylene), i.e., the average preform temperature was lower for propane infiltration.

3.3 Porosity and Density

Total and open porosity values were in the range 7-11% and 3.5-6.5%, respectively. As stated previously, the total final porosity was determined based on an assumed matrix density of 1.9 g/cm^3 . The average bulk density was $\sim 1.66\text{ g/cm}^3$ (excluding PA-9). The minimum and maximum values were 1.71 and 1.61 g/cm^3 . The bulk density values were analyzed against the independent variables and it was found that the bulk density was not affected by the operating conditions. This was a result of terminating the infiltration runs when the back pressure reached a set value. This, as was previously observed for propylene, shows that the measurement of back pressure is a reliable indicator of the end of the infiltration process, provided the cold side does not get infiltrated prematurely.

3.4 Density Gradient

The bulk densities of slices obtained from different parts of each composite were determined to evaluate the spatial uniformity of densification (Table 4). The variation of density with position is shown by the box-and-whisker plot (Figure 1). This figure shows that there is little difference between the density of slices from different parts of the composites. The density of slices from the hot side was $\sim 1.63\text{ g/cm}^3$ compared with $\sim 1.68\text{ g/cm}^3$ for slices from the middle of the composite. The lower density of the slices from the hot side of the composite was due to uneven distribution of macropores in the preform. It was observed, via scanning electron

microscopy, that there were initially more pores in the hot side of the composite, apparently as a result of nonuniform pressure during preform compaction. This led to lower hot side density. The cold side of the composite typically had a density of $\sim 1.55 \text{ g/cm}^3$, slightly lower than that of the hot side or middle of the composite. To further analyze density variation within a given sample, the density range was computed for each sample. The minimum and maximum values were 0.12 (PA-10) and 0.23 (PA-7) g/cm^3 and the average was $\sim 0.16 \text{ g/cm}^3$. The variation in density was slightly lower with propane as compared with propylene. The reduced density variation was the result of the lower temperature difference between the hot and cold sides of the preform caused by use of the longer type 3 preform holder. Whereas, in the case of the type 2 preform holder used in the propylene experiments, there was a slight tendency for the hot side to densify more rapidly and block gas flow pathways. This resulted in a more porous structure near the cold side of the composite. However, the use of the type 2 preform holder reduced the processing time because of the higher average preform temperature versus that of the type 3 holder. Hence, there appears to be a trade off between the speed of infiltration and the uniformity of the densification.

3.5 Deposition Rate

The coating thicknesses in macropores (found between cloth layers and tows within a cloth layer) were measured using a scanning electron microscope. These values were divided by the infiltration time to obtain the average deposition rate. The thickness measurements were made as a function of distance from the cold side at three radial positions for a given composite sample. The deposition rates so obtained for different composites are plotted in Figures 2-4.

The radial position was denoted by the variable " r/R ", where " r " is the distance from the center of the composite, and " R " is the radius of the composite.

The deposition rate data did not show any consistent trend, in contrast to the propylene study. For propylene the deposition rate increased exponentially with increasing distance from the cold side. The difference in behavior between these two systems can be attributed to the different temperature gradients across the preforms. In the case of propylene, the temperature difference between the hot and the cold side was $\sim 350^{\circ}\text{C}$, using the type 2 preform holder, as compared with $\sim 150^{\circ}\text{C}$ for propane, using the type 3 preform holder. This appears responsible for the dominant effect of temperature over other variables in the propylene study. It was observed that the average deposition rates with propane were much lower than with propylene. This can be attributed to the combination of slower carbon deposition and lower hot side temperature for the propane infiltrations. Also, it was seen that the deposition rate curves were much flatter for propane infiltration, i.e., the ratio of the highest deposition rate to the lowest deposition rate for a given sample was much lower. For example, the value of the ratio for experiment "TCQ" was ~ 1.5 with propane versus ~ 9 for propylene. This can be attributed to the lower temperature gradient, in the case of the propane runs, resulting in more uniform densification. In conclusion, it can be seen that there is less spatial variation in deposition rates for propane.

3.6 Deposition Efficiency

Deposition efficiency describes the amount of carbon in the reagent that is used for deposition within the preform. The deposition efficiency with propane varied between 3-14%. The deposition efficiency for PA-9 was high because the infiltration run was terminated before

the full densification of the composite. It has been shown by Vaidyaraman for carbon [14] and Roman et al. [15] for SiC, that the deposition efficiency decreases during the course of infiltration of cloth preforms. The deposition efficiency with propane was slightly lower than with propylene. It was found that the deposition efficiency when using propane was positively affected by temperature and negatively by total flow rate. The resulting relationship is given by Equation (3).

$$\begin{aligned} \text{Deposition Efficiency} &= 8.1 + 2.91 T_{\text{cod}} - 1.95 Q_{\text{cod}} \\ S_{\text{regression}} &= 0.95, \quad R_p^2 = 91.5\%, \quad R_a^2 = 89.3\% \end{aligned} \quad (3)$$

3.7 Kinetic Analysis

The deposition rate data near the hot and the cold sides of each composite, obtained by measuring the coating thicknesses in the macropores, were used to obtain a first order kinetic rate constant. The carbon deposition process is typically first order with respect to the concentration of the hydrocarbon reagent [16]. The various steps involved in determining the rate constant were previously explained [10]. The natural logarithm of " k_s " values, obtained from different deposition rate data, were plotted against reciprocal absolute temperature (Figure 5). The data points were linearly regressed to obtain the following equation.

$$\ln k_s = 2.2 - \frac{23610}{RT} \quad (4)$$

Where,

k_s = rate constant based on unit surface, cm/s

R = ideal gas law constant, cal/mol K

T = temperature, K

The regression fit was satisfactory and the activation energy calculated from Equation (4) was 23.6 ± 5.6 Kcal/mol, where the uncertainty represents the 95% confidence interval. This activation energy is much lower than the 48-60 Kcal/mol [16,17] reported in the literature. The discrepancy can be attributed to one or all of the following: (1) use of average deposition rate to calculate k_d , (2) the use of deposition efficiency to estimate concentration of the reagent near the hot side, and (3) a temperature range in the present study of only $\sim 250^\circ\text{C}$.

4. CONCLUSIONS

The following conclusions were drawn from the present work on FCVI processing of carbon/carbon using propane as the reagent.

- (1) The infiltration time was affected only by the temperature of the bottom of the preform and the concentration of the reagent. The flow rate did not affect infiltration time. The rate of weight gain was affected by the temperature of the bottom of the preform, concentration, and interaction between these two variables.
- (2) Minimum infiltration time, 7 h, was achieved when the higher process set points were used for temperature, concentration, and flow rate. The infiltration time was longer when using propane, instead of propylene, as the reagent. This was the result of inherently slower carbon deposition from propane and a lower temperature gradient in the preform used for the propane infiltrations, i.e., lower average temperatures.
- (3) The final bulk density of the composite was independent of the processing conditions reflecting that back pressure is a reliable indicator of the extent of infiltration.

- (4) The experiment "TC" resulted in preferential infiltration of the cold side of the preform due to the high residence time of the reagent.
- (5) Density variations within a composite averaged $\pm 0.08 \text{ g/cm}^3$.
- (6) There was less axial variation in density for propane-derived material than observed in an earlier propylene study. Accordingly, deposition rates within macropores did not correlate in a consistent manner with position within a given composite. The enhanced uniformity and lower spatial correlation were caused by the smaller axial temperature gradient across the propane-derived composites.
- (7) The deposition rate data were adequately described by an Arrhenius equation, $\ln k_p = 2.2-23610/RT$, yielding an apparent activation energy of 23.6 kcal/mol.

Acknowledgements

This work was supported by the Air Force Office of Scientific Research. The guidance of Dr. Alexander Pechenik throughout the course of this work is appreciated. We thank Dr. Lisa Detter-Hoskin for help with scanning electron microscopy. Typing and editing of the original manuscript by Ms. Virginia Myers and Joey Goddard are gratefully acknowledged.

REFERENCES

- [1] W. V. Kolensky, in *Chem. Phys. Carbon*, edited by P. L. Walker, Jr., and P. A. Thrower, **9**, 173 (1972).
- [2] E. Fitzer, *Carbon*, **25**, 163 (1987).
- [3] W. J. Lackey and T. L. Starr, in *Fiber Reinforced Ceramic Composites*, edited by K. S. Mazdidasni, Noyes Publication, NJ, 397 (1991).
- [4] G. Savage, *Carbon-Carbon Composites*, Chapman & Hall, NY, 1993.
- [5] C. R. Thomas, ed., *Essentials of Carbon-Carbon Composites*, Royal Society of Chemistry, London, 1993.
- [6] J. D. Buckley and D. D. Edie, eds., *Carbon-Carbon Materials and Composites*, Noyes Publications, Park Ridge, NJ (1993).
- [7] M. A. Wright and K. R. Palmer, eds., *Research into structural carbons*, Southern Illinois University at Carbondale, 1994.
- [8] S. Vaidyaraman, W. J. Lackey, G. B. Freeman, P. K. Agrawal and M. D. Langman, *J. Mat. Res.*, **10**, 1469 (1995).
- [9] S. Vaidyaraman, W. J. Lackey, G. B. Freeman and P. K. Agrawal, *Carbon*, (1995).
- [10] S. Vaidyaraman, W. J. Lackey, P. K. Agrawal and M. A. Miller, submitted to *Carbon* (1995).
- [11] W. J. Lackey and A. J. Caputo, U.S. Patent 4,580,523, 1986.
- [12] A. J. Caputo and W. J. Lackey, *Ceram. Eng. Sci. Proc.*, **5** (7-8), 654 (1984).
- [13] A. J. Caputo, W. J. Lackey, and D. P. Stinton, *Ceram. Eng. Sci. Proc.*, **6** (7-8), 694 (1985)

- [14] S. Vaidyaraman, Ph.D. Thesis, Georgia Institute of Technology, Atlanta, GA 30332 (1995).
- [15] Y. Roman, D. P. Stinton and T. M. Besmann, *J. de Physique IV*, Colloque, 1, 689 (1991).
- [16] P. A. Tesner, in *Chem. Phys. Carbon*, edited by P. A. Thrower, 19, 65 (1983).
- [17] J. Y. Lee, J. H. Je, W. S. Ryu and H. S. Kim, *Carbon*, 21, 523 (1983).

LIST OF TABLES

- Table 1:** List of independent variables for infiltration with propane.
- Table 2:** Operating conditions of the FCVI runs with propane.
- Table 3:** Properties of the infiltrated composites.
- Table 4:** Bulk density (g/cm^3) of slices from composites fabricated using propane.

LIST OF FIGURES

- Figure 1: Bulk density as a function of axial and radial position within composite disk.
- Figure 2: Deposition rates for experiments at high temperature (a) near the center of the composite disk, (b) between the center and circumference of the composite disk, (c) near the circumference of the composite disk.
- Figure 3: Deposition rates for experiments at low temperature (a) near the center of the composite disk, (b) between the center and circumference of the composite disk, (c) near the circumference of the composite disk.
- Figure 4: Deposition rates for midpoint experiments (a) near the center of the composite disk, (b) between the center and circumference of the composite disk, (c) near the circumference of the composite disk.
- Figure 5: Arrhenius plot for deposition of carbon in the preforms.

Table 1. List of independent variables for infiltration with propane

Variable	Name	Low Value	Mid Value	High Value	Coded Variables
T	Preform Bottom Temp (°C)	900	950	1000	$(T-950) \div 50$
C	Concentration (%)	25	37.5	50	$(C-37.5) \div 12.5$
Q	Total Flow Rate (cm³/min)	200	300	400	$(Q-300) \div 100$

Table 2. Operating conditions of the FCVI runs with propane

Run Number	Experiment	Actual Values			Coded Values		
		T (°C)	C (%)	Q (cm ³ /min)	T _{cod}	C _{cod}	Q _{cod}
PA-2	(1)	903	25	200	-0.940	-1	-1
PA-12	(1)	903	25	200	-0.940	-1	-1
PA-4	T	1008	25	200	1.153	-1	-1
PA-14	C	901	50	200	-0.984	1	-1
PA-9	TC	1001	50	200	1.011	1	-1
PA-10	Q	905	25	400	-0.892	-1	1
PA-13	TQ	1001	25	400	1.011	-1	1
PA-7	CQ	895	50	400	-1.107	1	1
PA-5	TCQ	992	50	400	0.839	1	1
PA-6	TCQ	992	50	400	0.846	1	1
PA-3	Mid	952	37.5	300	0.032	0	0
PA-11	Mid	931	37.5	300	-0.376	0	0

Table 3. Properties of the infiltrated composites

Run Number	Initial Porosity (v/o)	Infiltration Time (h)	Rate of Weight Gain (g/h)	Total Porosity (%)	Open Porosity (%)	Density (g/cm ³)	Deposition Efficiency (%)
PA-2	47.2	28.3	0.3548	11.7	—	1.609	7.36
PA-12	48.9	34.0	0.3340	10.6	6.1	1.632	6.93
PA-4	49.7	19.0	0.6779	6.8	3.4	1.705	14.06
PA-14	47.9	19.0	0.5817	9.9	5.7	1.645	6.03
PA-9	49.8	2.9	2.5869	—	—	—	26.08
PA-10	49.1	34.0	0.3380	10.0	3.5	1.643	3.50
PA-13	48.1	17.0	0.7073	6.8	6.0	1.704	7.33
PA-7	48.6	18.5	0.6341	8.7	5.2	1.668	3.29
PA-5	49.5	7.0	1.7017	9.2	—	1.659	8.82
PA-6	49.4	7.0	1.7323	8.3	4.6	1.676	8.98
PA-3	48.8	12.5	0.9086	10.0	6.4	1.644	8.26
PA-11	48.9	12.5	0.8961	10.7	5.6	1.631	8.38

Table 4. Bulk density (g/cm³) of slices from composites fabricated using propane

Run Number	Experiment	Hot Side		Middle		Cold Side	
		Inside	Outside	Inside	Outside	Inside	Outside
PA-12	(I)	1.632	1.600	1.647	1.667	1.537	1.514
PA-4	T	1.616	1.584	1.683	1.629	1.604	1.557
PA-14	C	1.672	1.66	1.725	1.703	1.587	1.526
PA-10	Q	1.633	1.620	1.69	1.659	1.586	1.573
PA-13	TQ	1.663	1.676	1.671	1.701	1.592	1.541
PA-7	CQ	1.602	1.613	1.664	1.598	1.501	1.434
PA-6	TCQ	1.664	1.598	1.684	1.688	1.555	1.625
PA-3	Mld	1.578	1.593	1.647	1.631	1.533	-
PA-11	Mid	1.634	1.592	1.682	1.681	1.603	1.626

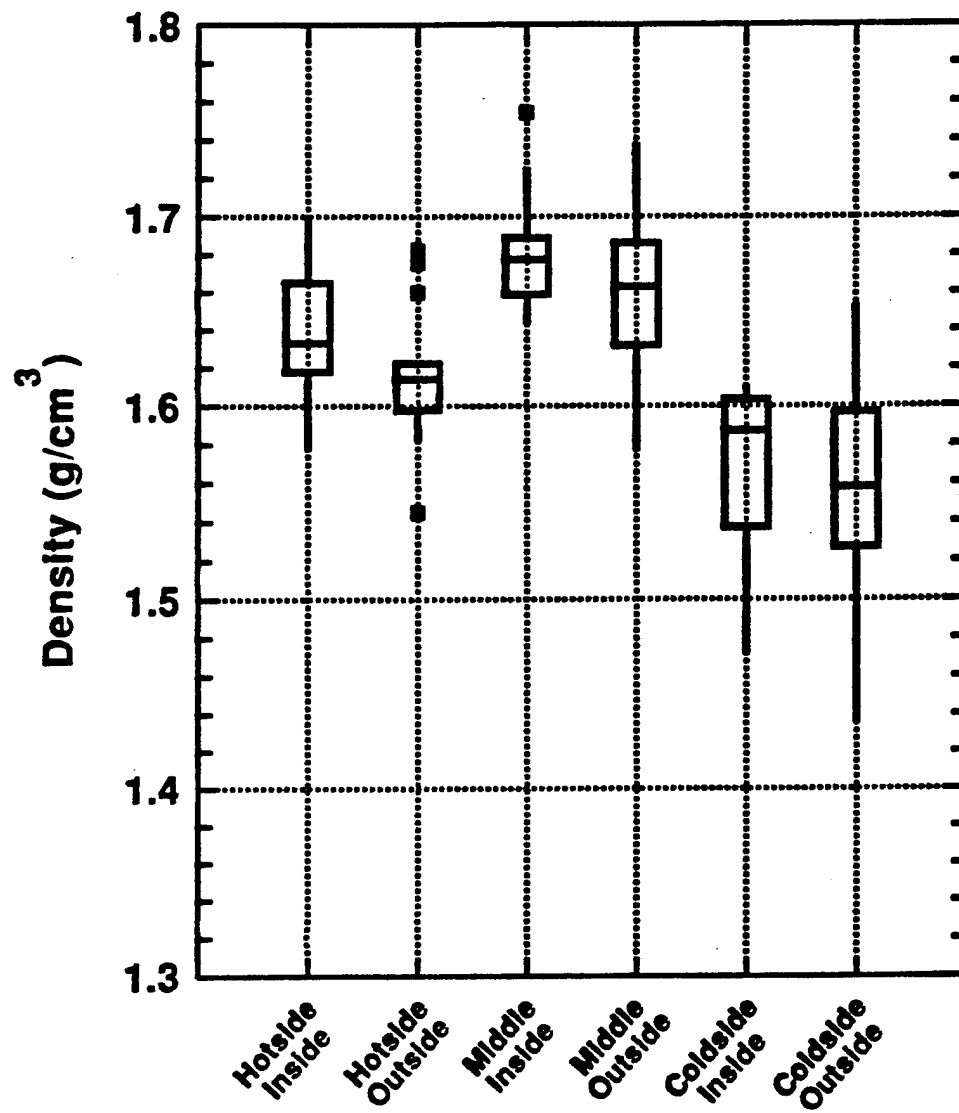


Figure 1: Bulk density as a function of axial and radial position within the composite disk.

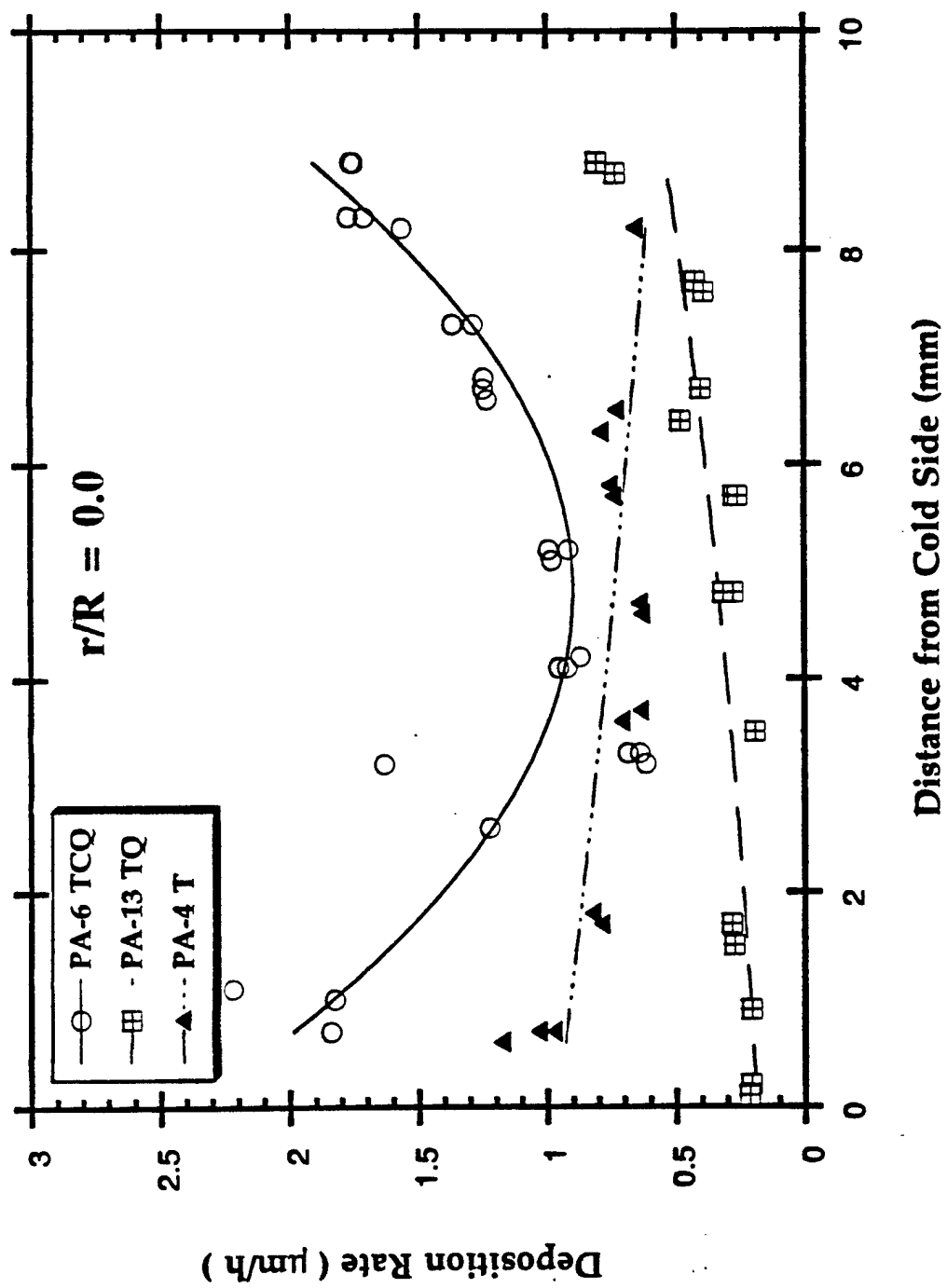


Figure 2: Deposition rates for experiments at high temperature (a) near the center of the composite disk.

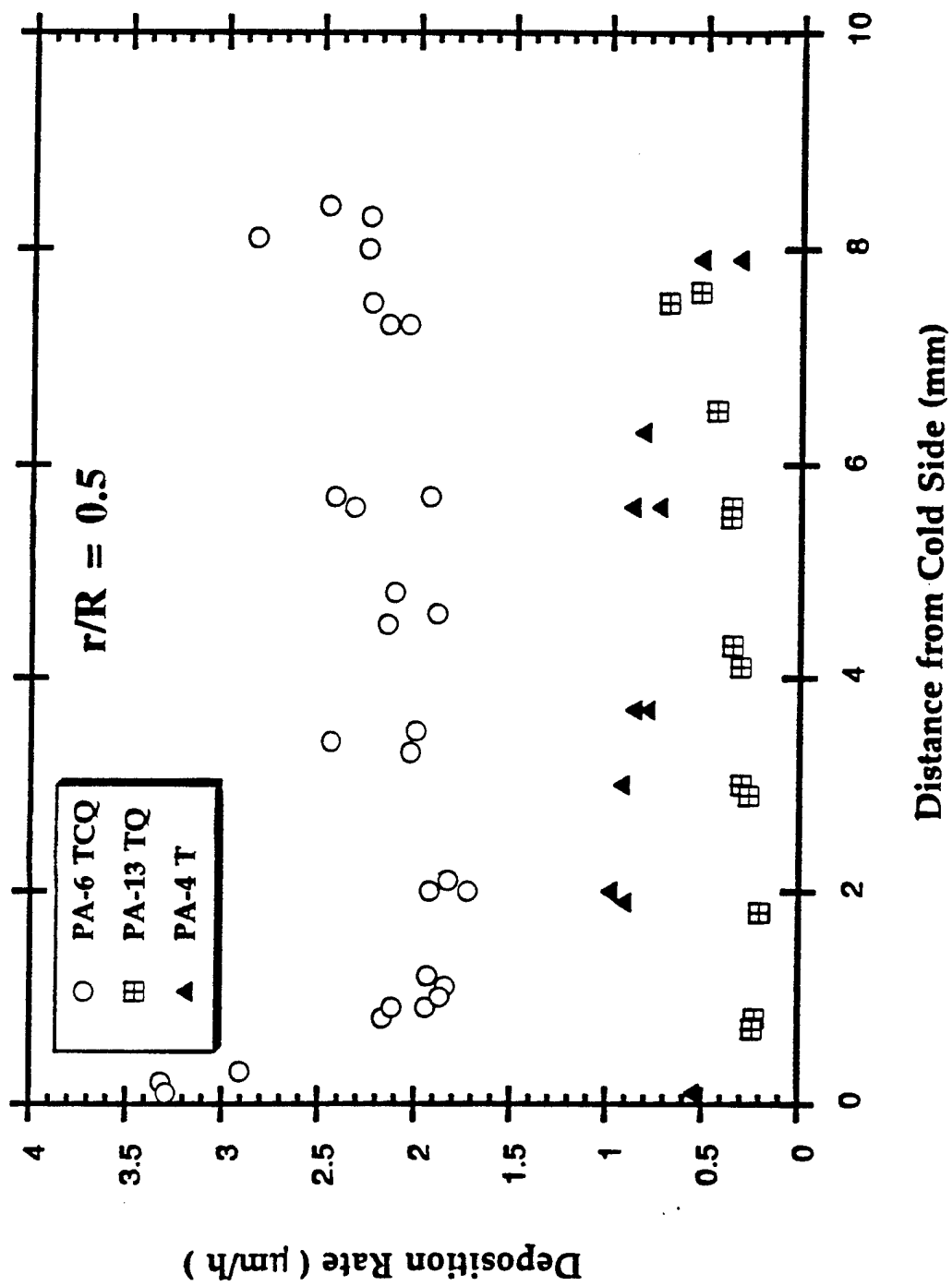


Figure 2: (b) between the center and circumference of the composite disk.

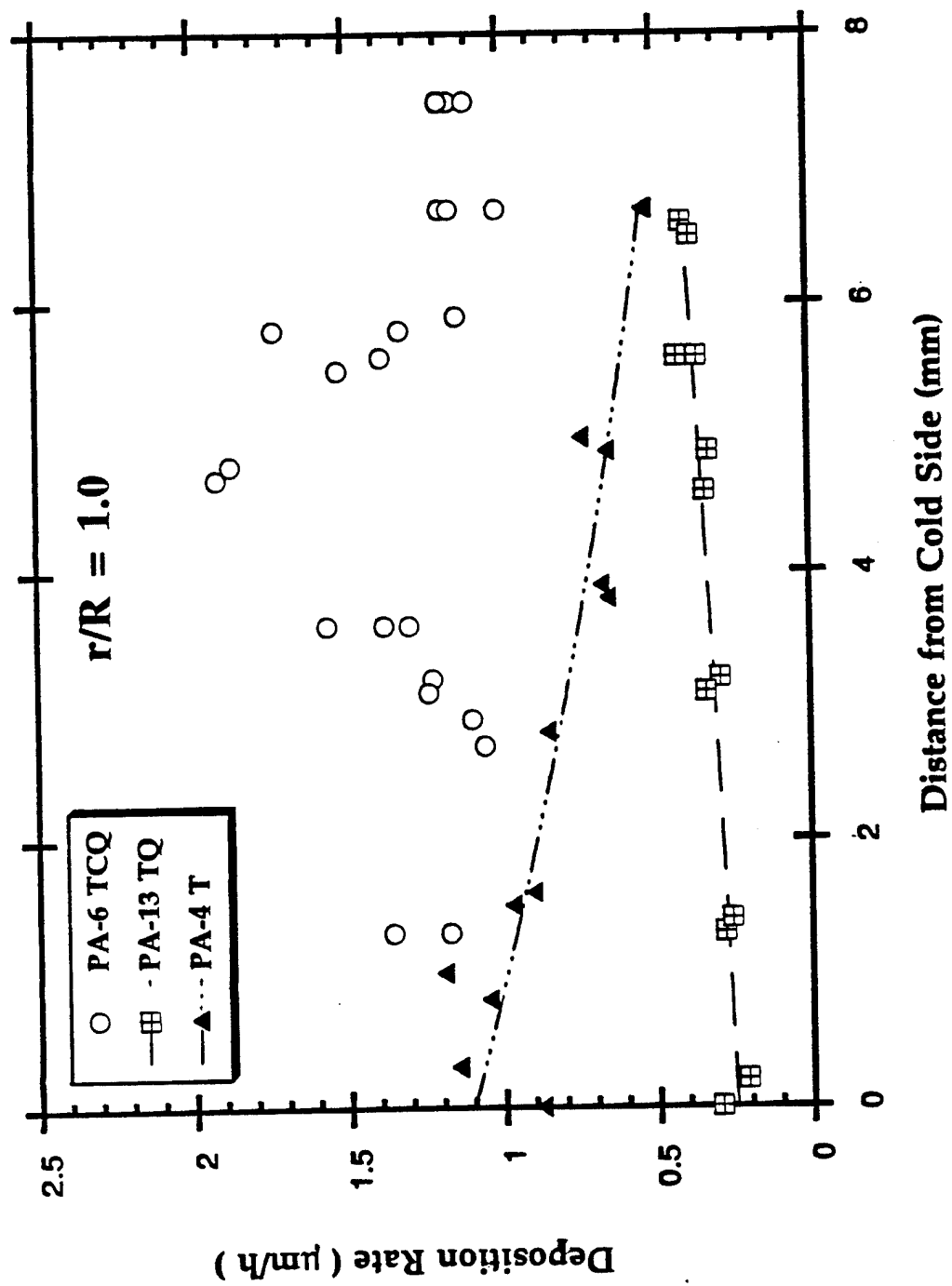


Figure 2: (c) near the circumference of the composite disk.

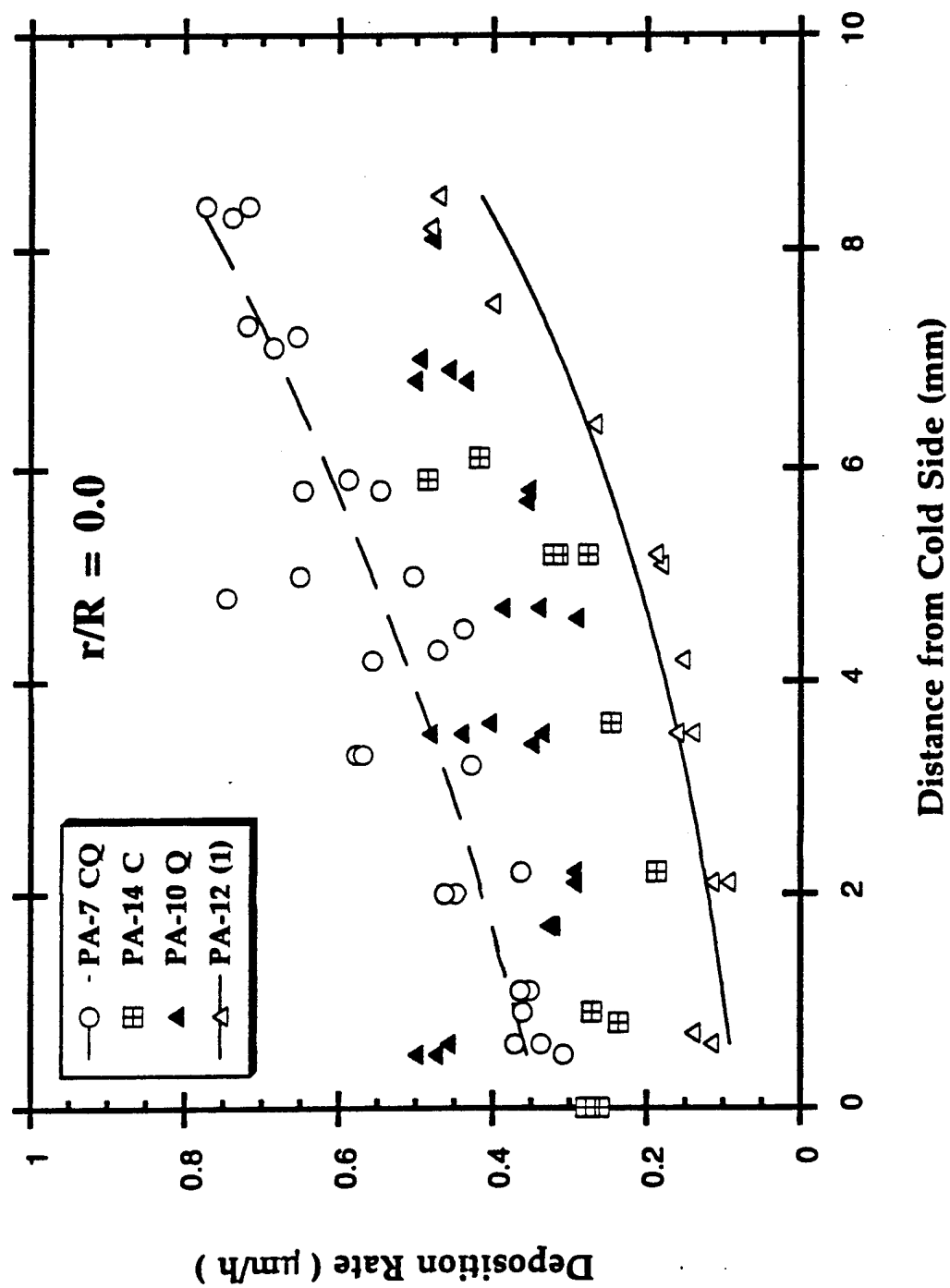


Figure 3: Deposition rates for experiments at low temperature (a) near the center of the composite disk.

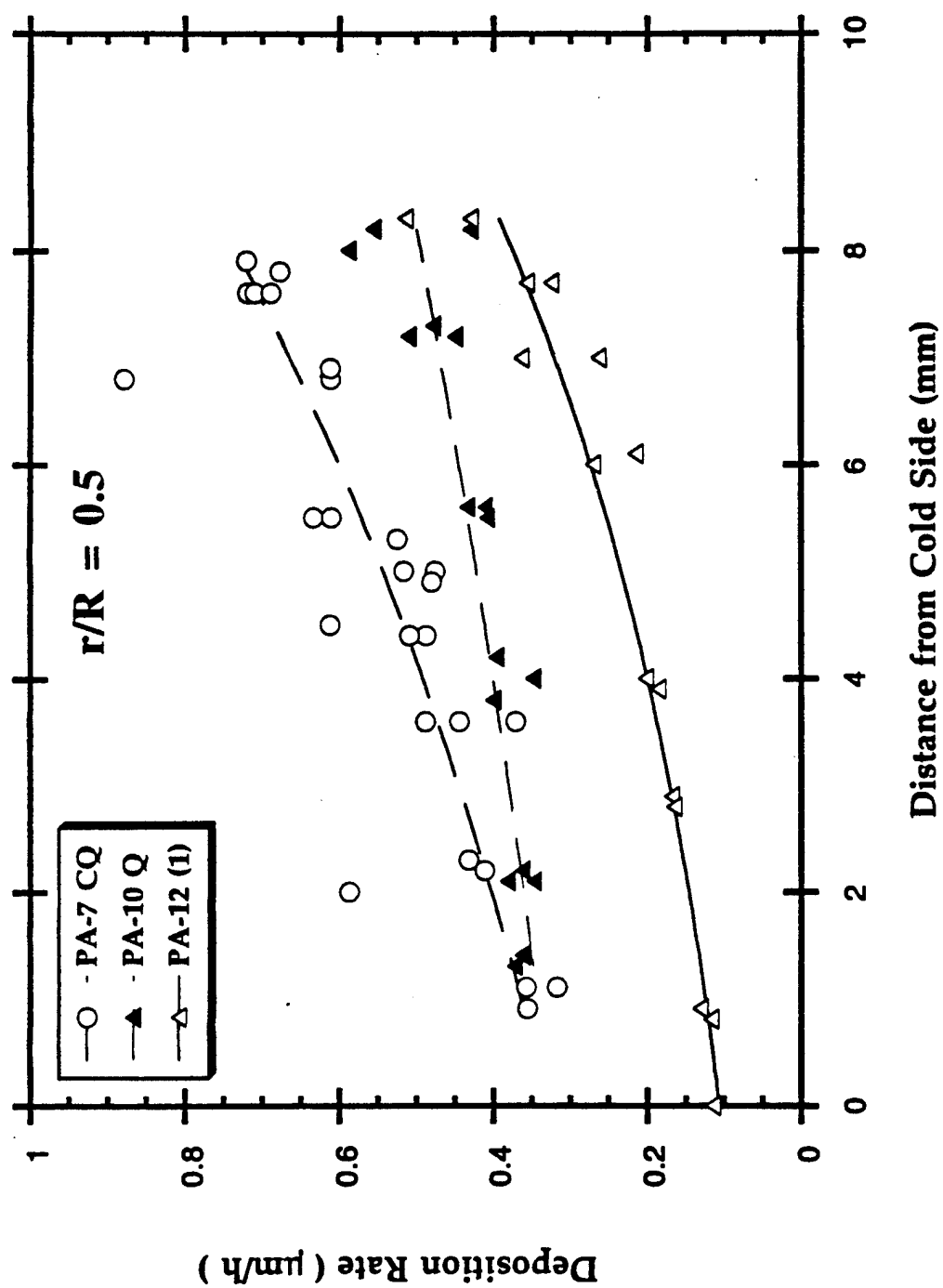


Figure 3: (b) between the center and circumference of the composite disk.

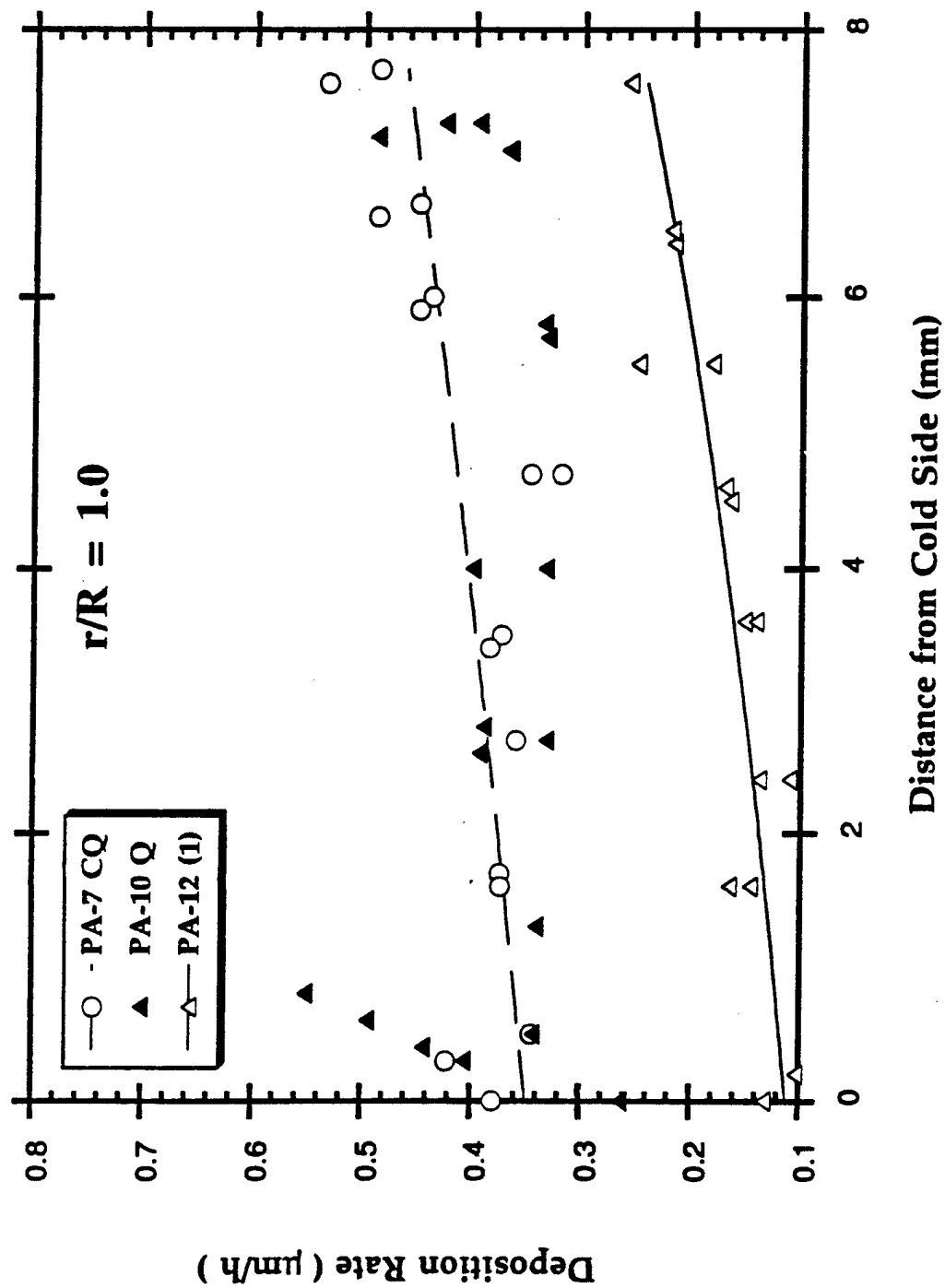


Figure 3: (c) near the circumference of the composite disk.

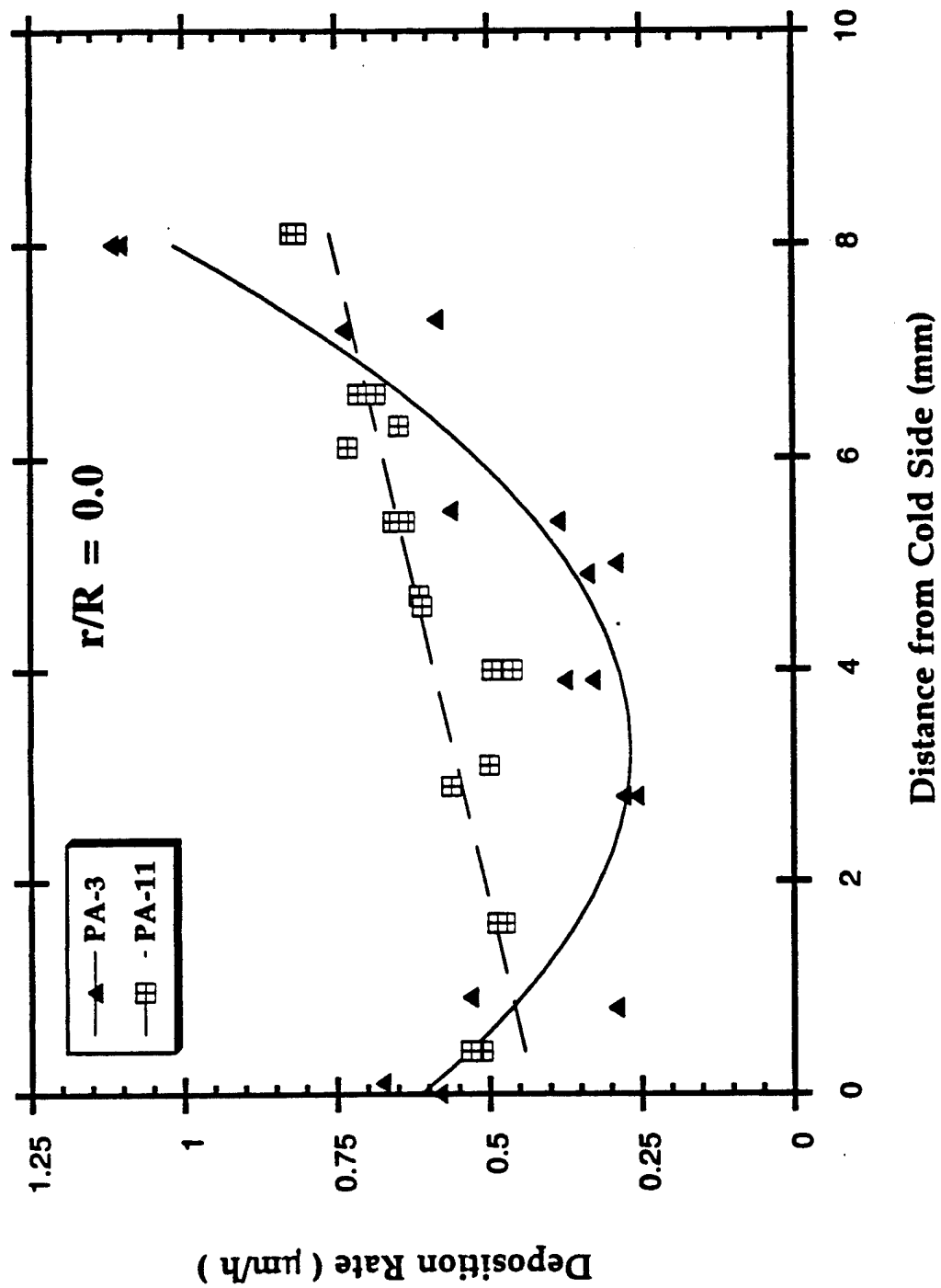


Figure 4: Deposition rates for midpoint experiments (a) near the center of the composite disk.

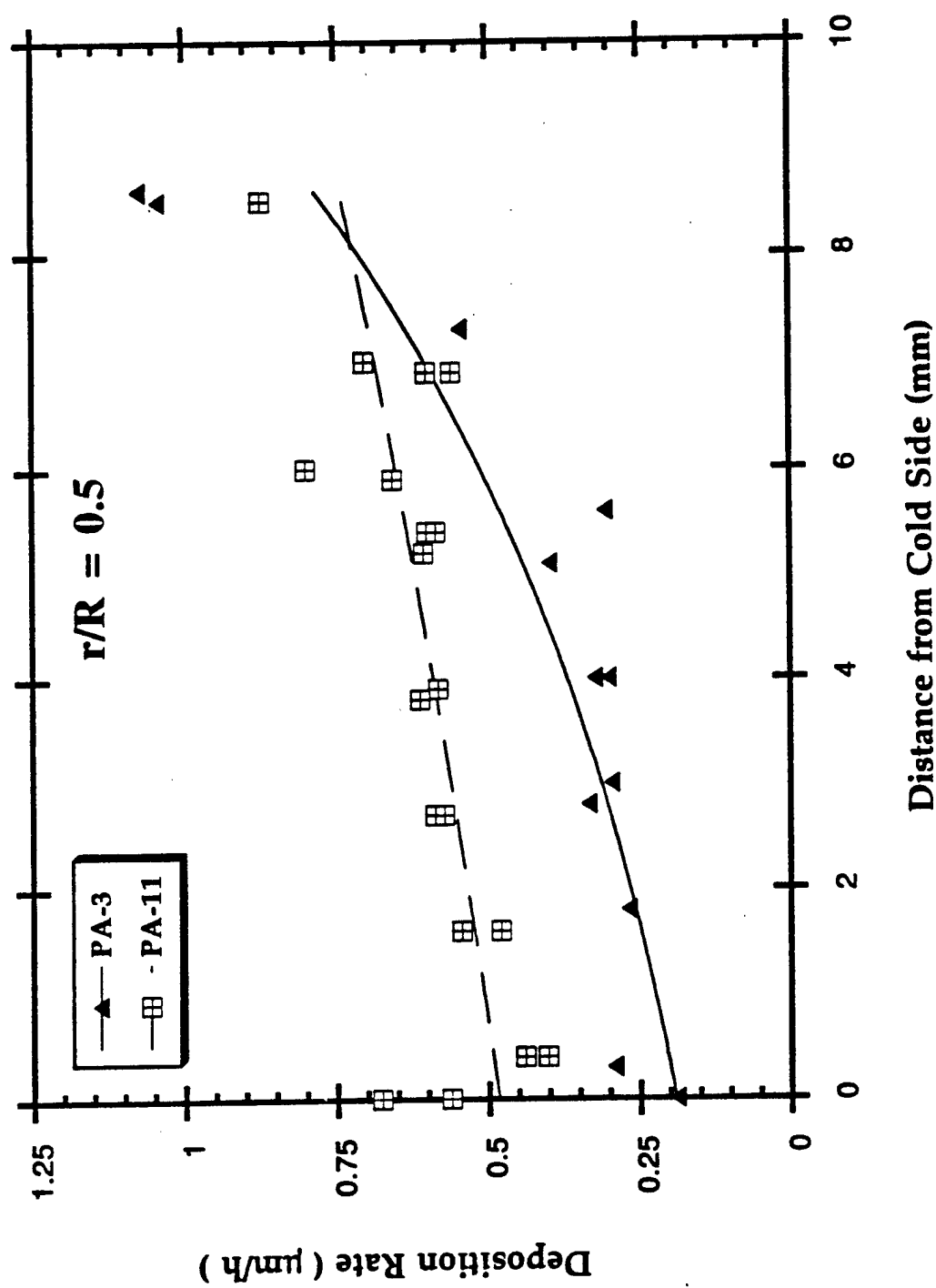


Figure 4: (b) between the center and circumference of the composite disk.

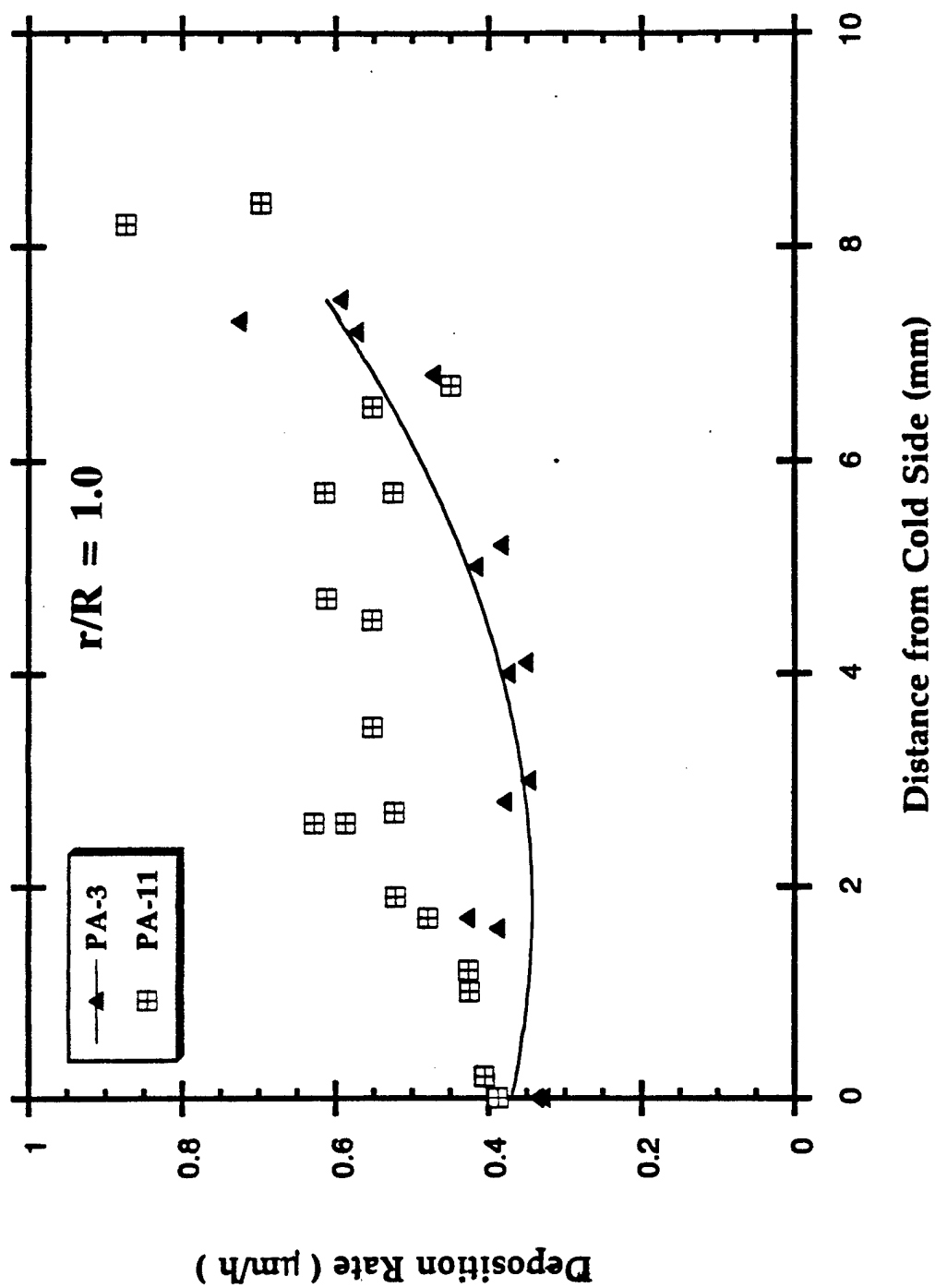


Figure 4: (c) near the circumference of the composite disk.

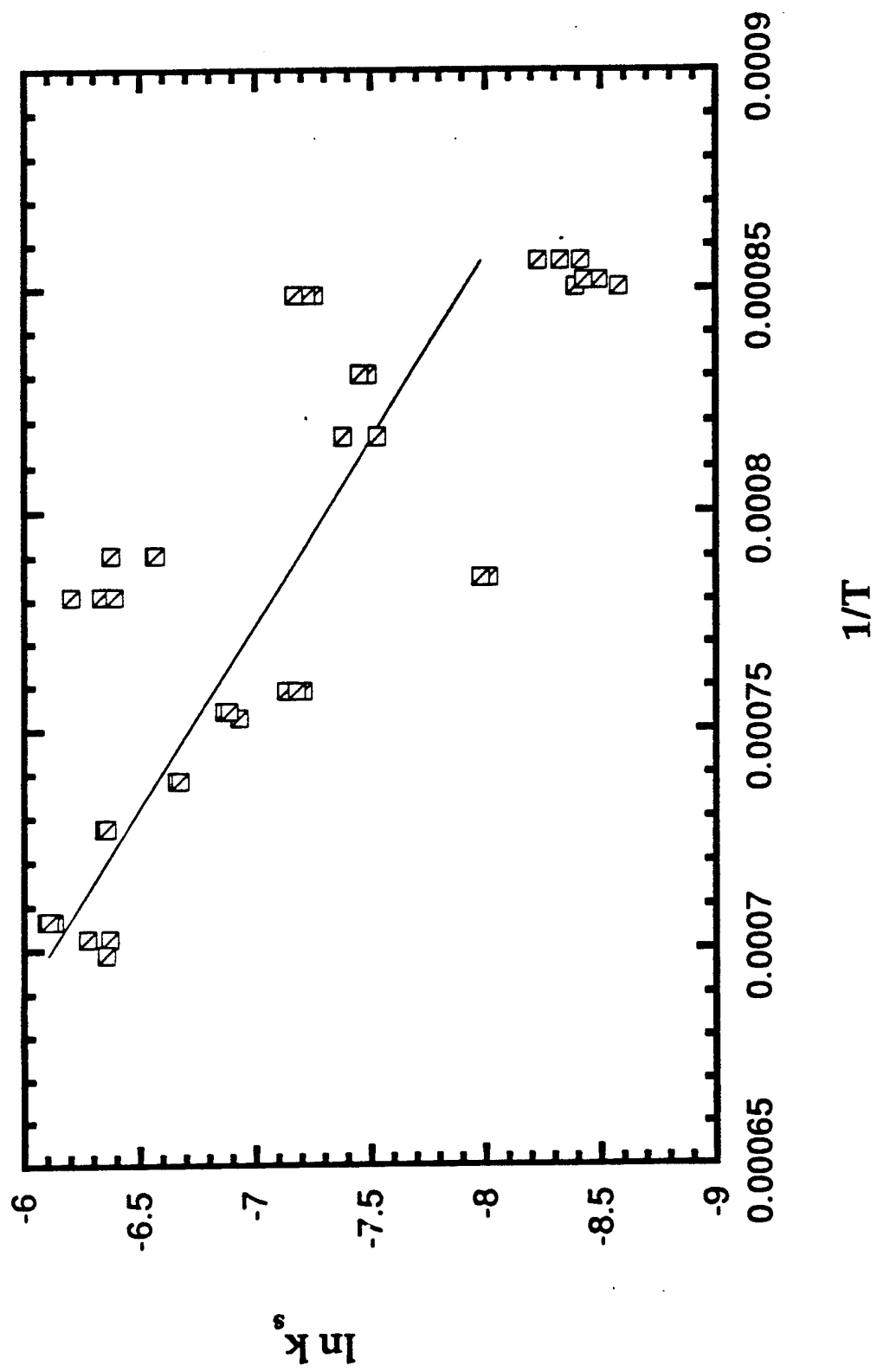


Figure 5: Arrhenius plot for deposition of carbon in the preforms.

Technique for Monitoring Densification during Chemical Vapor Infiltration

W. Jack Lackey,* Sundar Vaidyaraman, Garth B. Freeman, and Pradeep K. Agrawal

Georgia Institute of Technology, Atlanta, Georgia 30332

A new technique for studying the progression of densification during the fabrication of composites by chemical vapor infiltration is presented. The preparation of a carbon-matrix composite was investigated by momentarily interrupting, at various times, the carbon infiltration process to permit deposition of very thin layers of SiC. Microscopic examination of these layers on a polished cross section permitted determination of the extent of infiltration at various locations within the preform as a function of infiltration time. The technique also distinguishes open from closed pores and provides information on the existence of temperature gradients within the preform.

I. Introduction

CHEMICAL VAPOR INFILTRATION (CVI) is increasingly being used to fabricate fiber-reinforced ceramic- and carbon-matrix composites. In this process, a solid is chemically vapor deposited onto a fibrous preform to form the matrix of the composite. Advantages of this process include the use of low pressures and temperatures, avoiding damage to the fibers. Also, this process can be used to deposit a variety of matrix materials like carbides, nitrides, borides, silicides, etc.

There are six different types of CVI processes based on a classification system that considers whether the reagent is transported through the preform by sustained forced flow, pressure pulsing, or diffusion and whether a temperature gradient exists within the preform.¹ In each of these processes it is generally of interest to achieve high density uniformly throughout the preform with minimum processing time. As the infiltration process proceeds, some regions of the preform eventually become isolated from the gaseous reagent since deposition of the matrix closes gas flow or diffusion paths.

For research aimed at achieving high density, uniformity, and/or minimum processing time it is of interest to determine the rate of densification and the changes that occur in gas transport patterns within the preform as a result of pore closure. The influence of process variables such as preform architecture, temperature, temperature gradient, pressure, and gas flow rate and concentration on the infiltration process are also of interest. Sample characterization may involve density and porosity measurements, microscopic examination of polished cross sections, X-radiography, and X-ray computed tomography. At present, the most popular methods for studying the infiltration process are to carry the process to completion for various processing conditions and to infer, based on characterization results, how densification progressed with time or to examine samples infiltrated for different times. These methods of study are laborious. Hence, it is of interest to develop a more efficient methodology.

A new technique for studying CVI processing that utilizes markers is presented in this paper. It yields more detailed information with less effort. In addition, as described later, the new technique also provides information about temperature gradients within the preform and can identify which pores were open and which were closed off from the reagent supply at various times during the infiltration process.

II. Experimental Procedure

The forced flow-thermal gradient CVI process was used to fabricate a carbon fiber-carbon matrix composite in the shape of a right circular disk.^{1,2} In this process a pressure gradient forces the reagent stream to flow through a preform subjected to a temperature gradient. A carbon matrix was deposited within a 0.8-cm-thick 2-D carbon cloth preform using a flowing mixture of 50% propylene-50% hydrogen in a resistively heated, hot wall furnace. The total flow rate was 200 cm³/min. The temperatures on the hot and cold faces of the preform were 1220° and 870°C. A total infiltration time of 9.5 h was used. Additional details of the process and equipment are described elsewhere.²

During the carbon infiltration process, the flow of propylene was interrupted after 2, 4, 6, and 8 h to permit the deposition of a thin layer of SiC. Each SiC layer was obtained by flowing a 9% methyltrichlorosilane-91% H₂ mixture for 4 min. The total flow rate was 550 cm³/min. Microscopic examination of a single polished cross section of the composite revealed the location of each SiC marker layer and thus permitted determination of the exact location of the carbon deposition "front" after 2, 4, 6, and 8 h. For a second sample the carbon matrix was deposited using propane rather than propylene and the processing conditions were such that the densification proceeded more slowly than for the propylene run. The total run time was 14 h. Layers of SiC deposited, in this case, from a 20% methyltrichlorosilane-80% H₂ mixture were similarly used to permit monitoring of the progress of the carbon-matrix deposition after 2.5, 5, 7.5, and 10 h.

III. Results and Discussion

Scanning electron micrographs representative of several locations near the center line of the composite disk infiltrated using propylene are shown in Fig. 1. Two types of pores, i.e., micro- and macropores, are observed in the micrographs. In a cloth preform, micropores are typically located within the fiber tow and macropores are found between tows and between layers of cloth. The SiC markers are clearly visible in all of the micrographs. It can also be seen that the thickness of the SiC layers increases as the distance from the cold side of the composite increases.

In all of the micrographs for the propylene sample, no SiC layer is seen inside the fiber tow. This implies that infiltration of the tows was completed within the first 2 h of the process as was certainly the case when four layers of SiC were seen surrounding the tow as shown in Fig. 1(c). In other words, the gas passages within the tows were apparently blocked early and transport of the reagent stream was restricted to macropores. When propane was used as the reagent, SiC layers were

R. Naslain—contributing editor

Manuscript No. 193153. Received October 6, 1994; approved December 12, 1994.
Supported by Dr. Alexander Pechenik of the Air Force Office of Scientific Research.
*Member, American Ceramic Society.

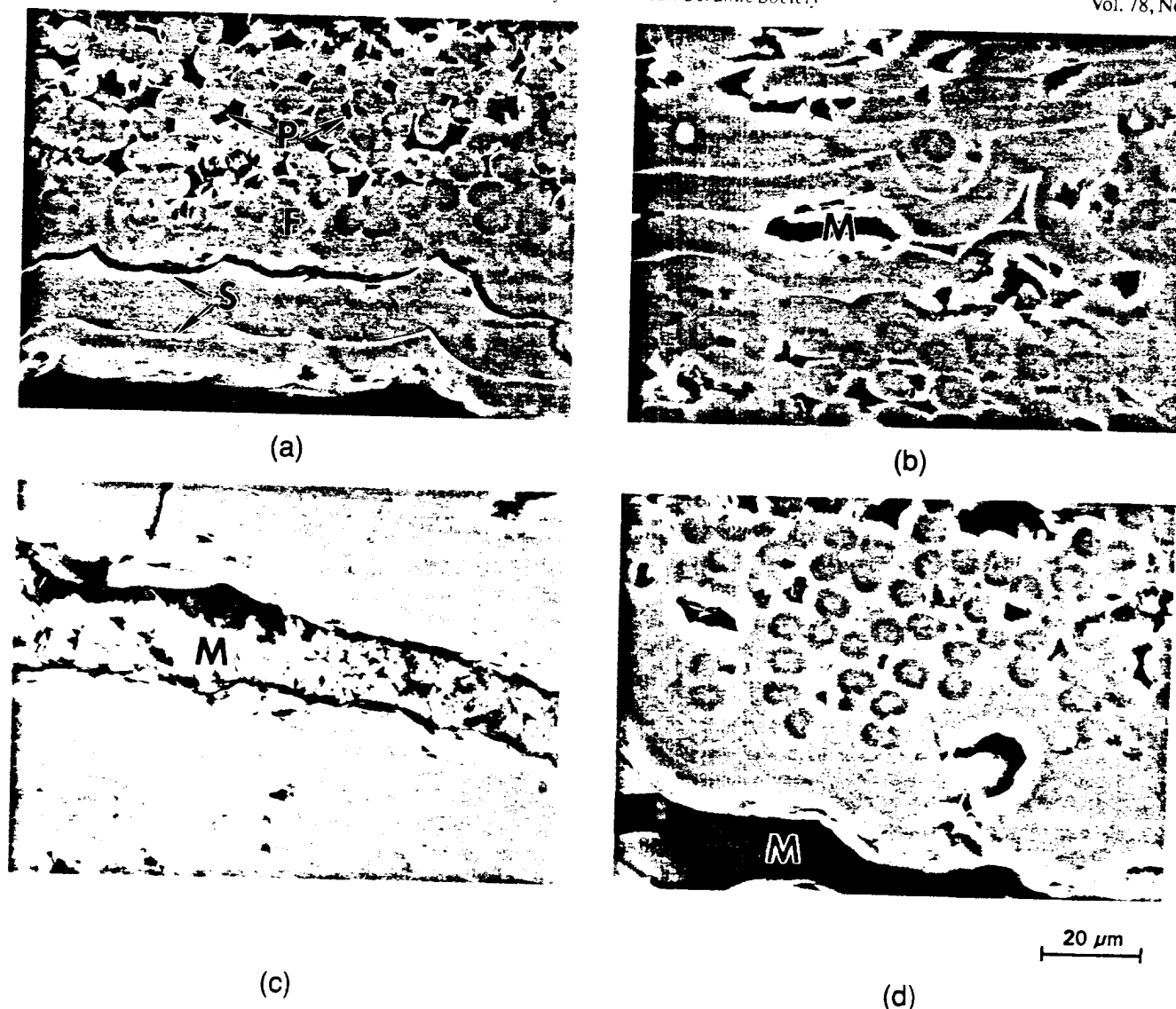


Fig. 1. Scanning electron micrographs of the propylene sample at the indicated distance from the cold side of the preform: (a) 7.9, (b) 6.8, (c) 5.0 and (d) 3.6 mm. Microstructural features are identified as follows: (F) fiber, (S) SiC marker layer, (M) macropore, and (P) micropore.

observed inside the tow as shown in Fig. 2. Thus, the infiltration proceeded more slowly for the propane run. This can be attributed to the lower reactivity of propane compared to propylene.

The location of the SiC layers in the micrographs allows one to measure the thickness of carbon deposited during different

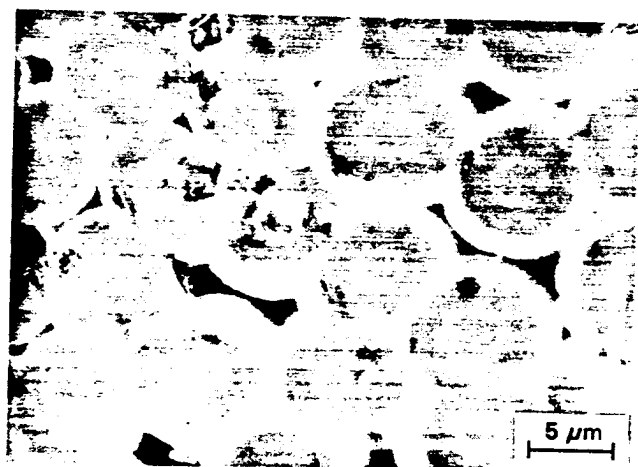


Fig. 2. SiC layers within the tow show that infiltration continued about 5 h for the sample infiltrated with propane.

time intervals. For example, the location of SiC layers in Fig. 1(c) shows that the thickness of the carbon deposited on the surface of this macropore was 5, 9.8, 14.5, 20, and 25 μm after 2, 4, 6, 8, and 9.5 h, respectively. The marker also helps one in knowing when a pore was blocked and became inaccessible to the reagent flow. For example, consider Figs. 1(a) and (b); in both cases the pores got closed after 4 h of infiltration; there are only two SiC layers. In the case of Figs. 1(c) and (d) four SiC layers are observed, which implies that both of these pores were open and accessible to the flowing reagent even after 8 h of infiltration.

From the micrographs just presented, and similar ones, it was possible to measure coating thickness as a function of the distance from the cold side of the preform. Graphical representation of these results (Fig. 3) reveals several features about the FCVI infiltration process. First, the lines have a positive slope. That is, the rate of deposition increased with increasing distance from the cold side of the preform. Also, the rate of matrix deposition, for a given location, did not vary appreciably with time as shown by the essentially equal spacing between the lines in Fig. 3. The two points in this figure labeled A and B depart from this general trend because the deposition ceased because of pore blockage.

Near the center line of the disk the average deposition rate was 4–6 $\mu\text{m}/\text{h}$ in the hot region (Figs. 1(a) and (b)) and reduced to 2–3 $\mu\text{m}/\text{h}$ (Figs. 1(c) and (d)) for the cold region. In a given

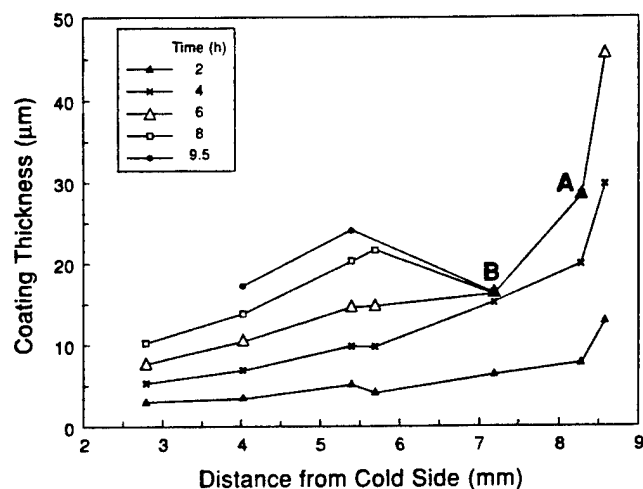


Fig. 3. Carbon coating thickness in macropores for five different infiltration times as a function of distance from the cooler side of the preform.

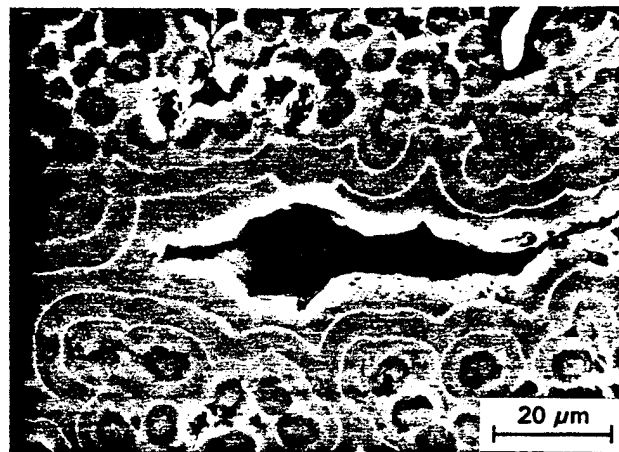
cloth layer, the deposition rate was highest at the center and lowest near the circumference of the disk. The deposition rate was 2–3 μm/h at the circumference in the hot region (Fig. 4(a)) compared to 4 μm/h in the center of the hot region. These differences in deposition rates are attributed to axial and radial temperature variations in the preform. At an intermediate position (6.2 mm from the cold side and 13.5 mm from the center line of the composite) the deposition rate was practically constant with time and averaged about 2.5 μm/h as shown in Fig. 4(b). This deposition rate is comparable to that measured in Fig. 1(c). This is reasonable since the former location was closer to the hot side of the preform but also closer to its cooler circumference.

The SiC layers were not detected in the bottom, cooler portion of the sample prepared with propylene, but were observed for the sample prepared with propane. While no appreciable effort was made to establish a minimum thickness of SiC which could be seen with our microscope (Hitachi S4100-feg, Tokyo, Japan) in the backscattered mode, layers less than 0.1 μm in thickness became difficult to image because of failing contrast. It is speculated that the temperature was too low for SiC deposition in the cooler region in the case of the propylene run. The temperature of the bottom cloth was 850°C in the case of the propylene run compared to 940°C for the propane run. The temperature of the bottom cloth in the former might have been too low for SiC deposition from methyltrichlorosilane. The variation of carbon and SiC deposition rates with position within the preform provides a qualitative measure of the temperature variations within the preform.

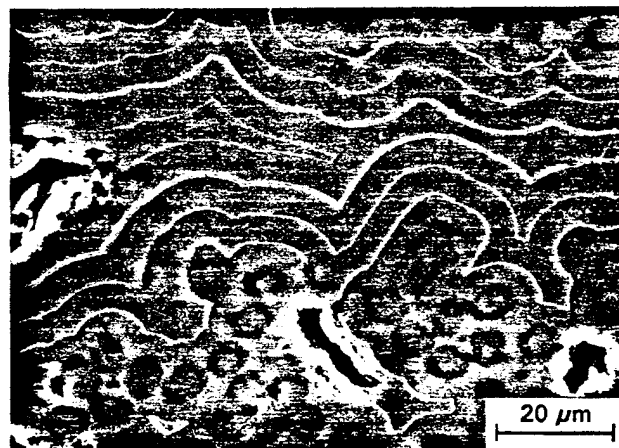
The selection of time intervals between marker layers is an important parameter which will determine which portions of the infiltration process are to be monitored. These preliminary results suggest that a logarithmic time interval would perhaps be most useful for this particular system rather than equitemporal intervals. The technique described here also appears to be a sensitive method for learning of the CVI characteristics of the "marker" material, in this case SiC. By observing where SiC occurs in this sample and the thickness of the SiC layers it is possible to deduce information about the FCVI process for SiC.

IV. Conclusions

The simple technique of using marker layers will be useful for studying isothermal, pulse, and forced flow CVI processes. It should be applicable to a number of material systems.



(a)



(b)

Fig. 4. Micrographs from propylene run: (a) near circumference; (b) approximately midway between center line and circumference.

However, any interaction between the matrix and the marker material should be minimal for the success of this technique. In the case of carbon and SiC they are immiscible. The fact that the same amount of carbon deposition occurred in the propylene sample described here as for one prepared under identical conditions except that the SiC layers were omitted shows that the carbon deposition process was not altered by the use of the SiC marker layers. If the nucleation or growth kinetics of CVD carbon on a SiC substrate were vastly different than for a carbon substrate, then the results obtained might not have been totally representative of the carbon CVI process. For the carbon–SiC system, the results appear to be valid.

Acknowledgment: We appreciate the typing of the original manuscript by Ms. Virginia Myers.

References

- W. J. Lackey and T. L. Starr, "Fabrication of Fiber-Reinforced Ceramic Composites by Chemical Vapor Infiltration: Processing, Structure and Properties", pp. 397–450 in *Fiber Reinforced Ceramics*, Edited by K. S. Mazdian, Noyes Publications, Park Ridge, NJ, 1990.
- S. Vaidyaraman, W. J. Lackey, G. B. Freeman, P. K. Agrawal, and M. D. Langman, "Fabrication of Carbon–Carbon by Forced Flow–Thermal Gradient Chemical Vapor Infiltration," *J. Mater. Res.*, in press.

LAMINATED MATRIX COMPOSITES

- A NEW CLASS OF MATERIALS

W. Jack Lackey^{†*}, Sundar Vaidyaraman[‡], and Karren L. More^{§*}

[†]Georgia Tech Research Institute, Atlanta, GA 30332,

[‡]School of Chemical Engineering, Georgia Institute of Technology,

Atlanta, GA 30332, [§]Oak Ridge National Laboratory, Oak Ridge, TN

37830

ABSTRACT

A new type of composite, which consists of a reinforcement phase plus a matrix composed of alternate thin layers of two different materials, has been conceived. Layered structures are known to enhance mechanical toughness and thus, their use as the matrix, along with the reinforcement phase, should enhance the toughness of the overall composite. CVI appears to be an appropriate process for the fabrication of this class of materials. The reinforcement could be either fibers, whiskers, platelets or particulates, used individually or as a mixture. The matrix layers could be either ceramic, metallic, or polymeric. We have successfully fabricated such a composite using the forced flow-thermal gradient CVI process. A carbon fibrous preform was infiltrated with alternate layers of C and SiC having thicknesses of 0.01 to 0.5 μm .

Supported by the Air Force Office of Scientific Research, the Georgia Institute of Technology, and the U.S. Department of Energy through the High Temperature Materials Laboratory User Program, under Contract No. DE-AC05-84OR21400 with Lockheed-Martin Energy Systems, Inc.

*Member, American Ceramic Society

I. Introduction

It is well known that ceramics have desirable properties, such as light weight, high stiffness, corrosion/wear resistance, and strength retention at high temperatures. However, their brittleness limits their use in most structural applications. Metals have excellent toughness but typically suffer from loss of strength at high temperatures, excessive creep, and high density. These shortcomings have been overcome for ceramics and metals using fibers or whiskers as reinforcement and also in metals using platelets and particulates. For example, the toughness of SiC and carbon have been improved by reinforcement with SiC and carbon fibers.^{1,3} Also, SiC fibers or platelets have been used to reinforce Ti, Al and other metals.² In these prior examples, the matrix was either single phase or contained a dispersed phase.^{4,5}

It is also well known that the mechanical properties of structures can be enhanced by using alternate layers of two materials.^{2,3,6,7} Examples of such laminated materials include Ni/Cu,⁸ Fe/Cu,⁸ ZrO₂/Al₂O₃,⁹⁻¹¹ SiC/C,^{12,13} TiC/TiN,¹⁴ TiC/TiB₂,¹⁵ TiC/Ni,¹⁶ Al₂O₃/Nb,¹⁷ and many others. Much of this work shows that mechanical and tribological properties improve as layer thicknesses decrease.¹⁸⁻²¹ For some systems, properties show non-linear changes as layer thicknesses approach $\sim 0.02 \mu\text{m}$, i.e., even more rapid improvement in properties with decreasing thickness. The high fracture toughness of mollusk shells ($\sim 10 \text{ MPa}\cdot\text{m}^{1/2}$) is sometimes offered as an example of the potential of layered structures.²²

The present work was undertaken to combine the advantages of fiber or particulate reinforcement and laminated structures. The resulting composite would have a reinforcement phase and a laminated matrix. It is suggested that this new class of materials be termed "Laminated Matrix Composites" (LMC). Laminated structures are typically fabricated by

stacking foils, followed by hot pressing or diffusion bonding,²³ various coating processes,^{12,18-21} sedimentation, centrifuging,¹⁰ and electrophoresis.^{24,25} These processes, with the exception of CVI, do not lend themselves to the infiltration of fibrous or particulate preforms. Furthermore, several of the processes are not applicable to submicron thick layers because of difficulties with handling or limitations on the size of the constituents. However, using CVI, a porous preform can be infiltrated with a laminated matrix by periodically changing the reagent stream from one type of precursor to another. In this way, many thin matrix layers may be easily deposited. Both CVD and CVI have been used to make multilayered fiber-matrix interface coatings²⁶⁻²⁸ and oxidation protection coatings for carbon and other composites.^{29,30} Naslain et al.³¹ have used CVI to deposit what they refer to as a hybrid matrix where the first portion of the infiltration process is accomplished using one material and the final infiltration step utilizes a second material. However, to our knowledge, a reinforced composite with a laminated matrix has never been prepared. Hence, this work was undertaken to investigate the feasibility of fabricating laminated matrix composites using forced flow-thermal gradient CVI. The two components chosen for the matrix were C and SiC with carbon fibers as the reinforcement phase. This system was chosen so as to obtain a composite with high toughness as well as light weight.

II. Experimental Details

Laminated matrix composites (LMC) in the shape of right circular disks were fabricated using the forced flow-thermal gradient CVI process. In this process, a pressure gradient forces the reagent stream to flow through a preform which is subjected to a temperature gradient. The details of the equipment and general experimental procedure have been explained elsewhere.³²

Briefly, the preforms consisted of 40 layers of T-300 plain weave carbon cloth, 4.8 cm in diameter, oriented at 0 and 90°. These layers were stacked in a graphite preform holder and lightly compacted giving a height of ~0.8 cm. Two types of preform holders, namely, type 2 and 3, which are described in a prior publication,³² were used. The type 2 and 3 preform holders extended 5.1 and 7.6 cm above the gas injector, respectively. The height of the preform holder influences the temperature and the temperature gradient through the preform. The temperature differences between the hot and cold sides for the type 2 and 3 preform holders were ~350°C and ~150°C, respectively.

The operating conditions for the infiltration experiments are given in Table 1. A thin carbon interface was deposited before the deposition of the laminated matrix. The interface was deposited by flowing 40 cm³/min of methane and 160 cm³/min of hydrogen through the preform for 20 minutes. The temperature of the bottom of the preform during the interface deposition was ~975°C. This step was followed by deposition of C and SiC, alternately. Carbon was deposited from a reagent mixture containing 50% propylene-50% hydrogen and the total flow rate was 400 cm³/min. The SiC layers were deposited using 50 cm³/min of methyltrichlorosilane (MTS) and 500 cm³/min of hydrogen. The deposition time for each laminate layer was 5 min except, for L-5, where each SiC layer was deposited for 10 min. Two infiltration runs (L-2 and -6) were conducted using only a carbon matrix for the purpose of comparison with the LMCs.

The temperature of the bottom of the preform during the course of depositing the laminated matrix fluctuated between 900 and 961°C. This temperature variation was caused by changing the reagent stream, thereby altering the thermal conductivity of the gas between the water cooled gas injector and the preform. The thermal conductivity of the propylene/hydrogen

mixture was lower than that of the MTS/hydrogen mixture for the concentrations used in the present work. Consequently, the temperature increased when the propylene/hydrogen mixture was used as the reagent, and the temperature decreased when the reagent was changed to MTS/hydrogen. About 60 s elapsed between ending the deposition of one layer and starting the deposition of the next layer. During this interval, hydrogen was flowed through the composite.

The apparent volume of the composite was determined using Archimedes' principle with methanol ($\rho = 0.79 \text{ g/cm}^3$). The open pore volume was calculated by weighing the composite saturated with methanol. These two values were added to obtain the bulk volume. To calculate total porosity it was assumed that the densities of the deposited carbon and SiC were 1.9 and 3.2 g/cm^3 , respectively and that the volume of carbon deposited was twice that of the SiC deposited.

An entire cross-section of each composite disk was mounted in epoxy and polished. The polished sections were observed via scanning electron microscopy to permit observation of the composite microstructure. Several samples were fractured, using flexure, to observe the propagation of cracks. Transmission electron microscopy was used to more clearly observe the thinner layers and to determine the phases deposited.

III. Results

The objective of this work was realized; laminated matrix composites were successfully prepared. The infiltration time, density, and porosity of the laminated matrix composites (L-1, -3 and -5), and carbon matrix composites (L-2 and -6) used as controls, are given in Table 2. The infiltration time for the laminated composites was 4.5-8 h versus ~4 h for the carbon matrix composites; apparently, this is the result of SiC deposition being slower than carbon

deposition for the conditions used here. The open porosity of the laminated matrix and carbon matrix samples are similar, but the closed porosity values are higher for the laminated matrix composites. This indicates that the conditions used for SiC infiltration require adjustment in order to achieve similar levels of closed porosity.

Scanning electron microscopy showed that the desired laminated matrix composites were achieved in each case (Figures 1-4). Both the C and SiC layers were generally continuous with the exception of the first few layers in sample L-3. Transmission electron microscopy and electron diffraction verified that the deposits were turbostratic carbon and crystalline SiC, as expected. The number of layers at a given location depended on the space between the fibers. In a cloth lay-up, as used in the present work, the distance between the fibers within a tow was 2-3 μm (micropores) and the distance between the tows was 50-100 μm (macropores). The tows became densified early in the infiltration process and most of the infiltration time was spent on filling the macropores found between the cloth layers and tows within a cloth.³³ Hence, all layers were not observed within a tow (Figure 4). However, all the layers were observed in the matrix deposited within the macropores (Figures 2 and 3).

As shown in Figures 1-4, layers of C and SiC $< 0.5 \mu\text{m}$ in thickness were achieved. The thickness of the deposited layers generally increased with increasing distance from the fiber surface during the deposition process. The thickness of the initial layers was as small as 0.01 μm (Figures 5 and 6) and increased to $\sim 0.5 \mu\text{m}$ near the end of the deposition process. The increase in the deposition rate, i.e. layer thickness, with infiltration time was caused by reduction of reagent depletion during the infiltration process. The term "reagent depletion" refers to the reduction in concentration of the reagent as the process gas stream traverses the

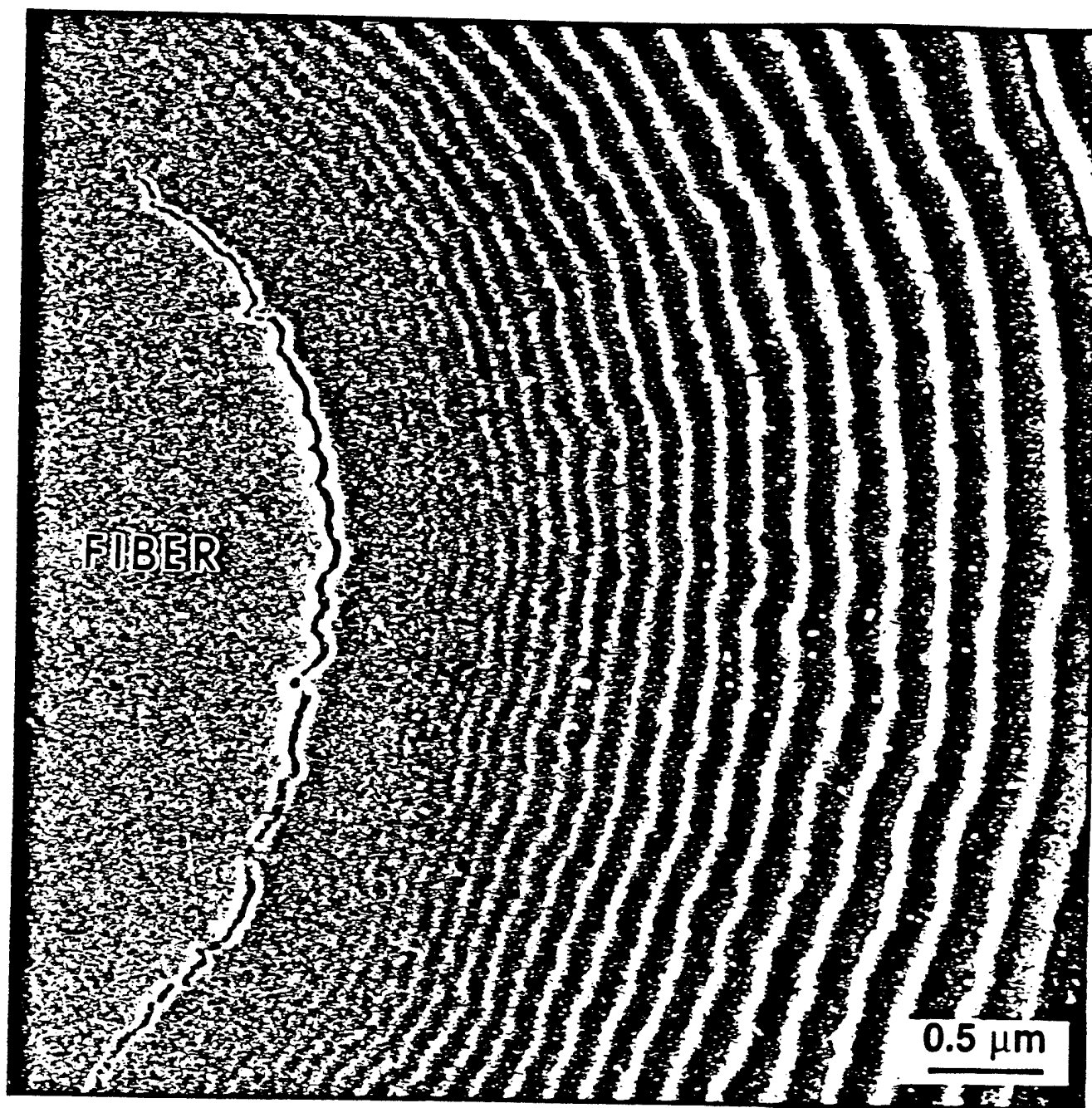


Figure 1. Laminated matrix composite prepared by FCVI showing carbon fiber and alternating layers of carbon (dark) and SiC (light). Sample L-1.

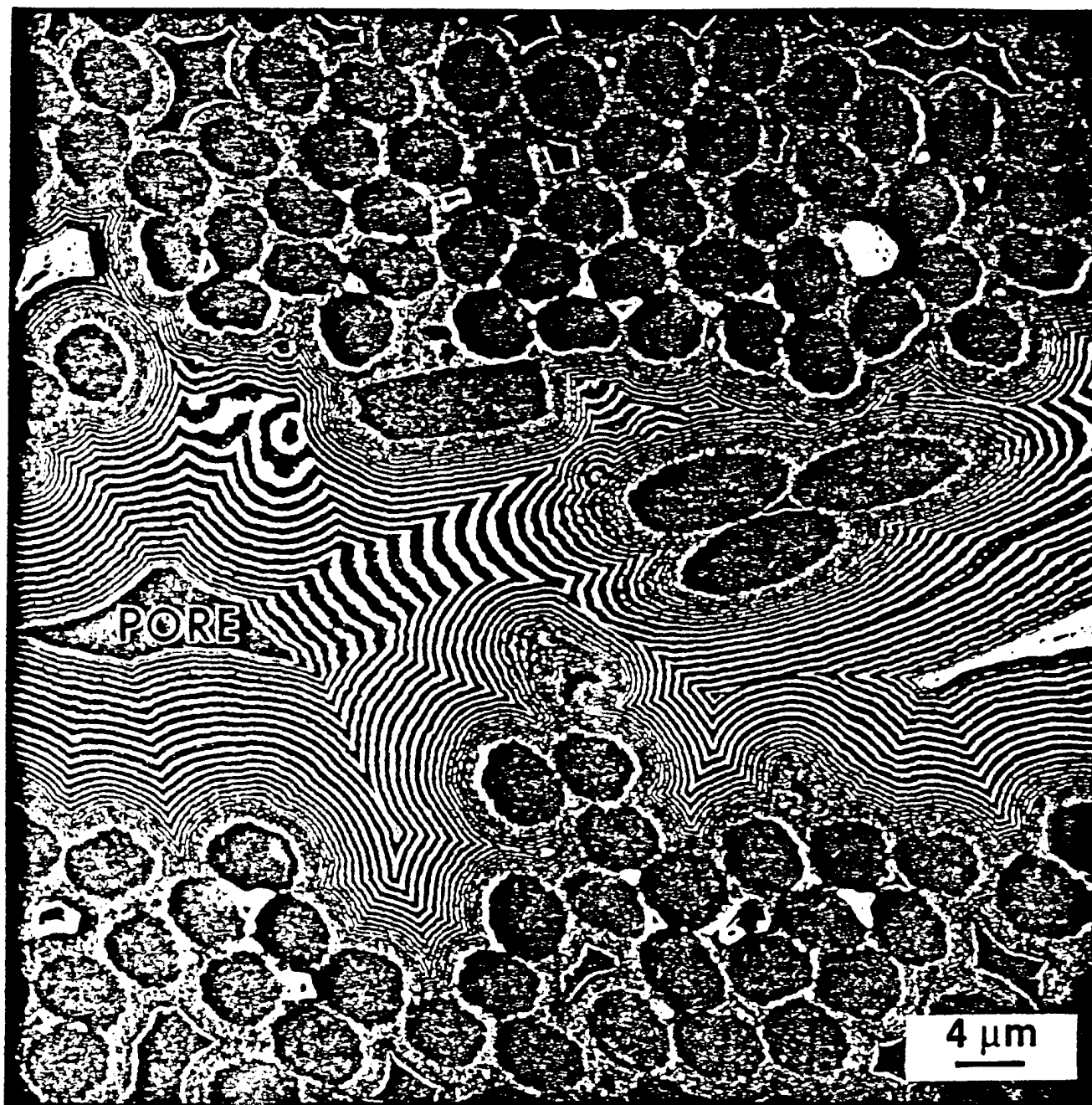


Figure 2. Laminated matrix fills region between layers of cloth. Sample L-3.

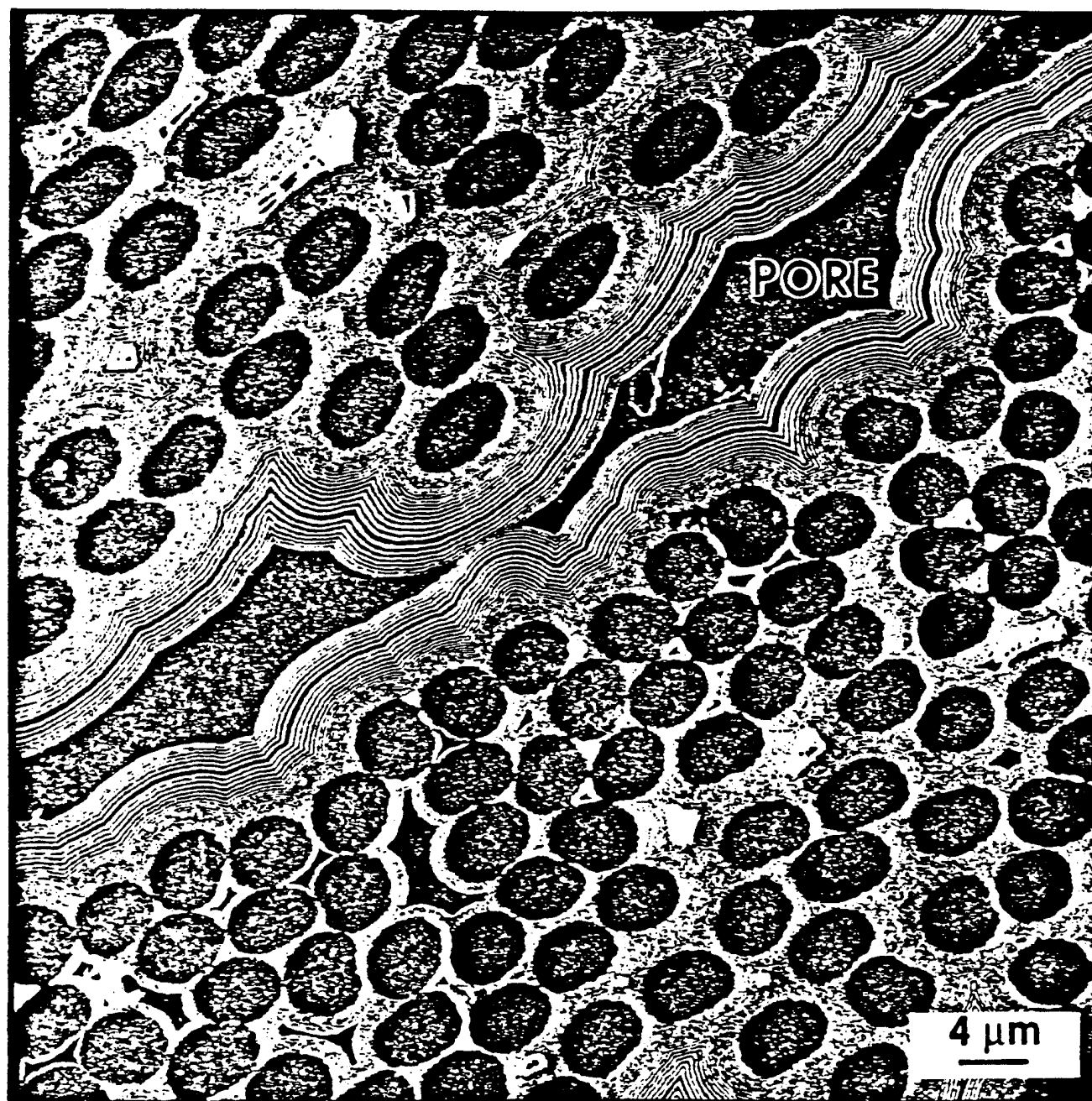


Figure 3. Laminated matrix composite. Sample L-5.

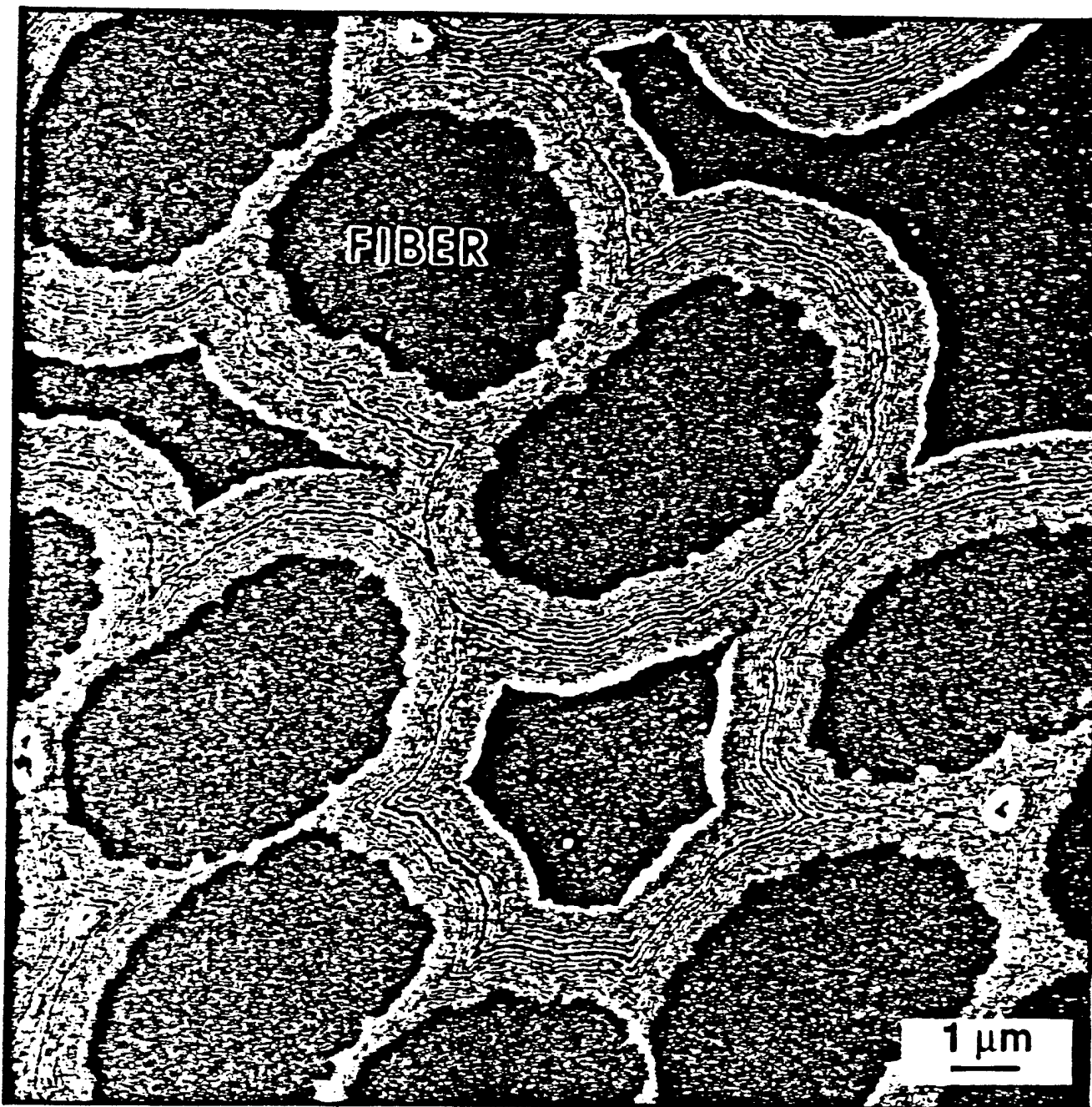


Figure 4. The number of laminate layers between individual fibers depends on the distance between fibers. Sample L-5.

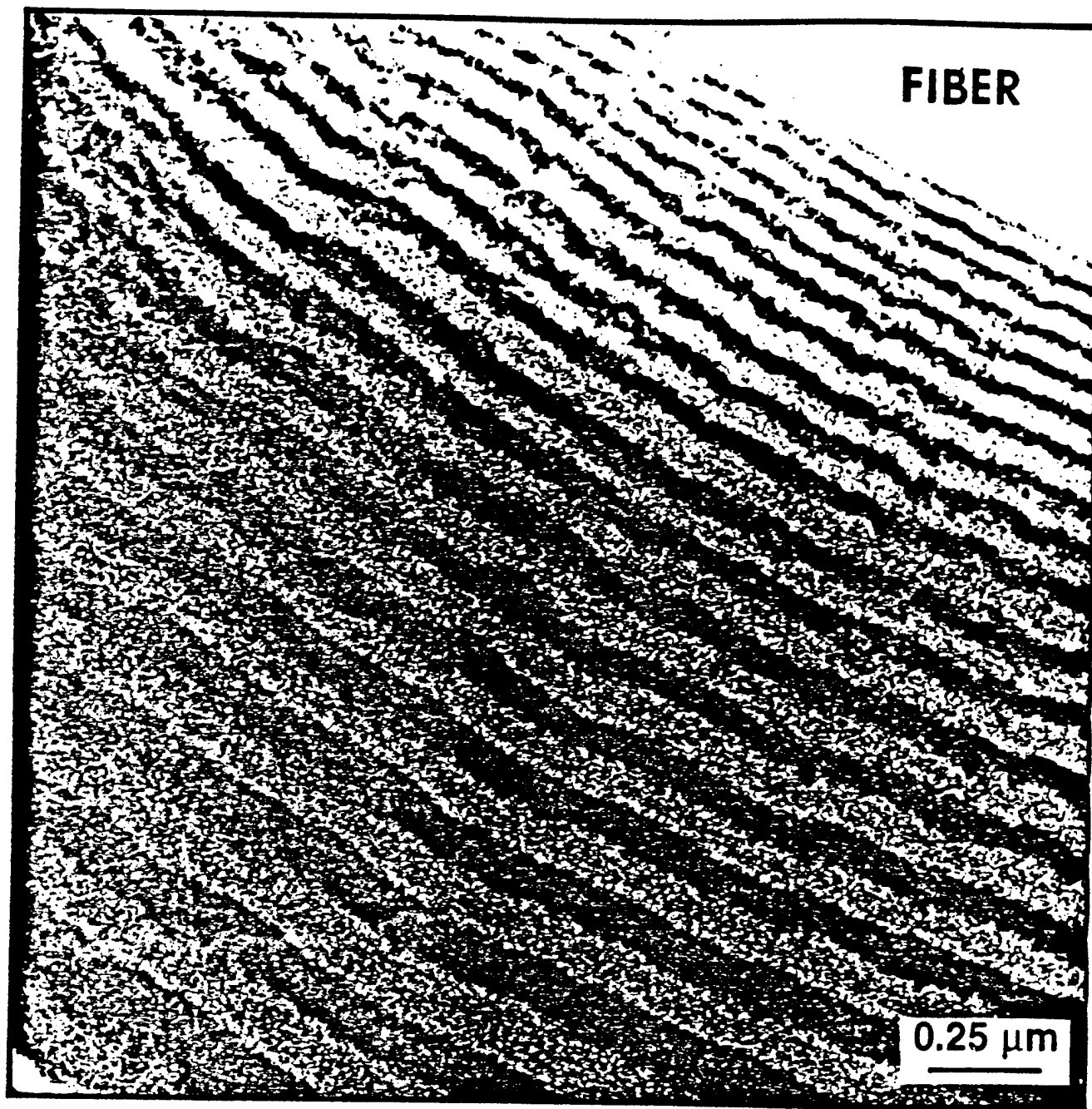


Figure 5. TEM of laminated matrix composite showing that layer thickness increases with distance from the fiber. The SiC layers appear dark. Sample L-5.

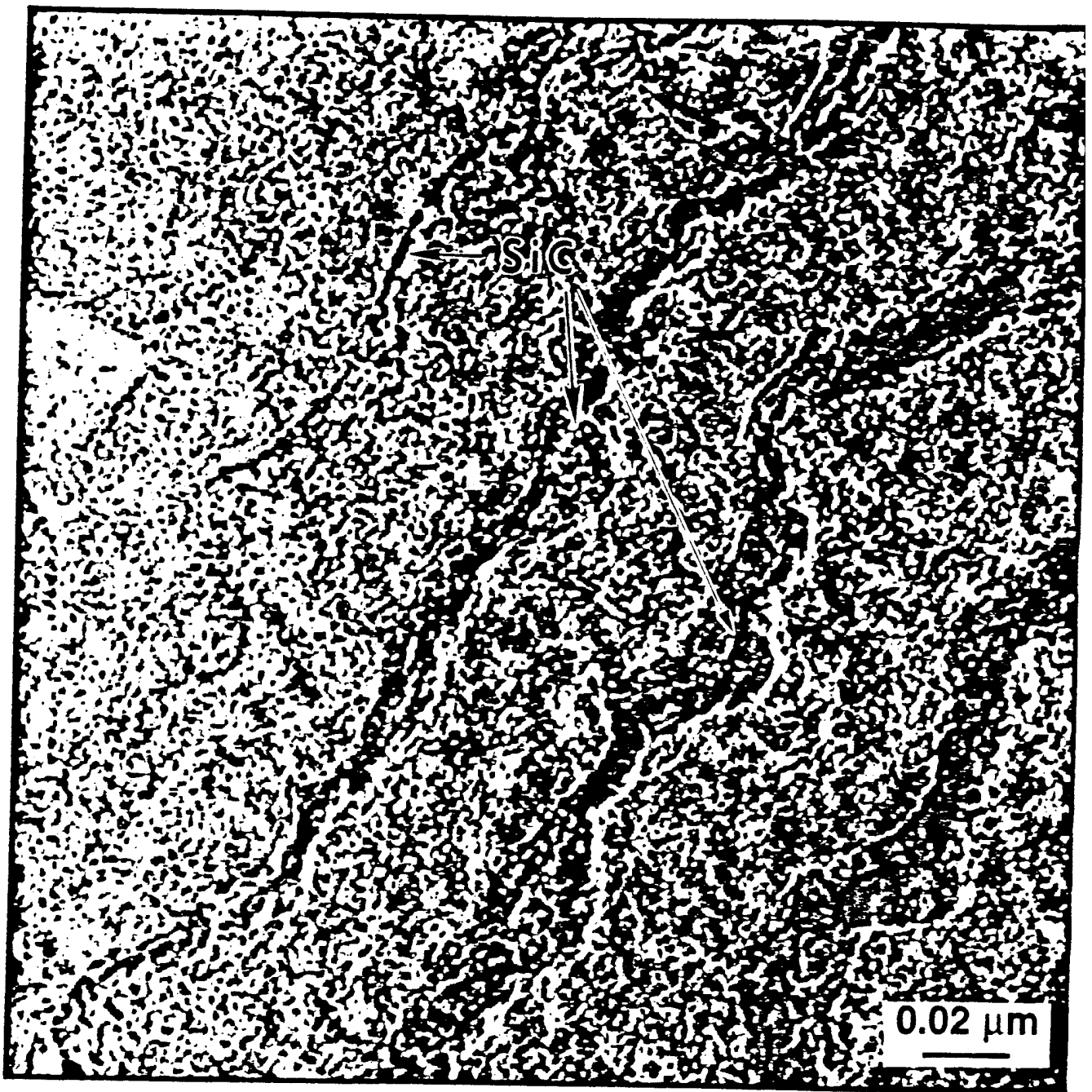


Figure 6. TEM of laminated matrix composite showing thin layers near the fiber. Sample L-1.

preform. Initially the reagent depletion was very high due to the high surface area of the preform, but since densification isolates an ever increasing number of tows, the surface area of the preform gradually reduces. This reduction in surface area, in turn, reduces reagent depletion and thereby leads to the observed increase in layer thickness with time.

Several samples were deliberately fractured in order to observe, via SEM, the crack path. As shown in Figure 7, evidence that the laminate layers offer resistance to crack propagation was seen. The crack shown here does not propagate in a straight line, but instead follows a tortuous path with jogs occurring from one laminate layer to an adjacent layer. Typical debonding at the fiber-matrix interface (not shown) was also observed. While these results are encouraging, extensive mechanical testing will be required to determine if the laminated matrix does indeed enhance composite toughness.

IV. DISCUSSION

Considerable experimental investigation and/or modeling of the fracture behavior of laminated matrix composites will likely be required in order to determine optimum material combinations and layer thicknesses for maximizing mechanical performance. Questions to be answered include identifying the preferred relative elastic moduli and strengths for the matrix materials, the modulus of the matrix compared to that of the reinforcement, and should the layers be ceramic, metallic, or one ceramic and one metallic. Also, it remains to be determined whether the laminate layers should be of equal thickness or should one type layer be thicker? Should a given type layer be of uniform thickness or should the layers vary in thickness with distance from the reinforcement phase?

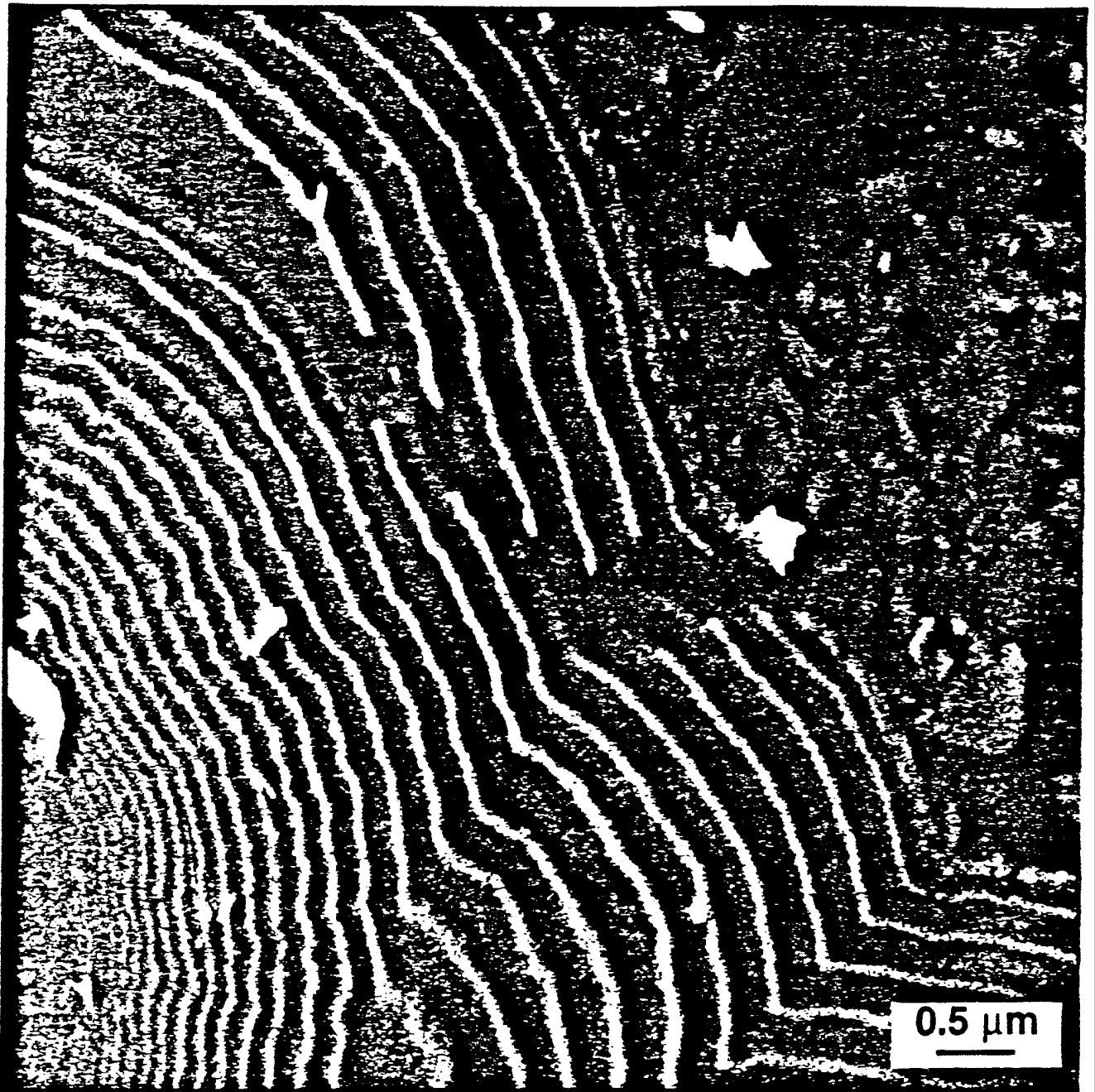


Figure 7. Deliberate fracture showing tortuous crack path in the laminated matrix. Sample L-1-M-3.

The laminated matrix composite concept offers a number of interesting options for improving performance and lowering costs. For example, if the multiple interfaces within the laminated matrix are effective in retarding crack propagation, that is, increasing toughness, then it may be possible to use particles or platelets as the reinforcement phase rather than fibers. If this is shown to be possible, then appreciable reduction in composite costs would result. Particles of SiC are commercially available in a variety of sizes for \$1-2/lb compared to \$300/lb for Nicalon SiC fiber. It may be that readily cleaved oxides, such as the β'' -aluminas, magnetoplumbites, or monazite, may be appropriate materials for use as the reinforcement or as one of the matrix layers.

If particulates, rather than fibers, are used as the reinforcement phase, it will be possible to use higher CVI processing temperatures. Often with current fibers, it is necessary to use low temperatures to avoid fiber degradation. The freedom to use higher processing temperatures would permit higher deposition rates and lower processing time and cost. There would also be increased latitude in selecting the processing temperature that yields optimum matrix composition and microstructure, and therefore, optimum properties.

Other options for tailoring the properties of laminated matrix composites also exist. By changing layer thicknesses or compositions it would be possible to grade the composition of the matrix so as to obtain desired properties, such as chemical compatibility, and to tailor the coefficient of thermal expansion. Use of more than two layers in the matrix should also be feasible. For example, a matrix composed of layers of carbon, boron carbide, and SiC should have improved resistance to oxidation compared to a pure carbon matrix. It may also be desirable to deposit matrix layers that are dispersed phase composites. Computer control could

facilitate control of layer thickness and composition, including varying the fraction of the dispersed phase.

In addition to improvements in mechanical properties, laminated matrix composites may prove useful in tailoring thermal conductivity. For example, it is well known that numerous interfaces interfere with phonon transport and thus laminated matrix composites may offer a route for preparing improved thermal insulators. Similarly, if a composite having a high thermal conductivity were desired, thicker layers could be used and one or more of the materials selected for the matrix should possess a high thermal conductivity.

V. CONCLUSIONS

A new class of composite, composed of a reinforcement phase plus a laminated matrix, was described and fabrication was shown to be feasible by using CVI to deposit alternating layers of carbon and SiC in a carbon fiber preform. Layer thicknesses in the range 0.01 to 0.5 μm were achieved. It is speculated that if the numerous interfaces present in a laminated matrix are effective in inhibiting crack propagation, it may be possible to use inexpensive particulates or platelets, rather than fibers, as the reinforcement phase. Laminated matrix composites may also be useful in tailoring the coefficient of thermal expansion and thermal conductivity of materials.

Acknowledgments

We appreciate the guidance of Dr. Alexander Pechenik of the Air Force Office of Scientific Research. The assistance of Michael Miller, Regina Richards and seven, diligent

undergraduate mechanical engineering students who performed most of the experimentation is appreciated. We also appreciate typing and editing of the original manuscript by Virginia Myers and Joey Goddard, respectively.

References

¹W. J. Lackey and T. L. Starr, "Fabrication of Fiber-Reinforced Ceramic Composites by Chemical Vapor Infiltration: Processing, Structure and Properties," pp. 397-450 in *Fiber Reinforced Composites*, ed. K. S. Mazdiasni, Noyes Publications, Park Ridge, NJ, (1990).

²Michael R. Piggott, *Load Bearing Fibre Composites*, Pergamon Press, New York, NY, (1980).

³K. K. Chawla, *Composite Materials Science and Engineering*, Springer-Verlag, New York, NY, (1987).

⁴S. R. Goujard, L. Vandenbulcke, J. Rey, J.-L. Charvet, and H. Tawil, "Process for the manufacture of a refractory composite material protected against corrosion," U.S. Patent 5,246,736, September 21, 1993.

⁵W. J. Lackey, A. W. Smith, D. M. Dillard, and D. J. Twait, "Codeposition of Dispersed Phase Ceramic Composites," *Proceedings of Tenth Int. Conf. on Chemical Vapor Deposition*, 1008-1027, ed. G. W. Cullen and J. M. Blocher, Jr., The Electrochemical Soc., Inc., Pennington, NJ, 1987.

⁶M. Y. He, F. E. Heredia, D. J. Wissuchek, M. C. Shaw, and A. G. Evans, "The Mechanics of Crack Growth in Layered Materials," *Acta Metall. Mater.* **41** (4) 1223-1228, (1993).

⁷W. J. Clegg, K. Kendall, N. M. Alford, D. Birchall and T. W. Burton, "A simple way to make tough ceramics," *Nature*, **347**, 455-457, (1990).

⁸R. F. Bunshah, R. Nimmagadda, H. J. Doerr, B. A. Movchan, N. I. Grechanuk and E. V. Dabizha, "Structure and Property Relationships in Microlaminate Ni-Cu and Fe-Cu Condensates," *Thin Solid Films*, **72**, 261-275, (1980).

⁹P. S. Nicholson, P. Sarkar and X. Haung, "Electrophoretic deposition and its use to synthesize ZrO_2/Al_2O_3 micro-laminate ceramic/ceramic composites," *J. Mat. Sc.*, **28** 6274-6278, (1993).

¹⁰David B. Marshall, Joseph J. Ratto, and Fred F. Lange, "Enhanced Fracture Toughness in Layered Microcomposites of Ce- ZrO_2 and Al_2O_3 ," *J. Am. Ceram. Soc.*, **74** (12) 2979-2987, (1991).

¹¹Private communications with James Strife, UTRC and John Appleby, Pratt and Whitney, July 24, 1995.

¹²M. Ignat, M. Nadal, C. Bernard, M. Ducarriour and F. Teyssandier, "Mechanical response and rupture mode of SiC/C lamellar composites," *J. de Physique*, **50** C5-259 (1989).

¹³A. J. Phillipps, W. J. Clegg, and T. W. Clyne, "The Correlation of Interfacial and Macroscopic Toughness in SiC Laminates," *Composites*, **24** (2) 166-176, (1993).

¹⁴H. Holleck and H. Schulz, "Preparation and Behavior of Wear-Resistant TiC/TiB₂, TiN/TiB₂ and TiC/TiN Coatings with Large Amounts of Phase Boundaries," *Surface and Coatings Technology*, **36**, 707-714, (1988).

¹⁵B. A. Morchan, A. V. Demchishn, G. F. Badilenko, R. F. Bunshah, C. Sans, C. Deshpandey, and H. J. Doerr, "Structure Property Relationships in Microlaminate TiC/TiB₂ Condensates," *Thin Solid Films*, **97**, 215-219, (1982).

¹⁶C. Sans, C. Deshpandy, H. J. Doerr, R. F. Bunshah, B. A. Morchan, and A. V. Demchishn, "Preparation and Properties of TiC/Ni Microlaminates," *Thin Solid Films*, **107**, 345-351, (1983).

¹⁷J. T. Beals and V. C. Nardone, "Tensile behavior of a niobium/alumina composite laminate," *J. Mat. Sc.*, **29**, 2526-2530, (1994).

¹⁸Scott A. Barnett, "Deposition and Mechanical Properties of Superlattice Thin Films", *Physics of Thin Films*, ed. M. H. Francombe and J. L. Vossen, Academic Press **17**, 1-77, (1993).

¹⁹X. Chu, M. S. Wong, W. D. Sproul, S. L. Rohde, and S. A. Barnett, "Deposition and Properties of Polycrystalline TiN/NbN Superlattice Coatings, *J. Vac. Sci. and Tech. A*, **10** (4) 1604-1609, (1992).

²⁰X. Chu, M. S. Wong, W. D. Sproul and S. A. Barnett, "Reactive Unbalanced Magnetron Sputter Deposition of Polycrystalline TiN/NbN Superlattice Coatings," *Surface and Coatings Technology*, **57**, 13-18, (1993).

²¹A. W. Ruff and D. S. Lashmore, "Effect of layer spacing on wear of Ni/Cu multilayer alloys", *Wear* **151** 245-253 (1991).

²²M. Sarikaya and I. Aksay, eds., *Biomimetics - Design and Processing of Materials*, American Institute of Physics, Williston, VT, 1995.

²³H.-C. Cao and A. G. Evans, "On Crack Extension in Ductile/Brittle Laminates," *Acta Metall. Mater.* **39**, 2997-3005, (1991).

²⁴L. Gal-Or, S. Liuborich, and M. Folman, "Multi-layer Ceramic Composite Formation by Electrophoretic Deposition," Interim Report for 1993-94. AFOSR Contract No. F49620-93-1-0233, Israel Institute of Metals, Technion Research and Development Foundation, Technion City, Haifa, Israel.

²⁵Zongtoa Zhang, Yong Huang, and Zuozhao Jiang, "Electrophoretic Deposition Forming of SiC-TZP Composites in a Nonaqueous Sol Media," *J. Am. Ceram. Soc.* **44** (7) 1946-1949, (1994).

²⁶T. Huynh and W. E. Bustamante, "Non-Oxidizing Interface (NOI) for Ceramic Matrix Composites Processed by CVI Technique," 17th Annual Conference on Composites, Materials, and Structures (Restricted Session) Cocoa Beach, FL, January 14, 1993.

²⁷Christine Droillard, Jacques Lamon, and Xavier Bourrat, "Strong Interface in CMCs, Condition for Efficient Multilayered Interphases," Proceedings of the Fall Meeting of the Materials Research Soc. Vol. 325, Boston, MA, November, 1994. In press.

²⁸Christine Droillard, "2D-SiC/SiC CVI Composite with a (C-SiC)_n Multilayered Interphase: Processing, Microstructure and Tensile Behavior at Room Temperature," Thesis, University of Bordeaux, France, June, 1993.

²⁹James E. Sheehan, "High-Temperature Coatings on Carbon Fibers and C-C Composites," pp. 223-266 in Carbon-Carbon Materials and Composites, eds. John D. Buckley and Dan D. Edie, Noyes Publications, Park Ridge, NJ, (1993).

³⁰L. Vandenbulcke, S. Goujard, H. Tawil, and J.-C. Cavalier, "Method of providing anti-oxidation protection for a composite material containing carbon, and a material protected thereby," U.S. Patent 5,194,330, March 16, 1993.

³¹R. Naslain, J. Y. Rossignol, P. Hagenmuller, F. Christin, L. Heraud, and J. J. Choury, "Synthesis and properties of new composite materials for high temperature applications based on carbon fibers and C-SiC or C-TiC hybrid matrices," *Revue de Chimie Minerale*, **18**, 544-564 (1981).

³²S. Vaidyaraman, W. J. Lackey, G. B. Freeman, P. K. Agrawal, and M. D. Langman, "Fabrication of Carbon-Carbon by Forced Flow-Thermal Gradient Chemical Vapor Infiltration," *J. Mat. Res.*, **10** (6) 1469-1477, (1995).

³³W. J. Lackey, S. Vaidyaraman, G. B. Freeman, and P. K. Agrawal, "Technique for Monitoring the Densification During CVI Processing," *J. Am. Ceram. Soc.*, **78**, 1131-1133, (1995).

LIST OF FIGURES

- Figure 1. Laminated matrix composite prepared by FCVI showing carbon fiber and alternating layers of carbon (dark) and SiC (light). Sample L-1.
- Figure 2. Laminated matrix fills region between layers of cloth. Sample L-3.
- Figure 3. Laminated matrix composite. Sample L-5.
- Figure 4. The number of laminate layers between individual fibers depends on the distance between fibers. Sample L-5.
- Figure 5. TEM of laminated matrix composite showing that layer thickness increases with distance from the fiber. The SiC layers are dark. Sample L-5.
- Figure 6. TEM of laminated matrix composite showing thin layers near the fiber. Sample L-1.
- Figure 7. Deliberate fracture showing tortuous crack path in the laminated matrix. Sample L-1-M-3.

Table 1. Processing conditions for laminated matrix composites.

Run Number	Preform Type	Temperature of Preform Bottom (°C)	Carbon Deposition Time per Cycle (mins)	SiC Deposition Time per Cycle (mins)
L-1	3	910-950	5	5
L-2	3	915-954	—	—
L-3	2	900-961	5	5
L-5	3	910-959	5	10
L-6	2	900-967	—	—

Table 2. Properties of the infiltrated composites.

Run Number	Fiber Content (%)	Total Number of Cycles	Infiltration Time (h)	Weight Gain (g)	Bulk Density (g/cm ³)	Total Porosity (%)	Open Porosity (%)
L-1	50.6	40	6.67	12.90	1.672	16.4	5.94
L-2	49.0	—	4.25	11.74	1.658	9.2	4.97
L-3	56.7	27	4.50	14.74	1.700	13.7	5.56
L-5	51.8	32	8.00	12.88	1.647	17.7	8.90
L-6	50.8	—	3.60	13.11	1.692	7.6	7.57

The Chemical Vapor Deposition of $B_{13}C_2$ from
Mixtures of BCl_3 - CH_4 - H_2 -Ar

Thomas S. Moss^{ab} and W. Jack Lackey,^a Georgia Tech Research Institute, Georgia Institute of Technology, Atlanta, GA 30332-0826 and Karren L. More, Oak Ridge National Laboratory, Oak Ridge, TN 37831

Abstract

The deposition of boron carbide, $B_{13}C_2$, onto graphite substrates was accomplished using a hot wall CVD reactor at a pressure of 10.1 kPa (0.1 atm) in the temperature range of 1000 to 1400°C. A modified impinging jet geometry was employed to simplify the mass transfer analysis. Coatings were characterized using x-ray diffraction (XRD), scanning electron microscopy (SEM), and transmission electron microscopy (TEM). The surface morphology was composed of well defined facets whose size was dependent on the growth rate and deposition time, as would be expected from a competitive growth mechanism. TEM micrographs of the coating showed long columnar grains emanating from a narrow nucleation zone. The growth rate was found to be adequately described by a first order kinetic expression with respect to the bulk gas phase BCl_3 concentration. The activation energy of the kinetic expression was estimated to be 93.1 kJ/mole. It was proposed that the deposition was limited by the adsorption of BCl_3 onto the substrate surface.

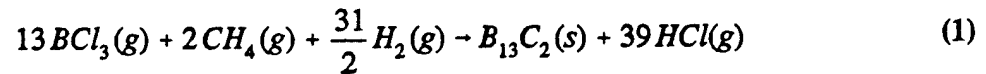
CVD, Boron Carbide, Microstructure, Coating, Kinetics

^aMember, ACS

^bLos Alamos National Laboratory

Introduction

The synthesis of boron carbide has been of interest to many fields, such as the aerospace, nuclear, and abrasives industries. However, because of its high melting temperature, processing using many conventional techniques can be both difficult and expensive. The process of chemical vapor deposition (CVD) is well suited for the production of refractory materials due to the relatively low processing temperatures. Further, materials synthesized in CVD reactors are typified by their high purity and low porosity. Also, because of the wide latitude of processing conditions, CVD allows for greater control of final properties of the deposition by tailoring microstructure, stoichiometry, and morphology. The objective of these deposition experiments was to determine not only the form of the reaction expression but also to learn appropriate conditions for the production of boron carbide for dispersed phase coatings. The overall deposition reaction has the form:



Background

Of the different boron carbide phases, $B_{13}C_2$ (commonly referred to by the B_4C misnomer) is the best known. It has a rhombohedral structure with a B_{12} icosahedron at the unit cell corner and is connected by a -CBC- chain along the unit cell diagonal.^{1,2} Boron carbide is a stable refractory compound which has a melting temperature of about 2450°C.³ The microhardness of boron carbide has been shown to be inferior to only diamond, diamond-like carbon, and cubic boron nitride,⁴ and excellent erosion resistance has also been

exhibited.⁵ In addition to its attractive mechanical properties, it shows interesting thermal and electrical properties making it of interest to the field of thermoelectric power generation.⁶

Boron carbide is commonly produced via CVD through the direct reaction of a boron species with a carbon species in the presence of hydrogen as a reducing agent. The boron halides, BCl_3 ,⁷⁻⁹ BBr_3 ,¹⁰ and BI_3 ¹¹ are the most common boron sources. While deposition temperature is highly dependent on the halide choice, temperatures over 1000°C are usually required. In general, the stability of the boron halides decreases from BCl_3 to BBr_3 to BI_3 which means that minimum deposition temperatures can be expected to decrease in the same order. This situation makes BBr_3 and BI_3 useful for certain applications where the deposition temperature must be kept low. However, the less stable species will be more reactive, especially with moisture, making them corrosive to vacuum pumps, mass flow meters, and reagent lines. The increased reactivity of BBr_3 and BI_3 makes BCl_3 the species of choice except where lower deposition temperatures are needed. Boranes (B_xH_y)¹² and carboranes ($\text{C}_x\text{B}_y\text{H}_z$)¹³ have also been tried to a much lesser extent. These classes of materials are even more unstable than the boron halides; so, their deposition temperature should be lower, although they must be carefully handled. However, they have not been thoroughly investigated and are expensive.

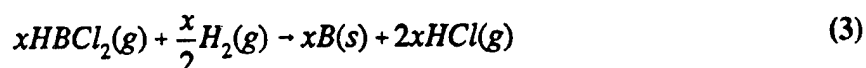
The choice for the carbon species has most widely been methane, CH_4 ,⁷⁻⁹ although deposition has been accomplished with other hydrocarbons such as C_2H_4 ¹⁴ and C_2H_6 ¹⁵ as well as with carbon halides.^{11,16,17} The role of CH_4 in the deposition of boron carbide has not been well established at this point. In general, lower deposition rates and carbon contents in the deposit are expected when CH_4 is used. This is thought to be due to the weak interaction

between CH_4 and graphite substrates which limits adsorption.¹⁸ However, studies have shown that the nucleation strongly depends on the concentration of CH_4 ; surface nucleation density, in fact, decreases with increases in the CH_4 concentration.¹⁹

There has been one systematic study of the kinetics of boron carbide CVD for a hot wall reactor from mixtures of BCl_3 , CH_4 , and H_2 by Hannache et al.²⁰ They produced B_{13}C_2 coatings in the ranges of 10 to 120 sccm total flow rate, 10 to 100 torr system pressure, and 850 to 1050°C. The effect of total flow rate on the deposition rate showed a linear relationship at 900 and 950°C, but at 1000°C, the deposition rate increased rapidly between 30 and 90 sccm. They attributed this increase to depletion of the reagent to the walls of the reactor at lower flow rates; however, as the flow rate increased, the degree of depletion decreased and eventually became insignificant compared to the active reagent in the gas phase. The influence of total pressure showed that, at low flow rates, the deposition increases rapidly with increasing pressure until about 50 torr, when the rate begins to drop. The lower flow rate was determined to be not suitable for proper investigation. At higher flow rates, the deposition rate increased rapidly with increasing pressure. They indicated that increasing the pressure resulted in a transition between surface and diffusion kinetic regimes. The effect of temperature was examined to determine the activation energy of the reaction. In the course, they discovered two separate regimes occurring above and below 950°C. The low temperature region had an apparent activation energy of 90 kcal/mole which did not depend on the total pressure or flow rate. The pre-exponential constant did, however, change with the total pressure and flow rate. At higher temperatures, the Arrhenius plot was not quite as steep as it was below 950°C and did not follow a simple law.

They explained this change as a transition from a surface kinetic regime to a diffusion controlled regime. The value of the apparent activation energy suggested to this group that CH_4 was a predominant step towards deposition, with a reaction order of one. They based this claim on previous results reported for the CVD of TiC from mixtures of TiCl_4 , CH_4 , and H_2 . Importantly, this work has been the only in-depth report of hot wall deposition of boron carbide; other research has been focussed on cold wall reactors.

In the work of Vandenbulcke and Vuillard,⁷ who used a cold wall impinging jet reactor, deposition was thought to be controlled by mass transfer at temperatures over 1427°C and by surface kinetics at lower temperatures. In the modeling of the low temperature surface kinetics, the following model was given:



From this model, rate expressions for the rate of formation of boron and carbon were separately determined. The rate expressions were as follows:

$$R_B = \frac{k \sqrt{p_{HBCl_2}} \sqrt{p_{H_2}}}{(1 + k_{CH_4} p_{CH_4})} \quad (5)$$

$$R_C = \frac{k_2 \sqrt{p_{CH_4}}}{(1 + k_{CH_4} p_{CH_4})} \quad (6)$$

Both rate expressions show the importance of CH_4 adsorption in the limiting of the reaction.

Rebenné and Pollard²¹ developed a mathematical model to describe the deposition of boron carbide in an impinging jet, cold wall reactor. They used a published set of data from Vandembulcke²² to match theoretical results to determine the reaction rate constants. They also hoped to learn the rate limiting steps for deposition based on the conditions which gave the best match to the data. Their comparison allowed for non-stoichiometric and multiple solid phases and used a comprehensive model which took into account fluid flow of the reagents, multicomponent heat and mass transfer, and simultaneous surface and gas-phase reactions. The conclusion reached stated that the deposition of B_yC was primarily controlled by the rate of CH_4 decomposition and the extent of surface coverage of CH_4 . However, their equilibrium model showed erroneous trends under conditions where kinetic reactions were important. For example, they found that the boron to carbon ratio in the coatings, y in B_yC , decreased as the surface temperature increased, but the mathematical model predicted an

increase in y . In general, kinetic limitations proved to be important at low system temperatures and pressures and at high volumetric flow rates. However, the validity of their model was based on a fit of a small amount of published data.

Dariel et al.²³ examined the deposition of boron carbide from both a cold wall and a hot wall reactor, at temperatures between 900 and 1200°C. They used BCl_3 , C_3H_6 , H_2 , and Ar as reagents, graphite as the substrate, and pressures of 730 to 800 torr. Chemical analysis of the coatings showed the B/C ratio to be between 5.4 and 5.9, within the range for single phase boron carbide. They found that at low temperatures, 950°C, the coating appeared amorphous based on x-ray measurements. Further, they found no evidence of any mass transport effects from the deposition in the temperature range studied. The surface kinetics controlled the reaction up to a temperature of 1050°C, when the coating showed strong 110 preferred orientation. The hardness of the coatings was determined to be extremely high, on the order of 4000 kg/mm².

Lartigue et al.²⁴ also studied the low pressure deposition of boron carbide from mixtures of BCl_3 , CH_4 , and H_2 onto nuclear purity graphite. They worked in the temperature range of 927 to 1477°C with heating done by RF-induction. They found that the growth rate of boron carbide was strongly dependent on both temperature and the carbon to boron ratio in the reagent flow. They measured this carbon to boron ratio in the reagent stream using a factor defined by the flow rates of CH_4 and BCl_3 . The factor R was the ratio of the CH_4 flow rate to the total flow rate of the CH_4 and BCl_3 . Examining the deposition rate as a function of this quantity at different temperatures showed that the CH_4 flow had an increasing effect with increasing temperatures. From the examination of the deposition rate

as a function of R, it was noted that the effects of increases in the methane do not become significant until 1237°C. Before that point, deposition was seemingly unchanged by increases in the CH₄ flow rate. They also examined the deposition areas for phases in the boron carbide system as a function of the temperature and R. There were large areas where non-equilibrium phases were predicted, i.e., B₈ and B₅₀C₂. The appearance of such phases may be attributed to the use of cold wall reactors, where the kinetics of such phases may become favorable.

The morphology and microstructure of the boron carbide phases has also been studied by several groups.^{8,25-27} Frequently, the metastable tetragonal (B₅₀C and B₅₀C₂) and orthorhombic phases (B₈C) have very large crystallites with well defined facets. These phases are typically found in areas of low carbon input and in systems which do not activate the carbon reagent (i.e., cold wall furnaces), especially when CH₄ is used. These phases are hard to produce in hot wall reactors and decompose to B₁₃C₂ and boron upon heating.²⁸ The rhombohedral B₁₃C₂, however, shows a more disorganized morphology with smaller crystal facets. Low temperatures tend to form smaller, more disorganized facets.²⁹ Transmission electron microscopy shows strong variations in the grain size with smaller grains at the substrate interface and large featherlike grains closer to the surface.³⁰ Amorphous boron carbide exhibits the typical nodular morphology.

Procedure

The experimental schematic used for the B₁₃C₂ deposition system is shown in Figure 1. The reagent supply system was used to accurately meter the flow of the species into the

deposition reactor. For this system the reagents (Ar, H₂, CH₄, and BCl₃) were gases at room temperature and atmospheric pressure, and delivery was completed by flowing the gases through MKS Type 1259B mass flow meters. Reagents were carried to the reactor in heated stainless steel lines and were introduced into the furnace through a single-path water cooled gas injector.

The deposition reactor was a vertical, hot-wall deposition furnace which contain a graphite heating element and a graphite reaction chamber. The temperature within the reactor was calibrated against an Ircon Type R optical pyrometer and a Type K thermocouple. The temperature of the furnace was controlled using a Microstar SCR moderator. The pressure within the reaction vessel was measured using an MKS Type 122A pressure transducer. Exhaust gas species were passed through a scrubber filled with soda lime, desiccant, and glass wool to remove the product acids and any particulates. Downstream from the scrubber was a corrosion-resistant Leybold vacuum pump which was used to operate at reduced pressures.

The choice of substrates for deposition was ATJ graphite, machined to 2 1/4" x 3/4" x 1/4". Other substrate types that were tried included alumina, titanium, and tungsten. However, these materials had thermal expansion mismatch problems, as well as a strong tendency to form undesirable reaction layers. In typical CVD reactors the substrate is positioned within the gas stream by suspending it or by fixing its position with a sample holder. A problem that develops with this type of geometry is the formation of a non-linear and uneven boundary layer over the surface. Further, the effect of reagent depletion can be viewed from changes in the coating thickness along the length of the substrate, complicating

the analysis. These are two complex problems which do not lend themselves well for kinetic modeling. However, they may be overcome by changing to the modified impinging jet geometry. With this reaction geometry, the reagent gases were delivered to the reactor after passing through the impinging jet disk located above the injector. The coatings produced by this method have a characteristic pattern of a series of concentric rings. The center-most circle was known as the stagnation region and was the area of interest for characterization. It has been previously shown that radial concentration gradients are eliminated within the stagnation region.³¹ This means that mass transfer effects need only be modeled in one dimension from a concentration gradient established between the bulk gas phase and the substrate surface. The necessary equations for the calculation of the diffusion coefficient and the boundary layer thickness are summarized elsewhere.³² The estimates of these values were easily calculated through the use of a computer program.

There were a total of 49 experiments performed for the deposition of $B_{13}C_2$: 12 at 1000°C, 15 at 1200°C, and 22 at 1400°C. The conditions at individual temperatures and corresponding sample numbers are summarized within Tables 1 to 3. These samples were characterized using several techniques including x-ray diffraction (XRD) and scanning electron microscopy (SEM). A few samples were identified to be examined using transmission electron microscopy (TEM).

For XRD and subsequent characterization, the small stagnation region was isolated from the surrounding area. The sample was then characterized using XRD analysis to identify crystalline phases. XRD patterns were taken using a Phillips 1800 automatic powder

diffractometer, using copper K_{α} radiation at 40 kV and 30 mA; scans were taken in a range of 20.0 to $75.0^{\circ}2\theta$.

Cross-sectional SEM micrographs were taken using a fractured surface produced by breaking the sample in half across the stagnation region. One of these halves was mounted and examined in the SEM. Micrographs were taken in a Hitachi 4100 and a Hitachi S-800. Both microscopes were operated at 5 kV, and micrographs were consistently taken at a magnification of 1000x. Direct measurements of the thicknesses were taken directly from the micrographs using digital calipers. Ten measurements were taken from each micrograph, and an average thickness was calculated, along with the standard deviation of the measurements. Morphological SEM micrographs were taken by viewing the sample so that the surface of the coated sample was observed. Micrographs were also taken at a magnification of 1000x for all samples.

Selected samples were thinned for examination using TEM. Micrographs and diffraction patterns were taken from several areas throughout the coating with particular emphasis on the substrate-coating interface. Based on these observations, additional information regarding the microstructure of the deposit could be gained.

Results

The results of the boron carbide experiments are summarized in Tables 4 to 6 for the three experimental temperatures. These tables show both the deposition rate in cm/sec, taken directly from cross-sectional micrographs, and the mass transfer coefficient, D/δ , in cm/sec, calculated from the equations presented elsewhere.³² The mass transfer coefficient was

calculated using two different binary diffusion equations, Chapman-Enskog (D/δ) and Slattery-Bird (D/δ)'. Phase identification was done based on x-ray diffraction measurements compared to patterns listed in the JCPDS file. All of the diffraction patterns were matched to $B_{13}C_2$, card 33-225.

Morphology and Microstructure

Due to the high number of deposition experiments, it would be quite cumbersome to display all of the cross-sectional and morphological micrographs. However, nine representative samples are displayed in Figures 2 to 10, showing low, medium, and high relative deposition rates for the three temperatures: 1000, 1200, and 1400°C.

The fracture of the coatings generally produced a very smooth and even surface where the crack moved directly through the compound, a sign of a brittle material. Such behavior was expected from the super-hard $B_{13}C_2$ and enabled the cross-sections to be examined without any polishing.

The changes in the morphology of the coatings reveal some interesting trends in the deposition behavior. The morphologies in all micrographs contain the same features on the surface. All micrographs have well defined facets, typically coming to a sharp point or sharp line. Examining the changes in the morphology as a function of the deposition rate at a constant temperature, it is possible to see that the surface features became larger as the deposition rate increases. This difference was especially accentuated at 1400°C in Figures 8 to 10, where the deposition thickness increases from 31.4 to 41.7 to 75.9 μm , respectively. The surface morphology goes from having a large number of smaller facets at the lowest deposition thickness to having a small number of very large facets at the highest deposition

thickness. The mid-value coating thickness showed a transition between the two morphologies, demonstrating how the facet density decreases and the facet size increased as the deposition rate increased. This same transition in the surface morphology may be seen in the micrographs from the other two temperatures, Figures 2 to 4 and Figures 5 to 7. However, at these lower temperatures, the change in deposition rate was not quite as stark as at the highest temperature, and the resulting surface morphology change was also not as graphic. Only at 1200°C and the highest deposition rate did the morphology not have as large of surface features as might be expected.

Also, the differences in the deposition temperature may be observed among the micrographs. It may be seen that going from lower, to intermediate to high temperatures resulted in changes in the facet density and size, much in the same trend that was previously described in increasing the deposition thickness. However, an accurate comparison of the morphologies in these micrographs was not entirely fair, since the deposition rates among all three temperatures was quite different. A better comparison would be among coatings prepared at different temperatures but having similar deposition thicknesses and growth rates. Such a comparison was possible at 1200 and 1400°C by examining Figures 6 and 8, where the deposition thicknesses were 32.8 μm and 9.11x10⁻⁷ cm/s and 31.4 μm and 11.62x10⁻⁷ cm/s, respectively. There does not appear to be a discernable difference between the two micrographs beyond what might be expected from the differences in the two growth rates, i.e., the facets appeared to be slightly smaller at 1200°C but the deposition rate was also slightly lower leading to somewhat less competitive growth. The result of this lack of difference indicates that the morphology was primarily controlled by the deposition thickness

and the growth rate. Of course, the deposition rate was a strong function of the temperature. Thus, changing the temperature while maintaining the same deposition conditions would produce differing morphologies, but these differences could be attributed to the temperature effect on the nucleation and growth rate.

These changes in the surface morphology may be correlated to the deposition behavior. In general, the surface features are defined by the nucleation and subsequent growth mechanisms. Under conditions where rapid nucleation was favored, i.e., high temperatures and supersaturations, a large number of smaller surface features would be expected because there were so many more grains which can grow. This certainly does not seem to be the case for the samples observed in this study. The size and number of surface features appears to be tied more strongly to the growth rate of the coating. Under high growth conditions, high temperatures and supersaturations again, there appear to be larger and less numerous features on the surface. A possible explanation for this would be a competitive growth mechanism between the active grains. This concept may be visualized as a series of cones growing outward from the substrate surface. As the cones grow longer, their diameter also increases, and they reach the point where they can impinge upon one another and can cut off the growth path of those which are slightly shorter. The result is that at the substrate there are a large number of grains which are nucleated, but moving out from the interface, the number of grains decrease and the size of the grains increase. Therefore, in samples which have thick coatings, the surface features are larger because there was a longer distance for the grains to grow competitively and extinguish the growth of neighboring grains. Thinner deposits under similar deposition conditions had more numerous and smaller

features since they do not have the same length of competitive growth. Examining samples which have similar thicknesses and growth rates but different deposition temperatures was done for DB-153 (31.4 μm) and DB-142 (32.8 μm). These samples have comparable features with only slight differences which can be attributed to the nucleation rate difference due to the temperature difference. Therefore, the morphology of the sample was very much a product of the deposition thickness and growth rate of the sample due to the high amounts of competitive growth which was occurring.

The presence of the well defined features at the surface also points to the high degree of crystallinity of the deposits. Because B_{13}C_2 is composed of light elements, diffraction patterns can be complicated by the low return signal. The linear mass absorption of B_{13}C_2 for Cu K_α radiation, given by the summation of the weight fractions of the components times the linear mass absorption of the individual elements, is $2.45 \text{ cm}^2/\text{g}$. From the linear mass adsorption equation, the transmitted signal through the sample when the sample is 20 μm thick is 98.78%, meaning that only 1.22% of the beam can be diffracted. Increasing the coating thickness to 40 μm decreases the transmitted value to 97.57%, almost doubling the available diffracted beam to 2.43%. Thus, in trying to compare diffraction patterns, it becomes important to keep in mind that the absolute heights of the observed peaks are highly dependent on the coating thickness. As a result, it is often best to observe the relative intensities of the peaks, normalized to the highest observed peak intensity. This information is summarized in Table 7.

The comparison of the relative intensities of the patterns listed in Table 7 does not show a firm relationship with deposition rate or temperature. It was expected that there

would be a trend to a more polycrystalline coating at higher deposition rates and lower temperatures. While there are instances where this trend does exist, such as between DB-231 and DB-228, DB-231 had the higher deposition rate and more polycrystalline pattern. Also, DB-219 showed a higher degree of orientation than DB-216 presumably due to the lower deposition rate in DB-219. However, an overall statement cannot be applied to all of the patterns. For example, a comparison of DB-142 and DB-153 was expected to show a trend towards a more single crystal coating since these deposits had roughly the same deposition rate but were deposited at different temperatures. However, if anything, the lower temperature coating appears to have less polycrystalline character to it.

There did, however, appear to be a change in the orientation of the deposition as the temperature was increased. At 1000°C, the patterns showed the strong presence of the 003 peak, with it being the 100% peak in DB-231 and DB-228 and a 71% peak in DB-233. But, at temperatures above 1000°C, the 003 peak intensity dropped severely and was not seen in several patterns. The 100% peak in all of the patterns from above 1000°C was the 021 peak, the most intense peak listed in JCPDS cards for $B_{13}C_2$, 33-225 and 26-233. Somewhat similarly, the observed intensity for the 018 peak was quite high compared to those seen in coatings produced at higher temperatures where the 018 peak was typically not seen. These differences in the orientations of the patterns may be attributed to the differences in the synthesis temperatures. As has been previously noted, at lower temperatures, the morphology showed smaller and more numerous features. The increased number of observable grains, each with its own orientation, results in a diffraction pattern which represent the orientations of all of the many grains. Comparing to a sample with larger

grains, the increased size of the grains will have a resulting larger representation in the diffraction pattern for the orientations of those select grains. Moreover, at 1000°C, the possibility of having unusual orientations is increased by virtue of the reduced surface mobility of the adsorbed species. As a result, the adsorbed species cannot reorganize themselves into crystallographically favorable locations prior to impingement by an arriving species. Thus, many peaks which would traditionally be much lower in intensity can have disproportionate values due to the nucleation of grains with these unusual orientations. To summarize the somewhat confusing issues involved here, the increased presence of orientations seen at low temperatures which was not seen at higher temperatures was due to the high number of grains which have an increased probability of nucleating with non-prevalent orientations. At higher temperatures, the grains are much larger with more favorable orientations due to the increased ability to reorient themselves from their increased surface mobility.

The examination of selected coatings using transmission electron microscopy (TEM) provided insight as to the nature of the deposition process. Two samples of boron carbide materials were examined. One sample (DB-109) was known to be $B_{13}C_2$ prior to examination, and the other (DB-85) was initially thought to be $B_{12}(B, Si, C)_3$ but was shown to be pure $B_{13}C_2$ by TEM. The XRD patterns for these two samples are shown in Figure 11.

The DB-109 sample was deposited at 1200°C and 76 torr with flows of 11.6 sccm BCl_3 , 46 sccm CH_4 , 81 sccm H_2 , and 4494 sccm Ar. The average coating thickness was 44.1 μm , which corresponded to a deposition rate of 12.2×10^{-7} cm/s. Uncertainty in the BCl_3 flow rate kept it from being used in the study of the reaction rate and allowed it to be

used for TEM examination. A micrograph of the coating-substrate interface is shown in Figure 12. This figure shows the appearance of the long, columnar grains of $B_{13}C_2$ as they grew away from their nucleation site on the graphite substrate. The columnar growth started very close to the interface with the substrate. That is, there was not a wide nucleation zone at the interface. The narrow nucleation zone shows that there was not a significant amount of competitive growth between the active sites. Under conditions where competitive growth was expected, such as high nucleation and growth rates, there would be a large number of nuclei which would form at the interface, but the density of grains would drop as the deposition increased as the coating became dominated by certain grains. The competitive growth process can be visualized as occurring when two grains come together and stop the growth of a grain between the two by occupying the space above the middle grain. The middle grain cannot therefore grow any further, and it is terminated at that point. An explanation for the lack of competitive growth could be that nucleation for all of the grains occurred close together and that the growth rate for all of these grains was roughly the same. The growth front away from the substrate would then be roughly constant and would not allow large amounts of intrusion of neighboring grains into each other. The diameter of the grains was on the order of 0.5 to 1.5 μm throughout the sample. This represents a fairly fine-grained specimen and was the smallest grain size of the samples examined.

Figure 13 shows a planar view of the same sample a distance away from the interface, confirming the columnar structure of the grains, i.e., the high length to width ratio. However, this micrograph also indicates that the cross-section of the columnar grains was rectangular instead of having a circular component. The width of the grains from this

view is between 1 and 5 μm , showing that the grains are growing competitively away from the substrate. This was in keeping with the features seen in the surface morphology, shown in Figure 14, where the somewhat rectangular surface facets ranged between 1 and 20 μm across.

The grains in Figure 12 also contain a feather-like structure which might imply a helical type growth. In such a mechanism, growth would start from a central nucleus, but, due to interfacial energy considerations, the reagents are more likely to adsorb and deposit onto the nucleus than they are on the substrate. As a result, deposition occurs preferentially onto the nucleus, as opposed to the substrate. The outcome would be grains which would grow rapidly due to the preferential adsorption, as opposed to nucleating rapidly due to the easy adsorption of species to the surface. As growth occurred, species would deposit at the low energy sites at the surface, i.e., a ledge. As the deposition occurs, the position of the ledge moved about the surface as material was deposited, often approximating a sweeping circular arm. This results in a helical grain which moved away from the interface. Such a mechanism could result during island growth but is highly dependent on the intrinsic properties of the substrate, deposit, and reagents, making it hard to quantify the observations. However, the result of depositing in an island growth regime would be the presence of columns in the microstructure.

The other boron carbide sample which was examined was DB-85, produced at 1200°C, 76 torr, and flows of 7.0 sccm BCl_3 , 5.5 sccm SiCl_4 , 31.5 sccm CH_4 , 112 sccm H_2 , and 5000 sccm Ar. As was previously mentioned, this sample was thought to be composed of $\text{B}_{12}(\text{B},\text{Si},\text{C})_3$ based on XRD and EDS measurements. However, analysis using parallel

electron energy loss spectroscopy (PEELS) failed to reveal the presence of any Si in the coating, and electron diffraction patterns showed a good match to $B_{13}C_2$, but the differences between the two patterns, $B_{13}C_2$ and $B_{12}(B,Si,C)_3$, are very slight and complete identification using only diffraction would be unwise without further confirmation. In the case of the areas examined in this TEM specimen, no Si was found in the coating, and the deposit was therefore concluded to be $B_{13}C_2$ in the region studied. Figure 15 is the image of the substrate-coating interface from this sample. Again, the deposit has a columnar growth pattern which began close to the substrate. Also, the nucleation zone is not very wide; a phenomenon observed previously in the DB-109 sample. The grain size of DB-85 was larger than that seen in DB-109. The change in grain size might be accounted for by the difference in the BCl_3 flow rate, 7.0 sccm in DB-85 versus 11.6 sccm in DB-109. Under higher supersaturations of BCl_3 , the nucleation rate should be slightly higher, resulting in a narrower grain size at the interface since there would initially be more nuclei produced. Thus, the observed larger grain size could result from fewer numbers of nuclei being formed in DB-85 due to the lower supersaturation.

A planar view of DB-85 is shown in Figure 16. This grain seems to show more of a star-like quality to its shape and ranges between 6 and 11 μm across. The presence of a central point in the grain argues for the possible confirmation of a helical growth mechanism within a columnar grain. The electron diffraction pattern for this grain is also included in Figure 16. The spots are indicative of a single crystal grain, as expected, but the spreading of the spots points to finite crystallite dimensions in the plane of view, i.e., within the planar

image. The possibility then exists for either columnar crystallites or for simply very small crystallites in all directions.

Deposition Mechanism

The development of functional relationships between the observed deposition and the experimental conditions is an important step towards understanding and optimizing the process. It was important that the model for deposition of $B_{13}C_2$ involve the use of both the diffusional and kinetic characteristics of the reaction to determine the intrinsic reaction parameters. The principle response variable in this type of analysis is the deposition rate, determined from an average of ten measurements made on the cross-sectional micrograph.

The first step in the reaction rate determination was to establish the relationship between the reagent concentrations and the reaction rate, i.e., the order of the reaction with respect to the reagents. The reaction rate of $B_{13}C_2$, $J_{B_{13}C_2}$, in mole/(cm²•s) was calculated by the following equation:

$$J_{B_{13}C_2} = \frac{r_D \rho_{B_{13}C_2}}{MW_{B_{13}C_2}} \quad (7)$$

where r_D was the average deposition rate in cm/s, $\rho_{B_{13}C_2}$ was the density of $B_{13}C_2$ (2.49 g/cm³), and $MW_{B_{13}C_2}$ was the molecular weight of $B_{13}C_2$ (164.552 g/mole).

The form of the kinetic expression has been a source of some contention, as was indicated in the Background section. To try to establish the general order of the reaction, the conditions which were used in the boron carbide deposition were input into the statistical analysis program Minitab 7.2, along with the observed deposition rate for the isothermal conditions. Minitab was then used in a no constant, stepwise regression mode using the

main, quadratic, and cross-product effects. The stepwise regression procedure examined each of the input regressors individually and selected the regressor with the highest t-ratio over some minimum criterion and added it to the regression equation. The procedure then completed the regression using the added regressors to calculate the standard deviation and R^2 value. The program then selected another regressor to add to the equation which would minimize the standard deviation and maximize the value of R^2 . This process continued until no regressors could be added whose t-ratio was over the minimum criterion. For all temperatures, stepwise regression revealed that the significant regressor was the concentration of BCl_3 . This fact is important in that no interactions were determined to be significant, such as a $\text{BCl}_3 \cdot \text{CH}_4$ interaction which would point to a surface reaction between the adsorbed BCl_3 and CH_4 . Also, the missing presence of a CH_4 main or quadratic effect indicates that it might be omitted in the kinetic expression.

From this analysis, it was therefore assumed that the deposition of B_{13}C_2 could be accurately described as first order with respect to the BCl_3 concentration, such that the following expression could be used to describe the deposition:

$$J_{\text{B}_{13}\text{C}_2} = k_{\text{B}_{13}\text{C}_2} [\text{BCl}_3]^* \quad (8)$$

where $J_{\text{B}_{13}\text{C}_2}$ was the reaction rate of B_{13}C_2 in mole/($\text{cm}^2 \cdot \text{s}$), $k_{\text{B}_{13}\text{C}_2}$ was the rate constant of B_{13}C_2 in cm/s, $[\text{BCl}_3]^*$ was the concentration of BCl_3 on the surface, R was the gas constant, and T was the absolute temperature.

Under steady state conditions, the net rate of production of B_{13}C_2 should be equal to the net rate of mass transfer across the boundary layer. The rate of mass transfer across the concentration boundary layer can be approximated by the expression,

$$J_{\text{BCl}_3} = \frac{D_{\text{BCl}_3}}{\delta_{\text{BCl}_3}} ([\text{BCl}_3]^o - [\text{BCl}_3]^s) \quad (9)$$

where D_{BCl_3} was the binary diffusion coefficient of BCl_3 in Ar in cm^2/s , δ_{BCl_3} was the concentration boundary layer thickness of BCl_3 in cm, and $[\text{BCl}_3]^o$ was the concentration of BCl_3 in the bulk gas phase. The calculation of the diffusion coefficient and the boundary layer thickness of BCl_3 has been outlined elsewhere.³² Solving Equation 8 for $[\text{BCl}_3]^s$ and substituting into Equation 9 under the assumption of steady state, i.e., $J_{\text{B}_{13}\text{C}_2} = J_{\text{BCl}_3}$, the resulting expression for $J_{\text{B}_{13}\text{C}_2}$ which now accounts for both the kinetic and mass transfer effects of the deposition reaction is described by:

$$J_{\text{B}_{13}\text{C}_2} = \frac{1}{\left(\frac{1}{k_{\text{B}_{13}\text{C}_2}} + \frac{\delta_{\text{BCl}_3}}{D_{\text{BCl}_3}} \right)} [\text{BCl}_3]^o \quad (10)$$

Van den Brekel³³ and later Jensen³⁴ described the $(1/k_{\text{B}_{13}\text{C}_2})$ term as the kinetic resistance to reaction and the $(\delta/D)_{\text{BCl}_3}$ term as the mass transfer resistance to deposition. In other words, as long as the kinetic rate constant is small compared to the mass transfer rate, such as would be expected in a kinetic-controlled regime, the $(1/k_{\text{B}_{13}\text{C}_2})$ term will dominate the denominator of Equation 10, and the overall equation can be approximated by a kinetic expression, such as:

$$J_{\text{B}_{13}\text{C}_2} \sim k_{\text{B}_{13}\text{C}_2} [\text{BCl}_3]^o \quad (11)$$

However, as the kinetic term begins to rise and approaches the mass transfer term, the denominator of Equation 10 results from the summation of the two effects. This situation

would occur as the reaction moves from a kinetic to a mass transfer limited regime. Finally, as the kinetic constant becomes much higher than the mass transfer, the denominator would be controlled by the mass transfer term, and Equation 10 could be approximated by:

$$J_{B_{13}C_2} \sim \left(\frac{D}{\delta}\right)_{BCl_3} [BCl_3]^0 \quad (12)$$

The use of Equation 10 is then an important method to illustrate how one process may become rate limiting and may be used to estimate the temperature and flow conditions at which the reaction would transition from a kinetic to a mass transfer limitation.

The validity of the overall reaction expression was checked by plotting the reaction rate versus the inlet BCl_3 concentration for all temperatures. These graphs are shown in Figures 17 to 19 for 1000, 1200, and 1400°C, respectively. The linear relationship between the reaction rate and $[BCl_3]^0$ does not, however, determine whether mass transfer or kinetics was controlling the deposition. There are two ways in which the regime may be ascertained: altering the total flow through the reactor and changing the system temperature. Increasing the total flow through the system would test for the mass transfer limitation since an increase in the total flow would result in the thinning of the boundary layer, thereby increasing the flux to the substrate. If the reaction was limited by this flux to the surface, i.e., mass transfer controlled, the observed deposition rate should increase; if the reaction was limited by the kinetics of the surface reaction, there should be no change in the observed deposition rate. An increase in the system temperature would be observed in the kinetic rate constant, as the rate constant is defined from the traditional Arrhenius relation where,

$$k_{B_{13}C_2} = k_{B_{13}C_2}^o e^{-\frac{E_a}{RT}} \quad (13)$$

where $k_{B_{13}C_2}^o$ is the frequency factor in cm/s and E_a is the activation energy in kJ/mole. An estimation of E_a can be made from a plot of the natural logarithm of $J_{B_{13}C_2}/[BCl_3]$ versus the inverse absolute temperature. The intercept of the regressed line is then the estimate of the frequency factor, $k_{B_{13}C_2}^o$, and the slope is an estimate of $-E_a/R$.

The Arrhenius plot of $\ln(B_{13}C_2)$ versus $1/T$ is included in Figure 20. The result of the regressed line estimates the intercept of the line to be 9.287 with a standard deviation of 0.178 and the slope to be -11197 with a standard deviation of 339.2. Regression produced an R^2 value of 96.1%, adjusting R^2 for the number of degrees of freedom reduced it slightly to 96.0%. The F statistic, used to determine the significance of regression, was 1089.6, making the probability of a Type I error, i.e., $P(\text{accept } H_0 \mid H_A)$, less than 0.0001. Based on this computation the value of the activation energy would be 93.1 kJ/mole (22.2 kcal/mole) with a standard deviation of 2.8 kJ/mole (0.7 kcal/mole). The form of the kinetic constant as a function of temperature is then given by:

$$k_{B_{13}C_2} = 10792 e^{(-\frac{93,100}{RT})} \quad (14)$$

where R is the gas constant in kJ/(mole•K) and T is the absolute temperature.

A comparison of the value of the activation energy for this system to other published values is hard since there have been so few values which have been reported. The only reported value came from Lartigue et al.³⁴ at approximately 90 kcal/mole. Obviously this number is significantly higher, by a factor of about 4 than the current reported value. There

are some substantial differences between the results which were reported by that group and this study. Most importantly, they found that they were in a kinetic regime at temperatures below 950°C and transitioned to a mass transfer regime at higher temperatures. Whereas, this study operated at the range of 1000 to 1400°C and found no evidence of mass transfer under regular conditions, although the high dilutions of active reagents might have kept the reaction within a kinetic regime. Moreover, Lartigue et al. indicated that, because of the determined activation energy, CH₄ had to be a predominant step towards deposition with an order of one. Based on the findings within this study, the effect of CH₄ was insignificant to the deposition within this temperature range. Thus, a fair comparison between the two is difficult, at best, and does not provide an accurate check for the validity of the results found in this system.

The determination of the simple kinetic relationship between the BCl₃ concentration and the reaction rate allows for some speculation on the possible surface mechanisms. The first order relationship with respect to the surface concentration would indicate that the rate limiting step to deposition may be either the adsorption of BCl₃ onto empty surface sites or a surface reaction between the two adsorbed species.

One of the possible ways to check for an adsorption mechanism involves working with different substrate materials. Since adsorption is a strong function of the intrinsic material properties, i.e., surface free energy considerations, working with a different substance should result in a different deposition rate. Because graphite is traditionally a weak adsorber, i.e., species do not readily adsorb onto graphite, the use of another substrate should increase the deposition rate. The use of titanium substrates was attempted in three

experiments. However, this type of metal had significant problems with the formation of a barrier layer between the substrate and the coating, most likely due to the high diffusivity of Ti in boron carbide, or possibly of B into Ti. The interdiffusion between the substrate and coating made measurements of the coating thickness complicated. Since Ti is a heavy element, especially compared to B and C, its presence in the coating was quite obvious. The extent to which the Ti interacted with the coating kept those runs from being considered since the density differences between $B_{13}C_2$ and the Ti-B compounds are significant, making any measurement of the deposition rate uncertain without taking into account the amount of the Ti-B phases. The possibility of other substrate materials was considered, but problems with thermal expansion mismatch with the very brittle coating and the risk of similar boundary layer problems deterred their use.

However, it was possible to make a statement regarding the adsorption of BCl_3 based on the TEM micrographs which were taken of the nucleation zone. Based on some of the observations regarding the morphology and microstructure of $B_{13}C_2$, it was possible to hypothesize that the adsorption of BCl_3 was extremely significant to the deposition of $B_{13}C_2$. This statement is possible based on the observed columnar growth away from the nucleation site, theorized to be an island growth mechanism. The important point to the island growth theory is disaffinity which the reagents have with the substrate surface, as evidenced by the long thin grains exemplified in Figure 12. If the adsorption of BCl_3 is slow onto the graphite surface compared to that of $B_{13}C_2$, then it becomes possible that its adsorption could be a rate limiting step. While this was not conclusive evidence for a surface adsorption mechanism

and the idea of a surface reaction has not been discounted at all, it did establish the possibility for adsorption-limitations.

The ability to move into a region controlled by diffusion was attempted by operating the reactor at higher pressures. Increasing the system pressure has the effect of decreasing the diffusion coefficient within the pseudobinary mixture, since the diffusion coefficient is related to the inverse system pressure. By raising the pressure, the diffusion coefficient should decrease, and, depending on the kinetics at the operating conditions, the reaction may transition into a mass transfer control regime. Four runs were done at 700, 500, 300, and 76 torr (DB-368 to DB-370 and DB-207) to attempt to examine the pressure effect. If the reaction is still in a kinetic regime at this point, then the ratio of the reaction rate to the BCl_3 bulk concentration should be a constant since the kinetic rate constant is only a function of the system temperature. However, examining this ratio showed that it moved from 2.273 to 2.407 to 3.750 to 5.397, as the pressure decreased from 700 to 76 torr. A plot of these values versus the system pressure is included in Figure 21. The trend in these values indicated that mass transfer was not negligible. Also in this figure are the calculated values of the kinetic rate constant and the mass transfer constant, along with the unified rate constant, based on Equation 10. There does appear to be some mismatch between the unified kinetic-mass transfer line and the observed data. However, the two lines do have the same form, i.e., initially dropping sharply before approaching some constant value at high pressures. The observed difference may be attributed to several factors in the calculation of the diffusion coefficient. Primarily, there could be some error tied to the use of the Chapman-Enskog coefficient to determine the diffusion coefficient for the given gas mixture;

also, there could be some uncertainty to the exact physicochemical properties of the reagent species. The ability to account for the transition from a kinetic to a mass transfer limited regime was, however, made possible by the use of the Chapman-Enskog equation.

As has been previously mentioned, the estimation of the diffusion coefficient by the Slattery-Bird equation was used to check against errors in the Chapman-Enskog equation. However, values of the diffusion coefficient and the resulting mass transfer coefficient were consistently five times higher in the Slattery-Bird coefficient than in the Chapman-Enskog coefficient. While this is unimportant in a kinetic controlled regime, it becomes a more serious problem as the observed deposition begins to move into an apparent mass transfer regime. That is to say that within the example of variation in the system pressure just covered the unified kinetic-mass transfer coefficient is still dominated by the kinetic contribution at 700 torr, i.e. 91% kinetic, using the Slattery-Bird coefficient versus a 65% kinetic response using the Chapman-Enskog equation. Thus, the Chapman-Enskog is better able to approximate the observed data, and its use was favored over the Slattery-Bird equation.

Conclusions

The work contained within this paper revealed that the deposition of $B_{13}C_2$ was possible from low pressure mixtures of BCl_3 - CH_4 - H_2 -Ar in the temperature range of 1000 to 1400°C. These coatings were examined using XRD, SEM, and TEM. From these observations, the surface morphology was found to be comprised of well defined facets whose size increased with deposition thickness and deposition rate. This indicated the presence of a

highly competitive growth mechanism following nucleation. TEM of the coating-substrate interface showed a narrow nucleation zone which pointed to a large difference between the nucleation rate and the growth rate. In this case (i.e., onto ATJ graphite substrates), the growth rate was high when compared to the nucleation rate, resulting in the columnar grains observed through the material.

The deposition mechanism was found to be accurately described by a first order mechanism, with respect to the BCl_3 bulk gas phase concentration. Within the range studied, the reaction was found to be kinetically controlled with an activation energy of 93.1 kJ/mole and a frequency factor of 10792 cm/sec. The interaction with the substrate was examined to investigate the nature of the limiting step to deposition. Several other substrates were used, but problems with the thermal expansion differences (especially with Al_2O_3) and with barrier layers (especially with Ti) prevented their continued use. Finally, the reaction rate was monitored as a function of the system pressure. As the pressure increased towards atmospheric, the rate was found to begin to transition to a mass transfer limited regime. Calculation of the overall mass transfer coefficient was best estimated using the Chapman-Enskog diffusion coefficient as opposed to using the Slattery-Bird diffusion equation, which yielded values that were too high.

Acknowledgments

We wish to thank Dr. Alexander Pechenik of the Air Force Office of Scientific Research for funding and supporting this research. We also appreciate typing of the original manuscript by Virginia Myers.

REFERENCES

- ¹G. Will and K.H. Kossobutzki, "An X-Ray Structure Analysis of Boron Carbide, $B_{13}C_2$," *J. Less-Common Met.*, **44**, 87-97 (1976).
- ²G. Will, A. Kirfel, and A. Gupta, "Is the Concept of Boron Icosahedra in Boron Carbide Correct?" *J. Less-Common Met.*, **67**, 13-8 (1979).
- ³Stumpf, "Boron and Carbon," pp 117-216 in Gmelin Handbook of Inorganic Chemistry, Supplement Vol. 2, ed. K.C. Buschbeck, Springer-Verlag, New York, 1981.
- ⁴P.A. Dearnley and T. Bell, "Engineering the Surface with Boron Based Materials," *Surface Eng.*, **1**, 203-17 (1985).
- ⁵P. Hedenqvist, M. Olsson, B. Stridh, and S. Soderberg, "Solid Particle Erosion of Hard Chemically Vapour Deposited Coatings," *Surface and Coat. Tech.*, **37**, 321-37 (1989).
- ⁶C. Wood, "Boron Carbides as High Temperature Thermoelectric Materials," pp 362-72 in AIP Conference Proceedings, Vol. 140 (Boron Rich Solids), ed. D. Emin, et al., American Institute of Physics, New York, 1986.
- ⁷L. Vandenbulcke and G. Vuillard, "Kinetics in the Chemical Vapor Deposition of Boron Carbide," pp 95-103 in Proceedings of the Eighth International Conference on Chemical Vapor Deposition. Edited by J.M. Blocher, Jr., G.E. Vuillard, and G. Wahl. The Electrochemical Society, Princeton, New Jersey, 1981.
- ⁸U. Jansson and J-O Carlsson, "Chemical Vapour Deposition of Boron Carbides in the Temperature Range 1300-1500 K and at Reduced Pressure," *Thin Solid Films*, **124**, 101-7 (1985).
- ⁹S. Lartigue and G. Male, "Contribution to the Study of Tetragonal Compounds in the Boron Carbon System," *J. Mat. Sci. Let.*, **7**, 153-6 (1988).

¹⁰K. Ploog, "Composition and Structure of Boron Carbides Prepared by CVD," *J. Cryst. Growth*, **24/25**, 197-204 (1974).

¹¹G. Will and K.H. Kossobutzki, "An X-Ray Diffraction Analysis of Boron Carbide, $B_{13}C_2$," *J. Less-Common Met.*, **47**, 43-8 (1976).

¹²H.O. Pierson and A.W. Mullendore, "The Chemical Vapor Deposition of Boron from Diborane," pp 360-7 in Proceedings of the 7th International Conference on Chemical Vapor Deposition, ed. T.O. Sedgwick, et al., The Electrochemical Society, Princeton, New Jersey, 1979.

¹³S. Vaidyaraman, W.J. Lackey, P.K. Agrawal, G.B. Freeman, E.K. Barefield, and J.S. Lewis, "Chemical Vapor Deposition of Boron-Carbon Films Using Organometallic Reagents," submitted to *J. Alloys Comp.*, 1995.

¹⁴J. Kouvetakis, R.B. Kaner, M.L. Sattler, and N. Bartlett, "A Novel Graphite-Like Material of Composition BC_3 , and Nitrogen-Carbon Graphites," *J. Chem. Soc., Chem. Communications*, 1758-9 (1986).

¹⁵U. Jansson and J-O Carlsson, "Area Selective Chemical Vapor Deposition of Boron Achieved by Molecular Masking," *J. Vac. Sci. Technol.*, **A6**, 1753-5 (1988).

¹⁶A.W. Mullendore, "Chemical Vapor Deposition of Boron-Based Refractory Solids," pp 41-50 in Boron-Rich Solids. Edited by D. Emin, T. Aselage, C.L. Beckel, I.A. Howard, and C. Wood. The American Institute of Physics, New York, 1986.

¹⁷D.N. Kevill, T.J. Rissmann, D. Brewe, and C. Wood, "Growth of Crystals of Several Boron-Carbon Compositions by Chemical Vapor Deposition," *J. Cryst. Growth*, **74**, 210-6 (1986).

¹⁸R.P. Gower, J. Hill, and D.G. Horne, "Some Aspects of Methane Pyrolysis in Contact with Graphite," pp 638-40 in Proceedings of the Seventh International Conference on Chemical Vapor Deposition. Edited by T.O. Sedgwick and H. Lydtin. The Electrochemical Society, Princeton, New Jersey, 1979.

¹⁹U. Jansson, J.-O. Carlsson, and B. Stridh, "Initial Stages of Growth during Boron Carbide Chemical Vapor Deposition," *J. Vac. Sci. Technol.*, **A5**, 2823-28 (1987).

²⁰H. Hanache, F. Langlais, and R. Naslain, Kinetics of Boron Carbide Chemical Vapor Deposition and Infiltration," pp 219-33 in Proceedings of the Fifth European Conference on Chemical Vapour Deposition. Uppsala University, Department of Chemistry, Uppsala, Sweden, 1985.

²¹H. Rebenne and R. Pollard, "Theoretical Analysis of Chemical Vapor Deposition of Ceramics in an Impinging Jet Reactor," *J. Am. Ceram. Soc.*, **70**, 907-18 (1987).

²²L. Vandenbulcke, "Mass Transfer, Equilibrium, and Kinetics in the CVD of a Polycomponent System: Application to Boron-Carbon," pp 315-31 in Proceedings of the Seventh International Conference on Chemical Vapor Deposition. Edited by T.O. Sedgwick and H. Lydtin. The Electrochemical Society, Princeton, New Jersey, 1979.

²³M.S. Dariel, S. Agam, G. Kimmel, O. Leibovitis, D. Edelstein, and Z. Barkay, "CVD of Boron Carbide as Coating and Matrix Material," *Israel J. Technol.*, **24**, 511-6 (1988).

²⁴S. Lartigue, D. Cazajous, M. Nadal, and G. Male, "Study of Boron Carbides Vapor-Deposited under Low Pressure," pp 413-9 in Proceedings of the Fifth European Conference on Chemical Vapour Deposition. Uppsala University, Department of Chemistry, Uppsala, Sweden, 1985.

²⁵S. Lartigue and G. Male, "Contribution to the Study of Tetragonal Compounds in the Boron Carbon System," *J. Mat. Sci. Let.*, **7**, 153-6 (1988).

²⁶U. Jansson, J.-O. Carlsson, B. Stridh, S. Soderberg, and M. Olsson, "Chemical Vapour Deposition of Boron Carbides, I: Phase and Chemical Composition," *Thin Solid Films*, **172**, 81-93 (1989).

²⁷M. Olsson, S. Soderberg, B. Stridh, U. Jansson, and J.-O. Carlsson, "Chemical Vapour Deposition of Boron Carbides, II: Morphology and Microstructure," *Thin Solid Films*, **172**, 95-109 (1989).

²⁸D.M. Bylander and L. Kleinman, "Structure of $B_{13}C_2$," *Phys. Rev. B*, **43**, 1487-91 (1991).

²⁹U. Jansson, "Chemical Vapor Deposition of Boron Carbides," *Mat. Manufact. Proc.*, **6**, 481-500 (1991).

³⁰I.D.R. Mackinnon, "High Resolution Imaging of Boron Carbide Microstructures," pp 114-20 in AIP Conference Proceedings, Vol. 140 (Boron Rich Solids), ed. D. Emin, et al., American Institute of Physics, New York, 1986.

³¹D.-T. Chin and C.-H. Tsang, "Mass Transfer to an Impinging Jet Electrode," *J. Electrochem. Soc.*, **125**, 1461-70 (1978).

³²T.S. Moss, "The Chemical Vapor Deposition of Dispersed Phase Composites in the B-Si-C-H-Cl-Ar System," Ph.D. Thesis, Georgia Institute of Technology, 1995.

³³C.H.J. van den Brekel, "Characterization of Chemical Vapour Deposition Processes," *Philips Res. Repts.*, **32**, 118-33 (1977).

³⁴K.F. Jensen, "Modelling of Chemical Vapor Deposition Reactors," pp 3-20 in Proceedings of the Ninth International Conference on Chemical Vapor Deposition. Edited by

McD. Robinson, C.H.J. van den Brekel, G.W. Cullen, J.M. Blocher, Jr., and P. Rai-
Choudhury. The Electrochemical Society, Pennington, New Jersey, 1984.

LIST OF FIGURES

- Figure 1. A vertical hot wall reactor was used to deposit coatings using the $\text{BCl}_3\text{-CH}_4\text{-H}_2\text{-Ar}$ system.
- Figure 2. Cross-section (a) and surface morphology (b) of boron carbide film deposited on graphite at 1000°C and a deposition rate of 2.109×10^{-7} cm/s (DB-233).
- Figure 3. Cross-section (a) and surface morphology (b) of boron carbide film deposited on graphite at 1000°C and a deposition rate of 3.722×10^{-7} cm/s (DB-231).
- Figure 4. Cross-section (a) and surface morphology (b) of boron carbide film deposited on graphite at 1000°C and a deposition rate of 5.339×10^{-7} cm/s (DB-228).
- Figure 5. Cross-section (a) and surface morphology (b) of boron carbide film deposited on graphite at 1200°C and a deposition rate of 6.379×10^{-7} cm/s (DB-140).
- Figure 6. Cross-section (a) and surface morphology (b) of boron carbide film deposited on graphite at 1200°C and a deposition rate of 9.112×10^{-7} cm/s (DB-142).
- Figure 7. Cross-section (a) and surface morphology (b) of boron carbide film deposited on graphite at 1200°C and a deposition rate of 21.63×10^{-7} cm/s (DB-208).
- Figure 8. Cross-section (a) and surface morphology (b) of boron carbide film deposited on graphite at 1400°C and a deposition rate of 11.62×10^{-7} cm/s (DB-153).
- Figure 9. Cross-section (a) and surface morphology (b) of boron carbide film deposited on graphite at 1400°C and a deposition rate of 23.19×10^{-7} cm/s (DB-219).
- Figure 10. Cross-section (a) and surface morphology (b) of boron carbide film deposited on graphite at 1400°C and a deposition rate of 37.19×10^{-7} cm/s (DB-216).
- Figure 11. X-ray diffraction patterns of DB-109 (a) and DB-85 (b), two samples examined using TEM.

- Figure 12. Transmission electron micrograph of $B_{13}C_2$ (DB-109) shows long columnar grains which are about 0.5 to 1.5 μm across.
- Figure 13. The TEM micrograph for the planar view of Sample DB-109 (seen in Figure 11) displays the rectangular shape of the $B_{13}C_2$ grains.
- Figure 14. The morphology of Sample DB-109 from an SEM micrograph shows features on the order of size seen in the TEM planar view.
- Figure 15. The TEM micrograph of Sample DB-85 at the interface between the substrate and the coatings shows wider columnar grains than in Sample DB-109 (Figure 11).
- Figure 16. The TEM micrograph of Sample DB-85 displays the star-like quality of the grains.
- Figure 17. The reaction rate versus BCl_3 bulk concentration at 1000°C verifies a first order relationship between the two quantities.
- Figure 18. The reaction rate versus BCl_3 bulk concentration at 1200°C verifies a first order relationship between the two quantities.
- Figure 19. The reaction rate versus BCl_3 bulk concentration at 1400°C verifies a first order relationship between the two quantities.
- Figure 20. The Arrhenius plot for $B_{13}C_2$ deposition at three temperatures shows that deposition is limited by the kinetics of the reaction instead of by the mass transfer to the substrate.
- Figure 21. Increasing the system pressure at 1200°C caused the $B_{13}C_2$ deposition to transition from a heavily kinetic regime into a mixed kinetic-mass transfer limited regime.

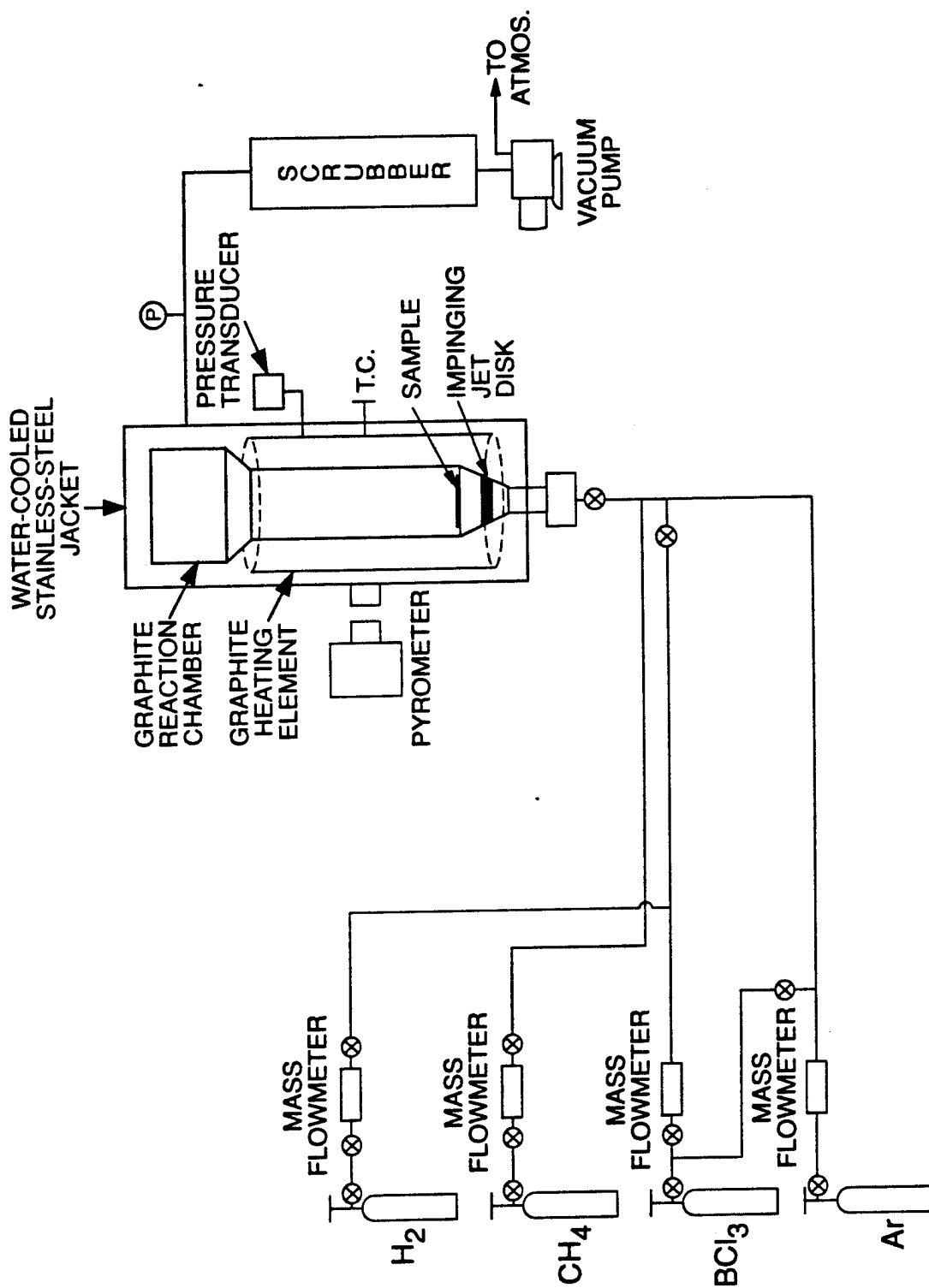
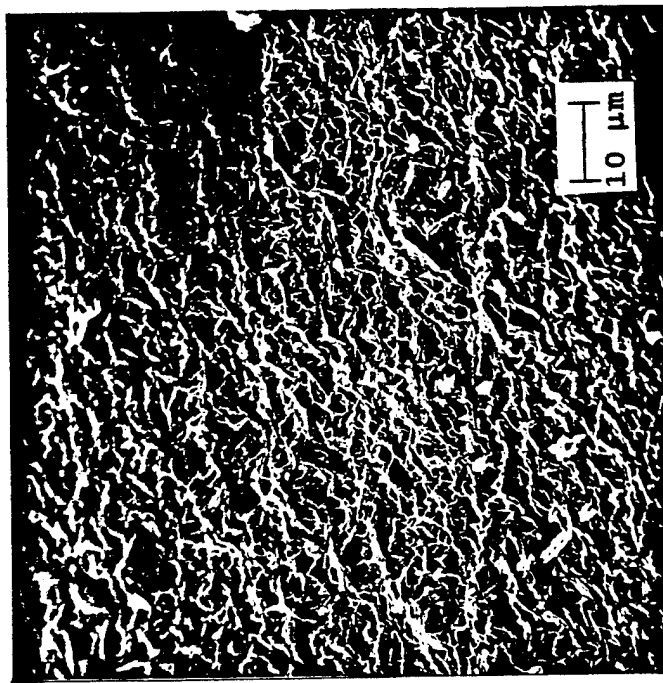


Figure 1. A vertical hot wall reactor was used to deposit coatings using the BCl_3 - CH_4 - H_2 - Ar system.

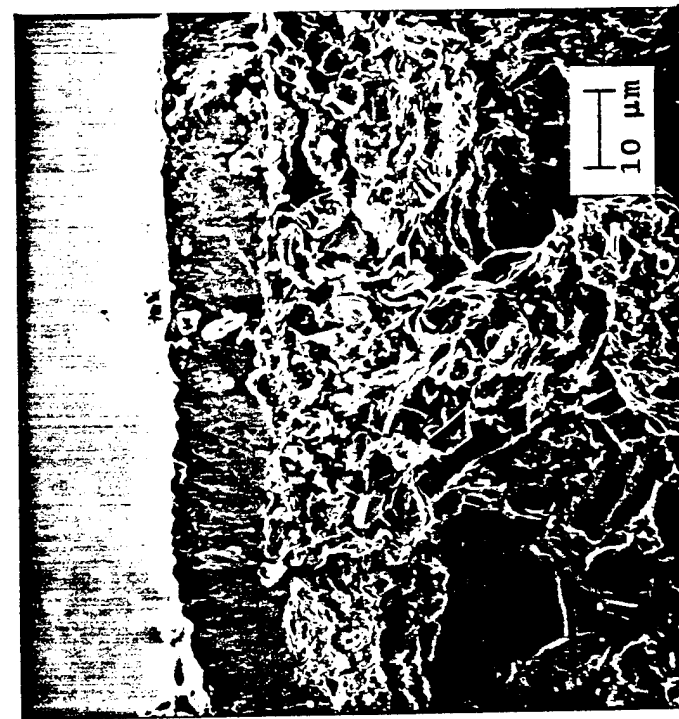


(a)

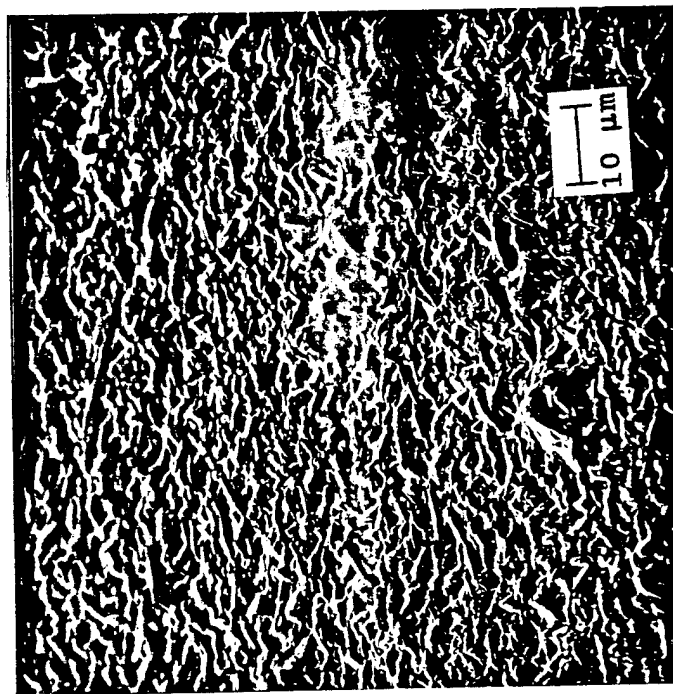


(b)

Figure 2. Cross-section (a) and surface morphology (b) of boron carbide film deposited on graphite at 1000°C and a deposition rate of 2.109×10^{-7} cm/s (DB-233).

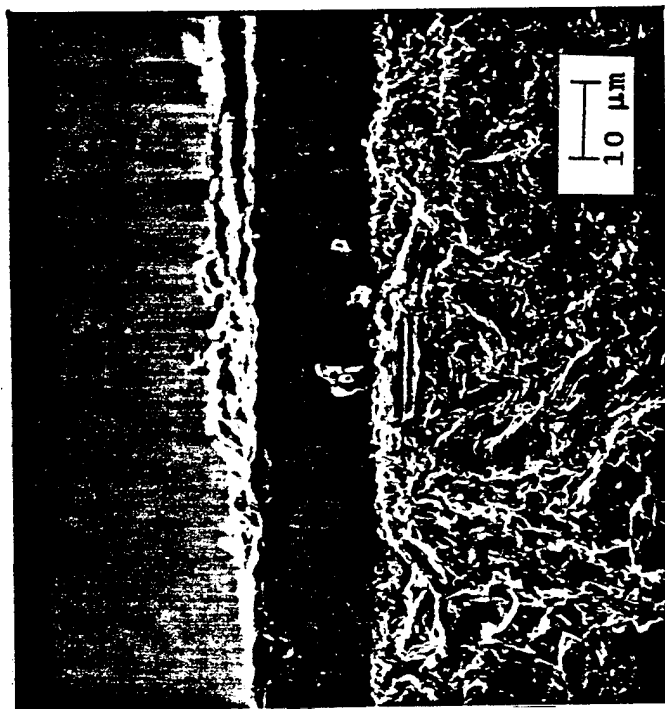


(a)



(b)

Figure 3. Cross-section (a) and surface morphology (b) of boron carbide film deposited on graphite at 1000°C and a deposition rate of 3.722×10^{-7} cm/s (DB-231).

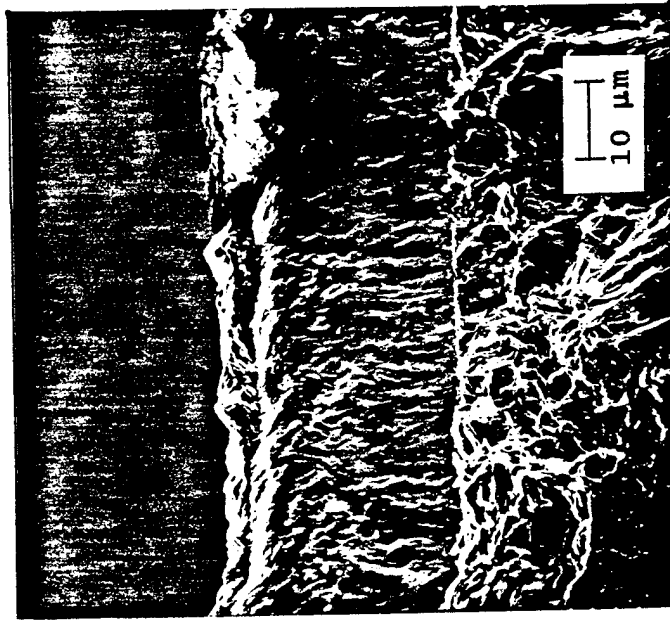


(a)

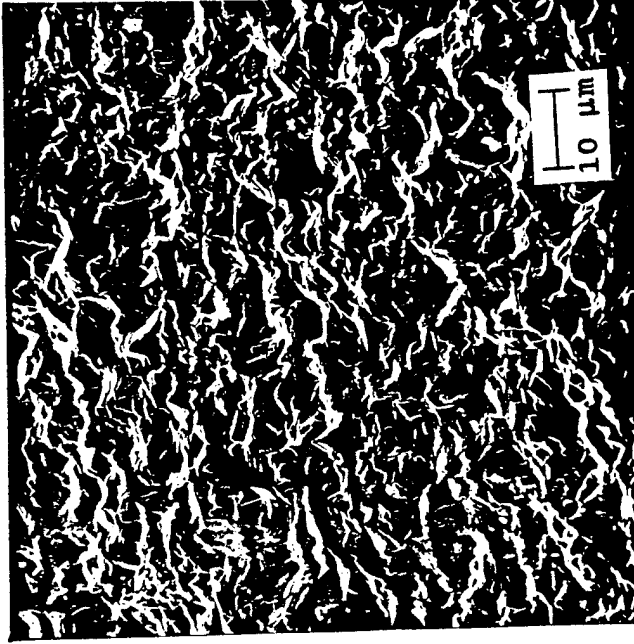


(b)

Figure 4. Cross-section (a) and surface morphology (b) of boron carbide film deposited on graphite at 1000°C and a deposition rate of 5.339×10^{-7} cm/s (DB-228).

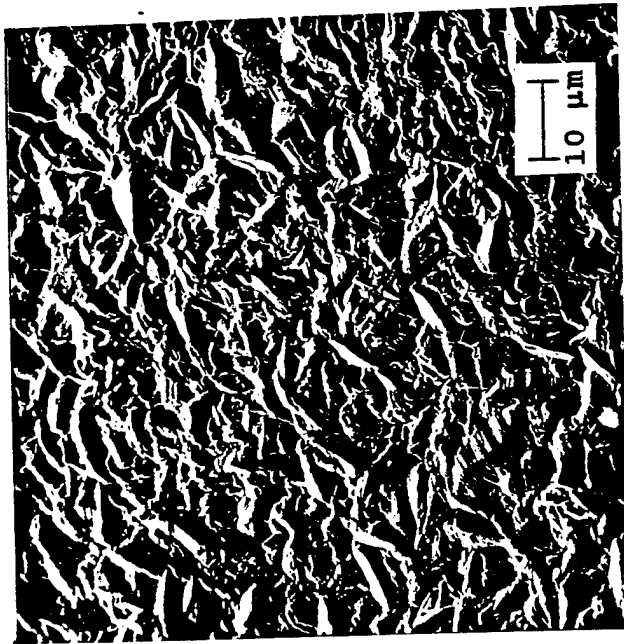


(a)

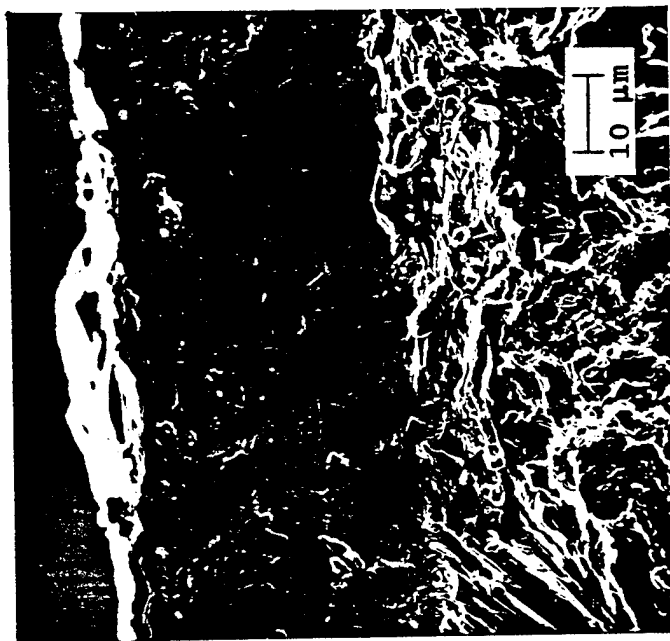


(b)

Figure 5. Cross-section (a) and surface morphology (b) of boron carbide film deposited on graphite at 1200°C and a deposition rate of 6.379×10^{-7} cm/s (DB-140).

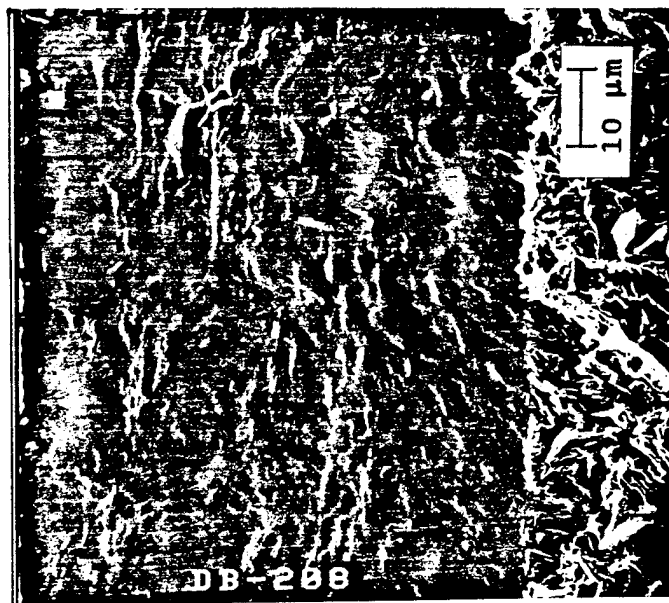


(b)

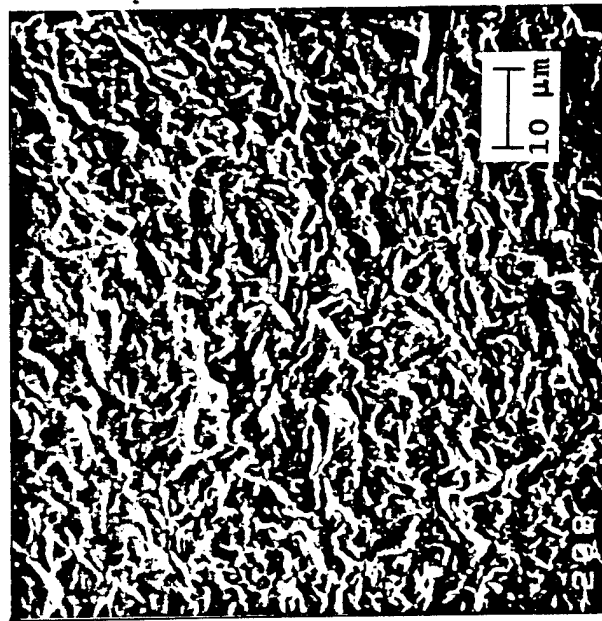


(a)

Figure 6. Cross-section (a) and surface morphology (b) of boron carbide film deposited on graphite at 1200°C and a deposition rate of 9.112×10^{-7} cm/s (DB-142).

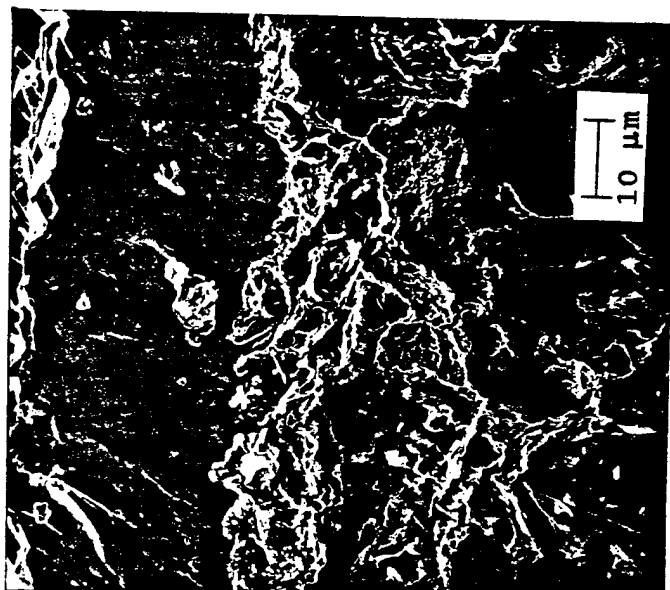


(a)

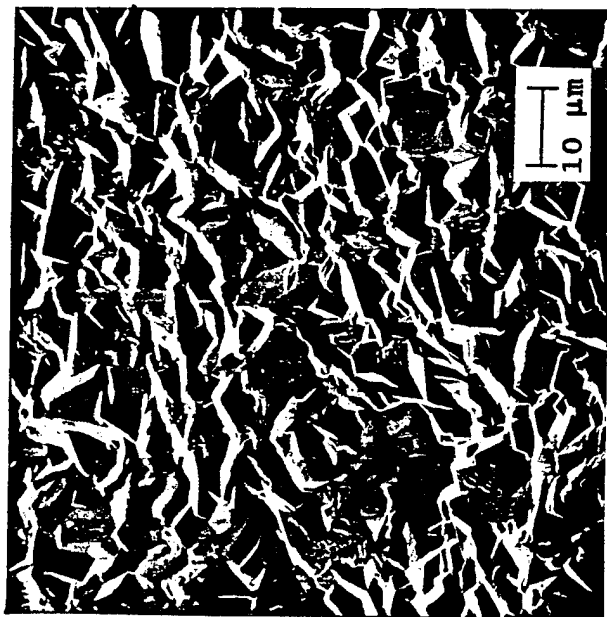


(b)

Figure 7. Cross-section (a) and surface morphology (b) of boron carbide film deposited on graphite at 1200°C and a deposition rate of 21.63×10^{-7} cm/s (DB-208).

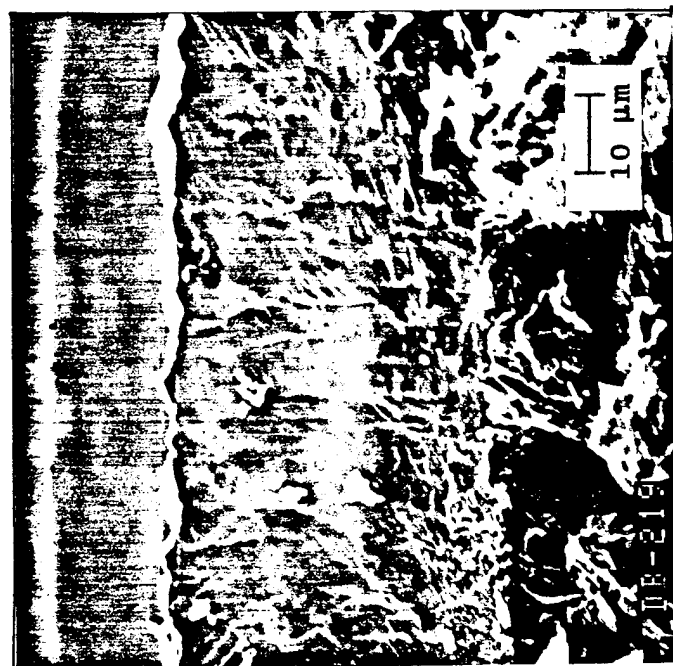


(a)



(b)

Figure 8. Cross-section (a) and surface morphology (b) of boron carbide film deposited on graphite at 1400°C and a deposition rate of 11.62×10^{-7} cm/s (DB-153).

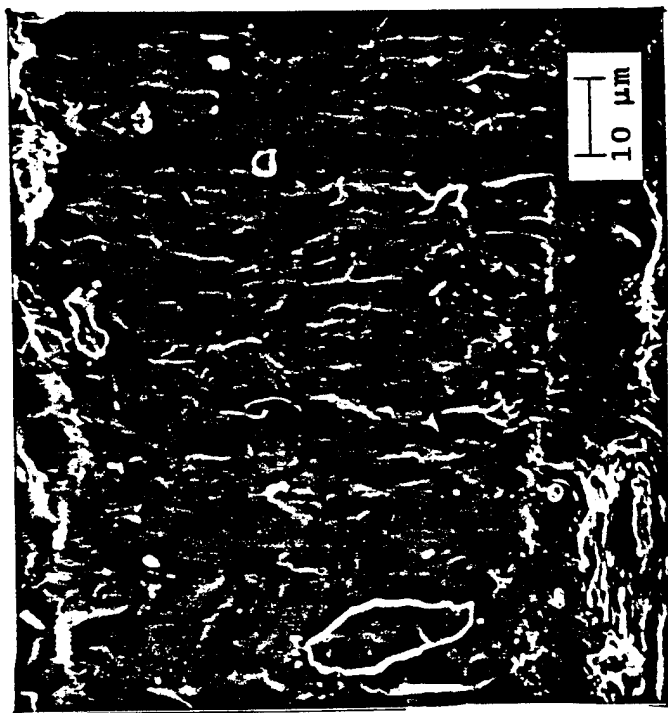


(a)



(b)

Figure 9. Cross-section (a) and surface morphology (b) of boron carbide film deposited on graphite at 1400°C and a deposition rate of 23.19×10^{-7} cm/s (DB-219).



(a)



(b)

Figure 10. Cross-section (a) and surface morphology (b) of boron carbide film deposited on graphite at 1400°C and a deposition rate of 37.19×10^{-7} cm/s (DB-216).

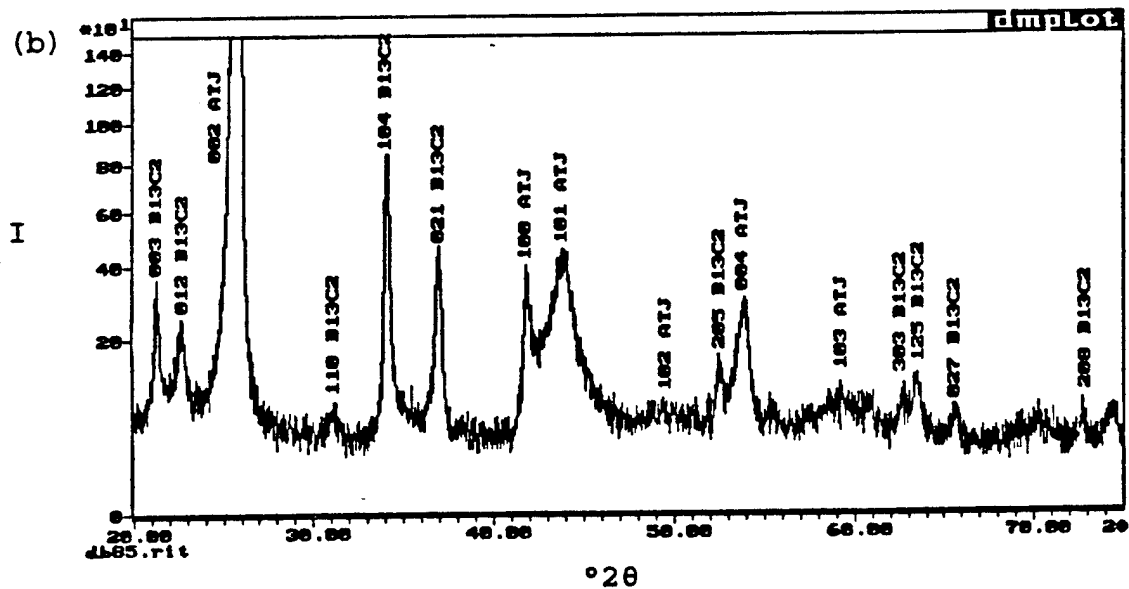
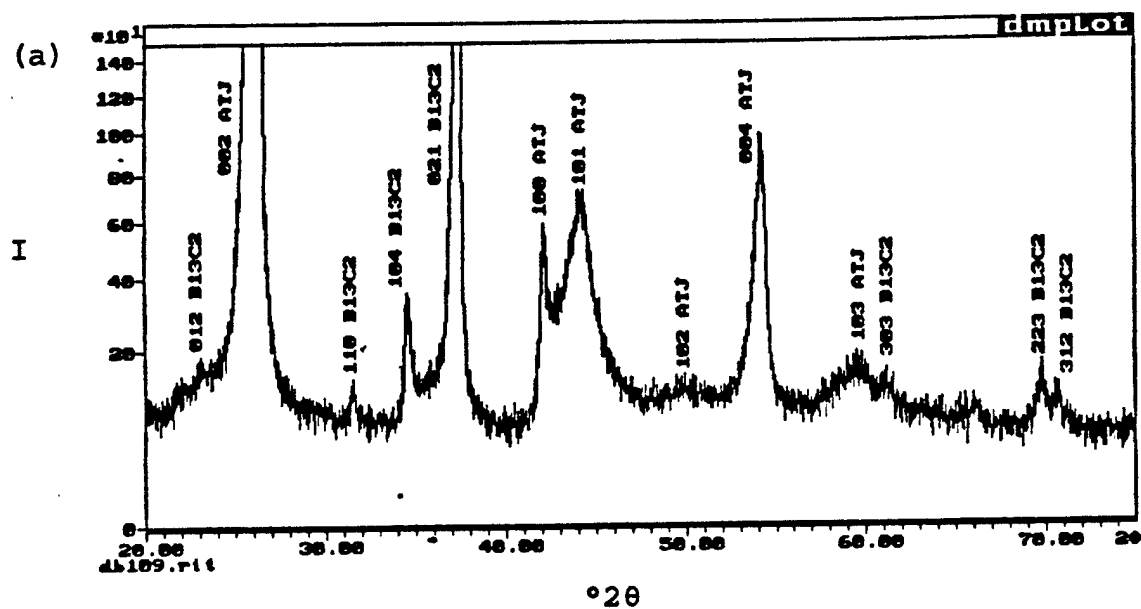


Figure 11. X-ray diffraction patterns of DB-109 (a) and DB-85 (b), two samples examined using TEM.

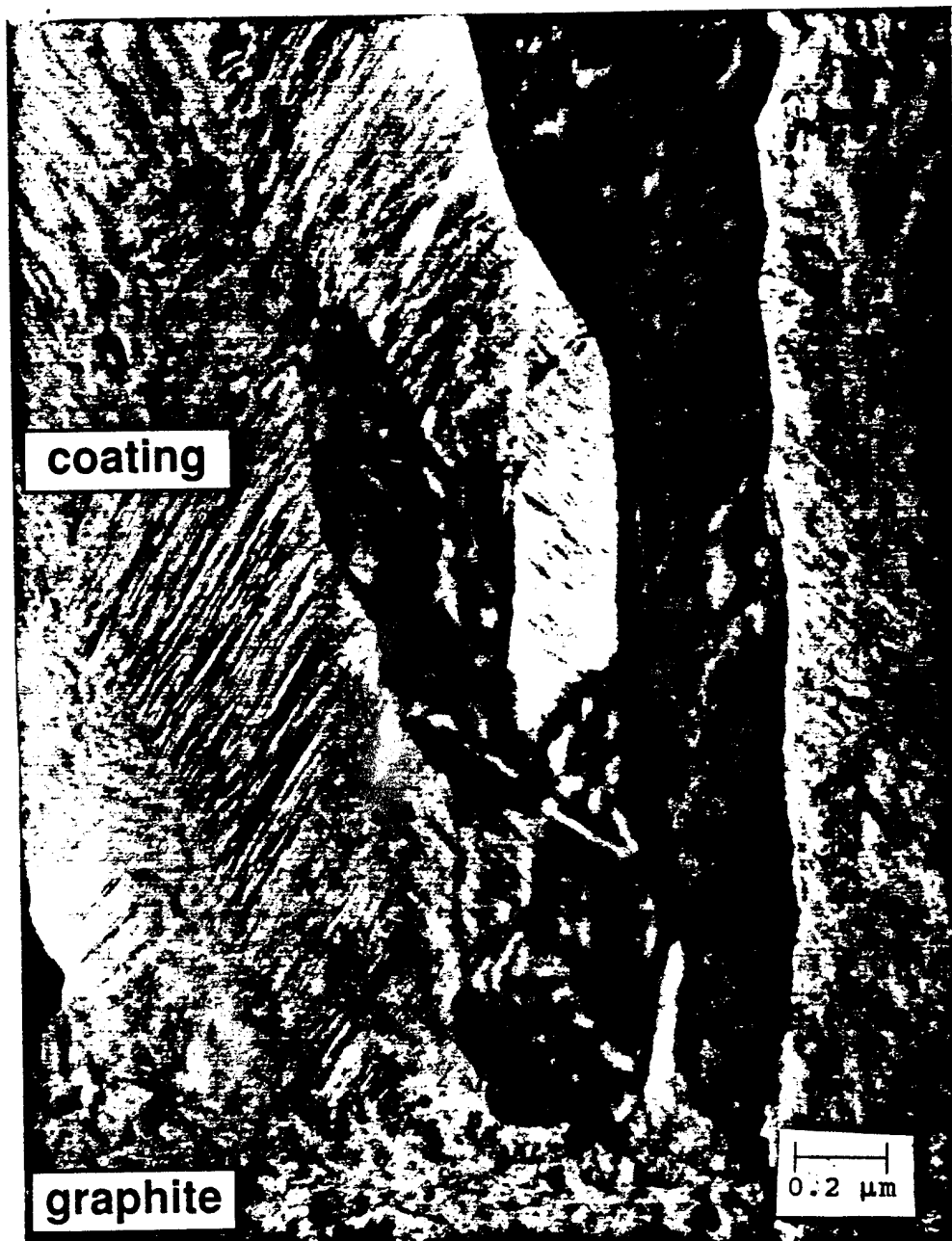


Figure 12. Transmission electron micrograph of $B_{13}C_2$ (DB-109) shows long columnar grains which are about 0.5 to 1.5 μm across.



Figure 13. The TEM micrograph for the planar view of Sample DB-109 (seen in Figure 5-19) displays the rectangular shape of the B₁₃C₂ grains.



Figure 14. The morphology of Sample DB-109 from an SEM micrograph shows features on the order of size seen in the TEM planar view.

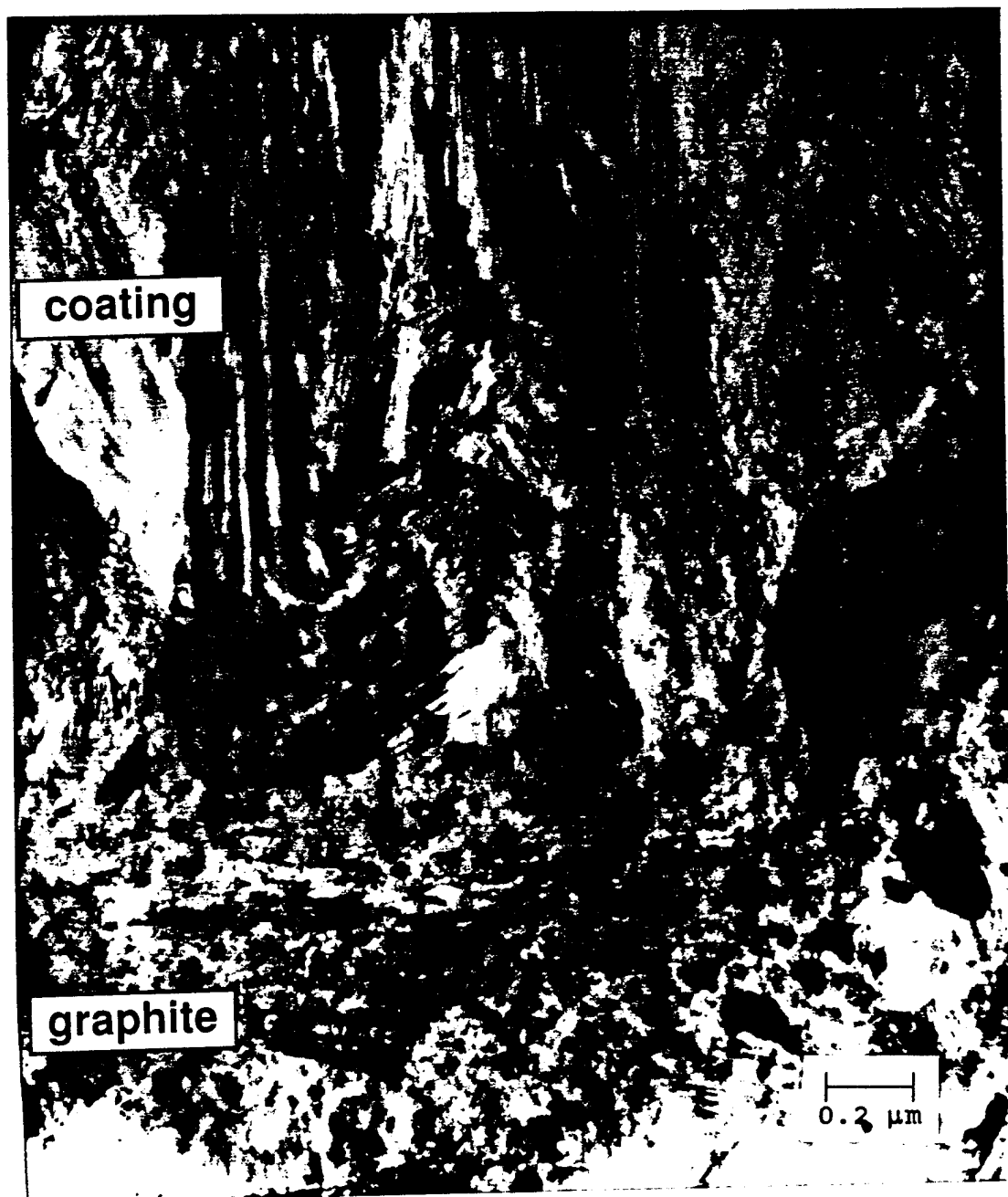


Figure 15. The TEM micrograph of Sample DB-85 at the interface between the substrate and the coating shows wider columnar grains than in Sample DB-109 (Figure 5-19).



Figure 16. The TEM micrograph of Sample DB-85 displays the star-like quality of the grains.

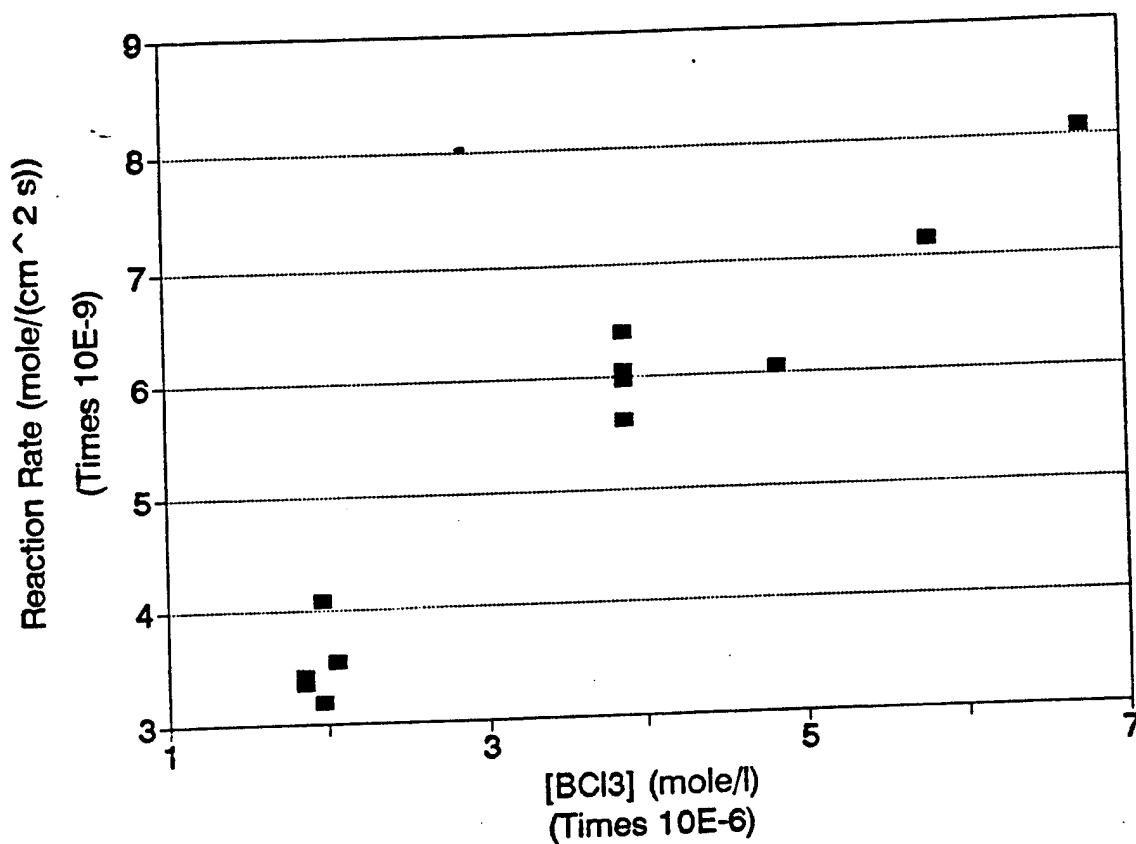


Figure 17. The reaction rate versus BCl_3 bulk concentration at 1000°C verifies a first order relationship between the two quantities.

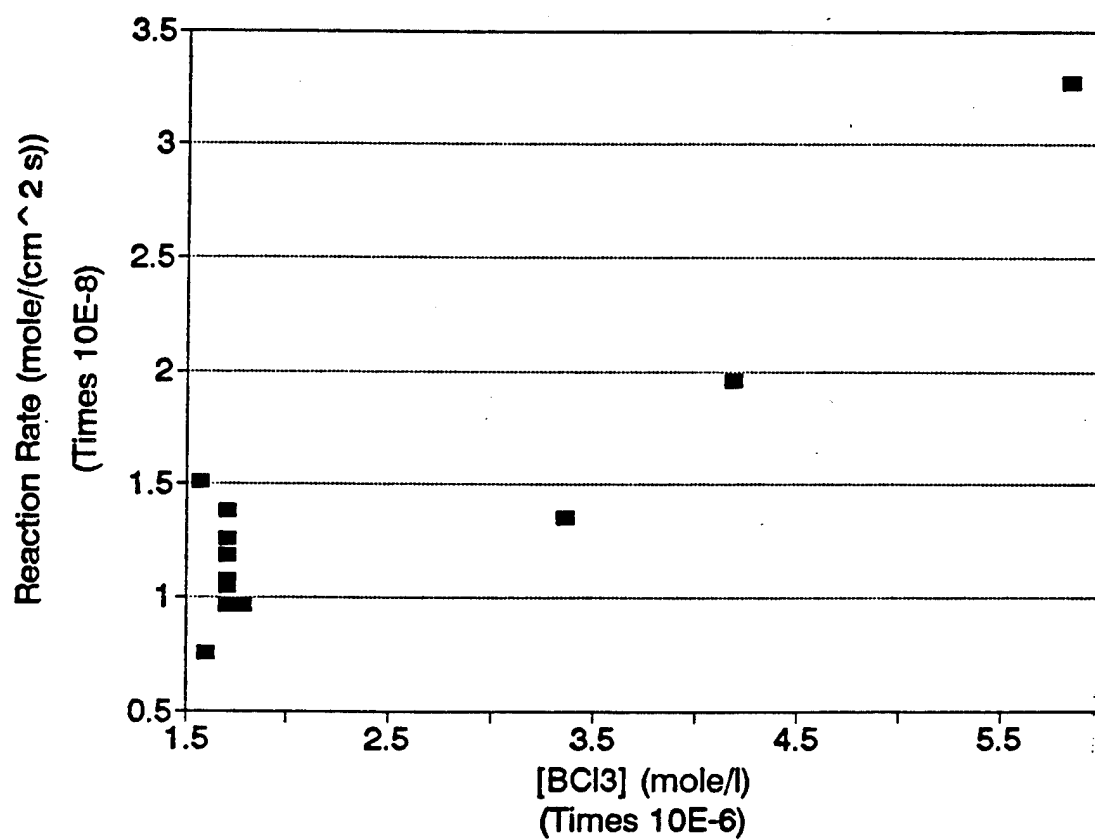


Figure 18. The reaction rate versus BCl_3 bulk concentration at 1200°C verifies a first order relationship between the two quantities.

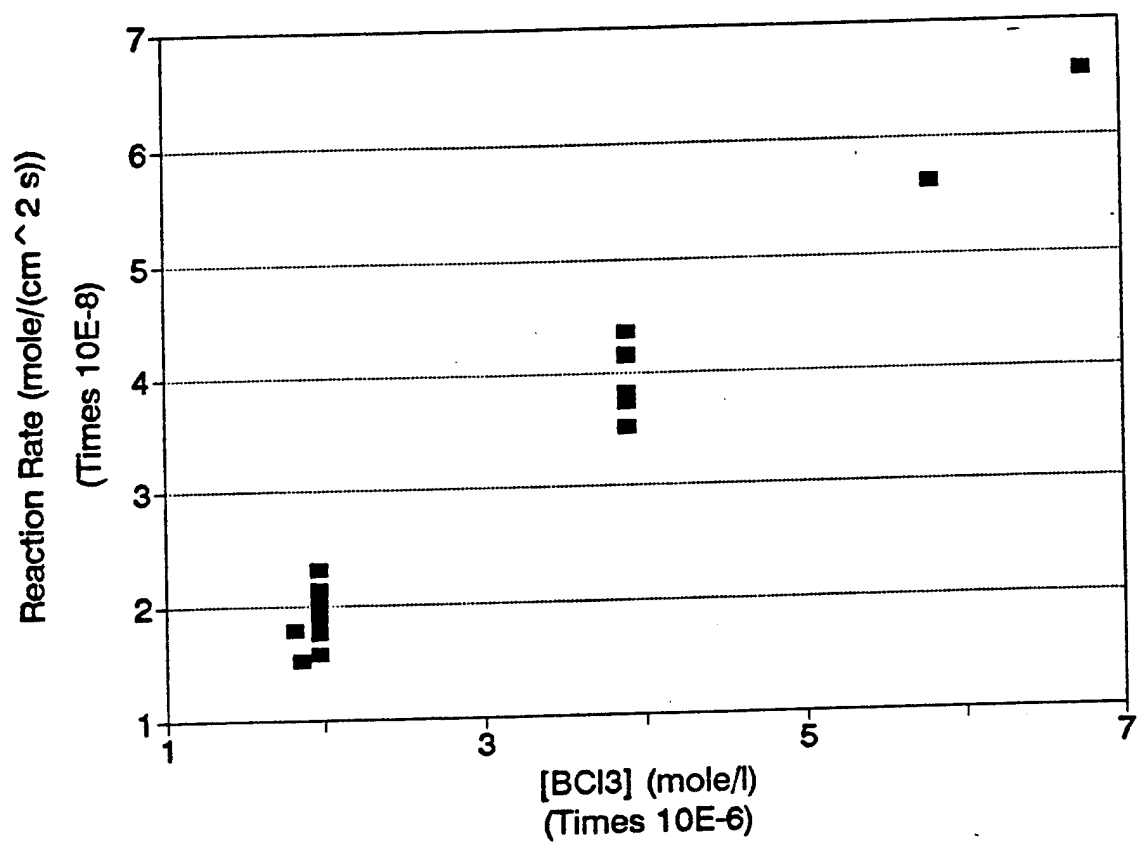


Figure 19. The reaction rate versus BCl_3 bulk concentration at 1400°C verifies a first order relationship between the two quantities.

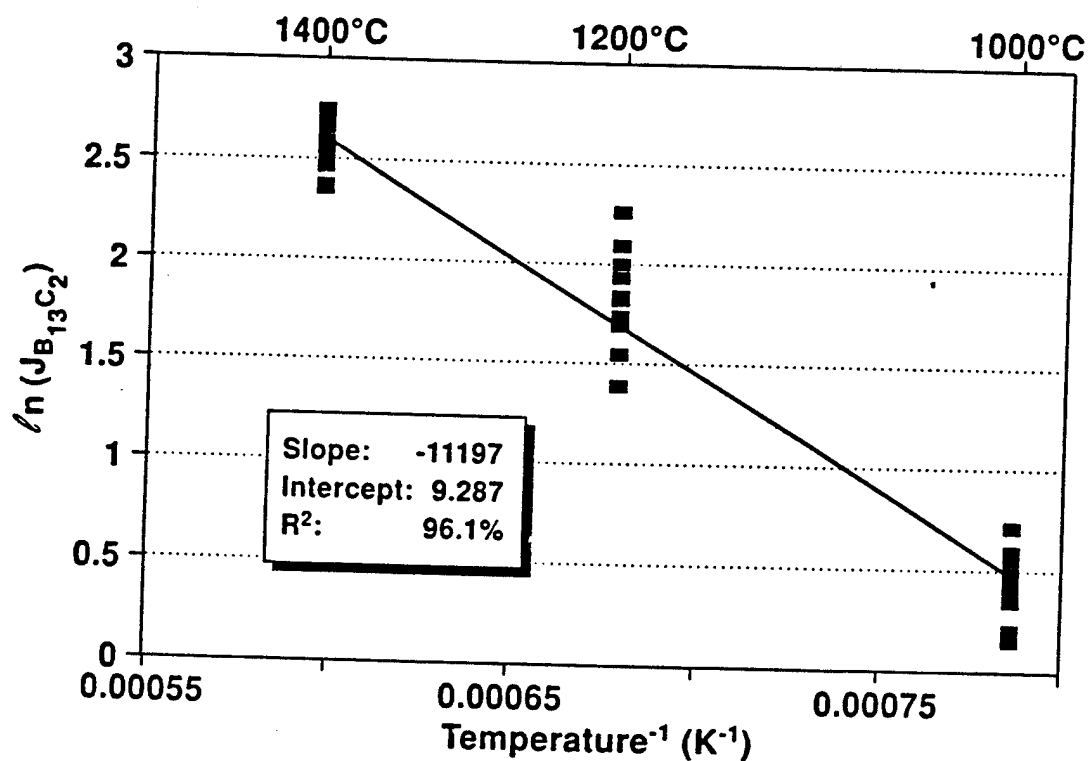


Figure 20. The Arrhenius plot for $B_{13}C_2$ deposition at three temperatures shows that deposition is limited by the kinetics of the reaction instead of by the mass transfer to the substrate.

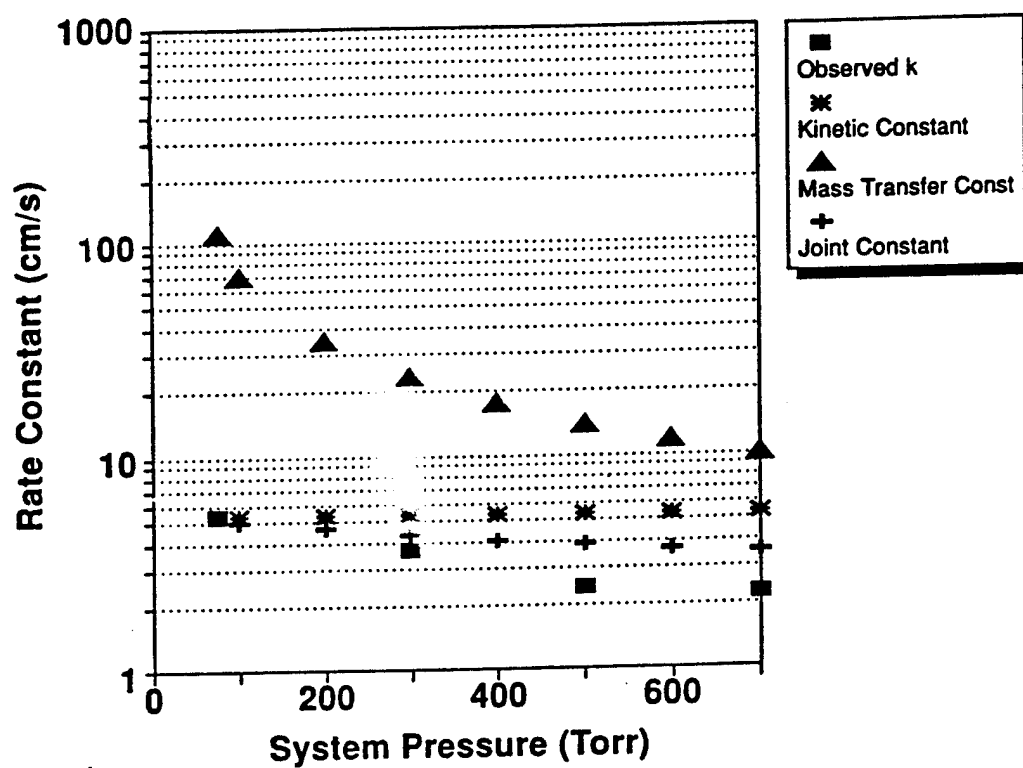


Figure 21. Increasing the system pressure at 1200°C causes the $B_{13}C_2$ deposition to transition from a heavily kinetic regime into a mixed kinetic-mass transfer limited regime.

Table 1. Conditions for the deposition of boron carbide at 1000°C. The units for time, pressure, and all flows are minutes, torr, and sccm, respectively.

DB	Time	P	BCl ₃	CH ₄	H ₂	Ar
58	90	76	10.0	20.0	109	4494
66	90	76	9.0	6.0	123	4494
116	90	76	9.0	6.0	123	4494
225	30	76	20.3	20.7	200	4759
226	60	76	20.3	20.7	200	4759
227	60	76	20.3	20.7	100	4859
228	60	76	35.3	20.7	124	4820
229	60	76	30.3	20.7	124	4825
230	60	76	25.3	20.7	124	4830
231	60	76	20.3	20.7	124	4835
233	60	76	10.3	30.7	124	4835
234	60	76	10.3	10.7	124	4855

Table 2. Conditions for the deposition of boron carbide at 1200°C. The units for time, pressure, and flow rates are minutes, torr, and sccm, respectively.

DB	Time	P	BCl ₃	CH ₄	H ₂	Ar
59	60	76	10.0	20.0	109	4494
61	60	76	9.0	6.0	123	4494
64	60	76	8.8	2.2	128	4494
140	60	76	10.3	25.9	124	4840
141	60	76	10.3	20.7	124	4844
142	60	76	10.3	10.3	124	4855
144	60	76	10.3	15.5	124	4850
203	45	76	10.3	20.7	224	4745
206	45	76	10.3	20.7	324	4645
207	45	76	20.3	20.7	124	4835
208	52	76	35.3	20.7	124	4820
209	45	76	25.3	20.7	124	4830
368	30	700	20.0	20.0	160	4800
369	30	500	20.0	20.0	160	4800
370	45	300	20.0	20.0	160	4800

Table 3. Conditions for the deposition of boron carbide at 1400°C. The units for time, pressure, and flow rates are minutes, torr, and sccm, respectively.

DB	Time	P	BCl ₃	CH ₄	H ₂	Ar
62	45	76	9.0	6.0	123	4494
77	45	76	8.8	2.2	128	4494
136	45	76	10.3	15.5	124	4850
137	45	76	10.3	10.3	124	4855
138	45	76	10.3	20.7	124	4844
145	45	76	10.3	10.3	134	4846
146	45	76	10.3	15.3	124	4850
147	45	76	10.3	20.3	114	4856
149	45	76	10.3	6.9	140	4843
150	45	76	10.3	6.9	160	4823
151	45	76	10.3	6.9	100	4883
152	45	76	10.3	6.9	200	4783
153	45	76	10.3	6.9	200	4783
212	30	76	10.3	10.7	124	4855
214	30	76	20.3	20.7	124	4835
216	34	76	30.3	20.7	124	4825
218	30	76	35.3	20.7	124	4820
219	30	76	20.3	20.7	100	4859
220	30	76	20.3	20.7	200	4759
221	35	76	20.3	20.7	300	4659
222	30	76	20.3	20.7	400	4559
232	30	76	20.3	20.7	250	4709

Table 4. Results for the deposition of $B_{13}C_2$ at 1000°C . The diffusion coefficient from the Chapman-Enskog equation, D_{BCl_3} , was $1.92\text{ cm}^2/\text{s}$, and the diffusion coefficient from the Slattery-Bird treatment, D'_{BCl_3} , was $24.11\text{ cm}^2/\text{s}$.

DB Run No.	Phase	Dep. Thick. (μm)	Dep. Rate ($\times 10^7$) (cm/s)	δ_{BCl_3} ($\times 10^2$) (cm)	δ'_{BCl_3} ($\times 10^2$) (cm)	$(D/\delta)_{BCl_3}$ (cm/s)	$(D/\delta)'_{BCl_3}$ (cm/s)
58	$B_{13}C_2$	12.66	2.344	1.630	3.853	117.7	625.9
66	$B_{13}C_2$	11.94	2.211	2.256	5.335	85.02	452.0
116	$B_{13}C_2$	12.19	2.257	2.187	5.170	87.74	466.4
225	$B_{13}C_2$	7.12	3.956	2.105	4.977	91.14	484.5
226	$B_{13}C_2$	15.25	4.236	2.105	4.977	91.14	484.5
227	$B_{13}C_2$	14.43	4.008	2.102	4.970	91.27	485.2
228	$B_{13}C_2$	19.22	5.339	2.100	4.966	91.34	485.6
229	$B_{13}C_2$	17.01	4.724	2.101	4.968	91.31	485.4
230	$B_{13}C_2$	14.42	4.005	2.102	4.970	91.27	485.2
231	$B_{13}C_2$	13.40	3.722	2.103	4.972	91.24	485.0
233	$B_{13}C_2$	7.59	2.109	2.104	4.975	91.17	484.7
234	$B_{13}C_2$	9.71	2.696	2.104	4.975	91.17	484.7

Table 5. Results for the deposition of $B_{13}C_2$ at $1200^{\circ}C$. The diffusion coefficient from the Chapman-Enskog equation, D_{BCl_3} , was $2.45 \text{ cm}^2/\text{s}$, and the diffusion coefficient from the Slattery-Bird treatment, D'_{BCl_3} , was $31.46 \text{ cm}^2/\text{s}$.

DB Run No.	Phase	Dep. Thick. (μm)	Dep. Rate ($\times 10^7$) (cm/s)	δ_{BCl_3} ($\times 10^2$) (cm)	δ'_{BCl_3} ($\times 10^2$) (cm)	$(D/\delta)_{BCl_3}$ (cm/s)	$(D/\delta)'_{BCl_3}$ (cm/s)
59	$B_{13}C_2$	22.93	6.369	2.319	5.524	105.7	569.6
61	$B_{13}C_2$	17.91	4.974	1.720	4.096	142.5	768.1
64	$B_{13}C_2$	35.94	9.981	2.296	5.468	106.7	575.4
140	$B_{13}C_2$	22.97	6.379	2.210	5.262	110.9	597.9
141	$B_{13}C_2$	28.13	7.812	2.210	5.263	110.9	597.8
142	$B_{13}C_2$	32.81	9.112	2.210	5.262	110.9	597.9
144	$B_{13}C_2$	30.00	8.331	2.210	5.262	110.9	597.9
203	$B_{13}C_2$	18.72	6.931	2.213	5.270	110.7	597.0
206	$B_{13}C_2$	19.20	7.109	2.216	5.277	110.6	596.2
207	$B_{13}C_2$	24.09	8.919	2.208	5.258	111.0	598.4
208	$B_{13}C_2$	67.50	21.63	2.205	5.253	111.1	599.0
209	$B_{13}C_2$	34.95	12.94	2.207	5.257	111.0	598.5
368	$B_{13}C_2$	82.44	45.79	2.637	6.281	10.09	54.39
369	$B_{13}C_2$	62.33	34.62	2.637	6.281	14.13	76.13
370	$B_{13}C_2$	87.41	32.37	2.637	6.281	23.55	126.9

Table 6. Results for the deposition of $B_{13}C_2$ at $1400^\circ C$. The diffusion coefficient from the Chapman-Enskog equation, D_{BCB} , was $3.03 \text{ cm}^2/\text{s}$, and the diffusion coefficient from the Slattery-Bird treatment, D'_{BCB} , was $39.68 \text{ cm}^2/\text{s}$.

DB	Phase	Dep. Thick. (μm)	Dep. Rate ($\times 10^7$) (cm/s)	δ_{BCB} ($\times 10^2$) (cm)	δ'_{BCB} ($\times 10^2$) (cm)	$(D/\delta)_{BCB}$ (cm/s)	$(D/\delta)'_{BCB}$ (cm/s)
62	$B_{13}C_2$	27.18	10.06	2.721	6.523	111.4	608.4
77	$B_{13}C_2$	31.88	11.81	2.395	5.742	126.6	691.1
136	$B_{13}C_2$	41.25	15.27	2.305	5.526	131.5	718.1
137	$B_{13}C_2$	38.24	14.16	2.305	5.526	131.5	718.1
138	$B_{13}C_2$	33.75	12.50	2.305	5.527	131.5	718.0
145	$B_{13}C_2$	37.50	13.89	2.305	5.527	131.5	718.0
146	$B_{13}C_2$	32.81	12.15	2.305	5.526	131.5	718.1
147	$B_{13}C_2$	34.69	12.85	2.304	5.525	131.6	718.2
149	$B_{13}C_2$	37.50	13.89	2.305	5.527	131.5	718.0
150	$B_{13}C_2$	35.63	13.19	2.306	5.529	131.5	717.7
151	$B_{13}C_2$	33.75	12.50	2.304	5.524	131.6	718.4
152	$B_{13}C_2$	28.13	10.42	2.307	5.532	131.4	717.3
153	$B_{13}C_2$	31.39	11.62	2.307	5.532	131.4	717.3
212	$B_{13}C_2$	22.15	12.30	2.305	5.526	131.5	718.1
214	$B_{13}C_2$	45.42	25.23	2.303	5.522	131.7	718.6
216	$B_{13}C_2$	75.89	37.19	2.301	5.518	131.8	719.2
218	$B_{13}C_2$	78.02	43.33	2.300	5.516	131.8	719.4
219	$B_{13}C_2$	41.74	23.19	2.302	5.520	131.7	718.9
220	$B_{13}C_2$	51.82	28.78	2.306	5.528	131.5	717.9
221	$B_{13}C_2$	57.79	27.51	2.309	5.536	131.3	716.8
222	$B_{13}C_2$	44.32	24.62	2.312	5.544	131.1	715.8
232	$B_{13}C_2$	49.35	27.41	2.307	5.532	131.4	717.3

Table 7. The relative intensities, given in %, of the observed peaks from the x-ray diffraction of $B_{13}C_2$ samples in the range of 2θ to 75° .

DB	003	012	110	104	021	113	303	125	018	220	131	223
233	71	14	0	100	14	0	0	0	18	0	0	0
231	100	0	0	36	4	0	0	0	27	0	0	0
228	100	0	0	45	15	0	0	0	36	0	0	25
140	0	6	6	10	100	0	0	3	0	5	0	8
142	7	12	16	8	100	0	0	0	0	0	0	7
208	0	<1	0	4	100	0	<1	0	0	<1	<1	0
153	10	24	15	50	100	0	0	7	7	0	7	6
219	0	5	7	5	100	0	0	0	0	6	8	0
216	9	20	36	30	100	5	6	7	6	0	4	6

Kinetics of the CVD of SiC in a Hot Wall Reactor
using a Modified Impinging Jet Geometry

Thomas S. Moss^{ab} and W. Jack Lackey,^{*} Georgia Institute of Technology, Atlanta, GA
30332-0826

Abstract

The deposition of SiC has accomplished for both the direct reaction of mixtures of SiCl₄ and CH₄ and the decomposition of MTS in a vertical, hot wall reactor using a modified impinging jet geometry. However, significant deposition was not seen from the SiCl₄-CH₄ reaction at temperatures below 1400°C, and the use of MTS was preferred because of the lower deposition temperatures. The morphology of the deposition produced from MTS was typified by its smooth, platy structure at low temperatures which became rougher at higher temperatures. The MTS deposition behavior was found to be kinetically controlled and was described by a first order model. The activation energy was estimated to be 302.929 kJ/mole, and the frequency factor was 1.374×10^{11} . A comparison to the estimated mass transfer limit showed that the deposition rate was still within a kinetic regime in the temperature range studied but was approaching a mass transfer limitation at temperatures over 1400°C.

CVD, SiC, Kinetics, Microstructure, Coating

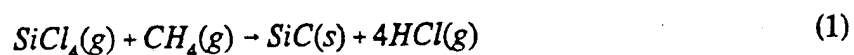
^{*}Member, ACS

^bPresent address Los Alamos National Laboratory, Los Alamos, NM

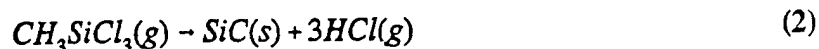
Introduction

Because of its importance as both a structural and electrical material, the production of silicon carbide (SiC) has been explored by a variety of methods. One of the best suited techniques for preparation of high quality SiC is chemical vapor deposition (CVD). The high purity and low porosity of the coatings, as well as low deposition temperatures, make CVD an ideal technique for the synthesis of SiC. However, there has been a lack of continuity among many of the reported results. The research completed for this paper uses a modified impinging jet geometry to allow for more accurate analysis by simplifying the mass transfer to the substrate surface. By using this simple geometry, a better estimation of the intrinsic reaction data should be possible.

Two reactions were studied using a hot wall reactor. The first involved the direct reaction of silicon tetrachloride, SiCl_4 , and methane, CH_4 , as follows:



The second and preferred method was by the decomposition of methyltrichlorosilane or MTS, CH_3SiCl_3 , in the presence of hydrogen, H_2 , by the reaction:



Both reactions were done in a hot wall reactor in the temperature range of 1000 to 1400°C at a system pressure of 76 torr.

Background

Silicon carbide is an extremely stable refractory material with a melting temperature of 2250°C. Its inertness to chemical attack, especially by O₂ at high temperatures, combined with its high strength, toughness, and resistance to wear, lend it to a variety of unique applications in very harsh environments. High thermal conductivity and controllable electrical properties also contribute to the exceptional physical qualities that make it a useful material. The structure of SiC prepared by CVD is typically the cubic β -SiC phase with a small second phase of an α -SiC polytype. The fraction of the α -SiC second phase increases with decreasing deposition temperature.^{1,2}

The CVD of SiC has been successfully accomplished using a variety of precursors. Pring and Fielding³ described the process first in 1909 as the reaction of C₆H₆ and SiCl₄ in the presence of hydrogen between 1700 and 2000°C. Other reagents that have been used have typically involved a silicon halide and a hydrocarbon.¹ Also, the production of SiC coatings has been accomplished through the reaction of a Si-based gas with a graphite substrate, as well as by the reaction of a hydrocarbon gas with a silicon substrate.^{4,5} More recently, volatile silane precursors, usually organometallic reagents, have been used to produce films. This group of chemicals is usually of the form (CH₃)_xSiCl_{4-x}. Reactions using this class of chemical involve the thermal pyrolysis of the gas in the presence of excess hydrogen. It has been shown that MTS, CH₃SiCl₃, is the easiest precursor with which to deposit stoichiometric SiC because of the 1:1 Si to C ratio in the parent molecule. Once the Si:C ratio deviates from unity in the reagent gas supply, the gas must be closely monitored

and controlled to guard against excess Si or C, which could deposit and diminish the desirable properties.¹

The deposition parameters, such as temperature, pressure, and H_2 /MTS ratio have great control over the morphology of the coating.^{2,6} The morphology is strongly related to the nucleation processes which occur.² While there are some system to system variations, it is clear that increasing the temperature moves the coating from smooth to faceted structures. Lower pressures and higher H_2 /MTS ratios also produce more faceted structures in the coatings.

The stoichiometry of the deposit is also altered by the same parameters which control morphology. Composition is apparently controlled by the carbon and silicon atom flux to the substrate.⁶ By manipulating the temperature, pressure, and reagent ratio, the amount of available Si or C from the decomposition of the MTS can be changed. A carbon-rich composite is favored by low H_2 /MTS ratios, low deposition pressures, and high temperatures. The Si rich region occurs at low temperatures, high pressures, and high H_2 /MTS ratios.

The generalities of the kinetics of the CVD of SiC from MTS, as understood prior to 1980, have been summarized by Schlichting^{1,2} and show that deposition is a linear function of time, with deviations occurring at high temperatures and long deposition times. Further, coating rate is characterized as a linear function of the MTS partial pressure, i.e., first order, but is also a square root function of the velocity of the reagent gas flow. The temperature dependence of deposition shows behavior which is typical for a pyrolysis mechanism with the deposition rate passing through a maximum as the deposition temperature is increased. The

temperature at which the maximum deposition occurs can be altered by the Si/C and H/Cl ratios in the reagent stream and the velocity of the gas stream.

The review of the calculated activation energy which is associated with the deposition of SiC from MTS varied widely.^{1,2} Recent research by Gao and Lin has been able to adequately model SiC deposition from MTS, H₂, and Ar in a hot wall, cylindrical reactor at atmospheric pressure. They were able to arrive at a solution by solving the continuity equations using a first order kinetic expression with an activation energy of 254 kJ/mole.⁷

However, the modeling of Besmann et al.⁸ of SiC deposition onto Nicalon fibers in a low pressure, hot wall furnace have indicated that the deposition rate is not a simple first order reaction but rather a series of competing forward and reverse reactions. The proposed kinetic expression had the form:

$$\mu = (k_R C_{Ro} - k_P C_{Po}) e^{\left[-\frac{S(k_R + 3k_P)T_a}{V_M F_a T} \right]} \quad (3)$$

where C_{Ro} and C_{Po} are the concentrations of MTS and HCl that are introduced into the reactor, S is the surface area of the hot surfaces upstream from the sample, V_M is the molar volume of SiC, V_a is the volumetric flow rate of MTS that is introduced into the reactor, and T_a and T are the ambient and reactor temperatures, respectively. Two different mechanisms were proposed that could occur based on whether the MTS molecule could dissociate into separate silicon and carbon containing fragments or not. Further, their work also demonstrated the effect which hydrochloric acid (HCl) had on reducing the deposition rate,

and they developed a kinetic model which included a simple etch mechanism to describe the significant HCl effect.

Allendorf and Outka⁹ have confirmed the etching ability of HCl by studying the reactivity of HCl and MTS with the surface of β -SiC. They have shown that HCl is adsorbed by SiC to produce a stable silicon chloride that can inhibit the further growth of SiC. The chlorine on the surface then desorbs as either HCl or silicon tetrachloride (SiCl_4), the later resulting in etching of the SiC by HCl. Also, they showed that MTS is dissociatively adsorbed in a method similar to HCl, but the removal of the adsorbed Cl is difficult since the rate of desorption is limited by the breaking of the surface Si-Cl bond. The dissociation energy of this bond was found to be 118 kcal/mole, much higher than any other bond in the system. This type of behavior would suggest that the removal of the surface chlorine is rate limiting.

Somewhat similarly, Papasouliotis and Sotirchos¹⁰ proposed a model for deposition which involved a series of fourteen reversible surface reactions, resulting in a total of twenty-eight reaction constants. The equilibrium constants of the adsorption reactions were treated as parameters in the model, while other reaction constants were calculated from available thermodynamic data. This approach also allowed for the inhibition of deposition by reaction byproducts, especially the etching mechanism of SiC by HCl.

Tsai et al.¹¹ modeled the deposition process with three reaction steps. The first step was the decomposition of MTS in the gas phase to produce silicon- and carbon-containing intermediate species. These intermediates then adsorb onto the surface of the growing film and undergo a reaction to produce SiC. A fit of their experimental data using a finite

element analysis to consider both the kinetic and diffusional components yielded a promising result, with a better fit of the data than the traditional first order model.

The uncertainty regarding a usable kinetic expression has led So et al.¹² to conclude that the reaction order shifts from first order with respect to MTS to a zero order reaction as the MTS concentration is increased beyond 2%. Alam and Puneet¹³ had success in simulating SiC deposition onto a monofilament in a hot wall reactor using a model which sought to approximate the shifting order by using a half order model with respect to the MTS concentration. Chu and Hon¹⁴ also used a half order reaction with respect to the MTS partial pressure but multiplied it by the total flow rate of reagent to examine the deposition from a cold wall reactor. They further learned that the addition of H₂ enhanced the thermal decomposition of MTS and increased the deposition rate of SiC.

The bulk of the literature regarding the deposition of SiC from MTS has focused on the kinetics of the reaction. There have been two groups, however, which sought to explain the deposition behavior from mass transfer effects.

Minato and Fukuda¹⁵ examined the deposition reaction of SiC from MTS onto pyrolytic carbon coated nuclear fuel particles within a fluidized-bed reactor. Their experiments were done at atmospheric pressure and in the temperature range of 1150 to 1700°C, with most of the runs between 1400 and 1700°C. Gas flows were composed of H₂ (0 to 7000 sccm), Ar (0 to 1750 sccm), and MTS, where the (H₂+Ar)/MTS ratio was varied from around 250 to 1000. From this work, they concluded that the reaction was limited by the flux of the active reagent across the boundary layer. They estimated the diffusion coefficient and the boundary layer thickness from basic equations and applied the results to

explain the observed deposition behavior. This mass transfer model explained the data fairly well, with some deviations seen at lower temperatures. The low temperature deviation could be accounted for by a change to a kinetic limited reaction. The temperature at which the limiting regime changed could be seen to vary as a function of the flow rate through the reactor. From the graphs which were presented in their papers, the transition temperature appeared to be lower under higher total flow conditions, although this point was not concluded.

Loumagne et al.¹⁶, in the process of investigating the kinetics of deposition of SiC, found the transition from a kinetic to a mass transfer regime. They deposited SiC onto graphite substrates located within the reactor on a microbalance. Growth rates were determined from the change in the weight of the substrate during the experiment. At a system pressure of 0.1 atm and for temperatures greater than 950°C, the deposition process was not thermally activated, meaning that diffusion to the substrate controlled the kinetics. Decreasing the pressure to 0.01 atm increased the transition temperature to a value out of the range of study, i.e., greater than 1050°C. In their study of the kinetic regime, they found two distinct temperature regions. At around 850°C, the deposition was limited by the decomposition of MTS in the gas phase. The activation energy was estimated to be higher than 300 kJ/mole, and the apparent reaction order was 2.5 with respect to the MTS concentration. At a slightly higher temperature of around 925°C, the reaction appeared to be limited by surface reactions with an activation energy of only 160 kJ/mole and an undetermined negative reaction order with respect to the HCl concentration.

Procedure

A schematic of the equipment used for SiC deposition is shown in Figure 1 and described in greater detail elsewhere.¹⁷ For H₂ and Ar, flow rates were controlled by MKS mass flow meters. However, the liquid source reagents (MTS and SiCl₄) were delivered by bubbling known flow rates of H₂ through the liquids; the saturated vapor was then directed into the furnace. The weight loss of the bubbler was measured following each experiment to check against the calculated flow based on complete saturation. Within the furnace, the temperature in the hot zone was monitored using an Ircon optical pyrometer and a type K thermocouple. The pressure was measured using a Baratron pressure transducer. ATJ Graphite was selected as the substrate due to the desire to apply this technology to carbon-carbon composites. The conditions which were used for deposition are included in Table I for the SiCl₄+CH₄ system and Table II for the MTS system.

The location of the substrate within the deposition reactor can be an important parameter. In typical CVD reactors the substrate is positioned within the gas stream by suspending it or by fixing its position with a sample holder. A problem that develops with this type of geometry is the formation of a non-linear boundary layer over the surface. Further, reagent depletion can occur along the length of the substrate. These are two complex problems which do not lend themselves well for accurate modeling. However, they may be overcome by changing to the modified impinging jet geometry. Within the modified impinging jet geometry, it has been previously shown that radial diffusion is eliminated within the stagnation region which develops just over the substrate surface.¹⁸ This simplifies

the mass transfer to a one dimensional problem across the concentration boundary layer. The equations necessary to estimate the overall mass transfer are presented elsewhere.¹⁷

Samples were characterized using x-ray diffraction (XRD), and scanning electron microscopy (SEM) of the cross-section and surface morphology. For XRD and subsequent characterization, the stagnation region was isolated from the surrounding area using a series of fractures initiated from the backside of the sample. XRD patterns were taken using a Phillips 1800 automatic powder diffractometer, using copper K_{α} radiation at 40 kV and 30 mA. Scans were taken in a range of 20.0 to $75.0^{\circ}2\theta$ and a counting time of 1.0 second per step.

Cross-sectional micrographs were taken using a fractured surface produced by breaking the sample in half across the stagnation region. One of these halves was mounted and examined in the SEM. These micrographs allow for the determination of an average growth rate of the coating. Micrographs were taken using Hitachi 4100 and Hitachi S-800 microscope; both microscopes were operated at 5 kV. Coating thickness measurements were taken directly from the micrographs using digital calipers. Ten measurements were taken from each micrograph, and an average thickness was calculated, along with the standard deviation of the measurements.

Morphological micrographs were taken by mounting the sample so that the surface of the coated sample was observed. These pictures provide an indication of the surface morphology. Micrographs were taken at a magnification of 1000x for all samples.

Results and Discussion

Reagent Selection

Initially, the deposition of SiC was attempted using the direct reaction of SiCl_4 and CH_4 . This reaction was seen as desirable because it allowed for wider control of the stoichiometry of the deposit, i.e., silicon-rich or carbon-rich, for application as an oxidation protective compound. Experiments were initially done in the single phase system to determine the feasibility of the reaction. A summary of the results is included in Table III for deposition temperatures of 1000, 1200, and 1400°C, respectively. These tables include the deposited phase(s), average coating thickness, and the average deposition rate for the conditions listed in Table I. These tables show that no distinguishable coatings were deposited at 1000°C and that only thin (1 to 10 μm) coatings were obtained at 1200°C. Deposition was improved at 1400°C where deposits of up to 17 μm were observed, but deposition rates were still fairly low, with the highest rate being 9.4×10^{-7} cm/s. However, since the deposition of SiC at temperatures as low as 1000°C was desired for the future study of dispersed phase composites and since higher deposition efficiencies were desirable, a better reagent choice was pursued.

The deposition of SiC from MTS was considered to be an excellent source for stoichiometric SiC because of its one-to-one Si to C ratio in the parent molecule.¹ It also simplified the modeling of the deposition since only a single reagent flow needed to be controlled. Further, MTS has been used to deposit SiC at temperatures below 1000°C.² Although the use of MTS has been well-explored, there still remains some disagreement regarding the mechanism of deposition. It was thus hoped that its use in a reactor with

simple geometric considerations would enable a better understanding of the intrinsic reaction mechanisms.

The results of the MTS experiments are summarized in Table II for the conditions which appeared in Table IV. Table IV includes not only the deposit thickness and deposition rate but also the mass transfer data based on calculations outlined elsewhere.¹⁷ Diffusion coefficients and the resulting concentration boundary layer thicknesses were calculated using both the Chapman-Enskog and Slattery-Bird diffusion equations. The diffusion resistances, $(D/\delta)_{\text{MTS}}$ and $(D/\delta)'_{\text{MTS}}$, were calculated based on these estimated values.

Deposition rates were very high during the study of MTS, especially compared to those from $\text{SiCl}_4 + \text{CH}_4$, with MTS rates approaching values as high as 153×10^{-7} cm/s at 1400°C (DB-254). There were large increases in the growth rates seen from increasing temperatures, as would be expected from a kinetically limited reaction. Importantly, it was possible to deposit SiC at 1000°C , although the coatings were quite thin, between 0 and $0.5 \mu\text{m}$ in the range studied. Based on the ability to deposit at 1000°C and the increased deposition rates at higher temperatures, MTS was selected for more complete study and for use as the SiC source for composite deposition.

Morphology and Microstructure

There were nine representative samples which were selected for discussion here. These samples were prepared at three temperatures (1000 , 1200 , and 1400°C) and at three growth rates (low, intermediate, and high); representative micrographs are presented in Figures 2 to 5.

Deposition thicknesses were measured from the cross-sectional fracture surfaces. Fractures were, for the most part, very clean, as would be expected for the brittle SiC, and enabled the coating to be examined without polishing. All of the samples appear to be very dense with no visible porosity, from the thinnest sample (DB-250) which was $0.2\text{ }\mu\text{m}$ thick to the thickest in Figure 5 (DB-254) at $412\text{ }\mu\text{m}$. The lack of apparent porosity in the deposits is indicative of a total heterogeneous nucleation and growth mechanism.

The morphological variations which were observed do follow some interesting trends. In general at 1000°C , the morphology was platy or flake-like in the thinner coatings produced. The plates were fairly layered and were located parallel to the substrate surface. The coating seemed to mimic the substrate surface below it, traditionally a sign of a kinetic regime although the thin nature of the coating made such observations difficult to support.

Moving to 1200°C (Figures 2 and 3), the coating takes a slightly different appearance. At the lowest deposition rate and thickness (DB-182), the coating looks as if the plates are oriented such that their thin dimension was parallel to the substrate surface, i.e., plates stacked on their edges. At higher growth rates and thicknesses, the morphology changed to smoother and more rounded features. At the highest deposition rate, the features became smaller and more numerous. This change would be expected from conditions which lead towards higher nucleation rates, i.e., higher supersaturations. Because of the seeming lack of competitive growth, this would suggest that the nucleation rate of SiC was quite high compared to the growth rate. The SiC could nucleate rapidly, and while the grains were growing it was possible for additional nuclei to form on the growing surface. The end result

is that the features were much smaller since nucleation took place quickly before competitive growth can occur.

At 1400°C, in Figures 4 and 5, the low deposition rate and thickness was again much different from that seen at the higher thicknesses. The morphology of the thin sample was smooth and had a platy and layered appearance. The surface was generally featureless, especially when compared to that for the high thicknesses. Those done at higher supersaturations had well defined surface features in the shapes of square columns. As was observed at 1200°C, at the lower thickness and growth rate, the features were larger and less numerous, and at the higher thicknesses and growth rates, the features were smaller and more numerous. The explanation of this trend is much the same as was described for the 1200°C results. At the higher supersaturation, the nucleation rate was high compared to the growth rate, and extensive competitive growth could not occur prior to renucleation of new grains. This type of mechanism resulted in the fine grain size which was observable on the surface.

The XRD of SiC samples showed that the deposits were primarily composed of β -SiC, as identified by JCPDS Card 29-1129. This phase had a zinc blend structure and, only four peaks were located within the diffraction range examined, due to the high symmetry of the structure. Two of these peaks overlapped with the graphite substrate, so identification of β -SiC in thinly coated samples had to be done using the other two peaks: the 111 peak at $35.60^\circ 2\theta$, which was the 100% peak, and the 311 peak at $59.99^\circ 2\theta$. In samples that had thicknesses of 40 μm or more, the XRD pattern had evidence of a slight amount of an α -SiC phase. The α -SiC polytype was not able to be identified since there was only a single non-

overlapped peak which was present. In the thinner coatings, it was unclear if the α -SiC was present since if it was present the quantity was so small that its peaks were simply not intense enough to be distinguishable. Without such clarification, the appearance of the α -SiC could also be attributable to the effect of a higher deposition rate or higher temperature, resulting in the inclusion of the α polytype.

The XRD peak intensities for the samples shown in Figures 2 to 5 are listed in Table V. It was possible to see some trends in the patterns. At the lower temperatures of 1000 and 1200°C, the coatings have a 111 orientation, which is the 100% peak in the powder diffraction card. Further, as the temperature was increased from 1000 to 1200°C, the deposit approached more of a single crystal 111 orientation. In fact, as the deposition rate and thickness were increased (DB-182 to DB-245 to DB-243), the other peak intensities drop to 1% and below. This trend would indicate that at 1200°C the vast majority of the grains which were in a diffraction condition had a 111 orientation. There were some grains which did have other growth orientations, but they were either very small or very rare in the deposit. The samples produced at 1000°C were very thin, and the peaks heights were low relative to the graphitic substrate peaks. This resulted in the 200 and the 220 being not discernable from the 100 and 103 graphite peaks.

At 1400°C, the orientation of the deposition changes dramatically, with the 220 peak becoming the most intense in the patterns as the deposition thickness and growth rate increase. The patterns moved away from the single crystal type orientations and became much more polycrystalline, as evidenced by the high relative intensities of the other peaks in the pattern which were previously less significant. This change might result from the coating

transitioning to a single crystal 220 orientation which could occur at a higher temperature and/or deposition rate than the range studied. This possibility was evidenced by the trend which exists towards a more intense 220 peak relative to the other peaks. Another explanation of the orientational change might be in the increase in the nucleation rate due to increased temperature.

Deposition Mechanism

The use of a unified model involving both diffusional and kinetic aspects of the deposition reaction was used to determine the intrinsic reaction parameters. The traditional measured variable for CVD systems is the deposition or growth rate of the deposit which was estimated from the average film thickness divided by the total deposition time. The growth rate needed to be converted into a reaction rate which could then be correlated to the reagent concentrations and experimental conditions. The reaction rate of SiC, J_{SiC} , in mole/(cm²•s) was calculated by the following equation:

$$J_{SiC} = \frac{r_D \rho_{SiC}}{MW_{SiC}} \quad (4)$$

where r_D was the average deposition rate in cm/s, ρ_{SiC} was the density of SiC (3.21 g/cm³), and MW_{SiC} was the molecular weight of SiC (40.096 g/mole).

The form of the kinetic expression for the deposition of SiC has been studied by many groups. Based on previous research,^{1,2,7} it was assumed that the reaction for the deposition of SiC could be accurately described by a first order surface kinetic expression. This equation had the form:

$$J_{MTS} = k_{SiC} [MTS]^s \quad (5)$$

where k_{SiC} was the kinetic rate constant in cm/s, $[MTS]^s$ and P_{MTS}^s were the MTS surface concentration and partial pressure, respectively, R was the gas constant, and T was the absolute temperature. The mass transfer of the active reagent to the substrate surface was approximated by:

$$J_{MTS} = \left(\frac{D}{\delta}\right)_{MTS} ([MTS]^o - [MTS]^s) \quad (6)$$

where D_{MTS} was the diffusion coefficient of MTS in cm^2/s , δ_{MTS} was the concentration boundary layer thickness in cm, and $[MTS]^o$ and P_{MTS}^o were the bulk concentration and partial pressure of MTS, respectively.

Under the assumption of a steady state reaction, Equation 4 may be substituted into Equation 5 and simplified to a unified equation. This unified model is given by the equation:

$$J_{SiC} = \frac{1}{\left(\frac{1}{k_{SiC}} + \frac{\delta_{MTS}}{D_{MTS}}\right)} [MTS]^o \quad (7)$$

where the $1/k_{SiC}$ was the kinetic resistance and δ_{MTS}/D_{MTS} was the diffusion resistance. Either kinetics or diffusion may limit the reaction and Equation 6 may be approximated by:

$$J_{SiC} \approx k_{SiC} [MTS]^o \quad (8)$$

for conditions where kinetics limit the reaction. When the mass transfer of MTS limits the reaction, Equation 6 can be described by the following:

$$J_{sic} = \left(\frac{D}{\delta}\right)_{MTS} [MTS]^o \quad (9)$$

For conditions where the reaction transitions from a kinetic controlled to mass transfer limited regime, Equation 6 remains valid to describe the deposition. The validity of the overall reaction expression in Equation 6 was checked by plotting the reaction rate versus the inlet MTS concentration for the three temperatures studied. These plots are shown in Figures 6 to 8 for 1000, 1200, and 1400°C, respectively. The trend of the data generally shows a first order relationship between the reaction rate and the bulk MTS concentration, as proposed.

The easiest way to distinguish between the two limitation regimes is by the manipulation of the temperature. If the coating reaction was limited by a surface kinetic reaction, the change in the rate constant should be a strong function of temperature and can be described by an Arrhenius equation, such that:

$$k_{sic} = k_{sic}^o e^{-\frac{E_a}{RT}} \quad (10)$$

where k_{sic}^o was the frequency factor in cm/s and E_a was the activation energy in kJ/mole.

Since low pressures were used, mass transport was expected to be quite high, and a kinetic limited regime was checked first. The Arrhenius plot of the data is presented in Figure 9. The least squares fit of the data is also shown. It has a slope of -36436 and an intercept of 25.65. The value of the coefficient of determination, R^2 , was 95.03%, which reduced to 94.72% when adjusted for the degrees of freedom. The F-statistic for the regression was 306.21, making the probability of a Type I error on the significance of the

slope below 0.0001. The t-ratio on the slope was -17.50, meaning that the standard deviation of the slope was small compared to the estimate of the slope. The estimate on the slope then was related to the activation energy of the kinetic surface reaction at 302.929 kJ/mole (72.353 kcal/mole) with a standard deviation of 17.311 kJ/mole (4.135 kcal/mole). The estimate of the frequency factor based on the intercept was 1.374×10^{11} cm/s. The form of the kinetic rate constant as a function of temperature was given by:

$$k_{SiC} = 1.374 \times 10^{11} e^{\left(-\frac{302.929}{RT}\right)} \quad (11)$$

A comparison of this estimate to the published activation energies shows that the estimate for this reaction is on the high side of previous values, especially compared to the recent work of Besmann et al.⁸ However, this value matches fairly closely to the work of Gao and Lin⁷ who used an activation energy of 254 kJ/mole in their kinetic expression. This is important since they were using a similar arrangement, in terms of a cylindrical hot wall reactor. A possible reason for the other lower apparent activation energies which have been previously observed could be the use of conditions which might favor mass transport regimes, such as high system pressures and temperatures, low total flow rates, and cold wall reactors. Without taking the mass transport into account, a fit of the data could result in lower observable slopes in the Arrhenius plots due to the reduced sensitivity of the diffusion coefficient to temperature.

A comparison between mass transport and kinetics is shown in Figure 10 which plots the natural logarithm of the observed rate constant data along with the fitted kinetic constant and the estimated mass transport coefficient as a function of the inverse system temperature.

The Chapman-Enskog diffusion equation was used to determine the mass transfer coefficient. Taking the estimated mass transfer effects into account, it can be seen that the reaction should stay within a kinetic regime for all temperatures investigated as long as the pressure and total flow rates are not altered. As can be seen from this graph, the observed rate constants increase rapidly with temperature, as would be expected for a kinetic system. However, the mass transport response still remains over twice the kinetic response, even at the highest temperature. It would be anticipated that at a slightly higher temperature (within 200°C) that the reaction would begin to become limited by the diffusion of reagents to the substrate. Within the temperature range studied though, the reaction is limited by the kinetics of a surface reaction.

Under the conditions which were used in this study, it was not possible to check the validity of the mass transport estimations in the system. Thus, no determination was made of which diffusion coefficient was more appropriate, either the Chapman-Enskog or the Slattery-Bird treatments.¹⁷ However, the difference in the mass transfer coefficients from the two methods is quite large in that use of the Slattery-Bird coefficients resulted in mass transfer coefficients which were over three times those of the Chapman-Enskog equation. The more correct usage should then be distinguishable under conditions which would lead to mass transfer limitations.

Conclusions

The deposition of SiC has been shown feasible for both the direct reaction of mixtures of SiCl₄ and CH₄ and from the decomposition of MTS. However, appreciable amounts of

SiC were not seen from the $\text{SiCl}_4\text{-CH}_4$ reaction at temperatures below 1400°C , and the use of MTS was preferred because of its reduction in the minimum deposition temperature to as low as 1000°C . The morphology of the deposition produced from MTS was typified by its smooth, platy structure at low temperatures which became rougher at higher temperatures. The deposition mechanism was found to be in a kinetic regime and was accurately described by a first order model with respect to the bulk gas phase concentration of MTS. The activation energy was estimated to be 302.929 kJ/mole , and the frequency factor was 1.374×10^{11} . A comparison to the estimated mass transfer limit showed that the deposition rate was still within a kinetic regime in the temperature range studied but was approaching a mass transfer limitation at temperatures over 1400°C .

Acknowledgments

We wish to thank Dr. Alexander Pechenik of the Air Force Office of Scientific Research for funding and supporting this research. We also appreciate typing of the original manuscript by Virginia Myers.

References

- ¹J. Schlichting, "Chemical Vapor Deposition of Silicon Carbide," *Powder Met. Int.*, **12**, 141-7 (1980).
- ²J. Schlichting, "Chemical Vapor Deposition of Silicon Carbide," *Powder Met. Int.*, **12**, 196-200 (1980).
- ³J.N. Pring and W. Fielding, *J. Chem. Soc.*, **95**, 1497-1506 (1909).

⁴J.M. Blocher, D.P. Leiter, and R.P. Jones, BMI-1349, June 1959, Battelle Memorial Institute.

⁵P. Rai-Choudhury and N.P. Formigoini, " β -Silicon Carbide Films," *J. Electrochem. Soc.*, **116**, 1440-3 (1969).

⁶J. Chin, P.K. Gantzel, and R.G. Hudson, "The Structure of Chemical Vapor Deposited Silicon Carbide," *Thin Solid Films*, **40**, 57-72 (1977).

⁷F. Gao and R.Y. Lin, "Theoretical Modeling of Chemical Vapor Deposition of Silicon Carbide in a Hot Wall Reactor," *Mat. Res. Soc. Symp. Proc.*, **335**, 177-82 (1994).

⁸T.M. Besmann, B.W. Sheldon, T.S. Moss, and M.D. Kaster, "Depletion Effects of Silicon Carbide Deposition from Methyltrichlorosilane," *J. Am. Ceram. Soc.*, **75**, 2899-903 (1992).

⁹M.D. Allendorf and D.A. Outka, "The Reactivity of HCl and Methyltrichlorosilane with Silicon Carbide Surfaces," *Mat. Res. Soc. Symp. Proc.*, **282**, 439-44 (1993).

¹⁰G.D. Papasouliotis and S.V. Sotirchos, "Heterogeneous Kinetics of the Chemical Vapor Deposition of Silicon Carbide from Methyltrichlorosilane," *Mat. Res. Soc. Symp. Proc.*, **334**, 111-6 (1994).

¹¹C.Y. Tsai, S.B. Desu, C.C. Chiu, "Kinetic Study of Silicon Carbide Deposited from Methyltrichlorosilane Precursor," *J. Mater. Res.*, **9**, 104-11 (1994).

¹²M.G. So and J.S. Chun, "Growth and Structure of Chemical Vapor Deposited Silicon Carbide from Methyltrichlorosilane and Hydrogen in the Temperature Range of 1100 to 1400°C," *J. Vac. Sci. Technology*, **A6**, 5-8 (1988).

¹³M.K. Alam and V. Puneet, "Simulation of Fiber Coating CVD Reactor," *Thin Film Heat Transfer: Properties and Processing*, **184**, 99-106 (1991).

¹⁴C.H. Chu and M.H. Hon, "Growth Mechanism fro CVD Beta-SiC Synthesis," *Scripta Metallurgica et Materialia*, **28**, 179-83 (1993).

¹⁵K. Minato and K. Fukuda, "Chemical Vapor Deposition of Silicon Carbide for Coated Fuel Particles," *J. Nuc. Mater.*, **149**, 233-46 (1987).

¹⁶F. Loumagne, F. Langlais, and R. Naslain, "Kinetic Laws of the Chemical Process in the CVD of SiC Ceramics from $\text{CH}_3\text{SiCl}_3\text{-H}_2$ Precursor," *J. De Physique IV*, **3**, 527-33 (1993).

¹⁷T.S. Moss, "The Chemical Vapor Deposition of Dispersed Phase Composites in the B-Si-C-H-Cl-Ar System," Ph.D. Dissertation, Georgia Institute of Technology, 1995.

¹⁸D.-T. Chin and C.-H. Tsang, "Mass Transfer to an Impinging Jet Electrode," *J. Electrochem. Soc.*, **125**, 1461-70 (1978).

LIST OF FIGURES

- Figure 1. A vertical hot wall reactor was used to deposit SiC coatings.
- Figure 2. Cross-section (a) and surface morphology (b) of SiC film deposited on graphite at 1200°C at a high deposition rate of 4.86×10^{-7} cm/s (DB-182).
- Figure 3. Cross-section (a) and surface morphology (b) of SiC film deposited on graphite at 1200°C at a high deposition rate of 24.92×10^{-7} cm/s (DB-243).
- Figure 4. Cross-section (a) and surface morphology (b) of SiC film deposited on graphite at 1400°C at an intermediate deposition rate of 68.91×10^{-7} cm/s (DB-241).
- Figure 5. Cross-section (a) and surface morphology (b) of SiC film deposited on graphite at 1400°C at a high deposition rate of 152.7×10^{-7} cm/s (DB-254).
- Figure 6. The reaction rate versus the MTS concentration at 1000°C verifies a first order relationship.
- Figure 7. The reaction rate versus the MTS concentration at 1200°C verifies a first order relationship.
- Figure 8. The reaction rate versus the MTS concentration at 1400°C verifies a first order relationship.
- Figure 9. The Arrhenius plot for SiC deposition at 1000, 1200, and 1400°C is fit by a regressed line with a slope of -36436 and an intercept of 25.646 with an R^2 of 95.0%, indicating that the reaction is controlled by the kinetics.

Figure 10. A comparison of the observed data to the fitted kinetic rate constant and the estimated mass transfer coefficient shows that the reaction approaches the estimated mass transfer limit as the temperature increases.

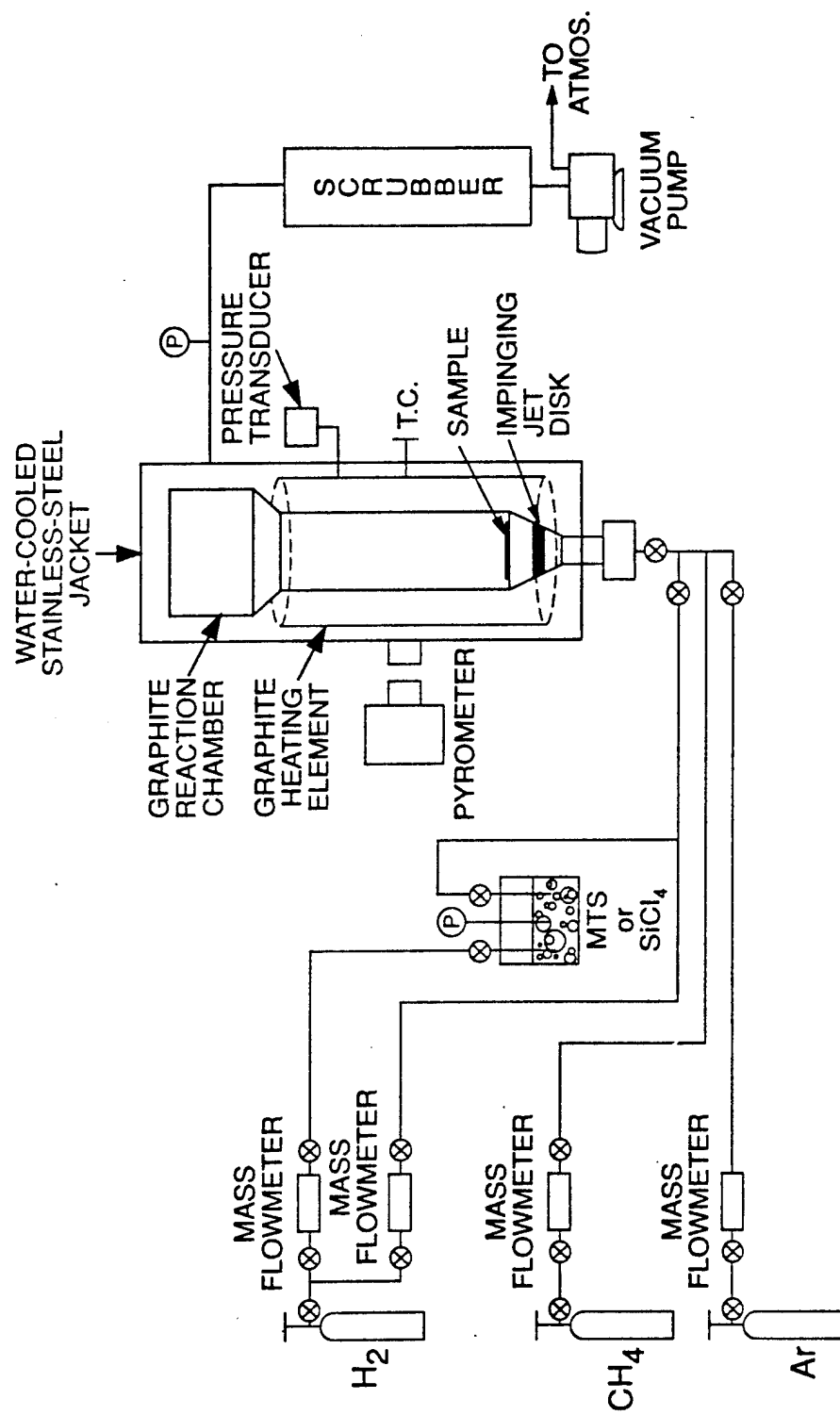
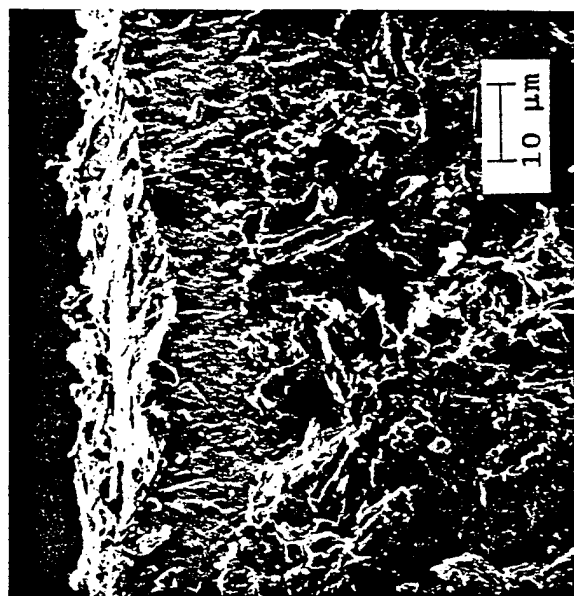


Figure 1. A verticle hot wall reactor was used to deposit SiC coatings.

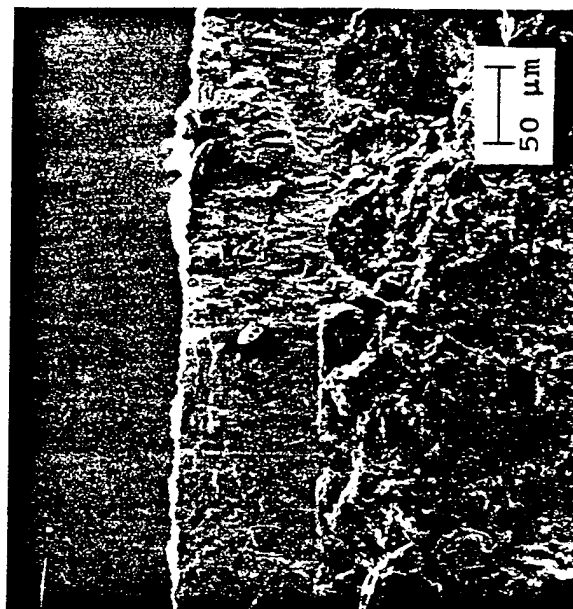


(a)

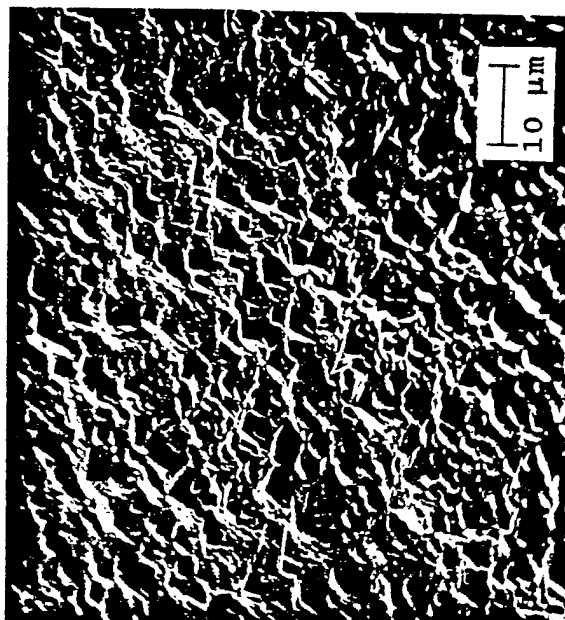


(b)

Figure 2. Cross-section (a) and surface morphology (b) of SiC film deposited on graphite at 1200°C at a high deposition rate of 4.86×10^{-7} cm/s (DB-182).

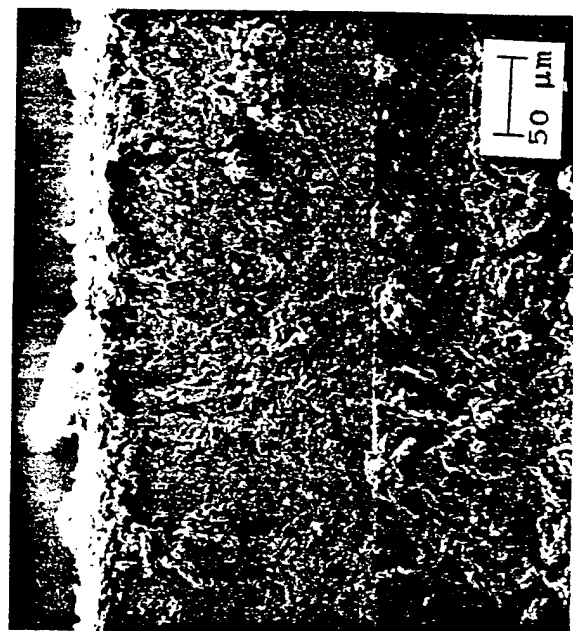


(a)



(b)

Figure 3. Cross-section (a) and surface morphology (b) of SiC film deposited on graphite at 1200°C at a high deposition rate of 24.92×10^{-7} cm/s (DB-243).

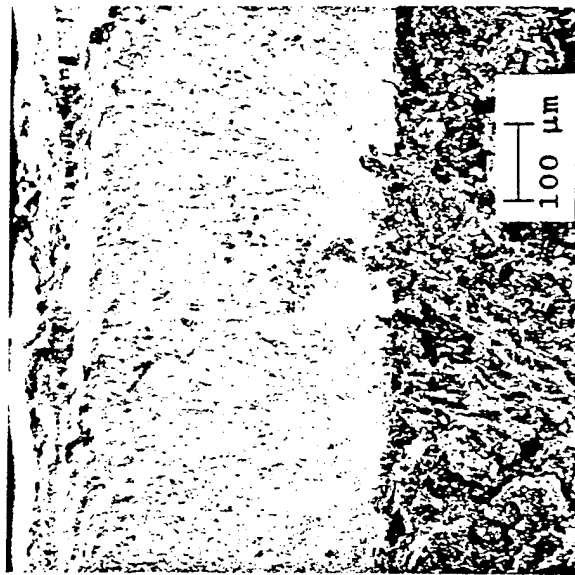


(a)

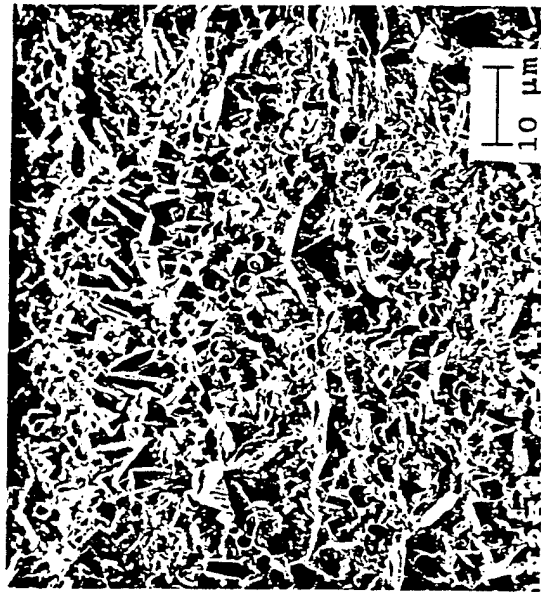


(b)

Figure 4. Cross-section (a) and surface morphology (b) of SiC film deposited on graphite at 1400°C at an intermediate deposition rate of 68.91×10^{-7} cm/s (DB-241).



(a)



(b)

Figure 5. Cross-section (a) and surface morphology (b) of SiC film deposited on graphite at 1400°C at a high deposition rate of 152.7×10^{-7} cm/s (DB-254).

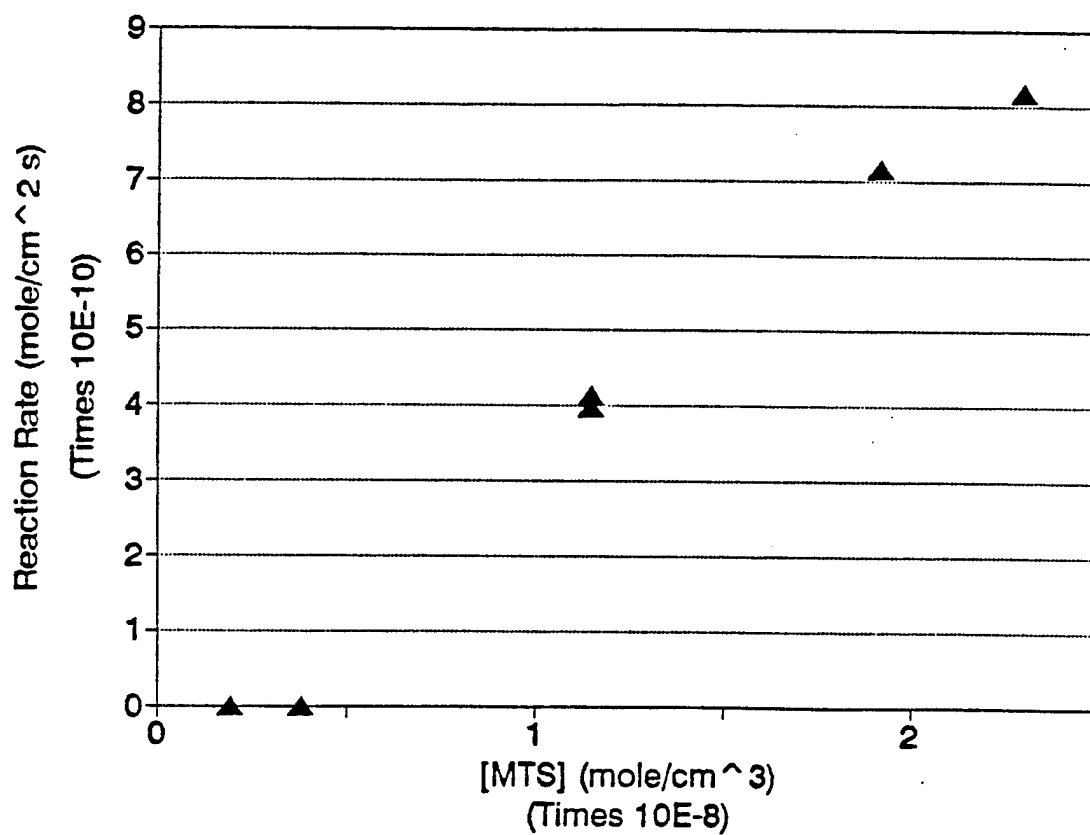


Figure 6. The reaction rate versus the MTS concentration at 1000°C verifies a first order relationship.

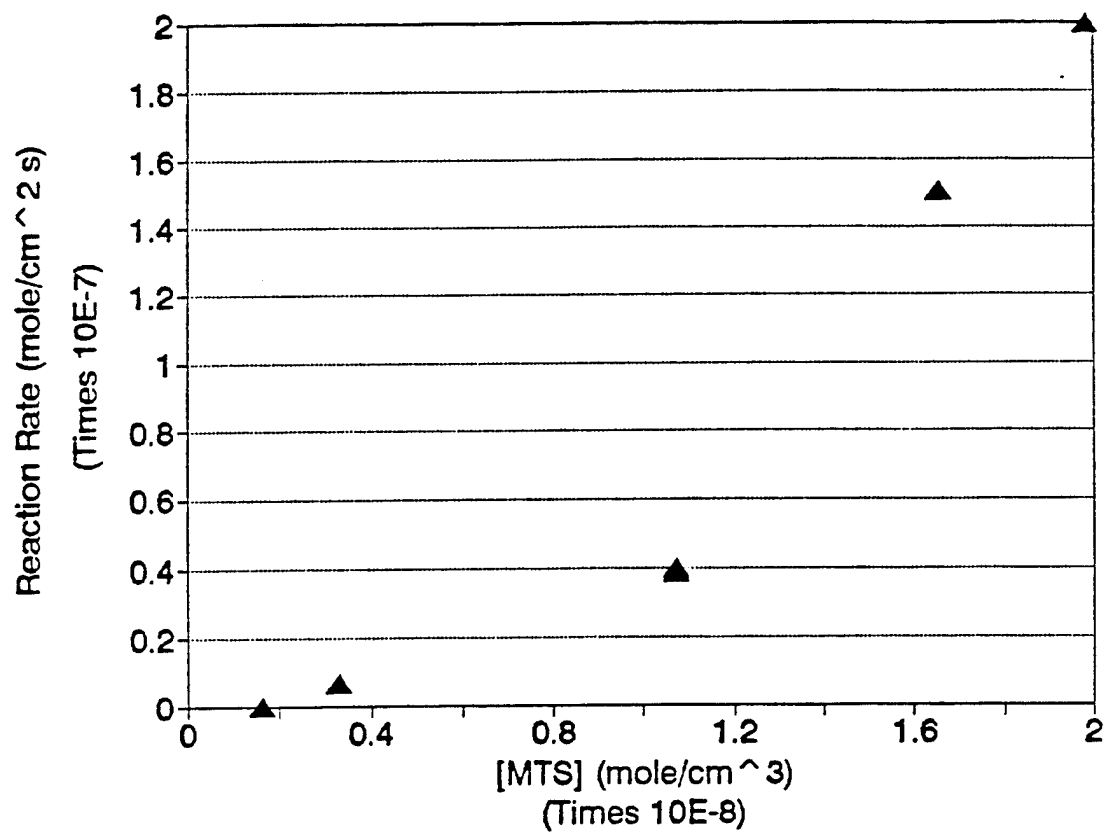


Figure 7. The reaction rate versus the MTS concentration at 1200°C verifies a first order relationship.

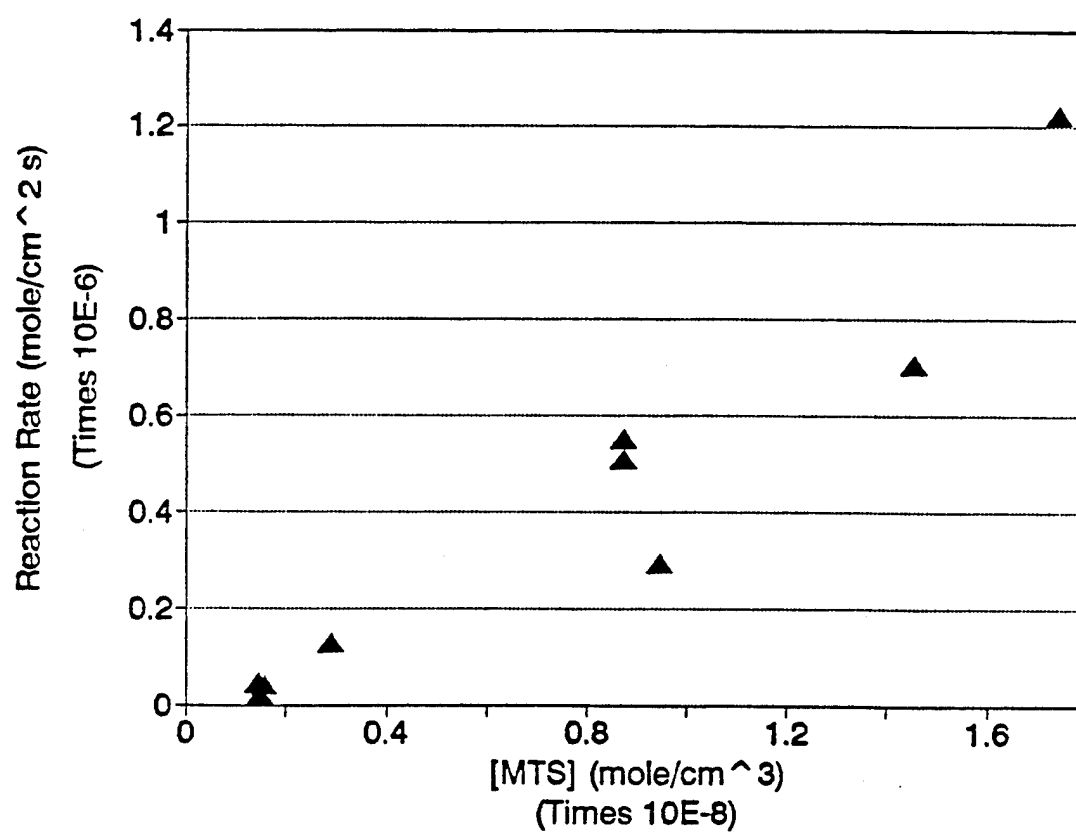
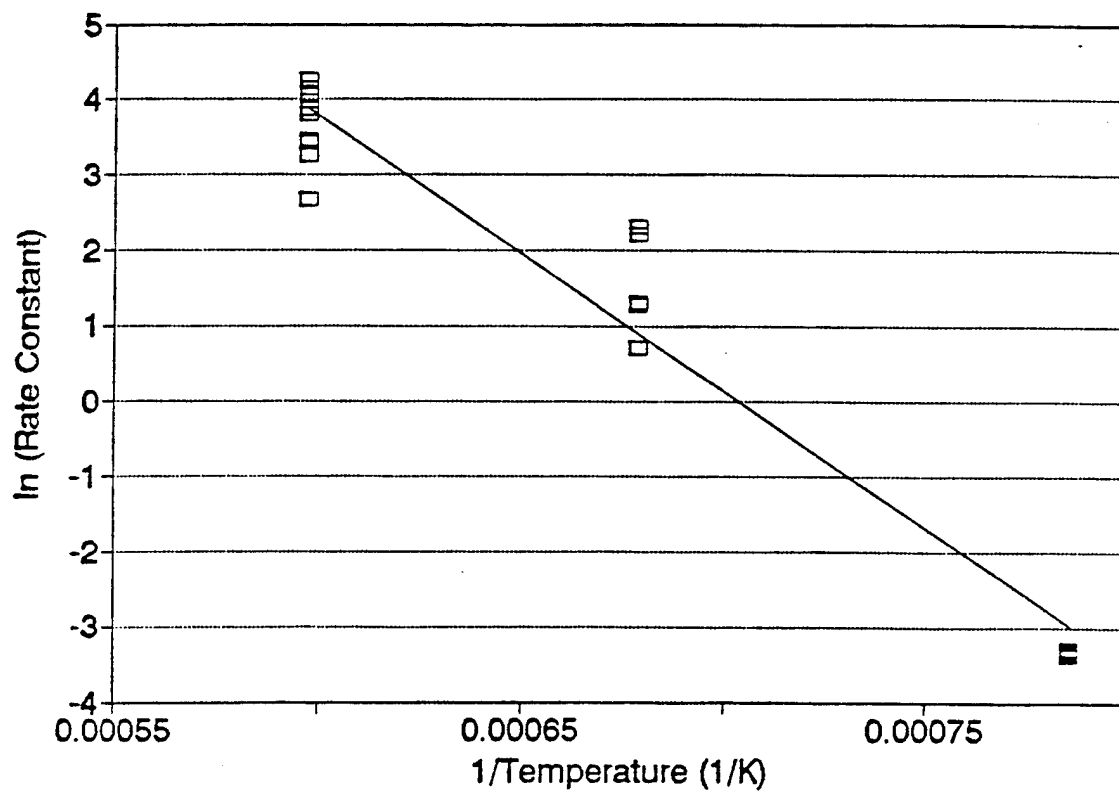


Figure 8. The reaction rate versus the MTS concentration at 1400°C verifies a first order relationship.



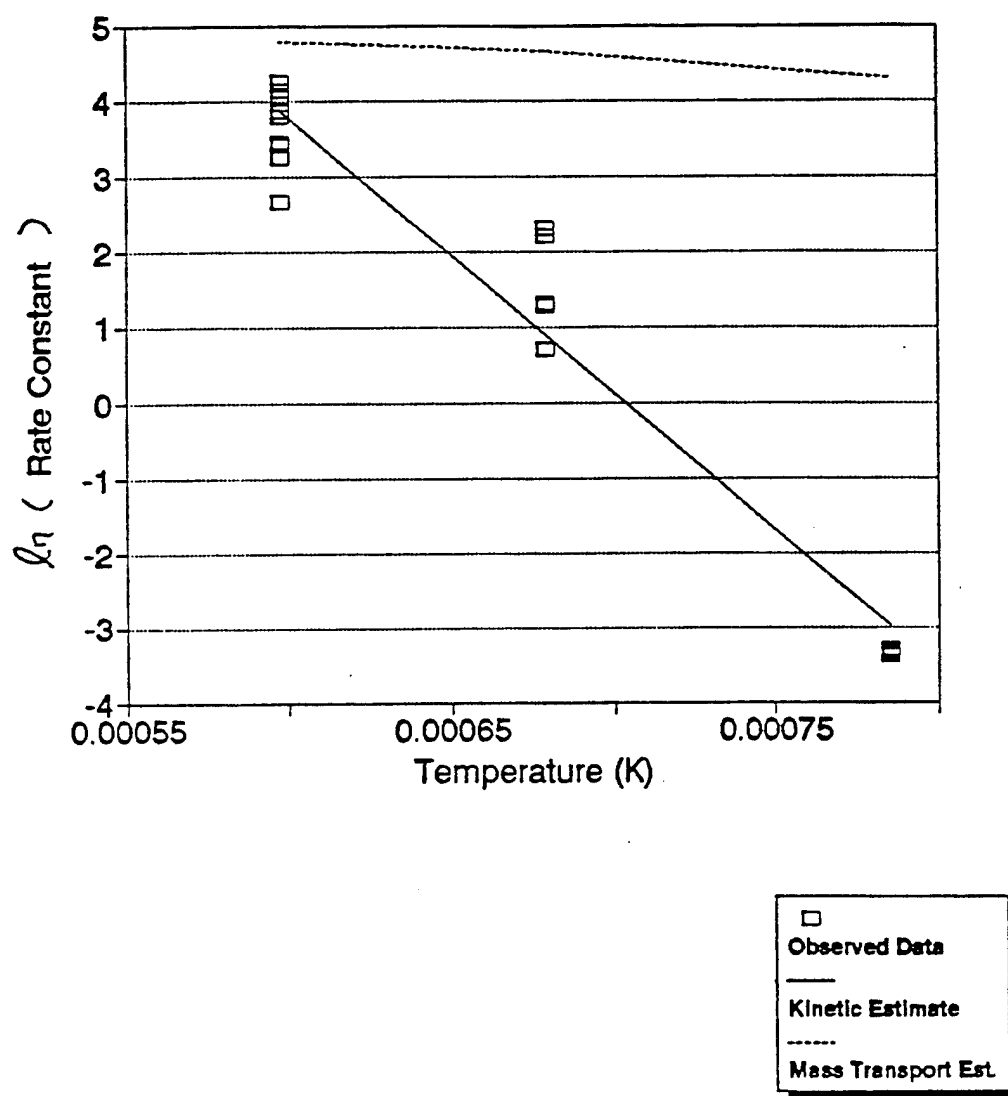


Figure 10. A comparison of the observed data to the fitted kinetic rate constant and the estimated mass transfer coefficient shows that the reaction approaches the estimated mass transfer limit as the temperature increases.

Table I. Conditions for the deposition of SiC from $\text{SiCl}_4 + \text{CH}_4 + \text{H}_2 + \text{Ar}$ at the indicated temperatures.

Run No. DB-	Time (min)	Pressure (torr)	Flow Rate (sccm)			
			SiCl ₄	CH ₄	H ₂	Ar
Temperature = 1000°C						
70	90	76	7.4	14.7	118	4527
73	120	76	7.0	7.0	126	4527
76	120	76	7.8	23.6	109	4527
163	75	76	124.3	25.0	116	4735
Temperature = 1200°C						
69	60	76	7.4	14.7	118	4527
72	60	76	7.0	7.0	126	4527
75	90	76	7.8	23.6	109	4527
161	60	76	47.4	25.0	116	4811
169	60	76	19.7	145.0	116	4720
Temperature = 1400°C						
71	45	76	7.0	7.0	126	4527
74	60	76	7.8	23.6	109	4527
153B	45	76	8.5	25.0	116	4850
154	45	76	47.4	25.0	116	4811
155	45	76	86.2	25.0	116	4772
165	45	76	19.7	25.0	116	4839
166	45	76	19.7	65.8	116	4799
167	45	76	19.7	145.0	116	4720
168	30	76	19.7	145.0	216	4619
171	30	76	19.7	145.0	316	4519
173	30	76	19.7	145.0	416	4419

Table II. Conditions for the deposition of SiC from MTS+H₂+Ar at the indicated temperatures.

Run No. DB-	Time (min)	Pressure (torr)	Flow Rate (sccm)		
			MTS	H ₂	Ar
Temperature = 1000°					
123	120	76	9.4	128	4430
250	75	76	60.0	600	4340
251	75	76	60.0	600	4340
258	90	76	20.0	200	4780
259	90	76	100.0	1000	3990
260	90	76	120.0	1200	3680
Temperature = 1200°					
175	45	76	10.0	100	4890
182	45	76	65.0	600	4335
184	45	76	65.0	400	4535
243	60	76	120.0	1200	3680
245	60	76	100.0	1000	3900
248	60	76	20.0	200	4780
Temperature = 1400°					
119	30	76	10.0	127	4430
122	30	76	9.4	128	4430
176	30	76	10.0	100	4890
183	30	76	65.0	600	4335
240	45	76	100.0	1000	3900
241	45	76	60.0	600	4340
252	45	76	60.0	600	4340
253	45	76	20.0	200	4780
254	45	76	120.0	1200	3680

Table III. Characterization of SiC produced from $\text{SiCl}_4 + \text{CH}_4 + \text{H}_2 + \text{Ar}$ at the indicated temperatures.

Run No. DB-	Phase	Deposit Thickness (μm)	Deposition Rate ($\times 10^7$) (cm/s)
Temperature = 1000°C			
70	None	0.00	0.000
73	None	0.00	0.000
76	None	0.00	0.000
103	None	0.00	0.000
Temperature = 1200°C			
69	$\beta + \alpha$ -SiC	4.069	1.130
72	$\beta + \alpha$ -SiC	1.563	0.434
75	$\beta + \alpha$ -SiC	10.47	1.939
161	$\beta + \alpha$ -SiC	1.753	0.487
169	$\beta + \alpha$ -SiC	1.725	0.479
Temperature = 1400°C			
71	$\beta + \alpha$ -SiC	1.678	0.621
74	$\beta + \alpha$ -SiC	7.440	2.067
153B	β -SiC	0.744	0.276
154	$\beta + \alpha$ -SiC	1.912	0.708
155	$\beta + \alpha$ -SiC	6.788	2.514
165	$\beta + \alpha$ -SiC	4.106	1.521
166	$\beta + \alpha$ -SiC	10.08	3.733
167	$\beta + \alpha$ -SiC	4.744	1.757
168	$\beta + \alpha$ -SiC	9.703	5.391
171	$\beta + \alpha$ -SiC	16.98	9.433
173	$\beta + \alpha$ -SiC	16.69	9.272

Table IV. Results for the deposition of SiC from MTS at the indicated temperatures.*

Run No. DB-	Phase	Dep. Thick. (μm)	Dep. Rate ($\times 10^7$) (cm/s)	δ_{MTS} ($\times 10^2$) (cm)	δ'_{MTS} ($\times 10^2$) (cm)	$(D/\delta)_{\text{MTS}}$ (cm/s)	$(D/\delta)'_{\text{MTS}}$ (cm/s)
Temperature = 1000°C, $D_{\text{MTS}} = 1.79 \text{ cm}^2/\text{s}$ and $D'_{\text{MTS}} = 9.39 \text{ cm}^2/\text{s}$							
213	None	0.000	0.000	2.153	3.771	83.36	249.1
250	β -SiC	0.223	0.0496	2.391	4.189	75.04	224.2
251	β -SiC	0.298	0.0515	2.437	4.269	73.63	220.0
258	β -SiC	0.000	0.000	2.433	4.262	73.75	220.4
259	β -SiC	0.483	0.0894	2.419	4.238	74.18	221.6
260	β -SiC	0.550	0.102	2.443	4.279	73.46	219.5
Temperature = 1200°C, $D_{\text{MTS}} = 2.29 \text{ cm}^2/\text{s}$ and $D'_{\text{MTS}} = 12.26 \text{ cm}^2/\text{s}$							
175	None	0.00	0.00	2.159	3.890	106.2	321.7
182	β -SiC	13.13	4.86	2.163	3.816	106.1	321.2
184	β -SiC	13.50	5.00	2.157	3.805	106.4	322.1
243	$\beta + \alpha$ SiC	89.70	24.92	2.169	3.826	105.7	320.3
245	$\beta + \alpha$ SiC	67.69	18.80	2.167	3.823	105.8	320.5
248	β -SiC	3.03	0.84	2.507	4.423	91.49	277.1
Temperature = 1400°C, $D_{\text{MTS}} = 2.84 \text{ cm}^2/\text{s}$ and $D'_{\text{MTS}} = 15.46 \text{ cm}^2/\text{s}$							
119	β -SiC	9.384	5.213	2.359	4.187	120.4	369.1
122	β -SiC	4.847	2.693	2.359	4.188	120.4	369.1
176	β -SiC	10.37	5.761	2.253	4.000	126.0	386.4
183	β -SiC	65.79	36.55	2.257	4.007	125.8	385.8
240	$\beta + \alpha$ SiC	237.0	87.79	2.261	4.015	125.5	385.0
241	$\beta + \alpha$ SiC	186.1	68.91	2.258	4.009	125.7	385.6
252	$\beta + \alpha$ SiC	171.3	63.44	2.620	4.652	108.3	332.2
253	$\beta + \alpha$ SiC	44.11	16.34	2.716	4.821	104.5	320.6
254	$\beta + \alpha$ SiC	412.3	152.7	2.677	4.752	106.1	325.2

*The Chapman-Enskog diffusion coefficient (D_{MTS}) and the Slattery-Bird coefficient (D'_{MTS}) are given for each temperature.

Table V. Relative intensities, in %, of diffraction peaks for the XRD of β -SiC samples (N/E: Peak was not estimable due to overlap of a neighboring graphite peak).

Run No. DB-	111	200	220	311
250	100	N/E	N/E	18
259	100	N/E	N/E	30
260	100	N/E	N/E	35
182	100	0	44	27
245	100	< 1	< 1	2
243	100	< 1	< 1	1
176	100	9	28	31
241	59	1	100	15
254	41	2	100	12

Factors Affecting the CVD of $B_{13}C_2$ +SiC Dispersed Phase Composites

Thomas S. Moss^{ab} and W. Jack Lackey,^a Georgia Institute of Technology, Atlanta, GA

30332-0826

Abstract

The codeposition of $B_{13}C_2$ +SiC has been shown to occur from mixtures of BCl_3 +MTS+ CH_4 + H_2 +Ar in a vertical, hot wall CVD reactor using a modified impinging jet geometry. A comparison of the observed and predicted deposition, based on prior results for the deposition of SiC and $B_{13}C_2$ separately, showed that the deposition of the two phases did not occur independently of one another. From an analysis of the difference between the actual and anticipated deposit thickness, more deposition was observed than predicted at low temperatures and MTS flow rates. At higher temperatures and low MTS flow rates, less deposition was observed than predicted. This difference was attributed to the influence of codeposition on nucleation phenomena. A methodology was developed for comparing actual codeposition rates with rates predicted from single phase deposition.

Codeposition, CVD, Boron Carbide, Silicon Carbide, Coatings

^aMember, ACS

^bPresent address Los Alamos National Laboratory, Los Alamos, NM

Introduction

The attraction to ceramic composite coatings results from the ability to alter and tailor the final properties of the coating to fit the requirements of the application. Such requirements quite frequently include the toughening of brittle ceramics. Zirconia toughened alumina and transformation toughened zirconia are two examples of composites where the fracture toughness may be increased by the inclusions of additional phases. Further, the chemical and oxidation properties of the composite may be favorably changed by the proper choice of components. Also, the electrical, tribological, thermal, and optical properties may be enhanced by the use of composite materials.

The process of chemical vapor deposition (CVD) offers a unique method by which composite coatings may be produced. Deposits which feature different chemical compounds or phases may be prepared by either the deposition of alternate layers or by the simultaneous deposition of multiple phases. Reviews of successes in the codeposition of composite coatings have appeared in the literature.¹⁻⁴

Background

This section reviews the limited work in the multiple phase deposition system, B-Si-C. Only two groups have published research from the CVD of compounds within this system. Also, a review of the investigations of the B-Si-C phase diagram are included.

Gugel et al.⁵ studied the ternary B-Si-C system in detail, in particular an investigation into the pseudobinary B_4C -SiC system. In all cases, x-ray analysis showed the presence of two phase SiC and B_4C , independent of the sintering conditions. There was evidence to

suggest some slight solubility of SiC in B_4C . These findings were based on a decrease in the lattice constants beyond the lowest values seen in the investigation of the B-C system. The lowering of these values were seen in samples with increasing sintering temperatures and increasing SiC content, leading to the conclusion of slight solubility. However, such solubility was not confirmed by the surrounding literature. The determination of the eutectic was found to lie at about 65 mole percent B_4C and at approximately $2250^{\circ}C$. The values differ slightly from those reported by Secrist, who found the eutectic to be about 62% B_4C and $2300^{\circ}C$.⁶ In Figure 1, a comparison of the two eutectic temperature and composition determinations is made. Further, Gugel reported that no ternary compounds were found within the B-Si-C system, although some compositions had been previously reported.⁷ The ternary phase diagram is shown in Figure 2, showing melting isotherms and eutectic lines.

The CVD of multiphase ceramics in the B-Si-C system was reported by Golda and Gallois.⁸ Their coatings were produced from reactions of MTS, BCl_3 , CH_4 , and H_2 in a hot wall reactor at 33 MPa (200 torr). Graphite plates were used as substrates and the total flow was fixed at 500 sccm. Below 1473 K, their coatings were amorphous, and at higher temperatures deposition was controlled by non-equilibrium reactions. The most common observed coating was comprised of a SiC matrix with a silicon boride, SiB_6 , dispersed phase. With control of the BCl_3 and CH_4 flow rates, composites of $B+B_4C+SiB_6$ and $SiC+SiB_6+SiB_{14}$ were possible. The qualitative aspects of the deposits were explainable using non-equilibrium thermodynamic calculations. However, no kinetic or microstructural analysis of the deposition was reported.

Goujard et al.⁹ also examined the CVD of compounds in the B-Si-C system at 1400 K and 0.395 atm (300 torr). They initially thoroughly studied the thermodynamics of the system to determine the deposition diagrams and used the calculations to compare against experimental results. Deposition was done on polished graphite substrates suspended within a hot wall reactor. Reagent gases were BCl₃, MTS, and H₂. However, no independent carbon source, such as CH₄, was used; the only carbon present in the system was delivered from the MTS molecule or at the surface of the substrate. It is unclear whether the amount of carbon in the MTS molecule was sufficient or if diffusion of carbon from the substrate was needed. Of particular interest was the issue of free carbon formation; in the thermodynamic analysis, mixtures with low hydrogen contents inhibited the reduction of the chlorosilanes, silicon chlorides, and the boron-containing species, and the formation of free carbon was predicted from the thermodynamics. In the experimentation, free carbon was observed in amounts higher than predicted from thermodynamic analysis, but some of this was explained from homogeneous nucleation since soot was present. The comparison between thermodynamic and experimental results showed good agreement at the bottom of the graphite substrates where the gas first came in contact with the surface. However, at positions along the substrate away from the bottom face deviations from the calculated equilibrium occurred, possibly due to fluid dynamic effects or due to heterogeneous kinetic differences between the boron and silicon chloride reagent molecules.

Goujard et al.¹⁰ were able to extend some of the information which they learned from the deposition of these compounds to the chemical vapor infiltration process. The latter process was of interest for the protection of oxidation sensitive materials, such as carbon

based composites. Once again, this group used mixtures of MTS, BCl_3 , and H_2 , with no separate carbon source reagent. Within their patent, they indicate that, using these reagents, it becomes possible to change from a SiC matrix to a B-Si-C matrix by the addition of BCl_3 gas to the reagent flow. This enabled them to grade the coating composition away from a pure SiC phase to a B-Si-C matrix by a slow increase in the BCl_3 flow up to the desired value. They found it best to put a layer of pure SiC, or another refractory carbide, between any pyrolytic carbon in the matrix and the B-Si-C protective layer. This prevented the carbon from reacting with the glassy phases formed in the B-Si-C layer and prevented the diffusion of boron into the carbon matrix." Results based on microprobe analysis show that they were successful in producing a graded coating transitioning between SiC and a B-Si-C phase through this control of the BCl_3 flow. However, no kinetic information for the reaction was provided, and no work was done towards discovering conditions which could optimize the deposition reaction.

Procedure

The deposition of dispersed phase composites was accomplished in a vertical, hot wall reactor from mixtures of $\text{BCl}_3 + \text{MTS} + \text{CH}_4 + \text{H}_2 + \text{Ar}$. A modified impinging jet geometry was employed for the substrate to simplify the diffusional modeling of the system. The details of this system have been previously described in greater detail.^{11,12}

Results and Discussion

The modeling of the codeposition reaction using statistical methods, as was covered elsewhere,¹¹ was effective. However, while the resulting regression equations accurately described the observed results (correlation coefficient of 95%), such as the Si to B ratio, the equations did not portray the exact deposition mechanism. For this type of analysis, a more fundamental approach was needed.

In previous publications,^{13,14} two kinetic equations were determined to adequately reflect the single phase deposition of $B_{13}C_2$ and SiC. These equations were:

$$J_{B_{13}C_2} = 10792 e^{(-\frac{93092}{RT})} [BCl_3]^0 \quad (1)$$

for the reaction (deposition) rate of $B_{13}C_2$, and

$$J_{SiC} = 1.374 \times 10^{11} e^{(-\frac{302929}{RT})} [MTS]^0 \quad (2)$$

for SiC.

If the reactions to produce the dispersed phase composites occurred independently, i.e., without regard to the other reaction, then the overall deposit thickness and deposition rate should be the summation of the two individual reactions. The overall reaction rate, J_{Total} , should then be

$$J_{Total} = J_{B_{13}C_2} + J_{SiC} \quad (3)$$

However, if the reactions did not occur independently but rather were interrelated, the overall reaction is complex and of the form:

$$J_{Total} = f(J_{B_{13}C_2}, J_{SiC}, X_{B_{13}C_2}, X_{SiC}) \quad (4)$$

where $X_{B_{13}C_2}$ and X_{SiC} represent the amounts of $B_{13}C_2$ and SiC present. The easiest way to check for independence of the deposition reactions was by comparing the observed deposition thickness against the calculated (predicted) thickness based on Equation 3. This comparison is shown in Table 1.

If the reactions occurred independently, then the difference between the observed and estimated deposition thickness, i.e., the 'Diff.' column, should be zero. However, an examination of this table showed that the deposition definitely cannot be explained by the simple addition of the two deposition rates. Differences between the observed and estimated deposition thicknesses ranged from $-171.98 \mu m$ to $98.51 \mu m$ and cannot realistically be explained by variability in the data.

As a result of this variation away from independence, the conditions which led to deviations were investigated using statistical analysis of the difference against the input (processing) conditions. The result of the stepwise regression showed that the variation was explained using a three variable equation at an R^2 of 87.2%, which only dropped to 86.0% with the adjustment for the degrees of freedom. The standard deviation of the fit was $18.60 \mu m$ and the F-statistic was 68.32. The normal scores of the standard residuals were fit by a

line with a slope of 0.91 and an intercept of 0.01. The significant effects were the temperature, temperature squared, and MTS flow rate squared. The form of the equation was given by

$$\Delta_{Dep} = 0.482 - 49.603 * x_5 - 20.472 * x_5 x_5 + 6.948 * x_2 x_2 \quad (5)$$

where Δ_{Dep} was the difference between the observed and predicted total deposition, x_5 was the coded value of the temperature, and x_2 was the coded value of the MTS flow rate.¹² The standard deviation of each were 3.882, 3.319, and 3.319, respectively. The standard deviation of the constant was estimated at 4.52; regression without a constant was tried but did not significantly change the regression surface. This analysis revealed that temperature was the critical parameter controlling the deviation away from independence of the reactions. At low temperatures, the reactions occurred faster than was predicted by the independent reaction rates. As the temperature increased towards the middle value, the observed and predicted deposition was about the same, i.e., the difference decreased to around zero. However, at the higher temperatures the observed deposition was much thinner than was predicted. The significance of the MTS flow rate was much lower than that from the temperature and its t-ratio was just above two, making it close to the 95% confidence limit. However, the fit was improved by its use in the expression above what was seen using only the temperature and temperature squared. A contour plot of the difference in the observed and the predicted deposition against the temperature and MTS flow rate is shown in Figure 3. This plot illustrated how the deviation was affected by the conditions, especially the strong effect of temperature. The more negative values of the difference occurred at the

higher temperatures and the lower MTS flow rates. Conversely, the more positive values of the difference occurred at lower temperatures and higher MTS flow rates. The appearance of a saddle point was observed, resulting from the linear and quadratic temperature terms.

The difference in the observed and predicted deposition rates was also checked against the predicted amounts of $B_{13}C_2$ and SiC based on the derived kinetic equations, i.e., Equations 1 and 2. The aim of this regression analysis was to examine the kinetic equations for conditions which would lead to deviations away from independence. That is, to check for instances where high deviations in the amount of observed deposit could be attributed to conditions which predicted high amounts of an individual phase. The results of the regression produced an equation defined by

$$\Delta_{Dep} = 45.17 - 1.462 * t_{SiC}^{Pred} - 0.960 * t_{B_{13}C_2}^{Pred} \quad (6)$$

where t_i^{Pred} was the predicted amounts of phase i in μm . The value of R^2 was 78.4% which dropped to 77.0% when adjusted for the degrees of freedom; the standard deviation of the fit was 23.79 μm ; and the F-statistic was 56.32. A fit of the normal scores of the standard residuals had a slope of 0.91 and an intercept of -0.02. This regression showed that the conditions which led to high predicted amounts of SiC deposition, i.e., high MTS flow rate and high temperature, had the greater effect on the difference, Δ_{Dep} . The negative sign preceding the t_{SiC}^{Pred} term showed that higher amounts of SiC decreased the actual codeposition to values below what would be predicted from the single phase deposition systems. Further, lower amounts of predicted SiC deposition led to more positive differences; that is, the actual deposition was higher than was predicted from the single phase systems. The significance of the estimated $B_{13}C_2$ deposition did show the same behavior as the SiC deposition, but the

standard deviation of this effect was high (0.404) compared to the magnitude of the effect, making the t-ratio -2.37 and placing it close to the 95% confidence limit. This was important especially when compared to the standard deviation of the SiC deposition effect which was only 0.262, giving a t-ratio of -5.59. A contour plot of the fit is shown in Figure 4.

A final type of comparison of the deviation of the observed data was done with the difference between the observed deposition of the individual phases and the predicted values based on Equations 1 and 2. This observed amount of the individual phase was calculated using the percentage of $B_{13}C_2$ and SiC based on Rietveld refinement of the X-ray diffraction patterns. These data, the difference in the individual predicted and observed phase deposition, are summarized in Table 2.

The regression of the difference in the observed and predicted $B_{13}C_2$ deposition was fit by a four parameter surface defined by the equation:

$$\Delta_{B_{13}C_2} = -8.790 - 25.503 * x_5 - 6.931 * x_5 x_5 - 9.088 * x_2 + 8.984 * x_2 x_2 \quad (7)$$

where $\Delta_{B_{13}C_2}$ was the difference between the observed and estimated $B_{13}C_2$ deposition thickness in μm , x_5 was the coded temperature value, and x_2 was the coded MTS flow rate value. The coefficient of multiple determination was 77.9% and dropped to 75.2% when adjusted for degrees of freedom. The standard deviation of the fit was $14.69 \mu m$ and the F-statistic was 28.27. The standard deviation of each of the effects was 2.941, 2.601, 2.777, and 2.300, respectively; the standard deviation of the constant was 3.539. The normal scores of the standard residuals was fit by a line with a slope of 0.91 and an intercept of 0.00. This surface demonstrated that high temperatures led to less deposition than predicted

by the single phase deposition equations. The influence of the MTS flow rate showed that the presence on MTS depressed the actual deposition to values below the estimated amount. A contour plot of the difference in the $B_{13}C_2$ deposition against the temperature and the MTS flow rate is shown in Figure 5.

A similar regression surface was derived for the difference in the SiC deposit thickness. This surface fit the data at a value of 90.1% (R^2_{Adj} of 86.8%) with an F-statistic of 27.39 and a standard deviation of $10.41 \mu m$. However, the surface was composed of nine parameters and, because of its size, is shown in Table 3. In this table, x_1 through x_9 represent the following coded variables: BCl_3 flow rate, MTS flow rate, CH_4 flow rate, H_2 flow rate, and temperature, respectively. From this surface, it was evident that the temperature, the MTS flow rate and the BCl_3 flow rate were the most important in influencing the deviation of the SiC deposition by virtue of their high effect estimates and low standard deviations. However, this surface was not quite as stable as others, and this was reflected in the fit of the normal scores which had a slope of 0.87 and an intercept of -0.01. It was not possible to realistically develop a contour plot to describe the surface since there were so many significant terms present.

Considering all of the regression information together, it was obvious that the important parameters which controlled the deviation away from independence for the dispersed phase deposition were the temperature and the MTS flow rate. This can be seen in the fit of the total deposition rate, in the fit of the $B_{13}C_2$ deposition, and, to some extent, in the fit of the SiC deposition. From this, the presence of MTS and, consequently, the presence of SiC from the MTS led to decreases in the actual observed deposition and the

observed $B_{13}C_2$ deposition, although much of the decrease in the total deposition may be attributed to the decrease in the $B_{13}C_2$ deposition. This trend which was confirmed by regressing the difference in deposition thickness against the individual predicted deposition amounts, i.e., Equation 6. On the other hand, under conditions which led to small amounts of SiC deposition, i.e., low temperatures and MTS flow rates, the actual observed total deposition and observed deposition of $B_{13}C_2$ were increased, in some cases by a dramatic amount. Again, this trend was confirmed by the regression of the deviation against the predicted phase amounts.

This change in the $B_{13}C_2$ deposition was hypothesized to be the result of two factors, both of which involved the SiC deposition. The first was that conditions which produced small amounts of SiC actually improved the deposition of $B_{13}C_2$ due to the reduced free energy of nucleating onto SiC rather than graphite and to some extent $B_{13}C_2$. The lower interfacial free energy enabled the $B_{13}C_2$ to nucleate and grow with shorter lag times than was possible with a graphite substrate. Further, since SiC was present throughout the coating, $B_{13}C_2$ was able to renucleate during the course of the composite deposition, significantly increasing the reaction rate of the $B_{13}C_2$. This observation is supported by the examination of the surface morphology of the composite samples. In these samples, the $B_{13}C_2$ showed a finer surface feature size than was seen for the pure $B_{13}C_2$ deposition, especially when comparing the samples shown in Figures 6 and 7 which were both deposited at 1200°C and similar BCl_3 concentrations.

Under conditions which led to high amounts of SiC deposition, the deposition of $B_{13}C_2$ was actually retarded due to the competitive nucleation and growth which was

occurring between the $B_{13}C_2$ and the SiC. In other words, after a nucleus of $B_{13}C_2$ was able to form and its growth had commenced, its active growth was halted because of the nucleation of a neighboring SiC grain and perhaps overcoating of $B_{13}C_2$ by SiC. The result was that the observed deposition of $B_{13}C_2$ was lower than in single phase deposition and much lower than when its production was catalyzed by small amounts of SiC. Those conditions which yielded intermediate quantities of SiC showed a transition between the two extremes with variations occurring due to random variations in the surface chemistry. That is to say that the possibility of SiC grains being more concentrated in local regions due to random chance could lead to enhancing the deposition of $B_{13}C_2$ in some areas but retarding deposition in others. However, the deviation of the deposition of $B_{13}C_2$ was greatly affected, for better and for worse, by the presence of SiC. Thus, the actual deposition of $B_{13}C_2$ during codeposition conditions could be described by the equation:

$$t_{B_{13}C_2}^{Act} = t_{B_{13}C_2}^{Pred} + \Delta_{B_{13}C_2} \quad (8)$$

where $t_{B_{13}C_2}^{Act}$ was the actual thickness of $B_{13}C_2$ in μm , $t_{B_{13}C_2}^{Pred}$ was the predicted deposition thickness of $B_{13}C_2$ in μm based on Equation 1, and $\Delta_{B_{13}C_2}$ was the difference between actual and predicted deposit thickness in μm of $B_{13}C_2$ as defined by Equation 7.

The deviation in the SiC deposition was not quite as frequent as that observed for $B_{13}C_2$ but the differences that were present were generally quite high. This was seen in the differences in the form of the equations for the individual SiC deposition difference (Table III) and the total deposition difference (Equation 5). The form of the $B_{13}C_2$ difference equation (Equation 7) was almost exactly the same as the total deposition difference equation except for the presence of the linear MTS flow rate effect in the individual $B_{13}C_2$ equation.

However, because the variation of the SiC deposition was generally much less, the form of the difference equation was more sensitive to smaller variations which might have been due to random variability but were accounted for by the presence of the many interaction terms in Table III. The variation which was present in SiC deposition can be explained using the same reasoning for the $B_{13}C_2$ deposition presented in the previous paragraph. Conditions which led to high amounts of $B_{13}C_2$ deposition interfered with the nucleation and growth of SiC, as evidenced by the regression of the difference in total deposition against the individual predicted deposition. Further, conditions which would ordinarily lead to low amounts of $B_{13}C_2$ deposition promoted the deposition of SiC above what was expected from single phase deposition. Thus, the actual amount of SiC deposition had the form:

$$t_{SiC}^{Act} = t_{SiC}^{Pred} + \Delta_{SiC} \quad (9)$$

where t_{SiC}^{Pred} was calculated from Equation 2 and Δ_{SiC} came from Table III.

The overall deposit thickness which was observed following experimentation can be estimated by a similar equation given by:

$$t_{Tot}^{Obs} = t_{B_{13}C_2}^{Pred} + t_{SiC}^{Pred} + \Delta_{Dep} \quad (10)$$

where Δ_{Dep} was from Equation 5. Thus, the overall codeposited material was a result of the individual predicted deposition rates and an interaction term which either enhanced or inhibited the deposition over what would be predicted from an assumption of independence in the reactions. The form of Δ_{Dep} was not exactly equal to $\Delta_{B_{13}C_2} + \Delta_{SiC}$, although there were some strong similarities. The similarity was in the significant presence of the temperature and temperature squared terms. In fact, when the estimates of the temperature and

temperature squared terms for the individual $B_{13}C_2$ and SiC equations were added together, the resulting values were approximately the same as was seen in the joint difference equation. That is, the addition of the x_3 estimates for the individual equations was -46.513 versus -49.603 for the total difference equation; for the x_3x_5 term, the addition of the individual terms gave a value of -19.468 against a value of -20.472 in the total difference equation. Further, the value of the x_2x_3 term in the $\Delta_{B_{13}C_2}$ was 8.934 versus 6.948 in the Δ_{Dep} equation. Thus, the Δ_{Dep} may be realistically broken into two parts and applied to the individual deposition rates for the two phases. It was difficult to assign the differences to particular reasons, other than the presence of extra effects in the results from random variations which happened to correlate with particular regressors. However, codeposition could be explained using the individual deposition equations along with an interaction term.

Conclusions

The codeposition of $B_{13}C_2$ +SiC has been shown to occur from mixtures of BCl_3 +MTS+ CH_4 + H_2 +Ar in a vertical, hot wall reactor using a modified impinging jet geometry. The deposition thicknesses of the composite samples were compared to those calculated via the derived mechanisms for the single phase deposition of $B_{13}C_2$ and SiC. This comparison showed that the deposition of the two phases did not occur independently of one another. The deposition deviated away from independence positively (i.e., more deposition observed than predicted) at low temperatures and MTS flow rates. At higher temperatures and MTS flow rates, the deposition deviated away from independence negatively (i.e., less observed than predicted). This was attributed to the difference in nucleation which occurred

under codeposition conditions. When a small amount of SiC was present, the nucleation of $B_{13}C_2$ was increased and the observed deposit was thicker. However, under conditions which led to higher reaction rates, the competitive nucleation and growth of both phases retarded the observed deposition to values below what would be predicted from the independent equations. Examination of the individual phase amounts showed that similar conditions led to deviation from that which was predicted from the single phase conditions.

References

¹W.J. Lackey, A.W. Smith, D.M. Dillard, and D.J. Twait, "Codeposition of Dispersed Phase Ceramic Composites," pp 1008-27 in Proceedings of the 10th International Conference on Chemical Vapor Deposition, ed. G.W. Cullen, The Electrochemical Society, Pennington, New Jersey, 1987.

²T. Hirai and T. Goto, "CVD Fabrication of In-Situ Composites of Non-Oxide Ceramics," pp 165-77 in Materials Science Research, Vol. 20, ed. R.E. Tressler, et al., Plenum Press, New York, 1986.

³T. Hirai, T. Goto, and T. Sakai, "Preparation of Si_3N_4 -BN Composites by Chemical Vapor Deposition," pp 347-58 in Materials Science Research, Vol. 17, ed. R.F. Davis, et al., Plenum Press, New York, 1984.

⁴T. Hirai, "CVD of Si_3N_4 and Its Composites," pp 329-45 in Materials Science Research, Vol. 17, ed. R.F. Davis, et al., Plenum Press, New York, 1984.

⁵E. Gugel, R. Keiffer, G. Leimer, and P. Ettmayer, "Investigations in the Ternary System Boron-Carbon-Silicon," pp 505-13 in Proceedings of the Fifth Materials Research Symposium. National Bureau of Standards Special Publication 364, July, 1972.

⁶D.R. Secrist, *J. Am. Ceram. Soc.*, **47**, 127-30 (1964).

⁷V.A. Lipp and M. Roder, "Verbindungen im System B-C-Si bzw. B-Si," *Z. Anorg. Allg. Chemie*, **344**, 225-9 (1966).

⁸E.M. Golda and B. Gallois, "Chemical Vapor Deposition of Multiphase Boron-Carbon-Silicon Ceramics," pp 167-72 in Materials Research Society Symposium Proceedings, **250**, Materials Research Society, Pittsburgh, PA, 1992.

⁹S. Goujard, L. Vandenbulcke, C. Bernard, G. Blondiaux, and J.L. Debrun, "Thermodynamic and Experimental Study of the Chemical Vapor Deposition in the Silicon-Boron-Carbon System at 1400 K," *J. Electrochem. Soc.*, **141**, 452-61 (1994).

¹⁰S.R. Goujard, L. Vandenbulcke, J. Rey, J.-L. Charvet, and H. Tawil, U.S. Patent No. 5,246,736 (21 September, 1993).

¹¹T.S. Moss, W.J. Lackey, and G.B. Freeman, "The Chemical Vapor Deposition of Dispersed Phase Composites in the B-Si-C-H-Cl-Ar System," Chemical Vapor Deposition of Refractory Metals and Ceramics III, Materials Research Society Symposium Proceedings, **363**, 239-244, Materials Research Society, Pittsburgh, PA, 1995.

¹²T.S. Moss, "The Chemical Vapor Deposition of Dispersed Phase Composites in the B-Si-C-H-Cl-Ar System," Ph.D. Dissertation, Georgia Institute of Technology, 1995.

¹³T.S. Moss, W.J. Lackey, and K.L. More, "The Chemical Vapor Deposition of $B_{13}C_2$ from Mixtures of BCl_3 - CH_4 - H_2 -Ar," submitted to *J. Am. Cer. Soc.*, 1995.

¹⁴T.S. Moss and W.J. Lackey, "Kinetics of the CVD of SiC in a Hot Wall Reactor using a Modified Impinging Jet Geometry," submitted to *J. Am. Cer. Soc.*, 1995.

LIST OF FIGURES

- Figure 1. Eutectic temperatures and compositions differ slightly between Secrist⁶ and Kieffer.⁵
- Figure 2. Melt isotherms of the ternary B-Si-C phase diagram.⁵
- Figure 3. A response plot of the difference in the total observed deposit thickness from that predicted.
- Figure 4. A response plot of the difference in the observed thickness and that predicted as functions of the predicted quantities of $B_{13}C_2$ and SiC.
- Figure 5. A response plot of the difference in the observed $B_{13}C_2$ thickness from that predicted from Equation 7 showed the effect of temperature and MTS flow rate on this quantity.
- Figure 6. Cross-section (a) and morphology (b) of codeposited $B_{13}C_2 + SiC$; Sample DB-345 prepared using a low MTS flow rate.
- Figure 7. Cross-section (a) and morphology (b) of codeposited $B_{13}C_2 + SiC$; Sample DB-342 prepared using a high MTS flow rate.

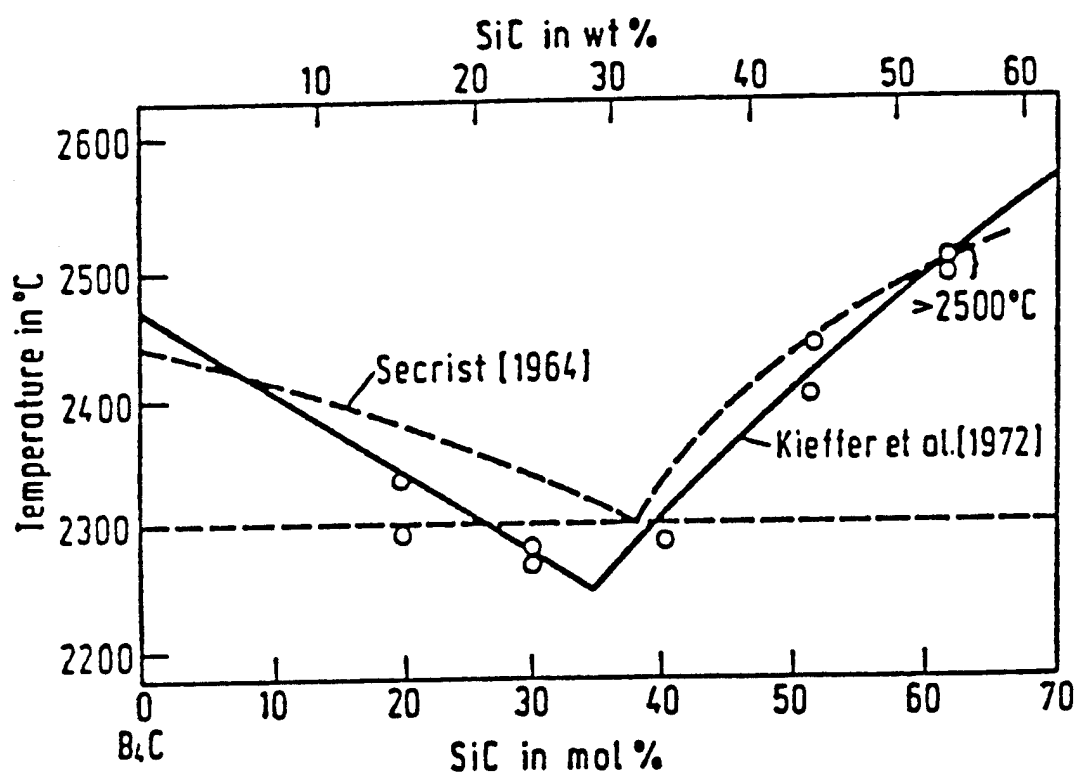


Figure 1. Eutectic temperatures and compositions differ slightly between Secríst⁶ and Kieffer.⁵

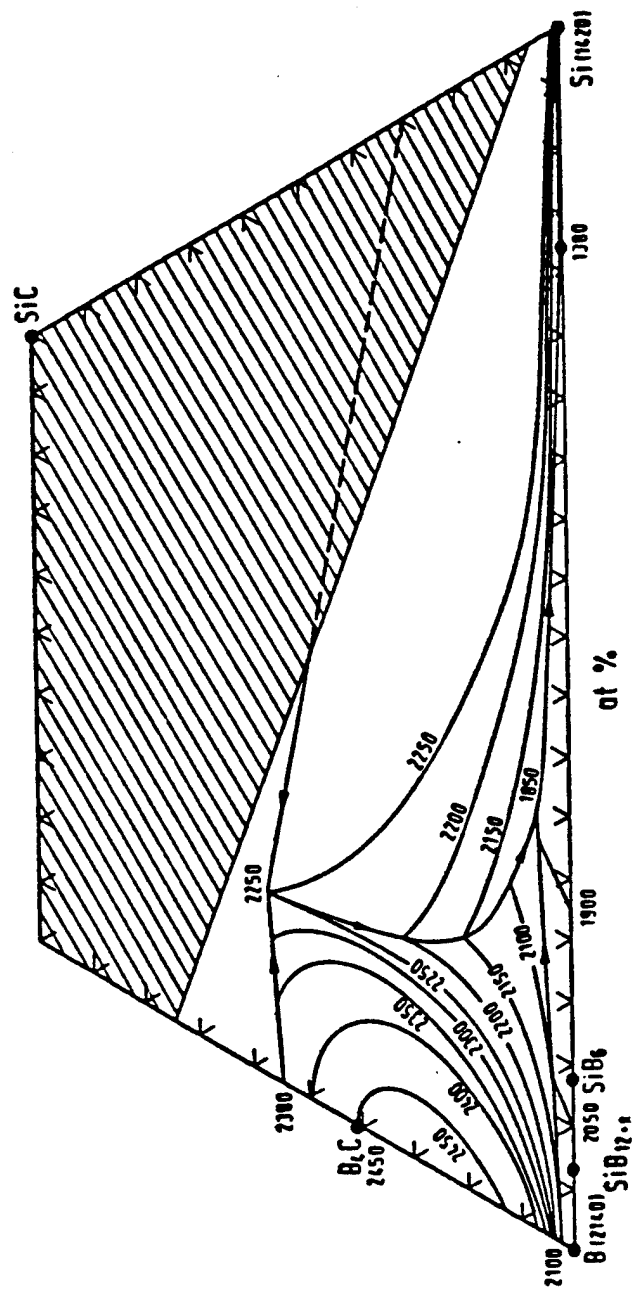


Figure 2. Melt isotherms of the ternary B-Si-C phase diagram.⁵

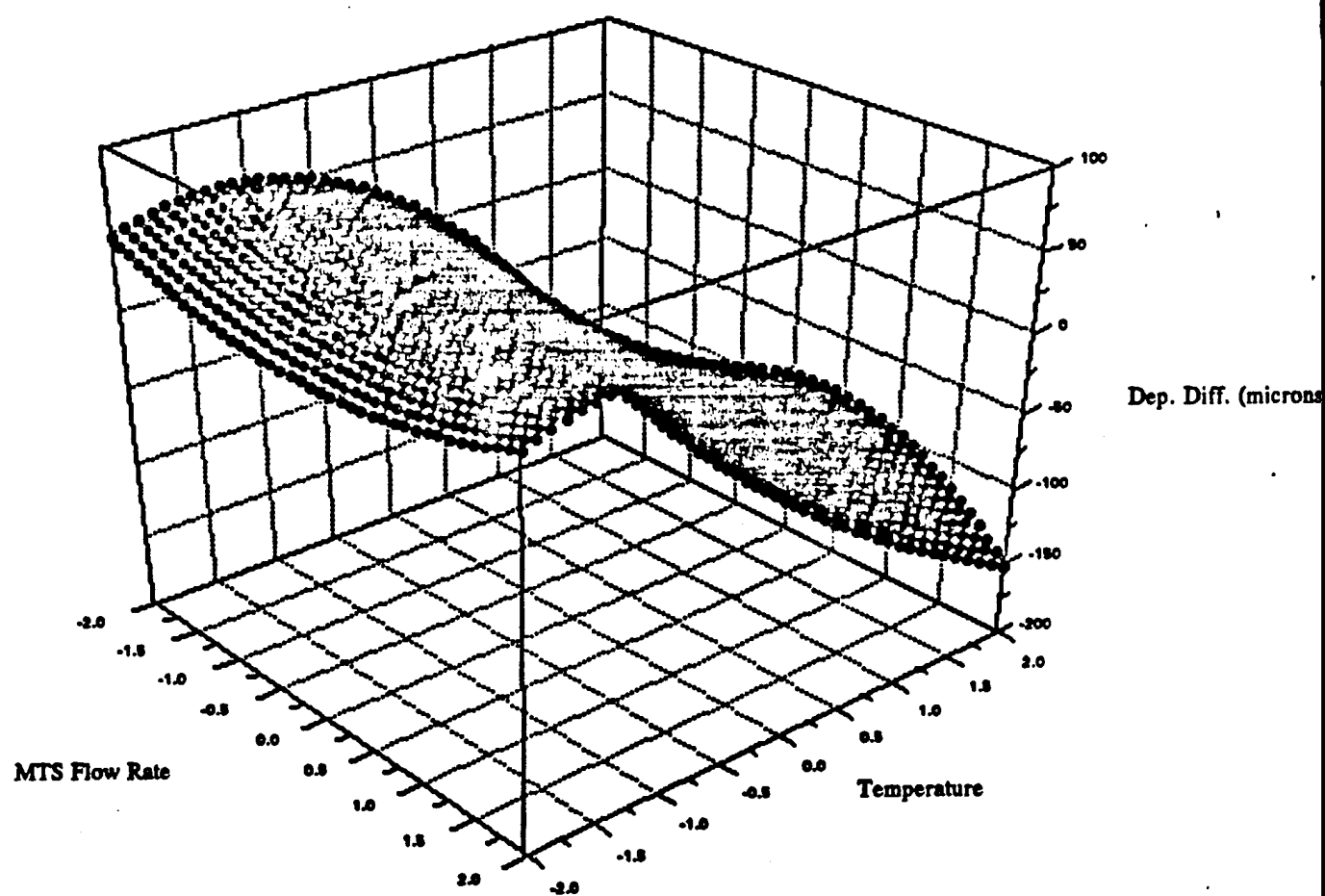


Figure 3. A response plot of the difference in the total observed deposit thickness from that predicted.

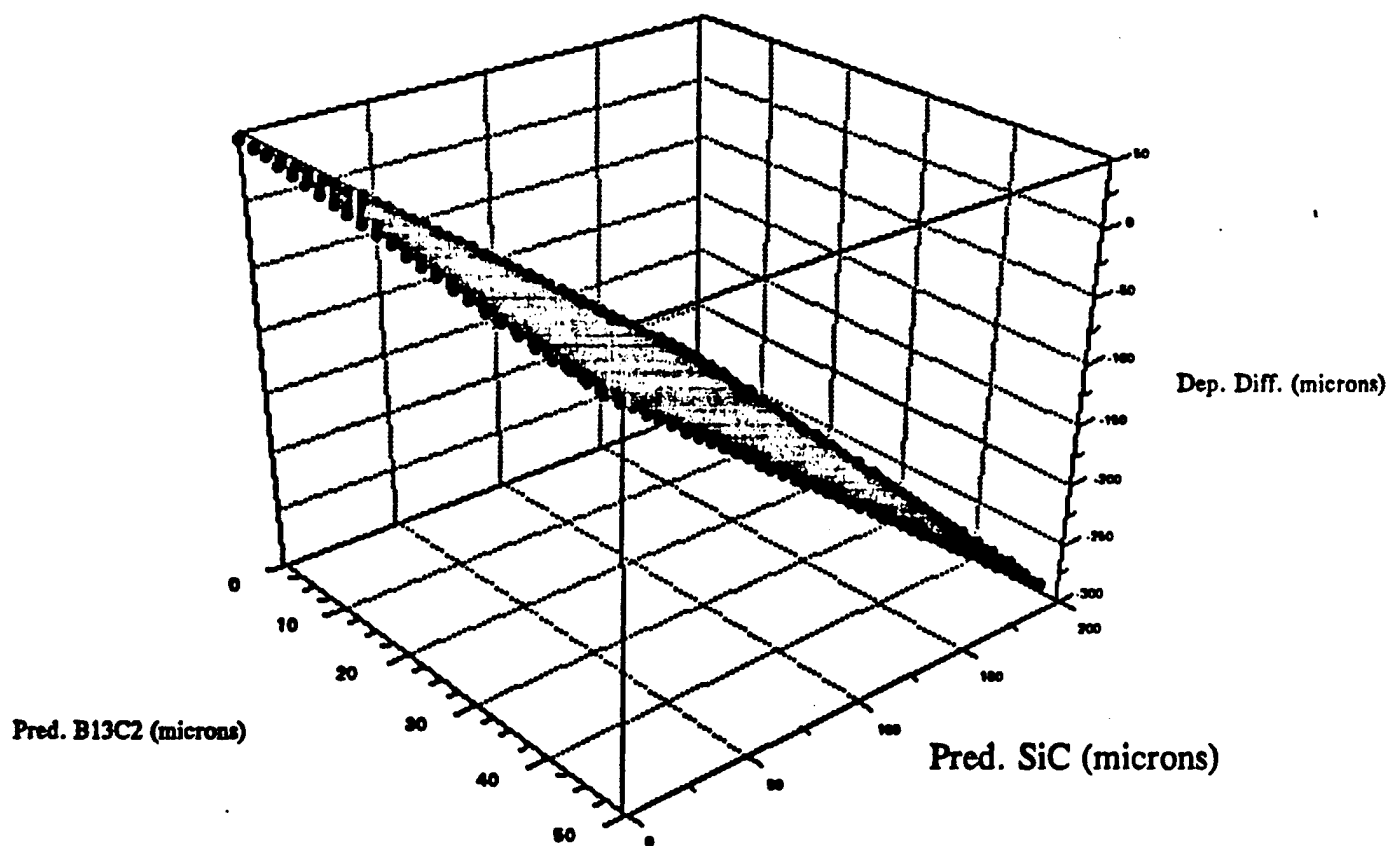


Figure 4. A response plot of the difference in the observed thickness and that predicted as functions of the predicted quantities of $B_{13}C_2$ and SiC.

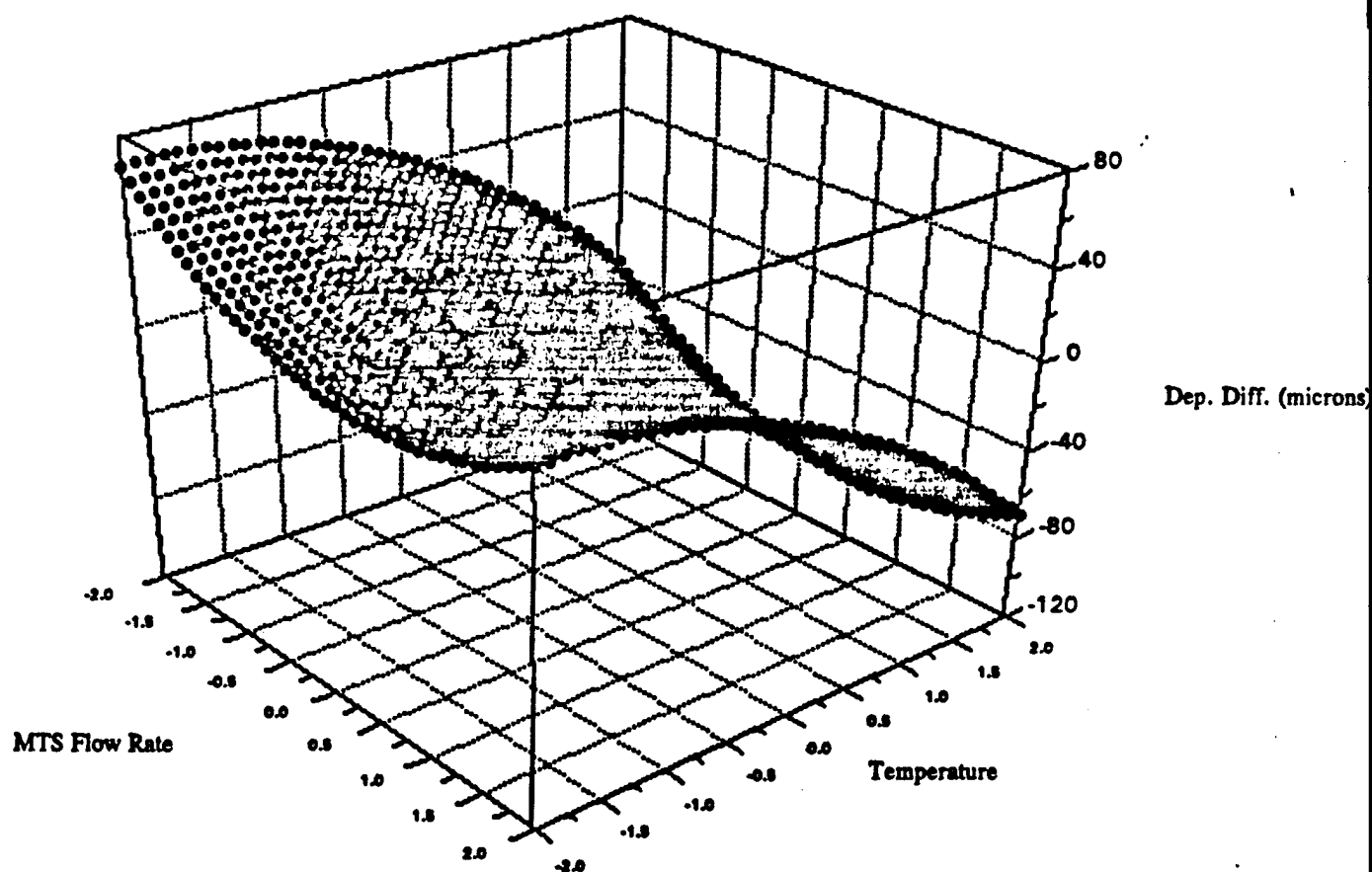


Figure 5. A response plot of the difference in the observed $B_{13}C_2$ thickness from that predicted from Equation 7 showed the effect of temperature and MTS flow rate on this quantity.

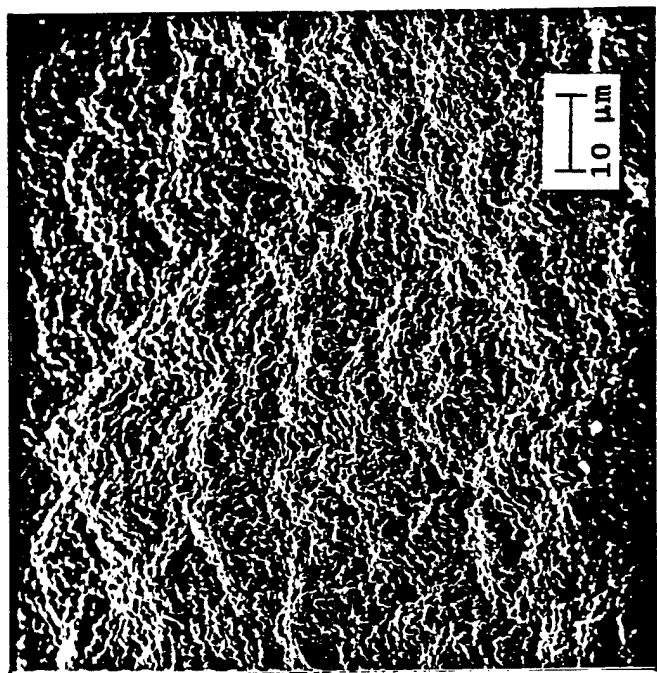


Figure 6. Cross-section (a) and morphology (b) of codeposited $B_{13}C_2 + SiC$; Sample DB-345 prepared using a low MTS flow rate.

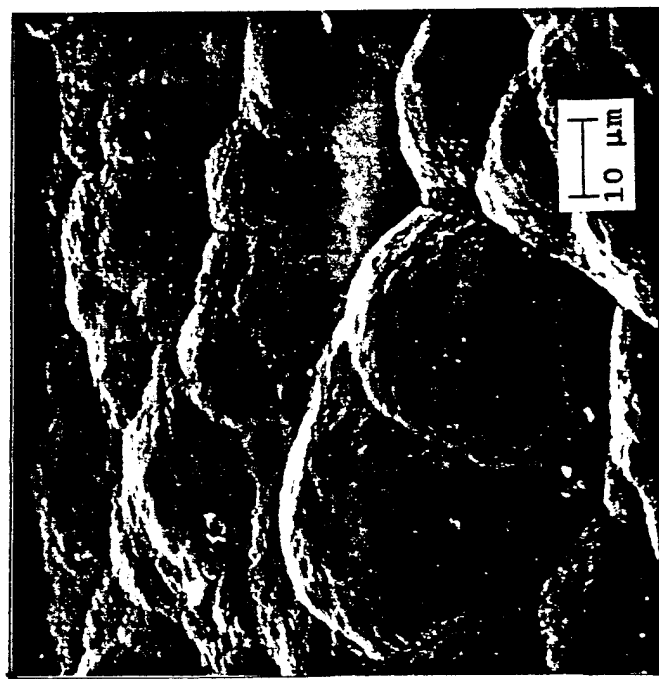
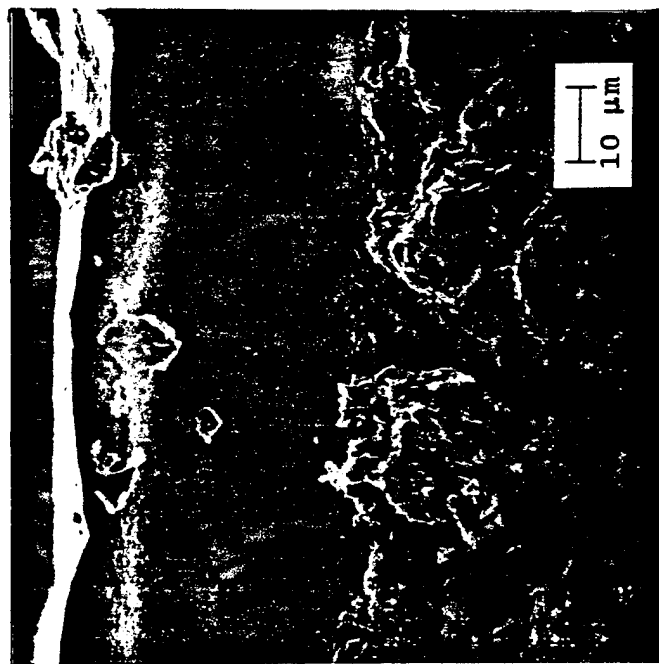


Figure 7. Cross-section (a) and morphology (b) of codeposited $B_{13}C_2 + SiC$; Sample DB-342 prepared using a high MTS flow rate.

Table I. Comparison of Predicted and Observed Deposit Thickness

Run No. DB-	B ₁₃ C ₂ Predicted (μm)	SiC Predicted (μm)	Predicted Total Deposit (μm)	Observed Total Deposit (μm)	Difference (μm)
325	31.84	6.93	38.77	30.96	-7.81
326	15.92	6.93	22.85	25.75	2.90
328	31.84	6.93	38.77	24.76	-14.01
329	24.55	1.71	26.26	55.72	29.46
330	31.84	6.93	38.77	29.20	-9.57
331	31.84	6.93	38.77	40.07	1.30
332	60.43	18.77	79.20	23.13	-56.07
333	36.26	43.80	80.06	6.12	-73.94
334	69.56	117.46	187.02	15.04	-171.98
335	31.84	6.93	38.77	24.42	-14.35
336	60.43	43.80	104.23	9.32	-94.91
337	36.26	18.77	55.03	4.33	-50.70
338	24.55	1.72	26.27	86.64	60.37
339	31.84	6.93	38.77	137.28	98.51
341	47.76	6.93	54.69	79.33	24.64
342	31.84	12.48	44.32	37.32	-7.00
343	31.84	6.93	38.77	22.95	-15.82
366	14.73	1.72	16.45	66.85	50.40
345	31.84	1.39	33.23	87.17	53.94
347	31.84	6.93	38.77	26.41	-12.36
348	24.55	0.74	25.29	71.41	46.12
349	31.84	6.93	38.77	10.74	-28.03
364	31.84	6.93	38.77	58.91	20.14
351	24.55	0.74	25.29	50.67	25.38
352	31.84	6.93	38.77	18.30	-20.47
353	11.16	0.16	11.32	10.88	-0.44
354	36.26	43.80	80.06	6.49	-73.57
355	60.43	43.80	104.23	65.10	-39.13
356	14.73	0.74	15.47	47.70	32.23
357	36.26	18.77	55.03	76.24	21.21
358	14.73	1.72	16.45	72.11	55.66
365	31.84	6.93	38.77	49.50	10.73
360	31.84	6.93	38.77	62.25	23.48
361	60.43	18.77	79.20	21.35	-57.85
362	14.73	0.74	15.47	54.43	38.96
363	31.84	6.93	38.77	66.02	27.25

Table II. Comparison of Predicted and Observed Quantities of $B_{13}C_2$ and SiC

Run No. DB-	$B_{13}C_2$ Predicted	SiC Predicted	$B_{13}C_2$ Observed	SiC Observed	Diff. $B_{13}C_2$	Diff. SiC
325	31.84	6.93	21.30	9.67	-10.54	2.74
326	15.92	6.93	9.15	16.60	-6.77	9.67
328	31.84	6.93	18.29	6.46	-13.55	-0.47
329	24.55	1.71	49.55	6.17	25.00	4.46
330	31.84	6.93	16.07	13.12	-15.77	6.19
331	31.84	6.93	13.91	26.16	-17.93	19.23
332	60.43	18.77	20.20	2.94	-40.23	-15.83
333	36.26	43.80	1.03	5.09	-35.23	-38.71
334	69.56	117.46	4.18	10.86	-65.38	-106.6
335	31.84	6.93	14.57	9.86	-17.27	2.93
336	60.43	43.80	3.94	5.38	-39.86	-38.42
337	36.26	18.77	1.53	2.80	-34.73	-15.97
338	24.55	1.72	21.48	65.16	-3.07	63.44
339	31.84	6.93	67.27	70.01	35.43	63.08
341	47.76	6.93	29.53	49.79	-18.23	42.86
342	31.84	12.48	24.01	13.31	-7.83	0.83
343	31.84	6.93	15.98	6.97	-15.86	0.04
366	14.73	1.72	26.50	40.35	11.77	38.63
345	31.84	1.39	87.17	0.00	55.33	-1.39
347	31.84	6.93	18.16	8.24	-13.68	1.31
348	24.55	0.74	70.44	0.97	45.89	0.23
349	31.84	6.93	6.97	3.77	-24.87	-3.16
364	31.84	6.93	27.07	31.84	-4.77	24.91
351	24.55	0.74	50.67	0.00	26.12	-0.74
352	31.84	6.93	11.62	6.69	-20.22	-0.24
353	11.16	0.16	10.39	0.48	-0.77	0.32
354	36.26	43.80	0.95	5.54	-35.31	-38.26
355	60.43	43.80	32.05	33.05	-11.75	-10.75
356	14.73	0.74	29.81	17.88	15.08	17.14
357	36.26	18.77	13.04	63.20	-23.22	44.43
348	14.73	1.72	37.04	35.07	22.31	33.35
365	31.84	6.93	33.96	15.54	2.12	8.61
360	31.84	6.93	54.34	7.91	22.50	0.98
361	60.43	18.77	17.84	3.51	-42.59	-15.26
362	14.73	0.74	50.17	4.26	35.44	3.52
363	31.84	6.93	59.78	6.04	27.94	-0.89

Table III. The deviation in the SiC deposition from the predicted amount was fit by a nine parameter surface shown with the standard deviation for each effect and its corresponding t-ratio.

Predictor	Coefficient (μm)	Standard Deviation (μm)	t-Ratio
Constant	5.293	2.450	2.16
x_5	-21.010	2.093	-10.04
x_5x_5	-13.077	1.837	-7.12
x_2x_5	-15.298	2.544	-6.01
x_1x_1	6.773	1.837	3.69
x_4	7.176	2.093	3.43
x_3x_5	8.715	2.544	3.43
x_2x_3	-7.136	2.544	-2.80
x_1x_2	6.428	2.544	2.53
x_1x_3	-6.031	2.544	-2.37

Chemical Vapor Deposition of Boron-Carbon Films Using Organometallic Reagents

Sundar Vaidyaraman[†], W. Jack Lackey^{*}, Pradeep K. Agrawal[†], Garth B. Freeman^{*},
E. Kent Barefield[‡] and John S. Lewis^{*}

[†]School of Chemical Engineering

^{*}Georgia Tech Research Institute

[‡]School of Chemistry and Biochemistry

Georgia Institute of Technology

Atlanta, GA 30332

Abstract

The feasibility of using organoboranes as precursors for the deposition of boron-carbon films in a hot-wall CVD furnace was investigated. The reagents studied include trimethylborane, triethylborane, tributylborane, and triphenylborane. The films deposited from trimethylborane were rich in carbon and did not contain boron. Films deposited from triethyl and tributylborane were rich in boron at low temperatures and pressures and rich in carbon at high temperatures and pressures. In the case of triphenylborane the vapor pressure was too low for film deposition.

Keywords: CVD, organoboranes, thin films

1. Introduction

The typical reagents used to deposit boron-carbon films using chemical vapor deposition (CVD) are boron trichloride (BCl_3) and a hydrocarbon such as methane (CH_4). However, the halogen present in the boron trichloride precursor can be corrosive to the deposition and effluent handling equipment. Finally, the trace quantities of halogen retained in the deposits can be deleterious to film properties. Further, the use of halogen-bearing precursors necessitates high operating temperatures (1100-1400 °C). These disadvantages

precursors necessitates high operating temperatures (1100-1400 °C). These disadvantages may potentially be overcome using organometallic reagents to deposit boron-carbon films. Boron-carbon deposits are of interest for use as oxidation and wear protective coatings, fiber-matrix interface coating, and as an oxidation inhibiting matrix for carbon fiber- carbon matrix composites.

Organometallic reagents have been extensively applied in the microelectronics industry. For example, deposition of gallium arsenide has been accomplished using trimethyl gallium and arsine [1]. The advantages of using organometallic compounds include high purity, low processing temperature, and the elimination of corrosion [2]. These advantages have prompted many investigations to test the feasibility of this class of compounds to deposit ceramic films. Girolami and Gozum [3] have provided an excellent review of the investigations of the organometallic precursors to deposit ceramic films.

Organometallic compounds have been successfully used to deposit silicon carbide, aluminum nitride, zirconium oxide, etc. [3], but no investigation has been undertaken to study the feasibility of organometallic compounds containing boron to deposit boron-carbon films. However, many researchers have used the organoboranes for doping of solar cells to increase their collection efficiency. For example, Higuchi et al. [4] have used trimethylborane and triethylborane for boron doping in solar cells using plasma enhanced CVD. They reported the deposition of boron with carbon from these compounds. However, the deposit was not analyzed for microstructure or composition. The present work was undertaken to study the feasibility of depositing boron-carbon films from some common organoboranes. Another goal

was to determine the effect of process variables such as temperature, pressure, and flow rates, on the structure and composition of films deposited using a hot-walled reactor.

2. Experimental Details

2.1 CVD Apparatus

Figure 1 shows a schematic of the CVD apparatus used to deposit the boron-carbon films. The overall arrangement can be divided into three parts: (1) reagent supply; (2) a resistively heated hot-wall vertical graphite furnace in a gas tight, water-cooled stainless steel shell, and (3) an effluent handling system.

2.1.1 Reagent Supply

Four different reagents, namely trimethylborane (TMB), triethylborane (TEB), tributylborane (TBB), and triphenylborane (TPB), obtained from Aldrich Chemical Company were used in the present study. Hydrogen and argon gases, used as diluents, were ultra high purity grade; obtained from Holox Gas Products, Atlanta, GA. The reagent supply system consisted of stainless steel lines, for the delivery of various reagents to the reactor, and mass flow controllers to control the flow rate of the feed to the reactor. The mode of reagent transport depended on its physical nature.

Trimethylborane was gaseous at room temperature and it was transported directly to the reactor using a flow controller. In the case of liquid reagents, namely triethylborane and tributylborane, a vaporizer was utilized (Figure 1) to transport the reagents to the reactor. Here, the reagent was transported by bubbling hydrogen through the vaporizer. The

concentration and the flow rate of the reagent was calculated from the weight loss of the vaporizer. Triphenylborane is solid in nature and a solid vaporizer was used to transport this reagent. The vaporizer containing the reagent was heated to $\sim 200^\circ\text{C}$ and the vaporized solid was carried to the reactor by a hydrogen gas flow. In many runs a diluent stream was also added to the reagent stream.

2.1.2 CVD Reactor

The CVD reactor was a resistively heated hot wall furnace with a water cooled stainless steel shell. The feed to the reactor entered through a water cooled stainless steel injector and the furnace was heated using a graphite heating element. The pressure in the furnace was measured using an MKS Baratron pressure gauge (Type 122 A). An optical pyrometer from Iacon Co. (Modline Plus, Type R) and a chromel-alumel thermocouple were used to measure the deposition temperature at the exterior surface of the graphite reaction chamber. The deposition temperature was controlled using a temperature controller from Research, Inc. (Micristar, Model 828D), which was interfaced with the pyrometer and the furnace power supply. In cases where the pyrometer was not operable (i.e., very low temperature) the temperature was controlled manually by adjusting the furnace power supply; the temperature could be controlled within $\pm 20^\circ\text{C}$.

2.1.3 Effluent Handling System

The exhaust system consisted mainly of a dry scrubber and a vacuum pump. The scrubber was typically filled with glass wool and soda lime. The function of the glass wool was to entrap the carbon soot and any other particulate; the soda lime was used to neutralize acidic gases in the exhaust stream. The vacuum pump was used to evacuate the reactor before

deposition, and control the pressure at some value between 10 to 760 torr during the deposition run.

2.2 Deposition Geometry

The present study was carried out by suspending the substrate vertically in the reaction chamber as shown in Figure 2, which will be referred to as the "vertical suspension geometry". This configuration is useful for exploratory studies of new reagents as it enables the observation of differences in the deposit as a function of vertical distance [5].

2.3 Substrates

Two types of α - Al_2O_3 plates were used as substrates : (1) 1.27 cm x 7.6 cm x 0.0794 cm, Coors Inc., Type -ADS-96, 99.6% and (2) 1.905 cm x 5.715 cm x 0.0635 cm, Materials Research Corporation. The first substrate was divided into six 1.27 cm squares. The different squares were designated A to F, with square F nearest to the gas injector as shown in Figure 2. The second substrate type was divided into three 1.907 cm squares. They were denoted by A, B, and C, with square C nearest to the injector (Figure 2).

2.4 Deposition Procedure

Tables 1, 2, and 3 summarize the operating conditions of the runs carried out with trimethylborane, triethylborane, and tributylborane, respectively. In this study the temperature of the runs was varied between 400-1100 °C, while the pressure was either 7-20 torr or 760 torr. In many runs, hydrogen or argon was added as a diluent to the feed. The general procedure for carrying out a run was as follows.

The substrate was weighed and placed inside the reactor and the system was evacuated to test for leaks. Once satisfied that the leak rate was less than 0.2 torr/min, the reactor was heated to the desired temperature while flowing argon through the shell, to prevent oxidation of the graphite heating element. The deposition was started by initiating the flow of reagent into the reactor. The deposition was terminated by stopping the reactant flow. The reactor was then cooled in flowing argon.

2.5 Characterization

Scanning electron microscopy (Hitachi S4100) was used to observe the morphology of the deposits, while energy dispersive spectroscopy (Noran Voyager) was used to determine elemental composition.

2.6 Quantification of Energy Dispersive Spectroscopy (EDS) Spectra

Figure 3 shows a typical EDS pattern obtained for a boron-carbon film. To first order, the elemental composition of the film was calculated based on the peak height. The calculations were based on the assumption that the carbon peak was symmetrical. The boron-to-carbon peak height ratio was calculated based on the following formula.

$$\frac{\text{Boron peak ht}}{\text{Carbon peak ht}} = \frac{B - A}{C}$$

Where,

B = Peak height of boron at $K_{\alpha} = 0.185$ KeV

C = Peak height of carbon at $K_{\alpha} = 0.282$ KeV

A = Contribution of the tail of carbon peak to height of boron peak.

3. Results and Discussion

3.1 Trimethylborane

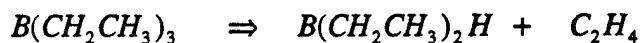
The initial runs were carried out with only trimethylborane (20 sccm) as the feed, i.e., no diluent was used. The films deposited in these runs were very rich in carbon and did not contain any boron. During the course of these runs a silvery deposit was observed in the lower portion of the reaction chamber, this material contained trace amounts of boron. Consequently, it was hypothesized that the boron containing radicals in the gas stream were over-reactive, resulting in boron deposition near the gas injector. This hypothesis was further strengthened by the observation of a reddish brown powder at the tip of the injector, whose color corresponded to the polymeric form reported by Brown et al. [6] on decomposition of trimethylborane at 500 °C in a closed tube.

To increase the effectiveness of boron radical transport to the substrate surface, the flow rate of the feed was increased by adding a diluent (runs 14-17). The diluents used in the present work was either hydrogen or argon. The flow rate of the reagent and the diluent were 20 and 200 sccm, respectively. The addition of the diluent to the feed did not result in deposition of boron. Considerable deposition of carbon occurred on the substrate but no boron was detected.

From the above set of runs it was concluded that the potential of trimethylborane to deposit thin films containing both boron and carbon in a hot-wall furnace is very limited.

3.2 Triethylborane

Table 2 summarizes the results of the runs with triethylborane. The chemistry of triethylborane indicated the potential of the reagent to deposit boron-carbon films. Triethylborane is subjected to a β -hydrogen elimination which does not take place in the case of trimethylborane. Triethylborane undergoes elimination of the β -H bond at relatively low temperatures (about 300 °C) [7], i.e.,



and subsequent elimination eventually produces borane and an additional olefin. It is well established that the borane (diborane) produces elemental boron at high temperatures [8] and hydrocarbons deposit carbon at comparable conditions. Consequently, triethylborane was expected to be a better reagent for the deposition of boron-carbon compounds. Substantial amounts of boron, in addition to carbon, were deposited in the triethylborane runs. The micrographs in Figure 4 show two morphologies observed for the films deposited using triethylborane. One of the micrographs namely, Figure 4(a) shows the deposit to be crystalline nature. Similar morphologies were observed when the run was conducted at 1000 °C. However, in the case of low temperature runs the film showed a nodular structure as shown in Figure 4(b) indicating an amorphous deposit.

The amount of boron deposited depended strongly on the operating conditions. The temperature, spatial position, pressure, and diluents, in the order of importance, affected the boron deposition from triethylborane. The following sections explain in detail the effects of these parameters.

3.2.1. Temperature

Temperature had the strongest effect on the amount of boron deposited. Lower temperature (400-600 °C) seemed to favor the deposition of boron. For example, from runs 19, 20, and 28 it can be seen that the boron-to-carbon ratio increases as the temperature of the run decreases. This trend was easily observable at low pressures due to large amounts of boron deposited at this condition. The same trend was observed for both hydrogen and argon diluents (runs 21 and 22). This phenomenon can be attributed to the relative stability of the carbon and boron radicals in the gas phase. At lower temperatures (400-600 °C) the carbon containing radicals are very stable resulting in very low amounts of carbon deposition. This, coupled with boron deposition, results in high boron-to-carbon ratios in the films deposited at lower temperatures. Whereas, at high temperatures (800-1100 °C) most of the boron radicals get depleted due to their high reactivity, even before reaching the substrate, resulting in reduced amount of boron deposition. This, coupled with the increase in the amounts of carbon deposited, results in low boron-to-carbon ratios at high temperatures.

3.2.2. Spatial Position

The amount of boron deposited depended strongly on the spatial position of the substrate. For example, for runs 20 and 33, the boron-to-carbon ratio decreased from position A to F. In all the runs where boron was deposited, the parts of the substrate that first came into contact with the feed were richer in boron. Apparently, the high reactivity of boron radicals coupled with low concentration resulted in reduction of the amounts of boron

deposited with distance from the gas injector. Consequently, the boron-to-carbon ratio varied over the length of the substrate.

3.2.3 Pressure

The deposition experiments were carried out both at atmospheric pressure and under vacuum (7-20 torr). The boron-to-carbon ratio in the deposits was higher at low pressures. For example, consider runs 20 and 26, which were carried out at 600 °C with hydrogen as the diluent. EDS spectra of the films deposited in these runs showed that more boron was deposited under vacuum than at atmospheric pressure. The same phenomena can be observed for the runs performed at 1100 °C (runs 19 and 27). However, the difference between the boron content deposited at the two pressures was much lower at 1100 °C, as compared to 600 °C, due to more carbon deposition at the higher temperature. The same trends were observed for the cases where argon was used as the diluent instead of hydrogen. The low boron deposition observed at atmospheric pressure may be attributed to mass transfer resistance. At atmospheric pressure, the reaction chamber is filled with argon and the boron radicals have to diffuse through the argon to reach the surface of the substrate. The low concentration of the boron radicals coupled with mass transfer resistance reduces the concentration of boron radicals near the substrate surface, thereby, reducing the amount of boron deposited in the films. However, in the case of carbon, six carbon atoms are present for every atom of boron in the reagent resulting in excess carbon radicals in the gas phase. Consequently, the effect of mass transfer on carbon deposition might not be very severe.

3.2.4. Diluent

The diluents used in this study were hydrogen and argon. The boron-to-carbon ratio was larger in those cases where hydrogen was used as the diluent compared to argon. For example, consider runs 20 and 21 (Table 2) which were conducted at 600 °C and under vacuum. The high boron-to-carbon ratios in the runs with hydrogen is due to the reaction of the deposited carbon with hydrogen resulting in lowering of the amount of carbon in the deposit [9]. This reduced amount of carbon deposition might be responsible for the high boron-to-carbon ratios in these runs.

3.2.5 Flow Rate

The effect of different flow rates of feed was obtained by changing the diluent flow rate. It was observed that the increase in flow rate of the feed increased the boron-to-carbon ratio by a small amount. Runs 19, 33, and 38 show, for example, that increasing the diluent flow rate from 975 to 4900 sccm increased the boron-to-carbon ratio from 0.07 to 0.5. This can be attributed to effective transportation of boron radicals due to increased flow rate of the feed.

In summary, triethylborane has the potential to be used as a reagent to deposit boron-carbon films. Films with boron-to-carbon ratios from 0 to as high as 1.5.

3.3 Tributylborane

Table 3 summarizes the results of the runs with tributylborane. Tributylborane undergoes a β -H elimination similar to triethylborane. Hence, the behavior of this reagent was expected to be similar to that of triethylborane. However, its behavior was very erratic. This

variability was due to the condensation of the reagent in the supply lines and low volatility of the reagent.

In the initial runs the feed contained only the reagent without any diluent. The films deposited in these runs were typically rich in carbon and did not show any presence of boron. One exception was the film deposited at a temperature of 500 °C and a pressure of 8.6 torr (run 44), which contained boron. This can be attributed to a high rate of reagent consumption compared to typical values. The lack of boron deposition in most of the above runs can be ascribed to the low volatility of the reagent.

In the next set of experiments an argon diluent was added to the feed containing tributylborane (runs 48-54). Substantial amounts of boron were deposited in addition to carbon at a temperature of 500 °C and a pressure of 18.6 torr. Boron was absent in the runs conducted at 800 or 1100 °C and low pressures. During the course of these experiments large amounts of liquid tributylborane was detected in the reagent lines. Consequently, the transportation of the reagents to the reactor was affected, thereby, hindering the film deposition. This limitation was circumvented by heating the reagent lines to 100°C with heating tapes and the vaporizer to ~50°C in a water bath.

The atmospheric pressure runs with argon as the diluent (runs 63-65) were conducted after cleaning the lines. Large amounts of boron and carbon were deposited for the run completed at 500 °C (run 65). However, films very rich in carbon without any boron were obtained for the runs at 800 and 1100 °C. Atmospheric pressure runs with hydrogen as the diluent were also completed with heated reagent lines and vaporizer. There was no deposition at 500 °C and only very thin films were obtained at 800 and 1100 °C.

In summary, tributylborane deposits boron and carbon only at very low temperatures. Also, the very low vapor pressure of the reagent complicates obtaining high deposition rates.

3.4 Triphenylborane

To study the feasibility of triphenylborane, runs were completed at different pressures, temperatures, and with different diluents. All the runs were 30 minutes in duration. Most of the runs did not result in film deposition. In cases where deposition occurred the films were very thin and contained only carbon.

The absence of film deposition in most of the runs can be attributed to the low vapor pressure of the reagent. Triphenylborane's vapor pressure is about 11 torr at 200 °C. This low vapor pressure makes the concentration, or the partial pressure, of the reagent in the feed very low, leading to a very low deposition rate. One way of increasing the concentration of the reagent in the feed is to reduce the pressure inside the vaporizer, this increases the partial pressure of the reagent in the feed. Accordingly, several runs were conducted keeping the vaporizer under vacuum. However, this method led to the blockage of the vaporizer outlet by triphenylborane crystals. It was never possible to conduct a 30 min run without experiencing blockage.

From the above it can be concluded that triphenylborane is not a very suitable reagent for preparation of boron-carbon deposits due its low vapor pressure. Also, the solid nature of the reagent poses problems in its uniform transport to the furnace. Perhaps feeding the reagent as a solid powder or aerosol would alleviate the problem of transporting the reagent to the CVD furnace [10,11].

4. Conclusions

- (1) Triethylborane is the most promising reagent of those investigated for deposition of boron-carbon films.
- (2) The ratio of boron-to-carbon in the deposit when using triethylborane depended strongly on the temperature, pressure, type of diluent and its flow rate. The highest boron-to-carbon ratio was obtained for runs conducted at low temperatures (400-600°C) and low pressures (7-20 torr).
- (3) Tributylborane showed potential to deposit films containing both boron and carbon at low temperatures. However, the low vapor pressure of the reagent would result in very low deposition rates.
- (4) Trimethylborane and triphenylborane are not very suitable reagents for preparing boron-carbon films in a hot-wall CVD furnace.

Acknowledgments

This work was supported by the Air Force Office of Scientific Research. The guidance of Dr. Alexander Pechenik throughout the course of this work is appreciated. We thank Ms. Shree Collins for her expertise and diligence in graphics preparation.

References

- [1] G. B. Stringfellow, "Organometallic vapor phase epitaxy: theory and practice," Academic Press, Boston, 1982.
- [2] P. D. Dapkus, "Metal organic chemical vapor deposition," *Annual Review of Material Science*, Vol 12, pp 243-269, 1982.
- [3] G. S. Girolami and J. E. Gozum, " Low temperature MOCVD routes to thin films from transition metal precursors," *Chemical Vapor Deposition of Refractory Metals and Ceramics* (eds. T. M. Besmann and B. M. Gallois), MRS Symposium Proceedings, Vol 168, pp 319-329, 1990.
- [4] K. Higuchi, K. Tabuchi, K. S. Lin, M. Konagai and K. Takahashi, "High efficiency delta-doped amorphous solar cells prepared by photochemical vapor deposition," *Japanese Journal of Applied Physics, Part 1: Regular Papers and Short Notes*, Vol 30, pp 1635, 1991.
- [5] W. Y. Lee, "Chemical vapor deposition of dispersed phase ceramic composites," Ph.D. Thesis, Georgia Institute of Technology, 1990.
- [6] M. P. Brown, A. K. Holliday, G. M. Way, R. B. Whittle, and C. M. Woodard, "Pyrolysis of trimethyl borane, Part II: Formation of carboranes and other boron containing compounds," *Journal of Chemical Society, Daltons Transactions*, pp. 1862, 1977.
- [7] J. D. Odom, "Non-cyclic three and four coordinated boron compounds," in *Comprehensive Organometallic Chemistry*, G. Wilkinson, F. G. A. Stone, and E. W. Abel, eds., vol. 1, Chapter 5.1.

- [8] H. O. Pierson and A. W. Mullendore, "Chemical Vapor Deposition of Boron from Diborane," Proceedings of 7th International conference on CVD, eds. T. O. Segwick and H. Lydtin, The Electrochemical Society, Princeton, pp 360, 1979.
- [9] P. R. Wentreck, B. J. Wood, and H. Wise, "The role of surface carbon on catalytic methanation", Journal of Catalysis, vol. 43, 363 (1976).
- [10] W. J. Lackey, E. K. Barefield, W. B. Carter, J. A. Hanigofsky and D. N. Hill, "Method for the rapid deposition with low vapor pressure reactants by chemical vapor deposition," U. S. Patent 5,108,983, April 28, 1994.
- [11] W. J. Lackey, W. B. Carter, J. A. Hanigofsky, D. N. Hill, E. K. Barefield, G. Neumeier, D. F. O'Brien, M. J. Shapiro, J. R. Thompson, A. J. Green, T. M. Moss, R.A. Jake and K. R. Efferson, "Rapid chemical vapor deposition of superconducting $\text{YBa}_2\text{Cu}_3\text{O}_x$ ", Applied Physics Letters, Vol 56, pp 1175-1177, 1990.

Table 1: Operating Conditions of Runs with Trimethylborane.

<i>Run No.</i>	<i>Temperature (°C)</i>	<i>Pressure (torr)</i>	<i>Reagent Flow Rate (sccm)</i>	<i>Diluent Type</i>	<i>Diluent Flow Rate (sccm)</i>
1	1100	7.7	13.6		
5	800	6.1	23.1		
2	500	5.7	18.3		
11	800	760	17.8		
7	500	760	17.0		
3	1100	760	20.4		
15	1100	9.5	13.0	Argon	200
16	1100	6.2	11.9	Hydrogen	200
14	1100	760	14.9	Argon	200
17	1100	760	13.8	Hydrogen	200

*All Substrates were Type 1.

Table 2: Operating Conditions and Results of the Runs Completed with Triethylborane.

Run No.	Temperature (°C)	Pressure (torr)	Reagent Flow Rate (sccm)	Diluent Type	Diluent Flow Rate (sccm)	Substrate Type	B/C Peak Heights					
							Sample Position					
							A	B	C	D	E	F
19	1100	8.6	30.5	Hydrogen	950	1	0	0	0	0	0.076	
33	1100	18	7.6	Hydrogen	2900	1	0.07	0	0.011	0	0.8	
38	1100	30.6	6.9	Hydrogen	4900	2	0.412	0.511	0.500		0.063	
20	600	8.8	10.7	Hydrogen	975	1	0.361	0	0.320	0.443	0.750	
28	400	12.9	3.8	Hydrogen	975	2	-	1.429	1.603			
27	1000	760	3.8	Hydrogen	975	2	0	0	0			
37	1100	760	8.4	Hydrogen	2900	2	0	0.65	0.099			
26	600	760	3.0	Hydrogen	975	2	0	0	0.438			
29	400	760	6.9	Hydrogen	975	2			No Film Deposited			
22	1100	19.4	37.4	Argon	975	1	0	0	0	0	0.393	
34	1100	33	10.7	Argon	2900	2	0	0.026	0.022			
21	600	17.1	19.8	Argon	975	1	0	0	0	0	0.673	
24	1100	760	2.3	Argon	975	1	0	0	0	0	0	
36	1100	760	7.6	Argon	2900	1	0	0	0	0	0.054	
23	600	760	3.0	Argon	975	1	0	0	0	0	0.127	

Table 3: Operating Conditions and Results of the Runs Done with Tributylborane.

Run No.	Temperature (°C)	Pressure (torr)	Reagent Flow (sccm)	Diluent Type	Diluent Flow Rate (sccm)	B/C Peak Heights		
						Sample Position		
						A	B	C
43	1100	8.1	16	-	-	0	0	0
42	800	8.3	4.8	-	-	0	0	0
44	500	8.6	45.3	-	-	0	0	0.15
46	1100	760	0.5	-	-	0	0	0
47	800	760	4.8	-	-	0	0	0
45	500	760	9.6	-	-	0	0	0
49	1100	20.1	3.2	Argon	975	0	0	0
54	800	20	4.8	Argon	975	0	0	0
50	500	18.6	6.4	Argon	975	0	0	0.39
51	1100	760	4.3	Argon	975	0	0	0.06
53	800	760	4.3	Argon	975	0	0	0
65	500	760	2.1	Argon	1000	0	0	0.03
61	800	13.2	3.7	Hydrogen	975	0	0	0.23
56	500	15	3.7	Hydrogen	975	No Film Deposited		
63	1100	760	3.7	Hydrogen	975	0	0	0
64	800	760	9.1	Hydrogen	975	0	0	0
68	500	760	9.1	Hydrogen	975	No Film Deposited		

* All the substrates were type 2.

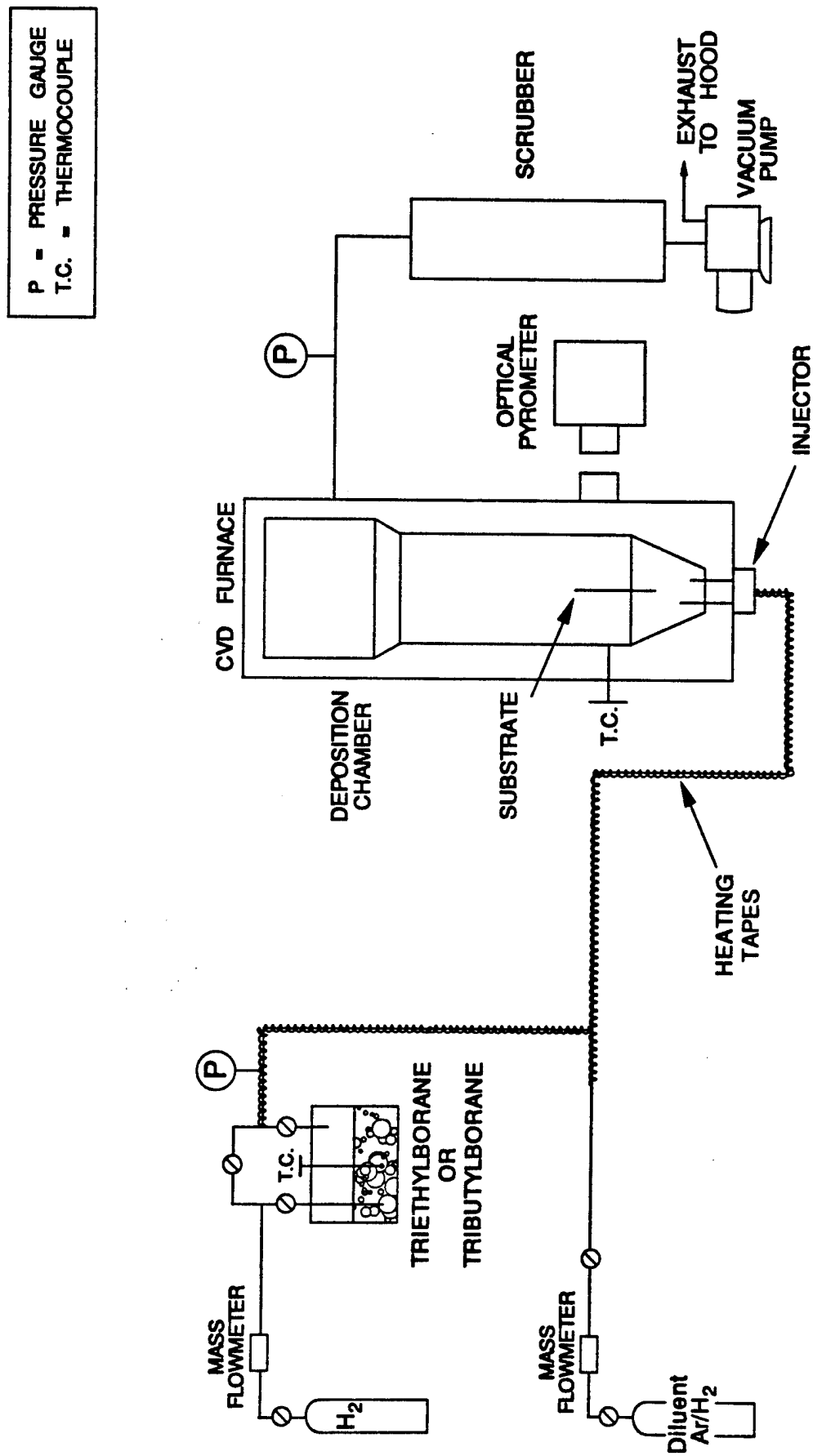


Figure 1. Experimental apparatus for CVD of boron-carbon films.

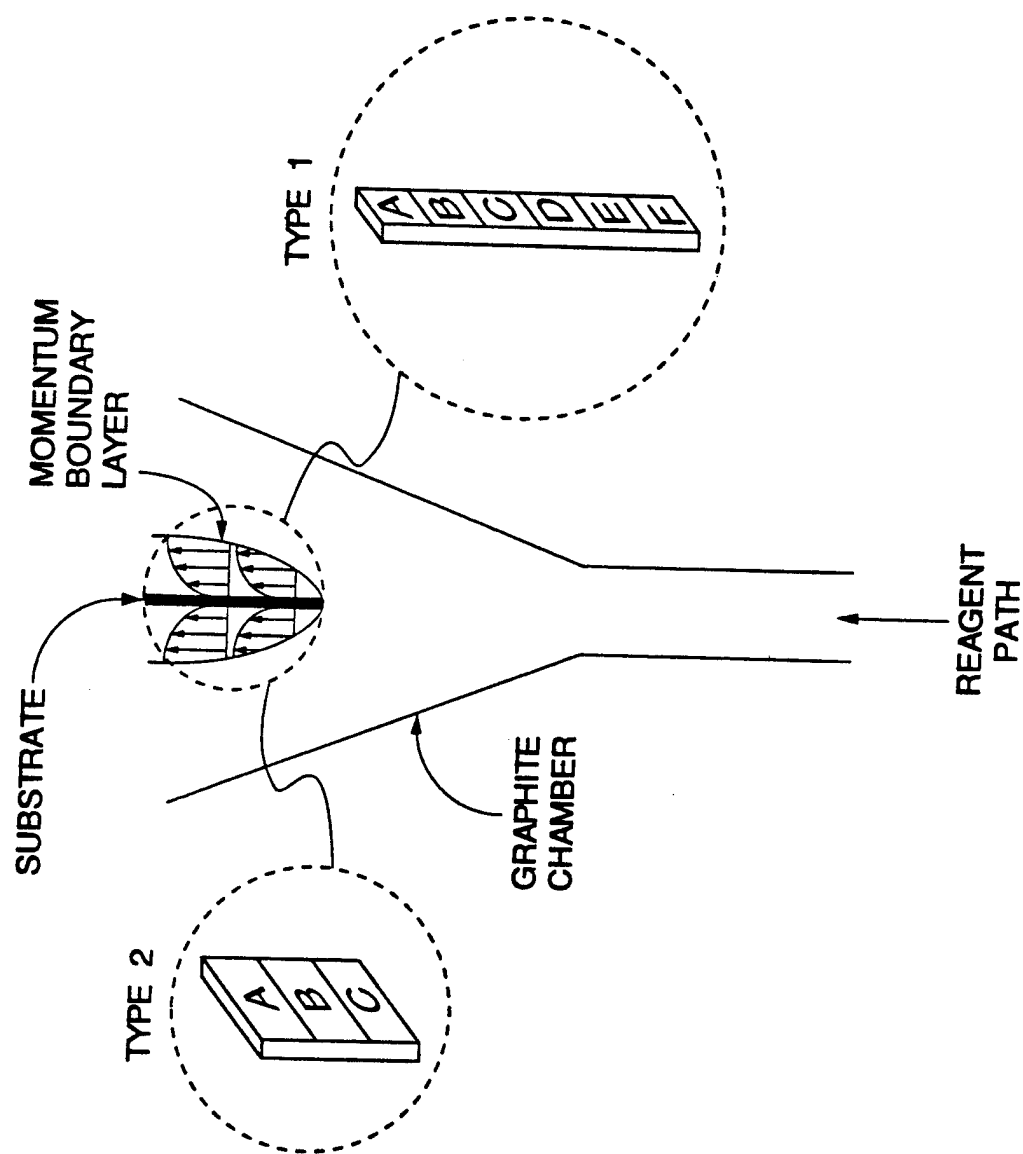


Figure 2. Vertical suspension geometry was used to study the deposition of boron-carbon film.

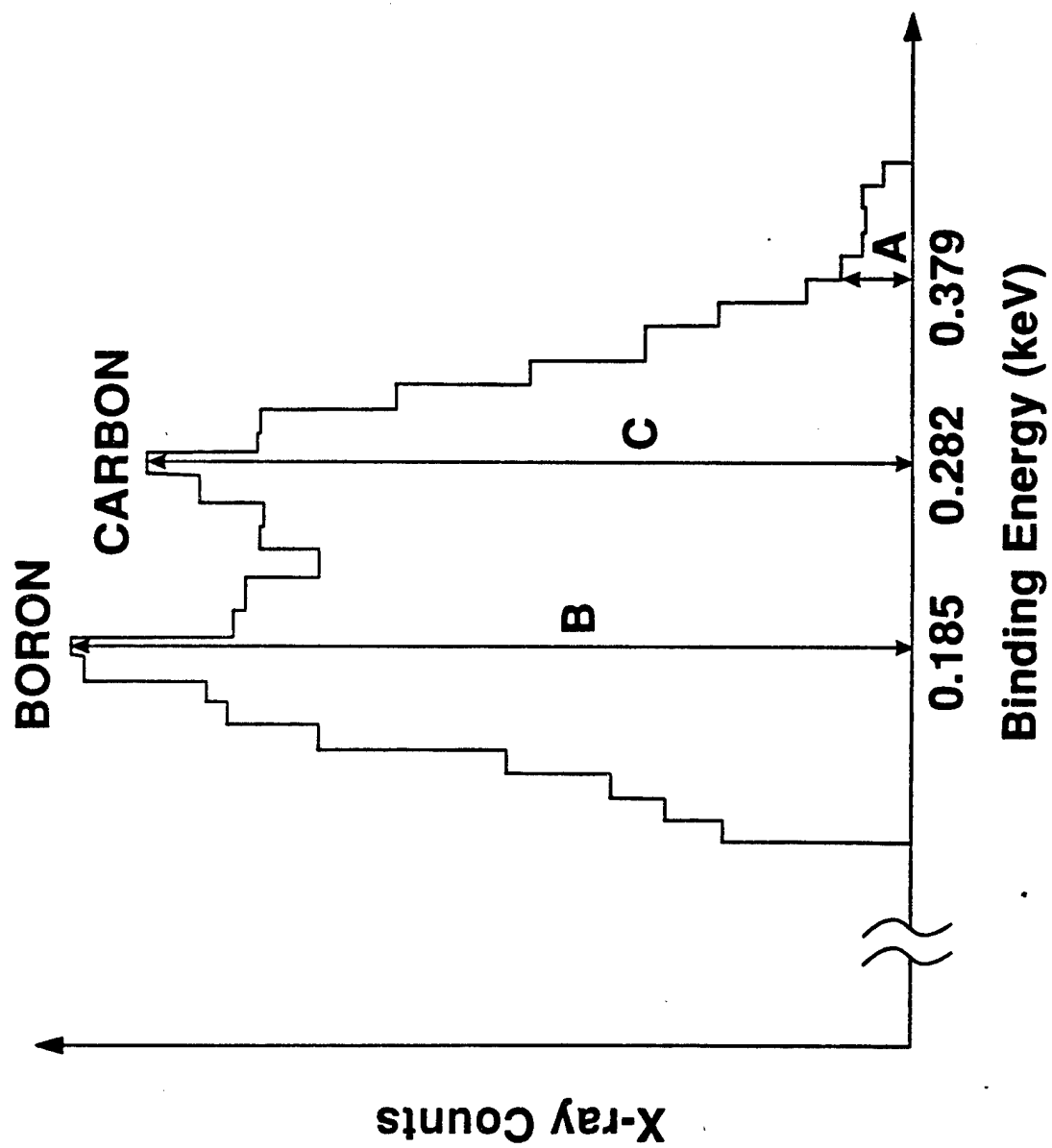


Figure 3. A typical EDS pattern obtained for boron-carbon films.

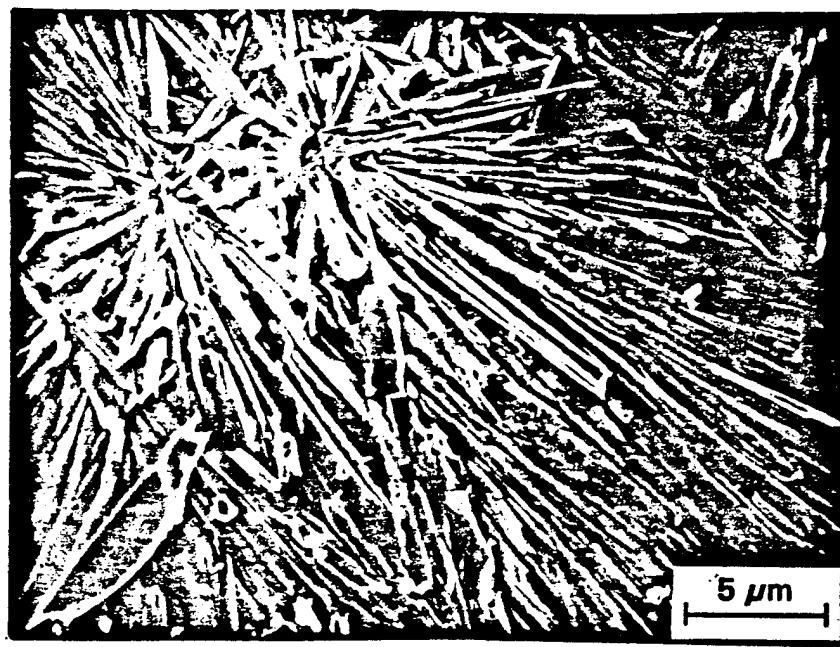


Figure 4 (a). Micrograph showing crystalline morphology of the films deposited at the higher temperature (1000°C).

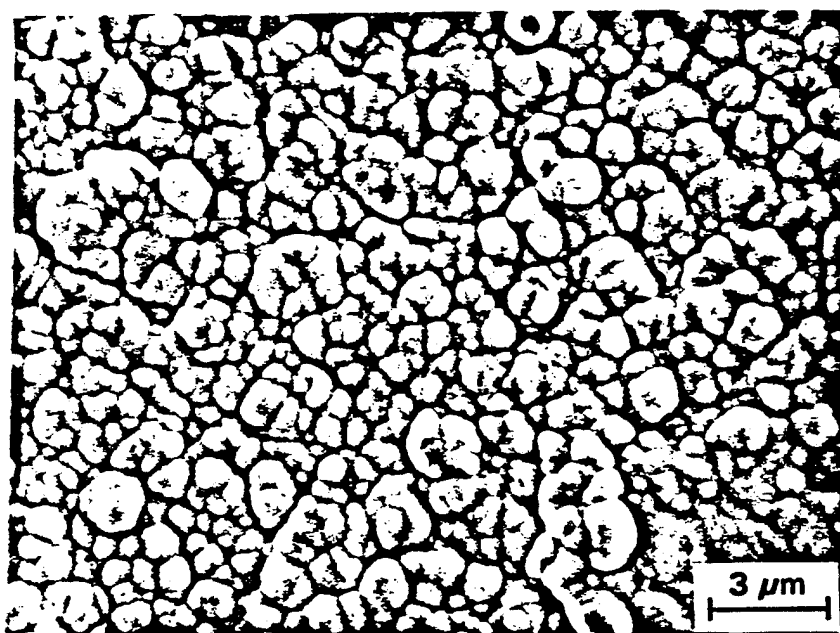


Figure 4 (b). Micrograph showing the typical amorphous morphology of the films deposited at lower temperatures (400-600°C).